FACULTY OF ENGINEERING AND ARCHITECTURE

Advances in the Analysis of Language Event-Related Potentials: From Simulations to Real-Life Evidence

Emma Depuydt

Doctoral dissertation submitted to obtain the academic degree of
Doctor of Biomedical Engineering

Supervisors

Prof. Pieter van Mierlo, PhD* - Prof. Miet De Letter, PhD**

* Department of Electronics and Information Systems
Faculty of Engineering and Architecture, Ghent University

** Department of Rehabilitation Sciences
Faculty of Medicine and Health Sciences, Ghent University

September 2025

GHENT UNIVERSITY

ISBN 978-94-93464-22-3
NUR 954
Wettelijk depot: D/2025/10.500/82

Members of the Examination Board

Chair

Prof. Joris Degroote, PhD, Ghent University

Other members entitled to vote

Prof. Evelien Carrette, PhD, Ghent University
Prof. Tom Francart, PhD, KU Leuven
Prof. Borbála Hunyadi, PhD, Technische Universiteit Delft, the Netherlands
Prof. Vitória Piai, PhD, Radboud Universiteit, the Netherlands
Prof. Emmeric Tanghe, PhD, Ghent University

Supervisors

Prof. Pieter van Mierlo, PhD, Ghent University
Prof. Miet De Letter, PhD, Ghent University

English Summary

Language is one of the most fundamental yet complex domains of human cognition. While gestures, facial expressions, and emotional tone contribute to communication, language remains the primary tool for expressing intricate and abstract ideas. Despite its apparent ease in daily life, language relies on highly specialized and distributed neural mechanisms, many aspects of which are still being actively investigated. Understanding these mechanisms is particularly important for developing better diagnostic tools and therapeutic approaches for individuals with language impairments resulting from conditions such as stroke, brain tumors, or traumatic brain injury.

Research increasingly shows that language processing is not confined to isolated brain regions but emerges from the dynamic interaction of distributed neural systems. Processing even a single spoken word consists of multiple stages, each recruiting multiple brain areas. Early auditory analysis, for example, includes the superior temporal cortex, lexical mapping requires the middle temporal gyrus, semantic retrieval involves the angular gyrus, and syntactic integration is mediated by the inferior frontal gyrus. Theoretical frameworks developed by Ellis and Young (auditory processing), De Deyne (semantic networks), and Dominey (syntactic parsing) underscore the interconnected nature of these processes and emphasize the importance of studying language processing in the brain as a network phenomenon.

This dissertation builds upon these frameworks and pursues two major objectives. The first objective is to characterize the neural dynamics of speech perception, which is a complex and multilayered process that transforms acoustic signals into meaningful linguistic information within a few hundred milliseconds, using electroencephalography (EEG). The second objective addresses key methodological challenges in EEG research through a series of targeted simula-

tion studies, aiming to refine techniques for analyzing event-related potentials (ERPs) and to augment the insights obtained from the improved results.

Chapter 1 serves as a general introduction to the topic and outlines the broader context of the dissertation. **Part I: From Neural Activity to Measured Brain Signals** lays the groundwork by explaining how brain activity is recorded and interpreted using EEG. **Chapter 2** introduces key neurophysiological principles, covering the generation of electrical activity in the brain, the fundamentals of electroencephalography, and the concept of event-related potentials (ERPs). **Chapter 3** then provides more details about EEG signal processing, focusing on EEG source imaging and functional connectivity. It discusses methods for estimating the sources of brain signals, including the formulation of the forward model and solutions to the inverse problem, as well as techniques for assessing how different brain regions interact.

In **Part II: Source reconstruction and functional connectivity of language ERP components**, speech perception is investigated empirically using EEG, which offers the temporal resolution needed to track fast-evolving cognitive processes. **Chapter 4** examines three well-established ERP components — the Mismatch Negativity (MMN), the P300, and the N400 — each reflecting distinct stages of linguistic analysis. The MMN captures early, pre-attentive detection of unexpected auditory changes; the P300 reflects attentive categorization and task-related decision processes; and the N400 is a robust index of semantic integration during language comprehension.

Source localization and functional connectivity analysis revealed differentiated but interacting cortical networks for each component. The MMN engaged a bilateral network comprising auditory, frontal, and parietal regions, consistent with models of automatic prediction error detection. The P300 activated a broader fronto-parietal-cingulate network, supporting its association with attention and cognitive control. The N400 was predominantly left-lateralized, involving frontal, temporal, and parietal regions linked to semantic processing. Connectivity analysis showed that these networks are highly dynamic, with strengthened fronto-parietal and intra-frontal coupling during higher-level linguistic tasks. Taken together, these findings highlight the distributed, flexible nature of speech processing networks. They offer a reference point for studying how these systems may be altered in clinical populations, such as individuals with aphasia or neurodegenerative disorders.

However, several methodological limitations should be acknowledged. First, the analyses assume a fixed latency for ERP components across all trials, poten-

tially overlooking meaningful trial-by-trial variability in neural timing. Second, the analyses focus primarily on time-domain ERPs and do not incorporate time-frequency methods that could capture oscillatory dynamics relevant to speech processing. Third, the studies rely on standard head models, without incorporating individualized or anatomically detailed forward modeling, which may limit spatial precision in interpreting EEG signals. These limitations underscore the need for a deeper examination of the assumptions and constraints inherent in ERP analysis.

To address these issues, this dissertation also explores methodological aspects critical to EEG research through simulations. **Part III: How simulations can help us understand the working mechanisms of the brain** presents a series of simulation studies addressing how choices made during the analysis can impact the interpretation of ERP data.

In **Chapter 5**, we address the variability in ERP latencies across trials, a longstanding challenge in EEG research. Conventional averaging methods assume consistent timing across trials, yet cognitive processes often vary substantially from trial to trial. To address this, we developed artificial neural network models capable of estimating single-trial ERP latencies. Simulations demonstrated that these models outperformed traditional methods under varying noise conditions. Applied to real EEG data, single-trial latency estimates showed stronger correlations with behavioral performance and revealed group-level differences that conventional averages failed to detect. These findings suggest that accounting for latency variability can enhance both the sensitivity and interpretability of ERP studies.

In **Chapter 6**, we investigate the relationship between ERPs and oscillatory activity by combining eLORETA-based ERP source localization with DICS-based oscillatory source analysis. Traditionally, ERP and oscillation studies have been treated separately, but emerging evidence suggests they reflect complementary aspects of brain function. Our findings indicated partial overlap between ERP components (such as the P300) and low-frequency oscillations (such as delta rhythms), while also revealing distinct contributions from alpha band activity. These results highlight the value of integrating multiple source analysis methods to gain a more comprehensive view of neural dynamics.

Chapter 7 examines how the choice of head model affects source localization accuracy. In the absence of individualized MRI scans, many EEG studies rely on standard template head models. However, simulations and empirical analyses demonstrated that using template models introduced systematic localization

errors, producing spatially diffuse and sometimes misleading results. Individualized head models significantly improved source specificity, underscoring their importance, particularly in clinical research settings where precise localization may guide intervention strategies.

Finally, **Chapter 8** explores how structural brain anomalies, such as lesions resulting from tumors or strokes, affect EEG measurements. Simulations incorporating lesion-informed forward models showed significant distortions in ERP topographies and source estimates near lesion sites. These findings were corroborated by analyses of EEG data from patients with craniotomies. Together, the results emphasize the necessity of incorporating individualized anatomical information when conducting source localization in clinical populations to ensure accurate and reliable interpretations.

In sum, this dissertation contributes both to the empirical understanding of speech perception and to the advancement of EEG research methodologies. The empirical results elucidate the dynamic and distributed nature of the networks in the brain supporting different levels of linguistic processing. The methodological work provides practical guidelines for improving the robustness and interpretability of EEG studies: emphasizing the need to account for trial-to-trial variability, advocating for individualized head models, encouraging the integration of multiple source localization approaches, and highlighting the importance of anatomical specificity in clinical contexts.

By combining empirical research with simulation-driven methodological innovation, this work aims to support future studies of language networks and to enhance the clinical relevance of EEG as a tool for diagnosing and treating language impairments. Through this dual focus, the dissertation advances our understanding of both the brain's capacity for language and the methods needed to study it effectively.

Nederlandse samenvatting

Taal is een van de meest fundamentele maar toch complexe domeinen van de menselijke cognitie. Hoewel gebaren, gezichtsuitdrukkingen en emotionele toon bijdragen aan communicatie, blijft taal het primaire middel om ingewikkelde en abstracte ideeën uit te drukken. Ondanks het ogenschijnlijke gemak waarmee taal in het dagelijks leven wordt gebruikt, berust taal op zeer gespecialiseerde en gedistribueerde neurale mechanismen, waarvan veel aspecten nog steeds actief worden onderzocht. Inzicht in deze mechanismen is vooral belangrijk voor het ontwikkelen van betere diagnostische hulpmiddelen en therapeutische methoden voor mensen met taalstoornissen als gevolg van aandoeningen zoals een beroerte, hersentumoren of traumatisch hersenletsel.

Onderzoek toont in toenemende mate aan dat taalverwerking niet beperkt is tot geïsoleerde hersengebieden, maar voortkomt uit de dynamische interactie van gedistribueerde neurale systemen. Het verwerken van een gesproken woord verloopt in meerdere stadia, waarbij steeds verschillende hersengebieden betrokken zijn. Zo vindt de vroege auditieve analyse plaats in de superieure temporale cortex, is de middelste temporale gyrus betrokken in lexicale mapping, betrekt semantische oproeping de angulaire gyrus en wordt syntactische integratie gemedieerd door de inferieure frontale gyrus. Theoretische raamwerken ontwikkeld door Ellis en Young (auditieve verwerking), De Deyne (semantische netwerken) en Dominey (syntactische verwerking) onderstrepen de onderlinge verbondenheid van deze processen en benadrukken het belang van het bestuderen van taal als een netwerkfenomeen.

Dit proefschrift bouwt voort op deze kaders en streeft twee belangrijke doelstellingen na. De eerste doelstelling is het karakteriseren van de neurale dynamiek van spraakperceptie, een complex proces dat akoestische signalen transformeert in betekenisvolle linguïstische informatie binnen een paar honderd milliseconden, gebruik makend van elektroencephalografie (EEG).

De tweede doelstelling richt zich op belangrijke methodologische uitdagingen in EEG-onderzoek door middel van een reeks gerichte simulatiestudies, met als doel technieken voor het analyseren van event-gerelateerde potentialen (ERP's) te verfijnen en de nauwkeurigheid van empirische bevindingen te verbeteren.

Hoofdstuk 1 dient als algemene inleiding op het onderwerp en schetst de bredere context van het proefschrift. **Deel I: Van neurale activiteit naar gemeten hersensignalen** legt de basis door uit te leggen hoe hersenactiviteit wordt geregistreerd en geïnterpreteerd met behulp van EEG. **Hoofdstuk 2** introduceert de belangrijkste neurofysiologische principes en behandelt hoe elektrische activiteit in de hersenen wordt gegenereerd. Daarnaast komen ook de basisprincipes van elektro-encefalografie en het concept van event-gerelateerde potentialen (ERP's) aan bod. **Hoofdstuk 3** gaat vervolgens dieper in op signaalverwerking met een focus op EEG bronlokalisatie en functionele connectiviteit, waarbij methoden worden besproken voor het schatten van de locatie van de bronnen van hersensignalen, inclusief de formulering van het voorwaartse model en oplossingen voor het inverse probleem. Daarnaast worden hier ook technieken voor het beoordelen van de interactie tussen verschillende hersengebieden besproken.

In **Deel II: Bronlokalisatie en functionele connectiviteit**, onderzoeken we spraakperceptie met behulp van EEG, dat de temporele resolutie biedt die nodig is om snel evoluerende cognitieve processen te volgen. **Hoofdstuk 4** onderzoekt drie bekende ERP-componenten - de Mismatch Negativity (MMN), de P300 en de N400 - die elk verschillende stadia van taalanalyse weerspiegelen. De MMN weerspiegelt vroege, pre-attente detectie van onverwachte auditieve veranderingen; de P300 weerspiegelt aandachtige categorisatie en taakgerelateerde besluitvormingsprocessen; en de N400 is een robuuste index van semantische integratie tijdens taalbegrip.

Bronlokalisatie en functionele connectiviteitsanalyses onthulden gedifferentieerde maar interagerende corticale netwerken voor elke component. Het MMN activeerde een bilateraal netwerk bestaande uit auditieve, frontale en pariëtale gebieden, wat consistent is met modellen van automatische detectie van voorspelfouten. De P300 activeerde een breder fronto-pariëtaal-cingulaat netwerk, wat de associatie met aandacht en cognitieve controle ondersteunt. De N400 was voornamelijk links-lateraal, waarbij frontale, temporale en pariëtale gebieden betrokken waren die verband houden met semantische verwerking. Connectiviteitsanalyses toonden verder aan dat deze netwerken zeer

dynamisch zijn, met versterkte fronto-pariëtale en intra-frontale koppeling tijdens linguïstische taken op een hoger niveau.

De experimentele bevindingen benadrukken de gedistribueerde, flexibele aard van spraakverwerkingsnetwerken. Ze bieden ook een referentiepunt voor het bestuderen hoe deze systemen kunnen veranderen in klinische populaties, zoals mensen met afasie of neurodegeneratieve aandoeningen.

Er moet echter rekening worden gehouden met verschillende methodologische beperkingen. Ten eerste gaan de analyses uit van een vaste latentie voor ERP-componenten over alle trials, waarbij geen rekening gehouden wordt met de trial-tot-trial variabiliteit in neurale timing. Ten tweede richten de analyses zich voornamelijk op ERP's in het tijdsdomein en bevatten ze geen tijd-frequentie methoden die de oscillerende dynamiek, die relevant is voor spraakverwerking, in kaart zouden kunnen brengen. Ten derde vertrouwen de studies op template hoofdmodellen, zonder geïndividualiseerde of anatomisch gedetailleerde voorwaartse modellering, wat de ruimtelijke precisie kan beperken bij het interpreteren van EEG signalen. Deze beperkingen tonen de noodzaak voor een dieper onderzoek naar de aannames en beperkingen die inherent zijn aan ERP analyse.

Om deze kwesties aan te pakken, verkent dit proefschrift ook methodologische aspecten die cruciaal zijn voor EEG-onderzoek door middel van simulaties. **Deel III: Hoe simulaties ons kunnen helpen bij het begrijpen van de werkingsmechanismen van de hersenen** presenteert een serie simulatiestudies die onderzoeken hoe keuzes gemaakt tijdens de analyses de interpretatie van ERP-data kunnen beïnvloeden.

In **hoofdstuk 5** gaan we in op de variabiliteit in ERP-latenties over proeven heen, een reeds lang bestaande uitdaging in EEG-onderzoek. Conventionele methodes, zoals het uitmiddellen over meerdere trials, gaan uit van een consistente timing over de trials heen, maar cognitieve processen variëren vaak aanzienlijk van trial tot trial. Om dit aan te pakken, ontwikkelden we kunstmatige neurale netwerkmodellen die in staat zijn om in een enkele trial ERP latenties te schatten. Simulaties toonden aan dat deze modellen beter presteerden dan traditionele methoden onder variërende ruiscondities. Toegepast op echte EEG-gegevens, vertoonden schattingen van enkelvoudige trial latenties sterkere correlaties met gedragsprestaties en onthulden ze verschillen op groepsniveau die conventionele gemiddelden niet detecteerden. Deze bevindingen suggereren dat rekening houden met de variabiliteit van de latentie

zowel de gevoeligheid als de interpreteerbaarheid van ERP-studies kan verbeteren.

Hoofdstuk 6 onderzoekt hoe de keuze van het anatomisch hoofdmodel de nauwkeurigheid van de bronlokalisatie beïnvloedt. Bij gebrek aan geïndividualiseerde MRI scans, vertrouwen veel EEG studies op standaard template hoofdmodellen. Echter, simulaties en empirische analyses toonden aan dat het gebruik van template modellen systematische lokalisatie fouten introduceert, wat leidt tot ruimtelijk diffuse en soms misleidende resultaten. Geïndividualiseerde hoofdmodellen verbeterden de bronspecificiteit aanzienlijk, wat hun belang onderstreept, vooral in klinische onderzoeksomgevingen waar precieze lokalisatie interventiestrategieën kan sturen.

In **hoofdstuk 7** onderzoeken we de relatie tussen ERP's en oscillerende activiteit door eLORETA-gebaseerde ERP-bronlokalisatie te combineren met DICS-gebaseerde oscillatoire bronanalyse. Traditioneel worden ERP en oscillatie studies apart behandeld, maar opkomend bewijs suggereert dat ze complementaire aspecten van de hersenfunctie weerspiegelen. Onze bevindingen gaven een gedeeltelijke overlap aan tussen ERP-componenten (zoals de P300) en laagfrequente oscillaties (zoals deltaritmes), terwijl ook afzonderlijke bijdragen van alfabandactiviteit zichtbaar werden. Deze resultaten benadrukken de toegevoegde waarde van het integreren van meerdere bronanalysemethoden om een uitgebreider beeld te krijgen van neurale dynamiek.

Tenslotte wordt in **hoofdstuk 8** onderzocht hoe structurele afwijkingen in de hersenen, zoals laesies als gevolg van tumoren of beroertes, EEG-metingen beïnvloeden. Simulaties met laesie-geïnformeerde voorwaartse modellen toonden significante vervormingen in ERP topografieën en in bron schattingen in de buurt van laesie locaties. Deze bevindingen werden bevestigd door analyses van EEG-gegevens van patiënten met die na een hersentumor een craniotomie ondergingen. Samen benadrukken de resultaten de noodzaak van het opnemen van geïndividualiseerde anatomische informatie bij het uitvoeren van bronlokalisatie in klinische populaties om accurate en betrouwbare localisaties te garanderen.

Samengevat draagt dit proefschrift bij tot zowel het empirisch begrip van spraakperceptie als tot de vooruitgang van EEG onderzoeksmethodologieën. De empirische resultaten verhelderen de dynamische en gedistribueerde aard van de netwerken in de hersenen die verschillende niveaus van taalverwerking ondersteunen. Het methodologische werk biedt praktische richtlijnen voor het verbeteren van de robuustheid en interpreteerbaarheid van EEG studies: het

benadrukt de noodzaak om rekening te houden met de variabiliteit over trials, pleit voor geïndividualiseerde hoofdmodellen, moedigt de integratie van meerdere bron lokalisatie benaderingen aan, en benadrukt het belang van anatomische specificiteit in klinische contexten.

Door een brug te slaan tussen empirisch onderzoek en simulatiegedreven methodologische innovatie, beoogt dit werk toekomstige studies van taalnetwerken te ondersteunen en de klinische relevantie van EEG als hulpmiddel voor het diagnosticeren en behandelen van taalstoornissen te vergroten. Door deze tweeledige focus bevordert het proefschrift ons begrip van zowel de hersencapaciteit voor taal als van de methoden die nodig zijn om dit effectief te bestuderen.

List of abbreviations

AMICA	adaptive mixture independent component analysis
ANOVA	analysis of variance
ASA	automatic spreading activation
ATL	anterior temporal lobe
BCI	brain-computer interface
BEM	Boundary Element Method
BOLD	blood-oxygen-level-dependent
CAT-NL	Comprehensive Aphasia Test-Dutch version
CNN	convolutional neural network
convLSTM	convolutional Long Short-Term Memory
CSD	current source density
CSF	cerebrospinal fluid
DAN	dorsal attention networks
dB	decibel
DC	directed coherence
DHI	Dutch Handedness Inventory
DICS	Dynamic Imaging of Coherent Sources
dSPM	dynamic Statistical Parametric Mapping
DTF	directed transfer function
DTW	dynamic time warping
DWI	diffusion weighted imaging
ECD	equivalent current dipole

EEG	electroencephalography
eLORETA	exact low-resolution brain electromagnetic tomography
EPSP	excitatory post-synaptic potential
ERP	event-related potential
ESI	EEG source imaging
FC	functional connectivity
FDM	Finite Difference Method
FDR	false discovery rate
FEM	Finite Element Method
FFT	fast Fourier transform
fMRI	functional magnetic resonance imaging
FN	false negative
FP	false positive
GC	Granger Causality
HAROLD	Hemispheric Asymmetry Reduction in Older Adults
ICA	independent component analysis
IFG	inferior frontal syrus
IFGop	pars opercularis of the inferior frontal gyrus
IPC	inferior parietal cortex
IPSP	inhibitory post-synaptic potential
ISI	inter stimulus interval
ITI	inter trial interval
ITS	inferior temporal sulcus
LCMV	Linearly Constrained Minimum Variance
LORETA	Low-Resolution Electromagnetic Tomography
MAG	magnitude difference measure
MEA	mean absolute error
MEG	magnetoencephalography
MFG	middle frontal gyrus
MI	Mutual Information
MMN	mismatch negativity

MNE	Minimum Norm Estimation
MoCA	Montreal Cognitive Assessment
MRAE	mean relative absolute error
MRI	magnetic resonance imaging
MUSIC	multiple emitter location and signal parameter estimation
NBS	Network Based Statistic
NN	neural network
PASA	Posterior-to-Anterior Shift in Aging
PCA	prinicple component analysis
PCC	posterior cingulate cortex
PDC	partial directed coherence
PLI	Phase Lag Index
PLV	Phase Locking Value
PM	premotor
pMTG	posterior middle temporal gyrus
RAP-MUSIC	Recursively Applied and Projected MUSIC
RDM	relative difference measure
RMAE	relative mean absolute error
ROI	region of interest
RRE	relative residual energy
rs-EEG	resting-state EEG
RMSE	root mean squared error
RT	reaction time
sLORETA	standardized low-resolution brain electromagnetic tomography
SNR	signal to noise ratio
SOA	stimulus onset asynchrony
Spt	Sylvian parietal-temporal
SSCT	semantic sentence congruity task
STG	superior temporal gyrus
STS	superior temporal sulcus
TBI	traumatic brain injury
TFA	time-frequency analysis

TFR	time-frequency representation
TN	true negative
TP	true positive
VAN	ventral attention networks
wMNE	weighted Minimum Norm Estimation

List of publications

Journal Papers

Accepted and published papers as (shared) first author

- Criel, Y., Depuydt, E., Cocquyt, E.-M., Miatton, M., Santens, P., van Mierlo, P., & De Letter, M. (2025). Frontal synchronisation facilitates taxonomic priming: insights from N400 source estimation and functional connectivity. LANGUAGE COGNITION AND NEUROSCIENCE, 1–18. https://doi.org/10.1080/23273798.2025.2501049
- Depuydt, E., Criel, Y., De Letter, M., & van Mierlo, P. (2024). Investigating the effect of template head models on Event-Related Potential source localization: a simulation and real-data study. FRONTIERS IN NEUROSCIENCE, 18. https://doi.org/10.3389/fnins.2024.1443752
- Criel, Y., Depuydt, E., Miatton, M., Santens, P., van Mierlo, P., & De Letter, M. (2024). Cortical generators and connections underlying phoneme perception: a mismatch negativity and P300 investigation. BRAIN TOPOGRAPHY, 37(6), 1089–1117. https://doi.org/10.1007/s10548-024-01065-z
- Depuydt, E., Criel, Y., De Letter, M., & van Mierlo, P. (2023). Single-trial ERP quantification using neural networks. BRAIN TOPOGRAPHY, 36(6), 767–790. https://doi.org/10.1007/s10548-023-00991-8

Accepted and published papers as co-author

- Criel, Y., Depuydt, E., De Clercq, B., Raman, N., Haekens, N., Miatton, M., ... De Letter, M. (2024). Long-term functional connectivity alter-

ations in the mismatch negativity, P300 and N400 language potentials in adults with a childhood acquired brain injury. APHASIOLOGY, 38(10), 1684–1721.
https://doi.org/10.1080/02687038.2024.2323223

- Cocquyt, E.-M., Depuydt, E., Santens, P., van Mierlo, P., Duyck, W., Szmalec, A., & De Letter, M. (2023). Effects of healthy aging and gender on the electrophysiological correlates of semantic sentence comprehension: the development of Dutch normative data. JOURNAL OF SPEECH LANGUAGE AND HEARING RESEARCH, 66(5), 1694–1717.
https://doi.org/10.1044/2023_JSLHR-22-00545

- Dorme, A., Van Oudenhove, B., Criel, Y., Depuydt, E., De Groote, E., Stalpaert, J., ... De Letter, M. (2023). Effect of healthy aging and gender on syntactic input processing: a P600 event-related potential study. JOURNAL OF SPEECH LANGUAGE AND HEARING RESEARCH, 66(8), 2701–2732.
https://doi.org/10.1044/2023_jslhr-22-00633

- Criel, Y., Boon, C., Depuydt, E., Stalpaert, J., Huysman, E., Miatton, M., ... De Letter, M. (2023). Aging and sex effects on phoneme perception: an exploratory mismatch negativity and P300 investigation. INTERNATIONAL JOURNAL OF PSYCHOPHYSIOLOGY, 190, 69–83.
https://doi.org/10.1016/j.ijpsycho.2023.06.002

Manuscripts in Preparation, Submitted, or Under Review

- Depuydt, E., Oostenveld, R., De Letter, M., van Mierlo, P., Piai, V. The impact of brain tumors and craniotomy lesions on scalp EEG [Manuscript in preparation]

- Depuydt, E., De Letter, M., van Mierlo, P. Disentangling ERP and Oscillatory Sources with eLORETA and DICS: A Comparative Study with Simulations and Empirical Data [Manuscript submitted]

- Cromheecke, O., Depuydt, E., Woumans, E., van Mierlo, P., Miatton, M., Szmalec, A,. De Letter, M. Overlap in the Cerebral Processing of Language and Executive Control: an ERP Study on the Effects of Age and Sex [Manuscript under review]

- Dorme, A., Depuydt, E., Eggers, K., Woumans, E., De Samblanx, E., Szmalec, A., De Letter, M. Inattentive (pre)phonemic discrimination in multilingual adults who stutter: a multi-feature MMN study. [Manuscript in preparation]

Conference Contributions

- Depuydt, E., Criel, Y., De Letter, M., & van Mierlo, P. (2024). Investigating the effect of average head models on event-related potential source localization. EEG & Clinical Neuroscience Conference, Abstracts. Poster Presented at the ECNS 2024 Conference, Toronto, Canada.
- Depuydt, E., Criel, Y., De Letter, M., & van Mierlo, P. (2024). Investigating the effect of average head models on event-related potential source localization. Neural Traces 2024 Workshop, Abstracts. Poster Presented at the Neural Traces 2024 Workshop, Berlin, Germany.
- Depuydt, E., Criel, Y., De Letter, M., & van Mierlo, P. (2023). Cortical Generators and Connections Underlying Phoneme Perception: an ESI and functional connectivity analysis approach. National Day of Biomedical Engineering 2023, Abstracts. Poster Presented at the National Day of Biomedical Engineering 2023, Brussels, Belgium.
- Depuydt, E., De Letter, M., & van Mierlo, P. (2022). A convolutional LSTM neural network for single trial latency estimation of ERP components. 28th Annual Meeting and Educational Courses of Organization for Human Brain Mapping (OHBM 2022), Abstracts. Poster Presented at OHBM 2022, Glasgow, the UK.
- Depuydt, E., De Letter, M., & van Mierlo, P. (2022). Neural networks for single trial latency estimation of ERP components. National Day of Biomedical Engineering 2022, Abstracts. Poster Presented at the National Day of Biomedical Engineering 2022, Brussels, Belgium.

Oral Presentations

- Depuydt, E., Criel, Y., De Letter, M., & van Mierlo, P. (2024). Investigating the effect of average head models on event-related potential source localization. Sinergia Meeting 2024, Abstracts. Presented at the Sinergia Meeting 2024, Ghent, Belgium.

- Depuydt, E., Criel, Y., De Letter, M., & van Mierlo, P. (2024). Frontal synchronization facilitates semantic priming: insights from N400 source estimation and functional connectivity. Afasie Jongerendagen 2024, Abstracts. Presented at the Afasie Jongerendagen 2024, Nijmegen, the Netherlands.

- Depuydt, E., Criel, Y., De Letter, M., & van Mierlo, P. (2024). Identifying neural networks involved in phoneme categorization through EEG source imaging and functional connectivity analysis. Psycholinguistics in Flanders (PiF 2024), Abstracts, 30–30. Presented Psycholinguistics in Flanders 2024, Brussels, Belgium.

- Depuydt, E., Criel, Y., De Letter, M., & van Mierlo, P. (2023). Identifying neural networks involved in phoneme categorization through EEG source imaging and functional connectivity analysis. Annual Worldwide Conference of the International Association for Mapping the Brain (IamBrain 2023), Abstracts. Presented at IamBrain 2023, London, UK.

Contents

1 Introduction

Language is one of the most fundamental aspects of human communication. While gestures and emotional tone also play a role in conveying meaning, language serves as the primary tool that facilitates complex expression (Friederici, 2017). Imagine traveling to a place where you do not share a common language — simple transactions, like buying an orange at a market, may be manageable with gestures, but asking for directions to your next destination quickly becomes much more challenging. Despite its complexity, our native language is something we acquire effortlessly, without formal instruction, and use daily without conscious effort.

Our understanding of how language functions in the brain originates from the study of individuals who have experienced language impairments. The first significant case was documented by the French scientist Paul Broca, whose patient, "Monsieur Tan," exhibited a severe language production deficit, being able to utter only the syllable "tan". Broca analyzed his patient's condition, but at the time, neuroscientists had to wait until a patient passed away to conduct a brain autopsy to identify the underlying neural damage. Upon examination, Broca identified a lesion in the left inferior frontal gyrus—an area now known as Broca's area (Broca, 1861). A few years later, Carl Wernicke studied the brains of patients with impairments in language comprehension (Wernicke, 1881) and found lesions in the left temporal cortex, now referred to as Wernicke's area. From these findings, Broca's area was linked to language production, while Wernicke's area was associated with language comprehension.

Thanks to the invention of neuroimaging technologies, researchers today are able to study language processing in living individuals. The classical view that Broca's area is solely responsible for production and Wernicke's area for

comprehension has undergone significant revisions. Contemporary research suggests that language processing is a complex cognitive function requiring the integration of multiple neural systems. Understanding a single word involves various stages—auditory perception, lexical access, and syntactic integration—each mediated by distinct but interconnected brain regions (Friederici, 2017). Several theoretical models, such as the Ellis & Young model for auditory analysis, the De Deyne model for semantic processing, and the Dominey model for syntactic integration (Ellis and Young, 1996; De Deyne et al., 2016; Dominey and Inui, 2009), highlight the importance of connectivity within multimodal neural networks. These findings emphasize that language processing is not confined to isolated brain regions but rather emerges from a dynamic interplay between multiple specialized and interconnected areas.

1.1 Understanding a spoken word

Understanding a spoken word is a complex, multi-stage process that begins with the perception of sound. When we hear speech, auditory information is first processed by converting sound waves into neural signals. These signals travel via the auditory nerve to the primary auditory cortex in the superior temporal gyrus, where early acoustic analysis enables the brain to distinguish phonemes, the smallest contrastive units of speech that differentiate meaning (Friederici, 2017).

According to the Ellis & Young model for auditory analysis, the comprehension of a heard word follows four key stages (Figure 1.1): (1) In the auditory phonological analysis stage, the continuous speech sound wave is segmented into individual phonemes. (2) These phonemes are temporarily stored in the phonological input buffer, a working memory system that maintains the sequence of phonemes for further processing. (3) The segmented phonemes then activate corresponding phonological representations in the phonological input lexicon, which serves as a mental repository for all known word forms. This stage facilitates lexical decision-making—determining whether a given speech sound sequence corresponds to a known word or a pseudoword. (4) If the phonological input lexicon identifies the sequence as a real word, it is mapped onto stored meanings in the semantic system, where long-term memory enables word comprehension by linking the word form with its associated meaning (Ellis and Young, 1996).

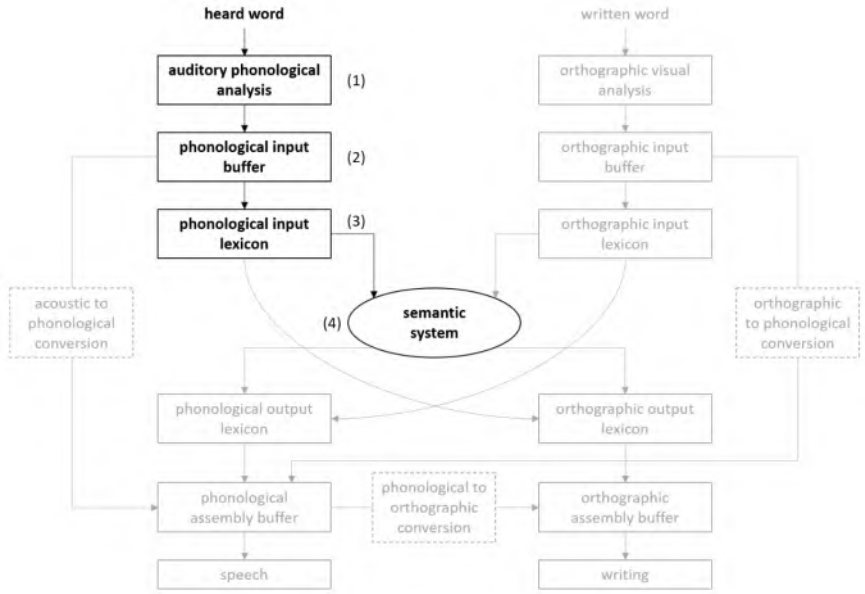

Figure 1.1. The psycholinguistic model for auditory and written word comprehension and production, as introduced by Ellis & Young (1996). The substages in bold relate to auditory word comprehension. Reprinted from Criel (2024) with permission from the author.

While this model provides a strong foundation for understanding the different stages of auditory word processing, it does not account for the underlying neural mechanisms. To address this, Hickok and Poeppel (2004) introduced a dual-stream model that explains how speech processing is organized in the brain (Figure 1.2). According to this framework, speech perception begins with the activation of the bilateral dorsal superior temporal gyrus (STG), where incoming auditory signals undergo spectrotemporal analysis. This is followed by phonological processing, primarily supported by the middle posterior superior temporal sulcus (STS). At this stage, the auditory system splits into two parallel processing streams. The dorsal stream links posterior temporal regions, the parietal operculum, and frontal areas such as the inferior frontal gyrus (IFG) and premotor cortex. It acts as a sensory-motor interface, integrating speech perception with production. Meanwhile, the ventral stream connects the posterior STG to the posterior middle temporal gyrus (pMTG), anterior temporal lobe (ATL), and IFG, facilitating the mapping of sounds onto meaning. Berwick et al. (2013) later expanded this model to encompass sentence-level processing, proposing an additional dorsal and ventral stream. In this extended frame-

work, the dorsal stream supports complex syntactic processing, while the ventral stream handles basic syntactic structures, further refining our understanding of language comprehension.

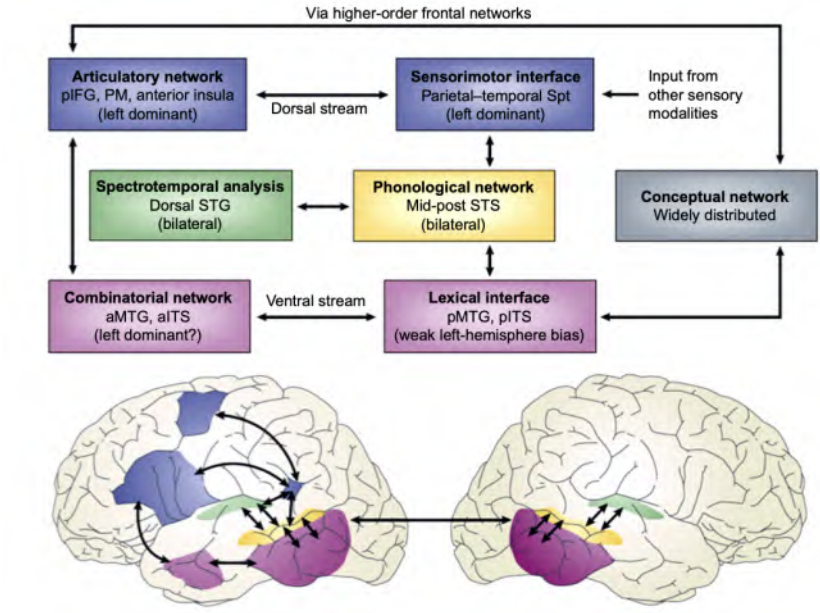

Figure 1.2. Dual stream model of speech processing. The dual stream model holds that early stages of speech processing occur bilaterally in the dorsal STG (spectrotemporal analysis; green) and STS (phonological access/representation; yellow), and then diverges into two broad streams: a temporal lobe ventral stream supports speech comprehension (lexical access and combinatorial processes; pink), whereas a strongly left-dominant dorsal stream supports sensory-motor integration and involves structures at the parietal-temporal junction (Spt) and frontal lobe. The conceptual network (gray box) is assumed to be widely distributed throughout the cortex. IFG, inferior frontal gyrus; ITS, inferior temporal sulcus; MTG, middle temporal gyrus; PM, premotor; Spt, Sylvian parietal-temporal; STG, superior temporal gyrus; STS, superior temporal sulcus. Reprinted from Hickok and Poeppel (2007) with permission from the publisher.

By integrating the cognitive steps of phonological and lexical processing with the neural pathways of speech perception, these models provide a more comprehensive view of spoken word recognition. While the Ellis & Young model focuses on the sequential stages of word comprehension, the dual-stream model maps these processes onto distinct cortical networks. This perspective is particularly relevant in cases where the brain's speech processing network is dis-

rupted, such as in patients with aphasia. Understanding these mechanisms not only deepens our knowledge of language function but also sheds light on how the brain can adapt and reorganize in response to injury.

1.2 Neuroplasticity of the language network in patients with an acquired brain injury

Acquired brain injuries, such as stroke and brain gliomas, can significantly impact the language network (Goldman et al., 2022). However, the brain has a remarkable ability to reorganize itself through neuroplasticity, enabling patients to regain language function to varying degrees. This plasticity involves structural and functional changes within the perilesional cortex, homologous areas in the opposite hemisphere, and broader language-related networks (Pasquini et al., 2022).

In the case of stroke, damage to traditional language areas often results in aphasia. Recovery depends on the recruitment of perilesional areas within the left hemisphere or the engagement of homologous right-hemispheric regions (Hamilton et al., 2011; Kiran and Thompson, 2019; Li et al., 2022). Studies using functional neuroimaging have shown that in the early stages of recovery, increased right hemisphere activation may compensate for left hemisphere deficits (Schneck et al., 2021). However, optimal recovery is typically associated with a gradual shift back toward left-hemisphere dominance as language processing is restored to its primary networks (Schneck et al., 2021; Hamilton et al., 2011; Kiran and Thompson, 2019). Rehabilitation strategies, such as speech therapy, aim to facilitate this process by strengthening residual connections and promoting cortical reorganization.

Another type of acquired brain injuries are brain gliomas. In these patients, neuroplasticity typically follows a different trajectory. Unlike stroke or traumatic brain injury (TBI), where damage is abrupt, gliomas grow gradually, allowing the brain time to adapt (Duffau et al., 2003; Krishna et al., 2021; Traut et al., 2019). This slow progression can lead to functional reorganization, where language-related activity shifts to surrounding cortical areas or even to homologous regions in the right hemisphere (Figure 1.3; Yuan et al. (2020); Nieberlein et al. (2023)). Studies using functional magnetic resonance imaging (MRI) and intraoperative mapping have demonstrated that language functions can be preserved despite tumor invasion, as the brain dynamically redistributes linguistic processing. However, the extent of reorganization depends on tumor

location, size, and growth rate (Noll et al., 2015). Low-grade gliomas, which develop more slowly, provide a greater window for plasticity, often allowing significant language recovery following surgical resection. In contrast, high-grade gliomas, which grow more aggressively, may outpace the brain's ability to reorganize, leading to more severe language deficits (Noll et al., 2015; Yuan et al., 2020, 2022). Understanding these mechanisms is crucial for neurosurgical planning, as awake brain mapping can help to identify and preserve critical language areas during tumor removal.

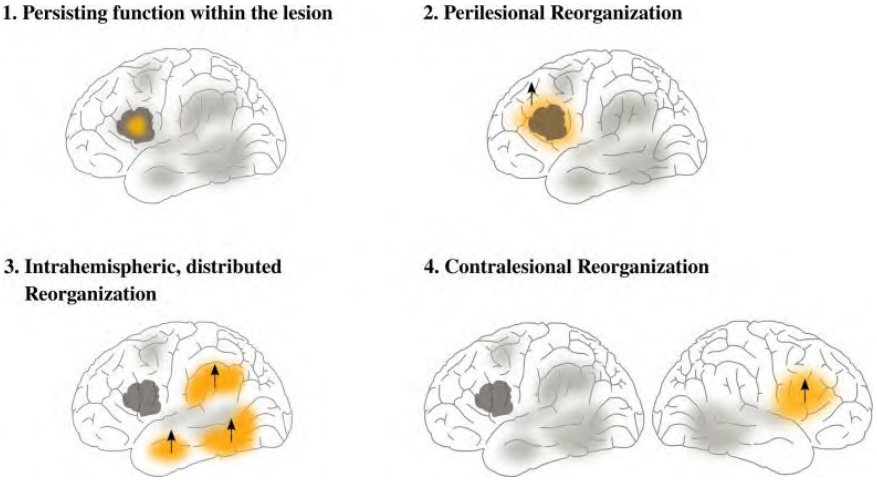

Figure 1.3. Visual representation of language-related reorganization patterns in relation to glioma growth. Reprinted with permission from Nieberlein et al. (2023).

1.3 Neuroimaging techniques for studying language processing in the brain

Several neuroimaging methods provide insights into how language is processed in the brain. Electroencephalography (EEG) and magnetoencephalography (MEG) are two time-sensitive techniques that measure respectively electrical and magnetic activity in the brain. EEG records electrical signals from the scalp capturing event-related potentials (ERPs), which reflect neural responses to linguistic stimuli with millisecond precision. Some key ERP components include the N100 (acoustic processing), the N400 (semantic processing), and the P600 (syntactic integration). Because individual ERP responses are small, they must be averaged across multiple trials to isolate meaningful patterns

from background neural noise. MEG, while similar to EEG in temporal resolution, detects the magnetic fields produced by neural activity, offering improved spatial localization thanks to its high-density sensor array. However, MEG is significantly more expensive and requires specialized, magnetically shielded rooms to minimize interference from external magnetic sources, making the method less accessible.

Functional magnetic resonance imaging (fMRI) is another essential tool for studying language, offering high spatial resolution. Unlike EEG and MEG, which track neural activity in real-time, fMRI measures changes in blood-oxygen-level-dependent (BOLD) signals, reflecting metabolic activity over seconds rather than milliseconds. This makes it ideal for mapping the functional anatomy of the language network but less suited for capturing rapid processing dynamics. Despite its lower temporal resolution, fMRI has been instrumental in identifying key brain regions involved in language, including Broca's area, Wernicke's area, and other distributed cortical and subcortical structures.

Each of these non-invasive methods provides either high temporal or high spatial resolution, but not both. To obtain a more complete understanding of brain function, researchers often combine techniques, integrating fine-grained temporal data from EEG and MEG with the detailed spatial mapping provided by fMRI.

1.4 Objectives and Outline of this dissertation

Language is a fundamental yet complex cognitive process. While we use it effortlessly in daily life, the neural mechanisms behind it remain a subject of ongoing research. Understanding these mechanisms is particularly important for individuals with language impairments, such as stroke survivors or patients with brain tumors.

The initial goal of this dissertation was to explore speech perception — a complex process that unfolds across multiple levels of analysis, from early acoustic-phonetic processing to higher-order lexical processing and semantic integration. Using event related potentials (ERPs), we investigated the cortical generators and functional connectivity of the MMN, P300, and N400 components. While state-of-the-art methods were used in this work, certain challenges and limitations emerged, highlighting the need for further refinement of these methods. This led us to a dual focus: first, on understanding the

neural basis of speech perception through source localization and functional connectivity, and second, on exploring some methodological questions that could have an impact on the obtained results.

The dissertation begins with some foundational background in **Part I: From Neural Activity to Measured Brain Signals**. Since our goal is to use non-invasive methods, **Chapter 2** explains how electrical signals in the brain generate the activity we can measure with EEG, along with a discussion of common ERP components. **Chapter 3** introduces EEG source imaging (ESI) and functional connectivity (FC), key methods used throughout this work.

The empirical work is presented in **Part II: Source reconstruction and functional connectivity of language ERP components**. In **Chapter 4** we investigate the P300, MMN, and N400 components, their cortical generators, and the underlying networks. However, certain limitations and assumptions could influence the obtained results, and applying these techniques to patient populations requires addressing several methodological challenges. To tackle this, in **Part III: How simulations can help us understand the working mechanisms of the brain**, simulation studies were conducted, each addressing a specific question:

- **Chapter 5**: How does latency jitter in single trials affect ERP analyses?
- **Chapter 6**: How can combining different source reconstruction techniques improve our understanding of the relationship between ERPs and brain oscillations?
- **Chapter 7**: How does using template head models instead of subject-specific models influence EEG source localization?
- **Chapter 8**: How do craniotomy-induced lesions impact EEG signals?

The findings from these simulation studies were also always applied to real data in these chapters. This way, we were able to obtain deeper insights into both the methodological limitations and the neurophysiological mechanisms underlying the recorded data.

Finally, in **Chapter 9**, we provide an overall summary of the results obtained in these chapters and discuss the general findings. By combining simulations with work on real data, this dissertation provides new insights into the neural basis of speech perception and the methodological considerations needed for future research and clinical applications.

Part I

From Neural Activity to Measured Brain Signals

2 The brain, electroencephalography and event-related potentials

Electroencephalography (EEG) is a recording technique used to measure the electrical activity in the brain. The first EEG recording was made in 1924 by German physiologist and psychiatrist Hans Berger. Experiments by Berger showed that recorded brain waves differed for healthy participants and patients with a neurological disorder. Furthermore, he also showed that brain waves change depending on whether a patient is paying attention, relaxing or sleeping (Berger, 1929; Sörnmo and Laguna, 2005). In 1934, Fischer and Löwenbach demonstrated epileptiform spikes, after which EEG found its way into clinical neuroscience. Since then, it has been one of the most used techniques to study brain activity and to diagnose different neurological disorders such as epilepsy and sleep disorders. EEG can also be used to check the depth of a patient's anaesthesia during surgery or to examine the brain activity of patients in coma (Kulkarni and Bairagi, 2018). The technique plays an important role in research fields such as cognitive neuroscience, where it is used to investigate brain function and cognitive processes. EEG is particularly valuable for studying the neural mechanisms underlying attention, perception, memory, and decision-making. Researchers use EEG to investigate how different brain regions communicate and coordinate during various mental tasks.

This first chapter aims to provide the necessary background to understand the work in this dissertation. We begin by explaining how electrical activity is generated in the brain, which helps in understanding EEG signals. Next, we describe how EEG is measured in the lab and explore the different types of brain activity it can capture. Finally, we focus on Event-Related Potentials (ERPs), a

common EEG method used in cognitive neuroscience to study brain responses to specific events.

2.1 Electrical activity in the brain

Nerve cells or neurons are specialised cells of the nervous system that receive and transmit information in the body through electrical and chemical signals. A nerve cell consists of three main components: the dendrites, the cell body and the axon. The dendrites receive signals sent by other neurons and transmit these signals towards the cell body. Each neuron typically has a number of dendrites that are strongly branched. This branching of the dendrites increases the contact surface for input from other neurons, allowing input from a multitude of neurons in proximity. The cell body then combines or processes this incoming information from the different dendrites. In turn, the neuron can then send information to other neurons via its axon. The anatomy of a neuron is illustrated in Figure 2.1.

When we look at this process of information transfer in more detail, typically, a distinction is made between the pre-synaptic neuron and the post-synaptic neuron (Figure 2.1). When a pre-synaptic neuron wants to send information towards post-synaptic neurons, the signal originates at the axon hillock of the pre-synaptic neuron and travels along the axon towards the axon terminals in the form of action potentials. During an action potential, the membrane potential at a specific location in the neuron will rise and fall in a very short time period of about 1 to 2 ms, after which the membrane potential again reaches its resting state (Hodgkin and Huxley, 1952). Changes in the membrane potential are caused by the active transport of K^+ and Na^+ ions over the membrane. When the action potential reaches the axon terminals, it will trigger the release of neurotransmitters into the synapse. The neurotransmitters that bind with the receptors of the post-synaptic dendrites will initiate a post-synaptic potential. Depending on the type of neurotransmitter that is released, the ion channels in the neuronal cell wall will increase the inflow of Na^+ ions or decrease the outflow of K^+ at the dendrite. This results in two types of post-synaptic potentials. In the first type, the membrane potential will increase, resulting in an excitatory post-synaptic potential (EPSP), while in the second, the membrane potential decreases, and an inhibitory post-synaptic potential (IPSP) is generated. The post-synaptic potentials travel along the dendrites towards the cell body and the axon hillock. All post-synaptic potentials of the different den-

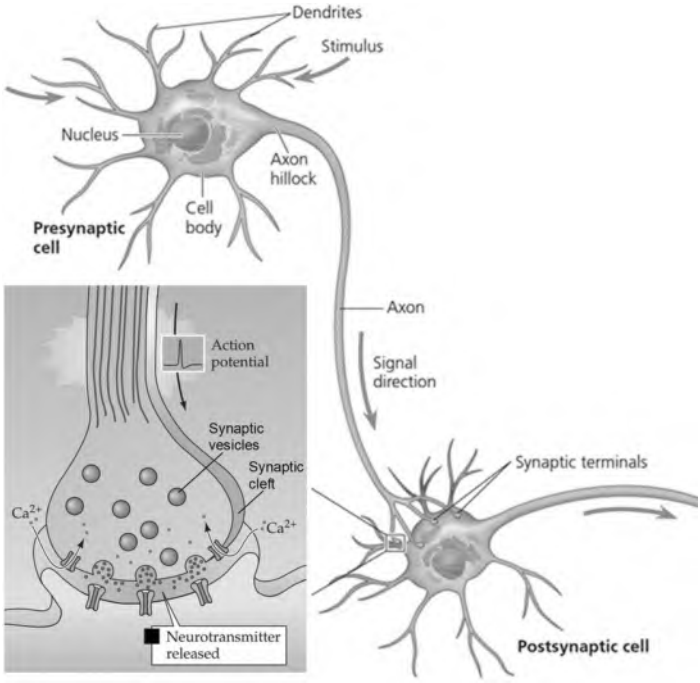

Figure 2.1. The anatomy of a neuron. The most important parts of the cell are the cell body, the axon, the dendrites and the axon hillock. An action potential is generated at the axon hillock after which it travels along the axon in the direction of the axon terminals. When the action potential reaches the axon terminals, it will trigger the release of neurotransmitters in the synapse, where it will bind to the post-synaptic receptors of a second neuron and will trigger a post-synaptic potential (figure adapted from Tang et al. (2019) with permission).

drites are summed up at the axon hillock. When the membrane potential at the axon hillock reaches a certain threshold, an action potential will be generated (Figure 2.1). More detailed information about these mechanisms can be found in Marieb and Hoehn (2015).

At the moment excitatory neurotransmitters bind with the receptors, the extracellular voltage at the dendrite becomes more negative than elsewhere along the neuron due to the increased inflow of Na^+. This means that the neuron becomes a dipole, in which a positive charge is separated from a negative charge, resulting in an electric field. The electric field of a single neuron is too weak to be measurable at the scalp. The signals measured by EEG are the result of both spatial and temporal summation of the dipoles of different neurons. Spatial summation is illustrated in Figure 2.3. In Figure 2.3a, the different neurons

have a parallel arrangement and are oriented identically. This configuration allows the dipoles to sum up and create a larger electric field, thus resulting in a larger signal. Figures 2.3b and 2.3c show two situations where spatial summation is impossible, as the electric fields will cancel each other out. Different types of neurons exist in the brain. Pyramidal cells are the largest cells in the cortex and have a parallel, radial orientation (Figure 2.2). As these specific characteristics of pyramidal cells are ideal for spatial summation, these neurons are the main generators of the electrical field in the brain (Mark F. Bear, 2006).

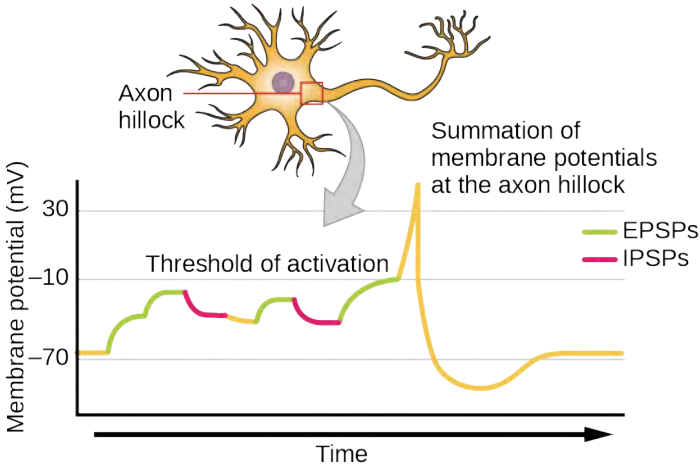

Figure 2.2. The summation of excitatory and inhibitory post-synaptic potentials results in an action potential if the threshold is reached. Excitatory post-synaptic potentials (EPSPs) will increase the membrane potential, and thus bring it closer to the threshold, while inhibitory post-synaptic potentials (IPSPs) will decrease it. The figure also shows that after the action potential, the membrane potential will return to its resting state (figure adapted from Biga et al. (2019)).

2.2 Electroencephalography

Electroencephalography (EEG) is a noninvasive method for recording the electrical activity of the brain. Four main hardware components are needed: electrodes placed on the scalp, an amplifier to amplify the measured signals, an analog-to-digital converter, and a recording device.

In most EEG recording systems, an electrode consists of an Ag/AgCl-metal disk or pellet that makes an electrical connection to the scalp through a con-

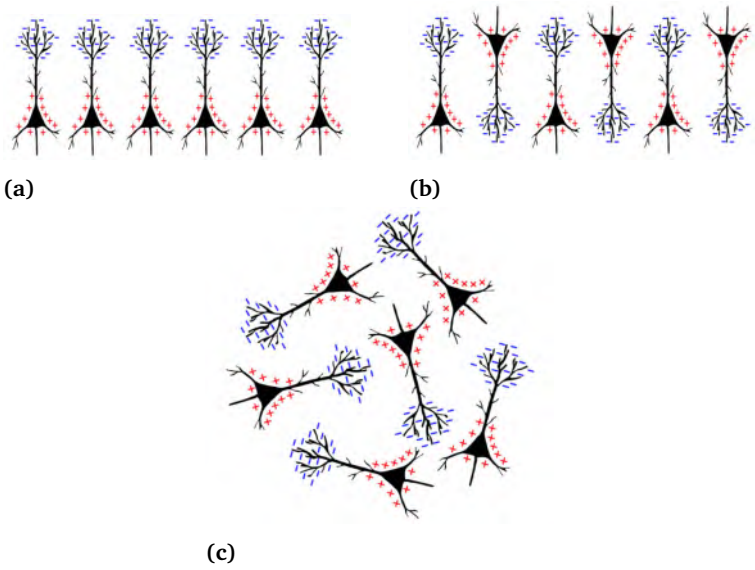

Figure 2.3. Spatial summation depends on the arrangement and orientation of the different neurons. In the first subfigure, each of the neurons is oriented and arranged in the same way. This way, the electrical field created by the different neurons is summated and becomes measureable. For the other subfigures, however, the electrical fields cancel each other out (figures based on Jackson and Bolger (2014)).

ductive gel and has a long lead that allows the electrode to be connected to the amplifier. While different systems exist to define and name the electrode positions, the most-used configuration is the International 10-20 system (Malmivuo and Plonsey, 1995). In its original version, the locations of the electrodes were determined using 10% and 20% intervals of the distance between different reference points, namely the nasion, the inion, and the left and right pre-auricular points (Figure 2.5). In more recent versions, more electrodes are used, and also 5% points are now included. Each electrode is given a label to indicate its position on the scalp. The letters 'P', 'T', 'F' and 'O' are used to indicate respectively the parietal, temporal, frontal and occipital lobes of the brain, while the letter 'C' is used for the central electrodes. The numbers in the label illustrate on which side of the brain the electrode is placed. Even numbers are used for electrodes on the right hemisphere and odd numbers for the left hemisphere. Larger numbers indicate greater distances from the midline, while electrodes on the midline are given the letter 'z' (zero) instead of a number because the number zero looks too much like the letter O.

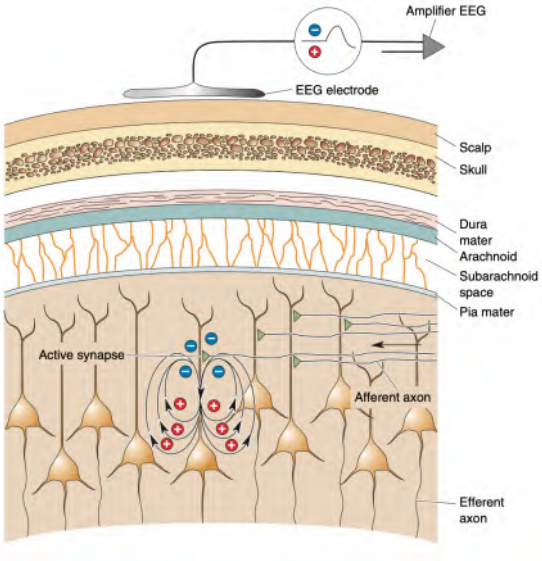

Figure 2.4. The electrical fields measured by EEG are generated by aligned pyramidal cells in the cortex (figure adapted from Mark F. Bear (2006)).

Apart from recording or active electrodes, the system also requires a ground and a reference electrode. The ground electrode serves as a common reference point for the electrical potential of the body. It helps to reduce electrical noise and interference from external sources, such as power lines and electronic devices. On the other hand, the reference electrode is used to compare the electrical activity recorded by the other electrodes on the scalp. The EEG will measure the voltage difference between the active and the reference electrodes. This differential measurement helps to isolate the brain's electrical activity from other sources of electrical noise.

Once the electrodes pick up the EEG signals, they are amplified and converted from a continuous, analog voltage into a discrete, digital form that can be stored in a computer. A typical amplification factor of 10,000 is used, ensuring that the EEG voltage is in an appropriate range for the analog-to-digital conversion. In the final step, the digital signal is stored on a recording device, such as a regular computer, allowing visualization and analysis of the measured signals.

2.2.1 Spontaneous and evoked EEG

When recording EEG data, researchers are typically interested in either spontaneous brain activity or in understanding brain activity in response to specific

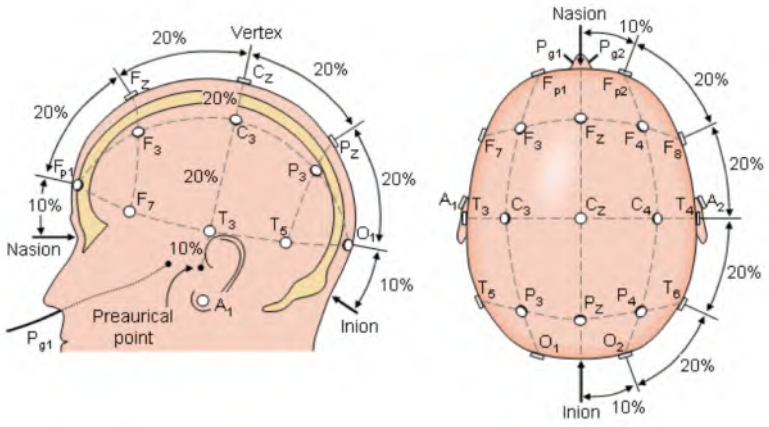

Figure 2.5. The international standardized 10-20 system for the placement of electrodes in EEG. The reference points in this system are the nasion and the inion. The locations of the electrodes are determined using 10% and 20% intervals of the distance between these reference points (figure reprinted with permission from Shriram et al. (2013)).

tasks or stimuli. When EEG is recorded in the absence of external stimuli, it is typically referred to as resting-state EEG. The primary focus of this dissertation, however, is on Event-Related Potentials (ERPs), which are time-locked brain responses to distinct sensory, motor, or cognitive events (Luck, 2014).

Resting-state EEG

Resting-state EEG (rs-EEG) captures the brain's ongoing, spontaneous electrical activity when no specific task is performed. It is typically considered to provide information on the intrinsic connectivity and the functional organization of the brain.

As the electrical activity measured by the EEG often shows oscillatory and repetitive behaviour, rs-EEG is often analysed using spectral analysis methods. The rhythm of the activity depends, among other things, on the alertness or the consciousness of the subject and is characterised by its frequency (Figure 2.6. Five different rhythms or frequency bands are distinguished in EEG research, namely delta rhythm (0-4 Hz), theta rhythm (4-8 Hz), alpha rhythm (8-12 Hz), beta rhythm (12-30 Hz) and gamma rhythm (30-100 Hz). Delta rhythm is typically observed during deep sleep, while theta rhythm is associated with other sleep stages and drowsiness. In awake subjects who are relaxed, activity in the alpha frequency band is most prominent. The frequency of electrical

activity in the brain increases further to the beta frequency band when subjects are having conversations or are focusing on a task. Finally, gamma rhythm indicates hyper brain activity, which is associated with learning (Sörnmo and Laguna, 2005).

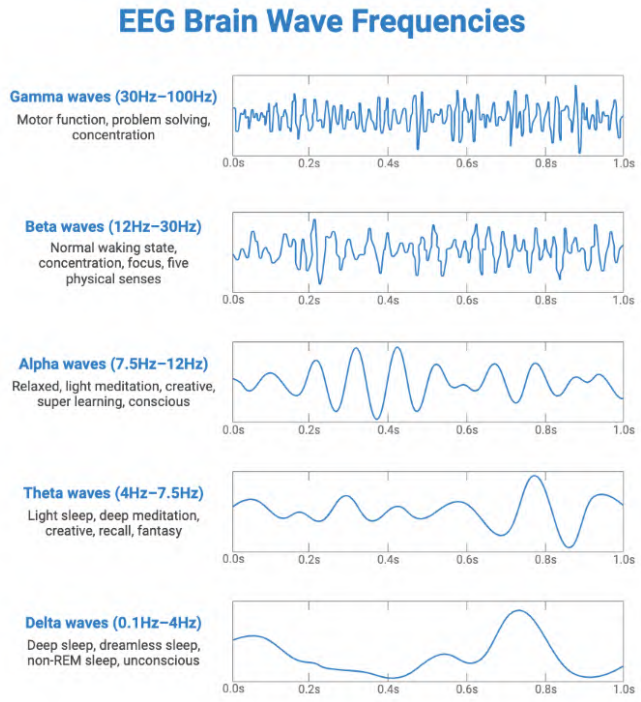

Figure 2.6. The frequency of the rhythm of brain activity depends on the alertness or the conciousness of the patient (figure adapted from Biorender with permission).

Changes in the spectral composition of the EEG signals can be observed across the lifespan. Studies comparing adolescents and adults, for example, have shown that EEG power typically decreases with increasing age, while functional networks become more organized probably due to structural changes of the brain. Changes in these features have also been associated with a number of disorders, including depression and dementia. To give an example, studies have found a decrease in spectral power in the alpha and beta bands in different types of dementia, such as Alzheimer's disease and fronto-temporal lobe dementia (FTLD). However, while patients with Alzheimer's also showed an increase in spectral power in the theta and delta bands, indicating slowing of the

brain oscillations, these frequencies were not affected in FTLD (Lindau et al., 2003; Nishida et al., 2011; Caso et al., 2012).

Task-related EEG

In addition to analyzing spontaneous EEG activity, another widely used approach in EEG research involves measuring the brain's responses to specific sensory, motor, or cognitive events (Luck, 2014). These time-locked responses, known as Event-Related Potentials (ERPs), provide a noninvasive window into the neural mechanisms underlying perception, attention, decision-making, and many other cognitive processes. Given that ERPs form the central focus of this dissertation, the following section offers a more detailed overview of how they are measured, interpreted, and applied in experimental research.

2.3 Event-Related Potentials

ERPs are small voltage fluctuations embedded within the ongoing EEG signal. Since raw EEG data is highly dynamic and contains a mix of background neural activity and noise, individual event-related responses are very difficult to distinguish in single trials. To extract ERPs, researchers use trial averaging, a method in which multiple EEG epochs (time segments) aligned to the same type of stimulus or event are averaged together. This process enhances the stimulus-related signal while minimizing the influence of unrelated brain activity and external noise, revealing characteristic ERP waveforms.

ERP components are defined by their latency (when they occur relative to the stimulus), polarity (positive or negative deflection), and topography (scalp distribution). These components are often classified into early and late responses. Early sensory components, such as P1, N1, and P2, typically occur within the first 100–200 milliseconds after stimulus onset and reflect the initial stages of sensory processing. Their amplitude and latency can be influenced by stimulus properties such as intensity, modality (e.g., visual vs. auditory), and attention. Cognitive components on the other hand, such as the P300 (associated with attention and decision-making) and the N400 (linked to language comprehension and semantic processing), appear later and are thought to reflect higher-order cognitive functions.

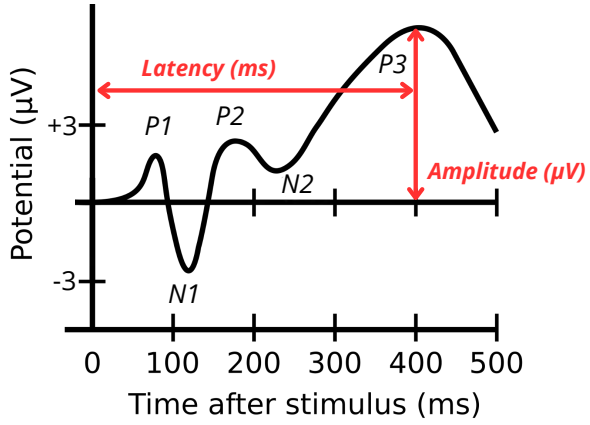

Figure 2.7. Visual representation of some common event-related potential components

2.3.1 Advantages of ERPs

One of the key advantages of ERPs is their high temporal resolution, allowing researchers to track neural processing on the millisecond scale. This makes ERPs particularly useful for studying the sequence and timing of cognitive processes that would be difficult to resolve using techniques like fMRI, which has much lower temporal precision.

ERPs are widely used in both basic and applied research. In cognitive neuroscience, they help uncover how the brain processes stimuli and how different mental functions unfold over time. In clinical settings, ERPs are very promising as biomarkers for neurological and psychiatric disorders, such as schizophrenia, autism spectrum disorder, and Alzheimer's disease. Certain ERP abnormalities can indicate deficits in sensory processing, attention, or memory, making them valuable tools for early diagnosis and treatment monitoring.

Another important aspect of ERP research is its adaptability to different experimental paradigms, allowing researchers to study a wide range of cognitive processes in both healthy individuals and clinical populations. The flexibility of ERPs comes from their ability to be elicited by carefully designed tasks that isolate specific cognitive functions while maintaining high temporal precision.

2.3.2 Common Experimental Paradigms in ERP Research

One widely used paradigm is the oddball task, which is commonly employed to investigate attention, novelty detection, and cognitive control. In this paradigm, participants are presented with a sequence of repetitive "standard" stimuli interspersed with infrequent "oddball" or "deviant" stimuli that differ in some characteristic, such as pitch in an auditory oddball task or color in a visual oddball task. When participants are asked to not pay any attention to the stimuli, this paradigm typically elicits a Mismatch Negativity (MMN) component, which can be used to study automatic change detection. On the other hand, when researchers ask the participant to pay attention and for example press a button when the rare oddball stimulus apprears, these stimuli will typically elicit a P300 component, a well-known ERP marker of attentional allocation and context updating. The amplitude and latency of the P300 provide insights into how quickly and efficiently the brain detects and responds to unexpected stimuli, making this paradigm useful for studying attentional processes and clinical conditions such as ADHD and schizophrenia.

Another common approach is the go/no-go task, which is used to study response inhibition, cognitive control, and executive function. In this paradigm, participants must execute a motor response (pressing a button) when they see a "go" stimulus but withhold their response when a "no-go" stimulus appears. The difference in ERP responses between go and no-go trials reveals neural mechanisms of impulse control. The N2 component (a frontocentral negative deflection occurring around 200–300 ms after the stimulus) is thought to reflect conflict detection, while the P3 (or P300) component in no-go trials is associated with inhibitory control. Go/no-go tasks have been widely applied in research on impulse control disorders, substance abuse, and developmental changes in executive function.

ERPs are also extensively used in language comprehension studies, where they provide insights into how the brain processes different linguistic elements in real time. For instance, the N400 component, a negative-going wave peaking around 400 ms after word onset, is sensitive to semantic incongruities. It is larger when a word is unexpected or does not fit the preceding context (e.g., "He spread the warm bread with socks"). Another important ERP component in language research is the P600, which is linked to syntactic processing and reanalysis, often appearing in response to grammatical errors or complex sentence structures. By using paradigms that manipulate lexical, semantic, and syntactic information, researchers can investigate the neural basis of language

comprehension in both typical and impaired populations, such as individuals with dyslexia or aphasia.

3 EEG source imaging and functional connectivity

As explained in the previous chapter, EEG provides a non-invasive window into brain activity with high temporal resolution, making it a valuable tool for studying neural dynamics. However, the interpretation of EEG data is often complicated by the fact that signals recorded at the scalp represent a mixture of contributions from multiple underlying neural sources. EEG source imaging (ESI) addresses this challenge by estimating the location and strength of the cortical generators that result in the observed EEG signals. By solving the so-called inverse problem, ESI reconstructs brain activity at the source level, allowing for an easier interpretation of neural processes.

Beyond identifying individual brain regions involved in specific cognitive functions, a growing interest in neuroscience focuses on how different regions interact. Functional Connectivity (FC) refers to the statistical dependencies between signals recorded from different brain regions. These measures provide insights into the functional neural networks in the brain. FC can be assessed both at the sensor level, using the original EEG recordings, and at the source level, following ESI. While sensor-level FC is often easier to compute, it may be confounded by volume conduction effects. Source-level FC, on the other hand, allows for network analysis in a more physiologically meaningful way, as it accounts for the true neural origins of EEG signals.

By combining EEG source imaging with functional connectivity analysis, researchers can study how brain regions coordinate their activity, offering valuable insights into cognitive processing, neurological disorders, and brain net-

work dynamics. In this chapter, both EEG source imaging and functional connectivity will be introduced, highlighting their methodological principles.

3.1 EEG Source Imaging

One of the limitations of EEG is its limited spatial resolution. As the electrical activity generated by the neurons travels through the brain in different directions, the activity recorded by each electrode does not represent a single underlying brain source but rather a composite of activities from various brain regions. To overcome this limitation, EEG source imaging was introduced as a computational technique to estimate the electrical neuronal activity in the brain. This technique identifies the underlying generators of the electrophysiological activity recorded at the scalp by combining the EEG signals with structural MR images. During recent decades, EEG Source Imaging (ESI) has been an important area of research, and it has introduced significant advances in multiple research domains such as epilepsy (Mégevand & Seeck, 2020) and sleep (Del Felice et al., 2014; Fernandez Guerrero & Achermann, 2019).

Source analysis of EEG data consists of two different processes: a forward model and an inverse model. The forward model, also called the head model, describes how a known source of electrical activity within the brain contributes to the signal observed at each EEG electrode on the scalp. Conversely, the inverse model estimates the location and strength of the electrical activity within the brain based on the EEG signals recorded at the scalp and relies on the forward model to obtain an accurate solution. This is a non-unique problem, which means that regularisation techniques or constraints are needed to find plausible solutions. A visual overview of the information flow and the basic components included in EEG source imaging is given in Figure 3.1.

3.1.1 The forward model

In EEG source imaging, the forward model is a crucial step in understanding how brain activity results in the electrical signals recorded at the scalp. It establishes the mathematical relationship between neural sources and the measured EEG signals, essentially predicting how neuronal activity propagates through different head tissues to reach the electrodes. This process requires an accurate representation of both the brain's electrical sources and the head's conductive properties. The forward model is constructed using three key components: the head model characterizing the geometric and electrical properties of the head,

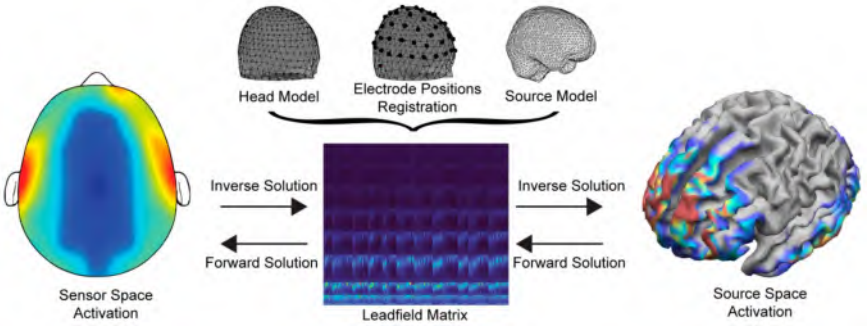

Figure 3.1. Information flow and basic components of the forward and inverse problems (adapted with permission from Zorzos et al. (2021)

the source model defining the possible location of neural activity, and the positions of the electrodes that were used for the EEG recording.

The head model

To understand how the neuronal sources generate measurable EEG signals at the scalp, a detailed representation of the head's structure is necessary. The head model accounts for the anatomical and electrical properties of different tissues, determining how electrical currents propagate through, among others, the brain, skull, and scalp.

Geometry: The complexity of the head model can vary. While simplified spherical models exist which allow for analytical solutions, they lack the realism and accuracy that is needed for accurate localizations. More detailed, subject-specific models are typically derived from MRI scans. These models include multiple layers representing different tissues, such as the brain, cerebrospinal fluid (CSF), skull, and scalp. Advanced segmentation tools exist in open source packages, such as FreeSurfer, SPM and Brainstorm, facilitating the construction of these models. The number of tissue types that are considered can vary. Some simple models only segment three different tissue types (i.e. brain, skull, and scalp), while more complex models sometimes include up to nine different tissues (i.e. white matter, grey matter, CSF, compact bone, spongiform bone, scalp, eyes, blood and muscle). More detailed models have been shown to improve accuracy, especially the inclusion of CSF in the model, however, they also increase computational demands and potential numerical errors.

When individual structural brain images are unavailable, which is often the case in studies with healthy participants, standardized anatomical templates can be used as a alternative. One commonly used template is fsaverage, a standard cortical surface template provided by FreeSurfer (Fischl, 2012). The fsaverage model is based on the alignment of multiple individual brain scans, resulting in an average cortical surface representation that facilitates group-level analyses and comparisons across studies. Other standardized templates, such as the ICBM152 or the Colin27 brain (Mazziotta et al., 2001; Holmes et al., 1998), offer additional options depending on the specific requirements of the study.

Electrical Conductivity: Each tissue type has unique electrical conductivity properties, which influence how the brain's electric fields propagate to the scalp. Conductivity values are typically estimated from literature, as direct in vivo measurements for every patient are currently impossible. Some tissues, like white matter and the skull, exhibit anisotropic conductivity, meaning their electrical properties also vary depending on direction. While Anwander et al. (2002) have shown localization errors of 5.1 mm for radial sources when white matter anisotropy was neglected, most models used today ignore the anisotropic nature of these tissue types and approximate them using isotropic conductivity values.

The source model

Neuronal sources in the brain generate electrical activity that can be modeled to simulate EEG signals. As discussed earlier, the primary generators of EEG are the pyramidal neurons in the cortex. These neurons create electrical currents through postsynaptic potentials, which can be represented at a macroscopic level as current dipoles. A current dipole consists of a paired current source and sink, separated by a small distance, and is mathematically characterized by its position, orientation, and intensity. The dipole moment describes both the direction and strength of this source.

The source space then represents the set of all possible locations where dipoles can be placed to model brain activity. Since pyramidal neurons are primarily located in the cortical gray matter, sources are usually restricted to this region. Dipoles can be positioned on the cortical surface or within a 3D grid inside the gray matter volume (cf. Figure 3.3). Their orientations may be fixed perpendicular to the cortical surface, reflecting the natural alignment of

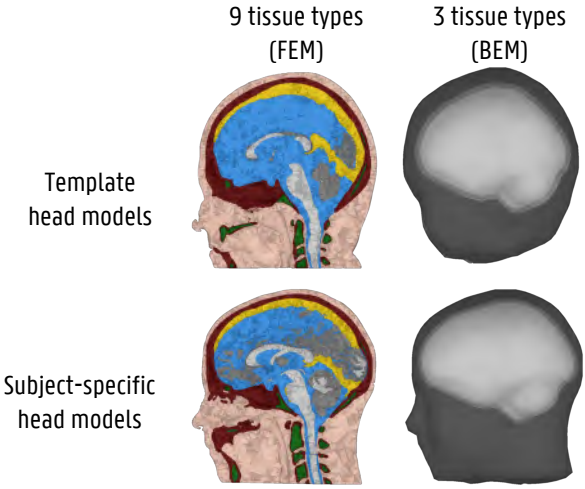

Figure 3.2. Examples of head models. In the different columns, examples are shown of head models including respectively 9 and 3 different tissue types, while in the different rows, examples are given for head models based on templates (top row) and based on subject-specific MRIs (bottom row).

neurons. The number of dipoles in the source space can range from hundreds to tens of thousands, depending on the required resolution.

Electrode positions

To accurately calculate the EEG signals resulting from modeled sources, precise knowledge of electrode positions on the scalp is essential. Standardized systems, such as the 10-20 system and its higher-density extensions (10-10 and 10-5 systems), provide predefined electrode placements, ensuring consistency across studies and compatibility with existing head models. In this system, which was originally designed to balance spatial coverage and practicality, electrodes are positioned based on distances between anatomical landmarks, including the nasion, inion, and preauricular points. The 10-10 and 10-5 extensions increase the density of electrodes, allowing for finer spatial resolution and improved source estimation. While high-density EEG (e.g., 128 or 256 channels) further enhance spatial sampling, they also introduce challenges related to setup time, patient comfort, and computational complexity in source modeling. To take into account individual variability in head shape and size, these standard electrode positions can be coregistered to the head model and projected on the scalp based on the anatomical landmarks. A visualization of these coregis-

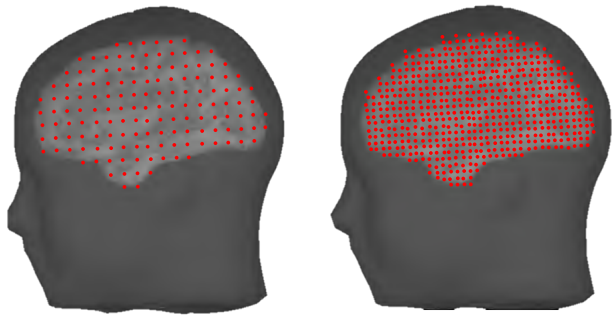

Figure 3.3. Examples of source models with a different number of dipoles. The dipoles are placed within a regular 3D grid inside the gray matter volume.

tered electrodes to the head model is shown in Figure 3.4 for different electrode set-ups including respectively 32, 64 and 128 electrodes. Alternatively, actual electrode locations can be measured using 3D digitization techniques. This approach is considered the most accurate one, and common methods include electromagnetic tracking systems (e.g., Polhemus), optical tracking (e.g., infrared cameras), and photogrammetry. These techniques ensure accurate alignment between the recorded EEG signals and the individual head model, reducing localization errors in EEG source imaging. By integrating accurate electrode positioning with detailed head and source models, the forward model can provide a reliable foundation for EEG source imaging, improving the ability to localize and interpret underlying neural activity.

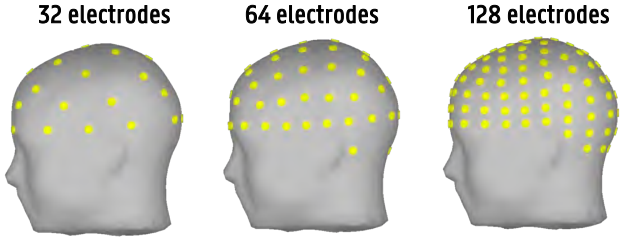

Figure 3.4. Visualization of the electrodes placed on the scalp of the head model based on anatomical landmarks including respectively 16, 64 and 128 electrodes.

Calculation of the Forward Model

Once the head model, source model, and electrode positions have been defined, the forward model can be computed. This step determines how electrical activity generated within the brain propagates through the head's tissues to produce the EEG signals recorded at the scalp electrodes. The fundamental part of the forward model is the leadfield matrix, which mathematically describes the contribution of each potential dipole source to the signals at each electrode. Essentially, the leadfield acts as a transformation between source space (the neural generators) and sensor space (the observed EEG signals).

Mathematically, the EEG potentials $\mathbf{V}$ recorded at the electrodes can be expressed as a linear combination of the source activities $\mathbf{J}$:

$$\mathbf{V} = \mathbf{L}\mathbf{J} + \epsilon \tag{3.1}$$

where $\mathbf{L}$ is the lead field matrix, which depends on the head model's geometry and conductivity, and ϵ represents measurement noise. Computing $\mathbf{L}$ requires solving Maxwell's equations, which describe the behavior of electrical fields within a conductive medium.

For simplified spherical head models, the forward model can be computed analytically using closed-form solutions. These models assume that the head consists of concentric spherical shells with uniform conductivity. While computationally efficient, spherical models oversimplify head anatomy, leading to localization errors and limiting their practical applicability in EEG source imaging. For realistic head models based on MRI-derived anatomy, numerical methods are needed to solve the electromagnetic field equations. The most widely used approaches include the Boundary Element Method (BEM), the Finite Element Method (FEM) and the Finite Difference Method (FDM). BEM treats the head as a set of nested surface compartments (e.g., brain, skull, and scalp) and solves the electrical potential at these boundaries. It assumes that each compartment has isotropic conductivity, making it computationally efficient while capturing some anatomical details. However, BEM cannot model conductivity variations within each tissue layer and is less accurate when dealing with highly conductive structures such as cerebrospinal fluid (CSF). FEM divides the head volume into small finite elements (e.g., tetrahedra or hexahedra) and approximates the electrical field within each element. Unlike BEM, FEM allows for inhomogeneous and anisotropic conductivity, making it more accurate in modeling complex tissue properties (e.g., anisotropic white matter). However, FEM

requires computationally intensive meshing and numerical solvers, making it more demanding in terms of processing time and memory. FDM discretizes the head volume using a regular grid and approximates differential equations governing electric potential propagation. While computationally efficient, the availability of FDM tools in open source software is very limited, making it the least often used option.

3.1.2 The inverse problem

The second part of the EEG source imaging technique involves solving the inverse problem. This problem refers to determining the location, orientation and magnitude of the cortical dipoles that explain the observed activity at the scalp (Luck, 2014). This process relies on the forward solution, but is fundamentally ill-posed as the number of possible sources vastly exceeds the number of electrodes where the EEG is measured, meaning that there is no unique mathematical solution. To overcome this limitation, inverse techniques incorporate certain assumptions or enforce specific constraints to regularize the solution. The final goal is to minimize the difference between the predicted EEG (based on the forward model) and the measured EEG, i.e. the residuals, while optimizing a particular cost function. Typically, inverse solutions are separated into two categories: the equivalent current dipole (ECD) approaches and the distributed dipoles approaches. Where the ECD approaches assume that the EEG signals are generated by a small number of focal sources, the distributed dipoles approaches consider all possible source locations simultaneoulsy.

Equivalent Current Dipole Models

ECD models assume that EEG signals arise from a small number of discrete dipoles, typically fewer than 10, each defined by its position, orientation, and strength. These dipoles are estimated through optimization techniques that iteratively adjust their parameters to best fit the observed EEG data. ECD models are particularly useful in cases where neural activity originates from well-defined focal sources, such as epileptic spike localization.

The estimation of dipole parameters relies on nonlinear optimization methods that refine dipole locations and orientations to minimize the residual error between the predicted EEG signals (derived from the forward model) and the observed EEG signals. The simplest case, involving a single ECD, is typically solved by minimizing the relative residual energy (RRE), which quantifies the

proportion of unexplained signal energy relative to the total measured signal energy. When multiple dipoles are assumed, the most widely used approach is multiple emitter location and signal parameter estimation (MUSIC), which searches for sources that best match the dominant components of EEG activity (Schmidt, 1986). More advanced techniques, such as Recursively Applied and Projected MUSIC (RAP-MUSIC), iteratively refine dipole estimates by sequentially localizing multiple sources while minimizing interference between them. These methods enhance source localization accuracy by iterating through multiple candidate dipole configurations and projecting out previously identified sources to improve subsequent estimates (Mosher and Leahy, 1999).

Despite their precision in localizing a small number of sources, ECD models require an a priori assumption about the number of dipoles present, which may not always be known. Additionally, the accuracy of the solution is highly dependent on the initial parameter estimates, as nonlinear optimization techniques can converge to local minima rather than the true global solution. This sensitivity to initial conditions necessitates careful selection of starting parameters and, in some cases, the incorporation of additional constraints or prior knowledge to guide the optimization process.

Distributed Dipole Models

In contrast to ECD approaches, distributed dipole models assume that brain activity is generated by a large number of simultaneous sources distributed across the cortical surface or within a volumetric source space. Instead of estimating a small number of dipoles, these models assign an activation value to thousands of potential sources and attempt to reconstruct a spatially extended representation of neural activity. However, since the number of sources exceeds the number of electrodes, additional constraints must be imposed to obtain a stable and physiologically plausible solution.

Different inverse methods apply various regularization techniques to achieve this. The most simple approach to regularization is the Minimum Norm Estimation (MNE) solution (Hämäläinen and Ilmoniemi, 1994), which assumes that the overall source activity should be as small as possible while still explaining the observed EEG signals. In other words, this approach tries to find the solution with minimum power. As this solution favours superficial sources over deep sources, the method was extended by Lin et al. (2006) who introduced the Weighted Minimum Norm Estimate (wMNE) solution in which the power of the sources is weighted using a weighting matrix that can be based on the

depth of the sources or other constraints. Another regularization approach is Low-Resolution Electromagnetic Tomography (LORETA), which enforces spatial smoothness constraints to enhance the continuity of reconstructed sources and improve localization accuracy (Pascual-Marqui et al., 1994). In this approach, if one source is active, there is a high probability that the neighbouring sources are also active. Other methods that build further upon this are the standardized low-resolution brain electromagnetic tomography (sLORETA) and exact low-resolution brain electromagnetic tomography (eLORETA) (Pascual-Marqui, 2002; Pascual-Marqui et al., 2011). Other methods, such as beamforming approaches like Linearly Constrained Minimum Variance (LCMV) and Dynamic Imaging of Coherent Sources (DICS), use spatial filtering techniques to isolate the contributions of specific brain regions while suppressing interference from other areas (Van Veen et al., 1997; Gross et al., 2001).

Distributed models offer the advantage of not requiring a priori assumptions about the number of active sources, making them particularly well suited for cognitive studies where multiple brain regions may be simultaneously engaged. However, they tend to exhibit lower spatial specificity compared to ECD models due to regularization constraints, which often result in spatially diffuse solutions. Additionally, these models are computationally more demanding, particularly when high-density EEG recordings are used to improve resolution. While they provide a more comprehensive picture of brain activity, their accuracy can be affected by the choice of regularization method and the assumptions that are made about signal smoothness.

3.2 Functional Connectivity

When looking at connectivity in the brain, two different types of connectivity can be distuinguished: structural connectivity and functional connectivity. Structural connectivity investigates the anatomical connections that exist between different areas of the brain, and is typically measured using diffusion weighted imaging (DWI). It provides the framework of physical white matter pathways through which signals in the brain can travel. While changes in these connections are possible over time, when looking at short time scales, structural connectivity remains stable. Functional connectivity (FC), on the other hand, refers to the statistical dependencies between neural signals recorded from different brain regions, reflecting coordinated activity rather than direct anatomical connections. Unlike structural connectivity, functional connectivity

is a dynamic measure that can change over time, depending on cognitive states, tasks, or pathological conditions, and is typically assessed using EEG or fMRI time series.

As mentioned in the introduction of this chapter, functional connectivity can be studied at two levels in EEG research: the sensor level (i.e., between EEG electrodes) and the source level (i.e., between reconstructed cortical sources). Sensor-level connectivity is more straightforward but is affected by volume conduction, which can introduce artificial correlations. Source-level connectivity, derived from EEG source imaging techniques, provides a more anatomically meaningful interpretation by mapping connectivity patterns onto specific brain regions, reducing the influence of spurious correlations caused by volume conduction.

Functional connectivity measures in EEG can be grouped into four different categories:

- **Correlation and coherence methods** typically assess the linear relationship between signals recorded from different electrodes or brain regions. Correlation quantifies the similarity in signal amplitude fluctuations over time, while coherence measures the consistency of phase relationships across specific frequency bands. These methods are widely used due to their simplicity and ability to reveal large-scale network dynamics.

- **Phase synchronization measures** focus on the temporal alignment of oscillatory activity between signals, independent of amplitude variations. Metrics such as the Phase Locking Value (PLV) and the Phase Lag Index (PLI) quantify how consistently two signals maintain a fixed phase difference, making them particularly useful for studying neural communication mechanisms.

- **Information based measures** capture both linear and nonlinear dependencies between EEG signals by evaluating shared information content. Mutual Information (MI) is a commonly used approach that detects statistical dependencies beyond simple correlation, offering insights into complex interactions that traditional linear methods might miss.

- **Granger causality measures** go a step further by estimating the directional influence between signals, distinguishing between mere correlation and potential causal relationships. Techniques such as Granger Causality (GC), directed coherence (DC), partial directed coherence (PDC) and directed transfer function (DTF) assess whether

past activity in one signal can predict future activity in another, providing valuable insights into the directional flow of information in the brain.

Each functional connectivity method has its own strengths and weaknesses, making the choice of method highly dependent on the research question, the characteristics of the EEG data, and the brain processes being studied. To help researchers select the right approach, connectivity measures are often grouped based on several key differences.

One important distinction is whether the method analyzes connections in the time domain or frequency domain. Time-domain methods, like correlation and Granger causality, examine how signals relate to each other over time, making them useful for studying short-lived neural responses or event-related activity. Frequency-domain methods, such as coherence and phase synchronization, break signals down into different frequency bands (e.g., alpha, beta, gamma) to investigate how brain regions interact through specific rhythmic patterns.

Another key difference is whether a method detects directed or undirected connectivity. Undirected methods, like correlation and coherence, measure how strongly two signals are related but do not indicate which one influences the other. Directed methods, such as Granger causality and Transfer Entropy, aim to determine whether activity in one brain region helps predict future activity in another. These methods are useful for studying causal relationships in brain networks but require careful interpretation since factors like volume conduction and hidden sources can complicate the results.

A third distinction is whether a method follows a model-based or model-free approach. Model-based methods, like Granger causality, rely on mathematical models that describe how one signal influences another, usually assuming linear relationships. These methods are useful when data follow predictable patterns but may not capture more complex interactions. Model-free approaches, like mutual information or phase synchronization, make fewer assumptions and can detect both linear and nonlinear connections. While these methods are more flexible, they are often more computationally demanding and can be harder to interpret.

Finally, connectivity methods differ in whether they examine bivariate or multivariate relationships. Bivariate methods assess connections between pairs of signals independently, making them easier to use and interpret. However, they do not account for indirect connections, meaning they may overlook complex brain interactions. Multivariate methods, like partial coherence or multivariate Granger causality, analyze multiple signals at once, allowing researchers

to study broader network interactions while reducing the impact of false connections. These methods provide a more complete picture of brain networks but require more data and computational resources.

By considering these key differences, researchers can choose the most suitable functional connectivity measure based on their study goals, the nature of their EEG data, and the assumptions they are willing to make. This choice ultimately affects how well the results reflect real brain activity and how meaningful the findings are for understanding neural function.

Part II

Source reconstruction and functional connectivity of language ERP components

4 | Cortical Generators and Connections Underlying Phoneme Perception and Semantic Priming: a Mismatch Negativity, P300 and N400 Investigation

Abstract

Speech perception is a complex process that unfolds across multiple levels of analysis, from early acoustic-phonetic processing to higher-order lexical processing and semantic integration. This study examined the cortical sources and functional networks underlying three Event-Related Potential (ERP) components often used to study different aspects of language: the MMN and P300 during passive and active phoneme discrimination, and the N400 during auditory taxonomic priming. Sixty healthy adults underwent high-density EEG recording while completing a phonemic oddball task and a categorical priming task. Source localization was performed using eLORETA, and functional connectivity was assessed via cross-correlation across ROI pairs.

The MMN, elicited during passive listening, showed activation in bilateral temporal (insula, superior temporal gyrus, temporal pole), frontal (rostral middle frontal, pars opercularis), and parietal (postcentral, supramarginal) cortices. Functional connectivity revealed a network linking right temporoparietal regions with left frontal areas supporting automatic detection of deviant phonemes. In contrast, the P300—evoked during active phoneme categorization—engaged frontal (caudal middle frontal, precentral), parietal (precuneus), and cingulate (posterior, isthmus) cortices, forming a distributed fronto-parieto-cingulate network for goal-directed speech processing. Finally, the N400, associated with semantic priming, showed left-lateralized activation in the frontal cortex and posterior cingulate. Enhanced connectivity within and between frontal areas, and between frontal and parieto-occipital cortices, supported efficient retrieval of lexical-semantic representations for primed words.

Overall, these results reveal that passive phoneme discrimination and active categorization recruit distinct yet overlapping bilateral networks, while semantic processing relies more heavily on a left-lateralized frontal system. Together, the MMN, P300, and N400 reflect complementary neural mechanisms underlying the transition from sound to meaning in spoken language.

This chapter is based on the following articles:

Criel, Y., Depuydt, E., Miatton, M., Santens, P., van Mierlo, P., & De Letter, M. (2024). Cortical generators and connections underlying phoneme perception: a mismatch negativity and p300 investigation *Brain Topography 37*(2024): 1089-1117. doi:10.1007/s10548-024-01065-z

Criel, Y., Depuydt, E., Cocquyt, E.-M., Miatton, M., Santens, P., van Mierlo, P., & De Letter, M. (2025). Frontal Synchronization Facilitates Taxonomic Priming: Insights from N400 Source Estimation and Functional Connectivity *Language, Cognition and Neuroscience*, 1-18. doi:10.1080/23273798.2025.2501049

For both of these articles, Yana Criel and Emma Depuydt are shared first authors. In this collaboration, Yana Criel focused on interpreting the results and situating them within the broader scientific context, while Emma Depuydt focused on designing the methodological approach and processing the data. Both contributions were essential to the conception and realization of the studies.

4.1 Introduction

Speech perception is a complex process that unfolds across multiple levels of analysis, from early acoustic-phonetic processing to higher-order lexical processing and semantic integration. According to the dual-stream model of spoken word recognition (Hickok and Poeppel, 2004), the dorsal and ventral streams play distinct but complementary roles in speech processing. The initial prelexical stages of spoken word processing provide the foundation for further lexical analysis in the ventral stream and access to articulatory sound representations through the dorsal stream. At the core of these processes is the ability to extract and interpret meaningful linguistic units from continuous auditory input.

Prelexical speech processing involves three key stages (Pettigrew et al., 2004). First, the auditory system analyzes the incoming speech signal based on its spectrotemporal features. Next, acoustic-phonetic cues are extracted, allowing for the identification of phonetic distinctions. Finally, phonological/phonemic representations are activated, enabling the discrimination and categorization of phonemes based on distinctive features such as articulation place, manner, and voicing (Becker and Reinvang, 2007). Impairments in these early stages can significantly impact spoken word recognition and comprehension, as observed in individuals with aphasia, where deficits in acoustic-phonetic analysis contribute to broader language impairments (Wertz et al., 1998; Auther et al., 2000). Understanding the neural circuits supporting phoneme-level processing is therefore essential for elucidating the mechanisms underlying speech perception.

Neurophysiological research has extensively relied on electroencephalography (EEG) to investigate the temporal dynamics of speech processing. Event-related potentials (ERPs) provide a powerful tool for examining how the brain responds to different aspects of auditory input in real-time (Luck, 2014). Two key ERP components, the mismatch negativity (MMN) and P300 (P3b), have been widely used to study phoneme discrimination and categorization using oddball paradigms (Aerts et al., 2013; Criel et al., 2023; Näätänen et al., 1997; Partanen et al., 2011). In this context, these components have been considered to reflect respectively passive discrimination (Kujala et al., 2007; Näätänen et al., 2012) and active categorization (Bledowski et al., 2004; Kok, 2001) of phonemes. Phoneme discrimination refers to the ability to perceive and distinguish acoustic differences between phonemes, irrespective of their categorical

boundaries. Phoneme categorization entails the perception of these linguistic units into distinct groups that are based on shared acoustic features. The MMN (Näätänen et al., 1978) typically occurs in the range of 160 to 220 ms after the onset of a deviance in an oddball task where attention is directed away from the auditory modality. In contrast, the P300 (Sutton et al., 1965) emerges between 300 and 700 ms after the presentation of a target when stimuli are actively attended to. Whereas the MMN is characterized by a frontocentral scalp distribution, the P300 is primarily detectable at parietal electrodes (Polich, 2007). MMN and P300 cortical generators and the functional connectivity thereof have been a topic of investigation, albeit mainly in relation to the perception of tonal contrasts. The question remains whether the same cortical regions and connections are engaged during phoneme perception, or whether the processing of speech sounds draws on distinct networks. Evidence on the neural generators of passive and active auditory deviance processing is provided by EEG/MEG investigations (Koshiyama et al., 2020; Sabeti et al., 2016; van Dinteren et al., 2018; Volpe et al., 2007; Wronka et al., 2012), fMRI (Rinne et al., 2005), combined EEG-fMRI investigations (Crottaz-Herbette and Menon, 2006; Doeller et al., 2003; Li et al., 2019b; Opitz et al., 2002), lesion mapping (Alho et al., 1994; Ehlers et al., 2015) and intracranial recordings (Halgren et al., 1998).

Beyond phoneme-level processing, successful speech comprehension requires access to stored semantic knowledge and the ability to integrate lexical information into meaningful representations. The controlled semantic cognition (CSC) framework (Jefferies, 2013; Chiou and Lambon Ralph, 2019) suggests that conceptual knowledge is distributed across modality-specific regions but is integrated within the anterior temporal lobe (ATL), which acts as an amodal semantic hub (Patterson and Lambon Ralph, 2016). Accessing and selecting relevant semantic information depends on a network of regions involved in semantic control, including the posterior middle temporal gyrus (pMTG), inferior frontal gyrus (IFG), and inferior parietal cortex (IPC) (Diveica et al., 2021; Jackson, 2021). The efficiency of semantic retrieval is often examined using semantic priming paradigms, where reaction times and ERP responses reveal facilitated processing for semantically related versus unrelated words (McNamara, 2005).

A key ERP component linked to lexical-semantic processing is the N400, a negative-going potential peaking around 300–500 ms after word onset (Kutas and Federmeier, 2000). The N400 is modulated by semantic priming, with larger amplitudes observed for unprimed or semantically incongruent words

compared to primed or congruent words (Cocquyt et al., 2022; Chen et al., 2014; Khateb et al., 2010). This modulation, referred to as the N400 priming effect, reflects the relative ease of lexical-semantic retrieval and integration. The N400 component is observed across both visual and auditory modalities, though its peak manifests differently depending on modality: as a centroparietal peak in visual presentation and as a more frontally distributed plateau in auditory processing (Kutas and Van Petten, 1994). Auditory N400 responses often show a slight latency shift, attributed to the additional temporal demands of spoken language processing (Pawlowski et al., 2019).

Theoretical accounts of the N400 have proposed different explanations for its functional significance. One dominant view holds that the N400 reflects the processing cost of retrieving lexical-semantic representations from long-term memory (Lau et al., 2008). In contrast, alternative models suggest that the N400 reflects post-lexical integration, where a word's meaning is incorporated into the preceding semantic context (Hagoort, 2008). More recent perspectives propose that the N400 represents an interplay of both automatic and controlled processes, with varying contributions from automatic spreading activation (ASA), controlled prediction, and controlled semantic integration (Steinhauer et al., 2017). ASA occurs when a prime word automatically activates semantically related target words in memory, such as "dog" pre-activating "cat." Prediction involves the controlled pre-activation of specific lexical candidates based on contextual information. Semantic integration, in turn, refers to the incorporation of the target word's meaning within the broader semantic context, which occurs after lexical access. The relative contribution of these mechanisms to the N400 effect depends on several factors, including stimulus onset asynchrony (SOA) and the strength of semantic relationships. ASA effects are most prominent at short SOAs (<300 ms), while controlled prediction requires stronger contextual constraints and is diminished when SOA is too long (Hill et al., 2002; Steinhauer et al., 2017). Recent studies have also linked the N400 to predictive coding frameworks, suggesting that it reflects a mismatch between top-down lexical-semantic predictions and the actual sensory input (Eddine et al., 2024). In this view, the N400 indexes a prediction error signal, where more unexpected words generate larger negative amplitudes due to greater discrepancies between expected and observed input.

In the following sections, we will examine the neurophysiological basis of each component in greater detail. Specifically, we will explore the underlying sources of the MMN, P300, and N400, drawing from functional MRI, EEG

source localization, magnetoencephalography (MEG), and lesion studies. Furthermore, we will discuss how these components interact within broader functional networks involved in auditory processing, attention, and semantic memory. By reviewing the existing literature on the spatial and functional organization of these ERP components, we aim to provide a more comprehensive understanding of how the brain transitions from early auditory discrimination to higher-order language comprehension.

4.1.1 Mismatch Negativity (MMN)

In relation to the MMN, the available evidence on pure tone discrimination mainly points in the direction of two dominant sources, one in the bilateral temporal cortex and a second generator in the (right) frontal cortex (Doeller et al., 2003; Fulham et al., 2014; Kim et al., 2017; Koshiyama et al., 2020; Li et al., 2019b; Opitz et al., 2002; Auther et al., 2000; Rinne et al., 2005). Whereas the temporal generator has been repeatedly localized to regions in and surrounding the auditory cortex, uncertainty remains on the exact nature of the frontal MMN source. Reviewing the existing literature, Deouell (2007) observed that in particular the caudal and rostral inferior frontal gyrus (for later evidence, see Li et al. (2019b)), the medial frontal cortex and the right superior precentral or motor cortex (for later evidence, see Hsu et al. (2014); Li et al. (2019b); MacLean and Ward (2016)) were found to underlie the frontal MMN. Accordingly, Fulham et al. (2014) concluded that widespread areas in the frontal cortex can account for the anterior portion of the MMN. The diverse nature of the component-specific time windows that were investigated and of the auditory stimuli and contrasts used to elicit the MMN, each addressing specific subsets of the functional network governing stimulus discrimination, might in part explain these varying results (MacLean and Ward, 2016; Molholm et al., 2005). The temporal-frontal engagement has been widely interpreted as evidence for the predictive coding hypothesis (Garrido et al., 2009). Following this framework, bottom-up propagations of sensory input are compared to top-down predictions regarding the incoming stimuli, which are based on memory traces of preceding sounds. If a mismatch emerges between bottom-up and top-down propagations, a change is detected and the predictive model is adapted. In the context of predictive coding, the temporal generator is thought to be responsible for the bottom-up processing of auditory stimulus features. In turn, the frontal generator is thought to be activated when change detection occurs, subserving automatic reallocation of attention to the deviant stimulus and updating of the

predictive model (Fulham et al., 2014). Supporting evidence for this hypothesis is provided by source localization studies that established different time courses for the frontal and temporal MMN generator, whereby activation of the temporal source precedes frontal activation (Fulham et al., 2014; Kim et al., 2017; Koshiyama et al., 2020). Investigations into the functional networks of passive auditory discrimination have provided further insight into the interaction of the temporal and frontal MMN sources. That is, in addition to considerable evidence pointing to phase synchronization between the bilateral temporal and (pre)frontal regions during pure-tone discrimination (Choi et al., 2013; Hsiao et al., 2010; MacLean and Ward, 2014), Choi et al. (2013) observed cortical synchronization directed from the temporal to the frontal cortex. The anterior cingulate cortex (Jemel et al., 2002), the hippocampus (Duncan et al., 2009) and several subcortical structures including the cerebellum (Schall et al., 2003) and thalamus (Yago et al., 2001) have additionally been mentioned in relation to the MMN. Finally, Zhang et al. (2018) suggested that the MMN might originate from the activation of a fronto-temporo-parietal network, rather than a fronto-temporal network. The authors compared long-range cortical connections during MMN deviance processing in awake state versus under anesthesia, based on the idea that the latter would preclude high-level cognitive but not lower-level sensory processing. A reduced number of long-distance connections between prefrontal, temporal and centroparietal areas during deviant processing under anesthesia lead them to assume a role of these areas in MMN generation. Diffuse engagement of the parietal cortex has indeed been reported in relation to the MMN (Fulham et al., 2014), more specifically in the postcentral gyrus, the precuneus and the inferior to superior parietal cortex (Levänen et al., 1996; Marco-Pallarés et al., 2005; Molholm et al., 2005; Schall et al., 2003). Synchronization between ipsilateral temporo-parietal cortices during deviant processing, as observed by Hsiao et al. (2010), also supports this theory. Several hypotheses have been put forward regarding the role of the parietal cortex in MMN generation, including the facilitation of multisensory integration and P3a-related attention reallocation (Fulham et al., 2014). Since evidence in support of both theories is available, the literature remains inconclusive at present. While the evidence presented above exclusively stems from the study of tonal contrast, passive discrimination of speech stimuli essentially relies on a similar fronto-temporal network (MacLean and Ward, 2016). Nevertheless, a number of aspects specific to the processing of linguistic stimuli should be highlighted. Both investigations of MMN scalp topography (Alho et al., 1994; Partanen et al.,

2011; Tervaniemi et al., 1999), as well as MMN source reconstruction, point to left-lateralized processing of speech stimuli (overall: Sorokin et al. (2010); temporal source: Näätänen et al. (1997); Pulvermüller (2001); frontal source: Deouell (2007)). Considering the predictive coding hypothesis in relation to phoneme discrimination, top-down predictions are not solely based on the previously presented speech stimuli, but are also derived from language-specific memory traces (Näätänen et al., 1997). Stored in the language-dominant auditory cortex (Näätänen et al., 1997; Shestakova et al., 2002), recall of these traces might explain the generalized lateralization to the left hemisphere. Using the phase locking value, MacLean and Ward (2016) investigated cortical connectivity in relation to the discrimination of phonemic articulation place contrasts and provided evidence for a predominantly left-lateralized network to underlie both bottom-up and top-down MMN projections. The authors established interactions between the left superior temporal gyrus and the left inferior frontal gyrus (IFG; BA45 and BA47). Moreover, both the left (BA47) and right (BA45) IFG showed connections with the ipsilateral superior frontal cortex.

4.1.2 P300

Source imaging generally indicates that the P300 in relation to pure tone target detection, showing a characteristic centroparietal scalp distribution, originates from the activation of a broad bilateral fronto-parietal network (Wronka et al. (2012); for a review see Bocquillon et al. (2011) and Linden (2005)). Within this network, a number of areas have been frequently reported: (1) widespread areas across the parietal cortex, including the postcentral gyrus (Ehlers et al., 2015), the precuneus (van Dinteren et al., 2018), the supramarginal gyrus (Crottaz-Herbette and Menon, 2006) and the inferior parietal cortex (Crottaz-Herbette and Menon, 2006; Li et al., 2016); (2) the cingulate cortex (Peng et al., 2012; Sabeti et al., 2016; van Dinteren et al., 2018; Volpe et al., 2007; Linden, 2005); and (3) widespread (pre)frontal activity with evidence for the orbitofrontal cortex (van Dinteren et al., 2018), the inferior frontal cortex (Ehlers et al., 2015; Li et al., 2016), the middle frontal gyrus (Ehlers et al., 2015; Li et al., 2016) and the precentral gyrus (Crottaz-Herbette and Menon, 2006; Ehlers et al., 2015). In addition to the source reconstruction data, a number of studies have investigated neural synchronization at sensor level, thus providing insight into the interaction of P300 generators. In this respect, phase synchrony between (temporo)frontal and (temporal-)posterior electrodes was evidenced during active auditory deviant processing (Choi et al.,

2010, 2015). Alternatively, Volpe et al. (2007) described early activation in frontal and cingulate areas, followed by increased parietal activation in the late P300 time window. In addition to the fronto-parieto-cingulate network, some evidence points to the role of a number of subcortical structures, specifically the basal ganglia and thalamus (Crottaz-Herbette and Menon, 2006), the cerebellum (Crottaz-Herbette and Menon, 2006) and hippocampus (Linden, 2005; Volpe et al., 2007) in active auditory discrimination. In view of the fronto-parieto-cingulate network governing P300 generation, this component is commonly linked to the process of stimulus categorization (Kok, 2001), and more specifically the attentional and working memory related aspects of this process. In this context, (Bledowski et al., 2004) associated the parietal P300 generator with top-down attentional processes that modulate the categorization of task-specific stimuli. That is, these processes facilitate the comparison of the sensory input to the established working memory representation. The posterior cingulate cortex has likewise been linked to the top-down regulation of attentional focus (Leech and Sharp, 2014). Alternatively, Sabeti et al. (2016) attributed activation of the cingulate cortex during active sound categorization to working memory engagement.

As the P300 indexes a late stage of information processing, the extent to which it is subject to sensory stimulus modality and specific stimulus characteristics is a matter of debate. Whereas certain evidence points to the P300 being a purely cognitive component independent of sensory modality (Linden et al., 1999; Peng et al., 2012; Sabeti et al., 2016), other studies suggest that the component contains an additional modality-specific aspect, as they identified activation of auditory or visual cortices in the P300 time window (Bledowski et al., 2004; Moores et al., 2003). In this context, Crottaz-Herbette and Menon (2006) demonstrated activation of Heschl's gyrus during auditory P300 target detection, as well as strong connectivity between the auditory cortex to the cingulate gyrus.

Only a limited number of studies have explored the P300 in relation to speech stimuli. Investigating auditory target detection using monosyllabic word stimuli, Geal-Dor et al. (2006) evidenced greater P300 amplitudes over left compared to right electrode sites in young individuals. Correspondingly, Criel et al. (2023) found maximal P300 strength over left and midline electrode sites in relation to active phoneme categorization based on an articulation place contrast. Similar results were also reported by Breier et al. (1999) and Justen and Herbert (2018). This raises the question of whether these topographic properties

stem from a specialization of the commonly described bilateral fronto-parietal network to the left hemisphere in relation to language processing.

4.1.3 N400

Areas in the frontal and temporal cortex have been demonstrated to govern semantic priming. A considerable amount of proof stems from (mostly event-related) functional magnetic resonance imaging (fMRI). Reviews by Holderbaum (2019) and Lau et al. (2008) point to two areas in specific to support automatic and controlled priming operations: the left MTG and the left IFG. Consistent activation of the posterior part of the MTG, and by extension adjacent areas in the superior (STG) and inferior (ITG) temporal gyrus, has been documented for unrelated compared to related target processing at both short and long SOAs. Activation of the IFG, especially the pars triangularis (BA 45) and pars orbitalis (BA 47), is specifically observed during semantic priming at a long SOA. Electroencephalography (EEG) and magnetoencephalography (MEG) source reconstruction of the scalp-recorded N400 potential has confirmed the presence of a dominant generator in the temporal lobe, governing lexical-semantic retrieval in a priming set-up (Geukes et al., 2013; Khateb et al., 2010). These reports, however, are less uniform on the precise location of this generator. In accordance with fMRI research, several studies identified an activation component in the left MTG, STG and ITG (Ghosh Hajra et al., 2018; Khateb et al., 2010; Matsumoto and Kakigi, 2014; Silva-Pereyra et al., 2003). Performing electrocorticographic (ECoG) recordings in a group of individuals with epilepsy, Khachatryan et al. (2019) likewise designated the left superior and middle temporal gyri as the main generator region for the N400. Alternatively, combining evidence from MEG source localization and fMRI, Lau et al. (2013, 2016) attributed the N400 to an activation cluster in the ATL at both short and long SOAs. Apart from the temporal generator area, EEG and MEG studies point to additional generators in the left inferior temporal gyrus (Ghosh Hajra et al., 2018; Matsumoto and Kakigi, 2014), the left insula (Khateb et al., 2010), the bilateral middle or superior frontal gyrus (Khateb et al., 2010; Silva-Pereyra et al., 2003), the posterior cingulate cortex (Khateb et al., 2010) and the putamen (Khateb et al., 2010). Combined results of fMRI, EEG and MEG research thus converge to a left dominant temporo-frontal network to underly semantic priming, albeit that the exact locations of these generator areas are still under debate. The enhanced engagement of frontal and temporal cortices in the retrieval of unprimed compared to primed words has generally been

interpreted in light of the hypothesis that the N400 (at least partially) reflects the facilitated access of primed lexical-semantic items (Lau et al., 2008). The access and retrieval of unprimed targets (i.e., targets preceded by an unrelated prime) requires more engagement of the semantic control system, which resides in posterior middle temporal and inferior frontal cortices (Ralph et al., 2017). At short SOAs, only automatic processes aid the retrieval of semantic representations, which translates to the activation of the temporal cortex. At long SOAs, frontal cortices additionally mediate the top-down retrieval (anterior IFG) and selection (posterior IFG) of lexical-semantic representations (Lau et al., 2008).

The above-discussed literature purely focused on areas showing increased activation during semantic priming. Some researchers have further explored the functional interaction between frontal and temporal regions that are engaged in semantic priming. Based on functional connectivity investigation of source localized EEG and MEG signals, Matsumoto et al. (2014) and Kujala et al. (2012) found evidence for enhanced synchronization between frontal and temporal N400 generators for the processing of related compared to unrelated target words. Matsumoto et al. (2014) identified a bidirectional causal flow between the left IFC and ITC in a sublimal (i.e., masked priming at short SOA) priming task. Adopting a categorical priming paradigm with a long SOA, Kujala et al. (2012) identified enhanced coherence between the left superior temporal, right frontotemporal and right inferior temporal cortex. The authors hypothesized that behavioural priming effects and reduced activation of frontal and temporal areas observed for primed compared to unprimed items, may result from a more efficient information transmission within the neural network in this condition, as manifested in enhanced neural synchronization. Also, some fMRI investigations targeted priming-related functional connectivity. Roelke & Hofmann (2020) demonstrated enhanced functional synchronization between the left inferior frontal cortex on the one hand, and the fusiform gyrus and the anterior cingulate cortex during the processing of word pairs with low compared to high semantic similarity.

4.1.4 The present study

While the neural generators of the MMN, P300, and N400 components have been explored in previous research, several questions remain regarding their precise cortical origins and functional network interactions, particularly in the context of speech and semantic processing. For the MMN and P300, the exact

source of the frontal MMN remains uncertain, as well as the precise locus of the frontal and parietal P300 generators. Moreover, the majority of existing studies have focused on tonal stimuli rather than speech, leaving open the question of whether phoneme discrimination and categorization engage distinct neural networks. Additionally, the temporal dynamics and interregional interactions underlying these components remain poorly understood. Similarly, while some source estimation studies have been conducted for the N400, the results are inconsistent, and little is known about the connectivity between its generator regions. Most prior studies have examined thematic semantic relations, leaving it unclear whether taxonomic relations engage a partially distinct network.

The present study aimed to enhance our understanding of the cortical sources and functional networks associated with the MMN, P300, and N400 components. Specifically, we investigated 1) the cortical generators of the MMN and P300 in relation to phoneme discrimination and categorization, as well as those of the N400 in relation to the processing of taxonomic semantic relations, and 2) the functional connectivity between cortical regions for each component, characterizing the interactions between generator areas during phoneme and semantic processing.

To achieve this, high-density EEG recordings were obtained during two paradigms: an auditory oddball task with a phonemic articulation place contrast (for MMN and P300) and an auditory categorical priming task (for N400). Component-specific cortical activity was reconstructed using exact low-resolution brain electromagnetic tomography (eLORETA; Pascual-Marqui et al. (2011)). This method minimizes localization errors, particularly for deeper sources (Jatoi et al., 2014), and reduces false positive connectivity estimates (Pascual-Marqui et al., 2018). Given the inherent limitations of EEG source reconstruction due to the inverse problem and the smoothing effects of the scalp and skull, spatial resolution remains constrained. However, recent work suggests that eLORETA provides an estimated spatial resolution of approximately 2 cm for ERP components, allowing for the identification of key cortical regions involved in cognitive processing (Depuydt et al., 2024).

We further examined the temporal dynamics of neural activation by segmenting reconstructed activity into early, middle, and late component-specific time windows. Functional connectivity was analyzed in source space by computing maximal cross-correlation between reconstructed signals across 68 cortical regions, providing insights into task-dependent neural synchronization patterns during phoneme discrimination, categorization, and semantic process-

ing. By integrating source estimation and functional connectivity approaches across these ERP components, this study aims to provide a more comprehensive understanding of the neural mechanisms underlying phoneme perception and lexical-semantic processing.

4.2 Materials and Methods

4.2.1 Participants

A total of 60 Dutch-speaking adults (30 men, 30 women) participated in this study. An equal number of male (n = 10) and female (n = 10) participants was recruited in each of the following age ranges: 20-39 years, 40-59 years and 60+ years. The age of the participants reached from 23 to 80 years, with the mean age equal to 49.3 years (SD = 16.84). A wide, balanced sample was constructed based on sex and age in order to obtain results representative for the broad population.

Included participants were right-handed, as objectified by a score ≥ 8 on the Dutch Handedness Inventory (DHI; (Van Strien, 1992)). Participants were screened for cognitive impairment by means of the Montreal Cognitive Assessment (MoCA; (Nasreddine et al., 2005)), where a cut-off score of 26/30 was adopted for inclusion (Thissen et al., 2010). General language function was assessed by means of the Dutch version of the Comprehensive Aphasia Test (CAT-NL; (Swinburn et al., 2014)). A score below the cut-off value for one or more test items was adopted as an exclusion criterion. Moreover, participants did not report any hearing impairments, described a normal or corrected to normal vision, reported a negative history of any neurological or psychiatric disorders, and did not have a history of any developmental disorders. Table 4.1 provides an overview of demographic variables, as well as the score on the DHI, MoCA and CAT-NL, for the participants grouped by age and sex. This study was approved by the Ghent University Hospital ethical committee (ONZ-2022-0127). All participants gave their written informed consent.

4.2.2 Electrophysiological recording

Experimental procedure

Participants were subjected to two auditory oddball paradigms containing a phonemic contrast and an auditory categorical priming task. First, an inatten-

Table 4.1. Demographic details on the participants, grouped by age and sex

	20-39 years		40-59 years		60+ years	
	Male	Female	Male	Female	Male	Female
n	10	10	10	10	10	10
Age (years)	30.2 (5.31)	29.2 (4.32)	49.8 (4.39)	49.9 (6.86)	68.4 (4.50)	69.0 (5.89)
Education level[a]	1.6 (0.84)	1.2 (0.42)	1.9 (0.99)	1.6 (0.70)	2.3 (1.06)	2.3 (0.67)
DHI (/10)	9.8 (0.63)	9.8 (0.63)	9.6 (0.84)	9.8 (0.42)	9.9 (0.32)	10.0 (0.00)
MoCA (/30)	27.6 (1.51)	27.9 (0.74)	28.2 (1.62)	28.4 (1.65)	27.7 (1.16)	27.6 (1.43)
CAT-NL cognition (/40)	38.3 (2.16)	38.5 (1.43)	38.9 (1.20)	37.9 (1.37)	37.3 (1.34)	38.0 (1.56)
CAT-NL language comprehension (/19)	17.1 (2.33)	18.6 (0.70)	17.3 (2.06)	17.2 (1.48)	16.4 (2.12)	17.7 (0.48)
CAT-NL language production (/35)	33.9 (1.37)	34.5 (0.71)	34.3 (0.82)	34.4 (0.70)	33.1 (1.01)	33.3 (1.25)

Reported values are mean (standard deviation); DHI = Dutch Handedness Inventory; MoCA = Montréal Cognitive Assessment; CAT-NL = Comprehensive Aphasia Test, Dutch Translation.
[a] Education level was rated on a four-point scale: 1 = higher education-academic, 2 = higher education-nonacademic, 3 = higher secondary school, 4 = lower educational school.

tive oddball paradigm, eliciting the MMN, was administered, followed by an attentive paradigm eliciting the P300 to investigate phoneme perception. In both of these paradigms, the same phonemic stimuli, differing only in terms of articulation place, were used. The standard stimulus [bə] was presented with an 80% probability while the deviant stimulus [gə] was presented with a probability of 20%. Both stimuli had a duration of 250 ms. The stimuli used in the current study were modified from the experiments of Aerts et al. (2013), who generated the stimuli from NeXTeNS.

The inattentive oddball paradigm (MMN) comprised 600 standard and 150 deviant stimuli, which were presented with a 500 ms inter stimulus interval (ISI). During the paradigm, participants were instructed to watch a silent movie (Donald Duck). The total duration of the inattentive oddball task was approximately 7 minutes. The attentive oddball paradigm (P300) consisted of 160 standard and 40 deviant phonemes, presented with a 2000 ms ISI, leading to a total duration of 8 minutes. The actual paradigm was preceded by a practice block, containing 16 standard and 4 deviant stimuli. In order to assess stimulus categorization, participants were instructed to press a button on a Chronos response box (Psychology Software Tools, Pittsburgh, PA, USA) when hearing a deviant stimulus.

The auditory categorical priming task used in this work was adapted from Hagoort et al. (1996) by Cocquyt et al. (2022). The task consisted of 120 Dutch word pairs, each including a prime and target word. In half of the pairs, the prime and target word were semantically related by being members of the same semantic category (e.g., cat – horse). In the other 60 pairs, the prime and target word were unrelated in meaning (e.g., pink – coffee). None of the word pairs were characterized by a thematic relation. To control for the ef-

fect of psycholinguistic variables, target words in the related and unrelated condition were matched for word frequency, phonological length, the number of phonological neighbours, concreteness, imageability, age of acquisition, valence, arousal, dominance and duration. For additional information on the stimuli, we refer to Cocquyt et al. (2022). The prime and target words were presented with a stimulus onset asynchrony (SOA) of 1800 ms, while the inter stimulus interval (ISI) between the two words ranged from 830 to 1520 ms to account for variations in word length. Following the presentation of the target word, participants were required to assess the semantic relatedness of the prime and target words through a button press response. A delayed response was adopted to avoid interference of movement artefacts and response-related potentials (Van Vliet et al., 2014). Button presses were again registered by the Chronos response box, on which participants were instructed to press a green button in case of a semantically related word pair and a red button in case of an unrelated pair. Following the button press, an inter trial interval (ITI) of 2500 ms was applied prior to the start of a new trial. The 120 trials were administered over seven blocks, each separated by a pause. The experiment was preceded by a practice block consisting of eight trials (four related, four unrelated pairs) to familiarize subjects with the task procedure. The time required to complete this task ranged between 15 and 20 minutes.

The auditory stimuli in all paradigms were delivered binaurally at the same comfortable hearing level in all participants using ER1-insert earphones, and E-Prime 3.0 (Psychology Software Tools, Pittsburgh, PA, USA) was used to present the different stimuli at random. Eye movement artifacts were limited by asking the participants to focus on a white fixation cross presented on a black background during the auditory stimulus presentation.

EEG Recording

EEG was recorded continuously from 128 electrode sites using an EasyCap electrode cap (Brain Products, Germany). The ground and online reference were recorded at AFz and FCz, respectively. Using an abrasive electrolyte gel (Abralyt 2000, EasyCap), impedances were kept below 20 kΩ. A BrainVision BrainAmp amplifier (Brain Products, Germany) was used to acquire the EEG signals, which were digitized with a sampling frequency of 500 Hz. To record the data, the BrainVision Recorder software was used (Brain Products, Germany).

4.2.3 Electrophysiological data analysis

Data preprocessing

Similar preprocessing was applied to the MMN, P300 and N400 data. For the P300 and the N400 data, the practice block preceding the experimental trials were excluded from analysis. First, bad electrode channels were automatically detected using different noisy channel detection methods implemented in the PREP pipeline (Appelhoff et al., 2022; Bigdely-Shamlo et al., 2015). The four primary measures used in this pipeline are extreme amplitudes (deviation criterion), lack of correlation with any other channel (correlation criterion), lack of predictability by other channels (predictability criterion), and unusual high frequency noise (noisiness criterion). The electrodes marked as bad by the algorithm were ignored in the subsequent analysis. The data were band-pass filtered using a zero phase shift Butterworth filter with half-amplitude cut-off frequencies of 0.3 Hz and 30 Hz and a 12 dB/octave slope. Also a 50 Hz notch filter was applied to the data to remove power line noise. Independent component analysis using the FastICA algorithm (Ablin et al., 2018) was performed for eye blink and horizontal eye movement artifact rejection. The number of independent components calculated per subject ranged between 117 and 128 (mean 124, std 2.8), as bad electrode channels were excluded in the calculation, and between 2 and 6 (mean 3, std 1.2) of the components have been identified to contain artefacts. In case bad electrode channels were identified and excluded in step 1, these channels were interpolated. Subsequently, data were re-referenced to an average common reference. The continuous EEG was segmented in 600 ms long epochs (-100 ms to 500 ms) for the MMN, 1500 ms long epochs (-300 to 1200 ms) for the P300 and the N400. Baseline correction was performed using a 100 ms prestimulus window for the inattentive paradigm and a 300 ms prestimulus window for the attentive paradigm and the categorical priming paradigm. Artifact rejection using the following criteria was applied: 75 μV maximum gradient criterion; 100 μV minimal/maximal amplitude criterion; 150 μV maximum difference criterion; 0.5 μV low activity criterion during 100 ms. Also trials for which in incorrect response was given to the stimuli were removed (P300 and N400). For the inattentive paradigm, these criteria led to the rejection of between 0 and 92 trials (mean 30, std 38) out of the 750 trials in total, in the attentive paradigm between 0 and 33 (mean 4, std 6.9) out of the 200 trials were excluded and finally in the categorical priming task between 0 and 43 trials (mean 14.8, std 9.5) were rejected.

Standard and deviant trials (MMN and P300), and related and unrelated trials (N400), were segmented separately in view of source reconstruction and functional connectivity calculation.

ERP Level Analysis

To investigate wheter the administered oddball tasks and the priming task did elicit the expected MMN, P300 and N400 effects in our participant sample, we extracted amplitude values from the scalp-recorded ERP signals. For the MMN, mean amplitude values in response to the standard and deviant condition were extracted in a 100–300 ms time window at six frontocentral electrode sites (F3, Fz, F4, C3, Cz, C4). For the P300, mean amplitudes for standard and deviant waveforms were extracted in a 300–800 ms time window at three parietal electrodes (P3, Pz, P4). Finally, also the mean amplitude of the N400 in response to the related and unrelated condition was extracted in the 400-800 ms time window at three central electrode sites (C3, Cz, C4). A paired samples t-test was performed to assess the presence of the MMN, the P300 effect and the N400 effect by comparing the average of the mean amplitudes at the different electrode sites between the two conditions.

ERP source reconstruction

Forward modeling: Source analyses were performed using the MNE-Python software package (v1.2.1) (Gramfort et al., 2013). As no individual MRI images were available, Freesurfer's standard template MRI subject fsaverage was adopted to create the EEG forward model (Fischl, 2012). A three-layer head model was created using the inner skull, outer skull, and outer skin as boundaries for the different compartments. Default electrical conductivity values were assigned to the scalp (0.3 S/m), skull (0.006 S/m) and brain (0.3 S/m) compartments of the model. Approximately 8200 equivalent current dipoles were distributed on the cortical surface, resulting in a spacing of about 4.9 mm between the dipoles. Dipole orientations were fixed to be normal to the cortical surface throughout the study. Finally, the EEG leadfield matrix was calculated using the boundary element method (BEM).

Inverse modeling: The source reconstruction was performed for each subject and each condition (standard and deviant, or related and unrelated) separately using the exact Low-Resolution Tomography (eLORETA) inverse

method (Pascual-Marqui et al., 2011). As the signal to noise ratio (SNR) of the signal is affected by the number of trials used for averaging, the number of epochs was equalized for both conditions before averaging and source reconstruction. In further analysis, the absolute magnitude of the dipoles, the current source density (CSD), was investigated, disregarding the orientation information of the dipoles. As indicated by Fulham et al. (2014), the CSD at each dipole location is not only proportional to the ERP, but also to noise. Therefore, we corrected for differences in noise conditions across subjects by converting the CSD signals to z-scores. This was done by creating a noise-signal for each subject using 50% of the standard/related trials and 50% of the deviant/unrelated trials. Of each set, the polarity of half of the trials was switched to obtain a signal that represents the noise. This resulted in a signal containing no ERP response but only noise with similar statistical properties as the original signals, which was then source reconstructed. This process was repeated 100 times to obtain mean and standard deviation values for the CSD noise bias for each subject separately, which was then used for the normalization of the original CSD signals in both conditions.

Source clustering: Significant effects of interest were explored in three separate time windows of 50 ms through statistical clustering analysis in source space. The early, middle and late time windows were selected based on the 25%, 50% and 75% fractional area latency of the MMN, P300 and N400 grand average difference wave of all participants in a broad time window of 100-300 ms, 300-800 ms and 400-800 ms, respectively. For the MMN, the 140-190 ms, 190-240 ms and 240-290 ms time windows were investigated. Clustering analysis for the P300 was performed in the 370-420 ms, 460-510 ms and 590-640 ms time windows, and for the N400 in the 460-510 ms, 520-570 ms and 630-680 ms time windows. These different time windows allowed us to investigate how the sources underlying the ERP components change as a function of time. A data-driven approach was applied by selecting these time windows based on the fractional area latency of the grand average component, thus assuring that the selected 50 ms time windows were of interest for early, middle and late processes underlying the ERPs. The data was averaged over the time dimension for each participant in each of the different windows. Two different approaches were used to test for significant differences in source activation between the standard and deviant condition. The first approach consisted of a cluster-based non-parametric permutation test, in which the

significance probability was computed under the permutation distribution using the Monte-Carlo method (Maris and Oostenveld, 2007). First, paired t-tests were performed for each dipole separately. Then, the dipoles for which the obtained t-value proved larger than the imposed threshold were selected as cluster candidates. In this study, a data-driven approach was used to determine the threshold, so that the 5% of the dipoles with the strongest differences were selected. In the next step, the selected dipoles were grouped in potential clusters based on spatial adjacency, and the cluster size was determined for each cluster. To form the permutation distribution, the standard and deviant conditions were randomly reassigned across all participants 5000 times and for each of these permutations, the largest cluster size was calculated. Finally, the differences between the conditions were considered significant if the cluster size fell into the highest 5% of the distribution. While the cluster-based permutation test controls the multiple comparison problem and at the same time maximizes power, no inference is made over individual dipoles. Consequently, no statements about the spatial location and extent of the significant effect between both conditions based on the cluster locations will be completely accurate. Therefore, a second approach to test for significant differences in source activation between both conditions was used. Here, paired t-tests are performed for each dipole separately, after which the obtained p-values are corrected for multiple comparison with False Discovery Rate (FDR) (Genovese et al., 2002).

Source Data extraction: To investigate activation changes in sources underlying the MMN, P300 and N400, regions of interest for further analysis were defined based on both the identified activation clusters and dipoles identified to have the strongest significant differences between both conditions. To this end, the cerebral hemispheres were parcelated in 34 regions of interest (ROIs) each, using the Desikan-Killiany atlas (Desikan et al., 2006). For each activation cluster identified in relation to the MMN, P300 or N400, the ROI comprising the majority of cluster dipoles was selected. For each selected ROI, as well as for the contralateral homologues ROI, the time series for both the standard and deviant, or related and unrelated conditions were extracted from the reconstructed signal by applying principle component analysis (PCA) decomposition to the time courses within the ROI, and using the first mode of the decomposition as the representative time course. From these ROI-specific time series, we extracted the mean CSD in the early, middle and late time

windows (MMN: 140-190 ms, 190-240 ms, 240-290 ms; P300: 370-420 ms, 460-510 ms, 590-640 ms; N400: 460-510 ms, 520-570 ms, 630-680 ms). Additionally, the mean CSD in the large time window was calculated for each ROI identified in relation to the MMN (100-300 ms), P300 (300-800 ms) and N400 (400-800 ms) in both hemispheres.

Functional connectivity analysis

The functional networks underlying phoneme discrimination (MMN) and categorization (P300), and categorical priming (N400) were mapped based on the 68 ROIs predefined by the Desikan-Killiany atlas (Desikan et al., 2006). For each participant and each condition, we extracted the time series for the different ROIs from the source reconstructed data using PCA decomposition, selecting the first mode of the decomposition as the representative time series. The functional networks were then created using the maximal cross-correlation as functional connectivity measure. The cross-correlation function was calculated between all ROI-pairs, limiting the signals to the time windows of interest for each ERP component (MMN: 100-300 ms, P300: 300-800 ms, N400: 400-800 ms). The correlation coefficients were then calculated by normalizing the cross-correlation function by the energy of each signal. The connection strength in the functional network was set to the maximal cross-correlation coefficient for which the corresponding absolute time lag was larger than 6 ms and smaller than 100 ms. This restriction on the time lags was imposed to reduce the effect of instantaneous interactions within the network due to source leakage or the spreading of the CSD signals over multiple ROIs. Finally, the values within each functional connectivity network were normalized by subtracting the mean and dividing by the standard deviation.

To identify significant differences between the networks obtained for the standard and deviant, or related and unrelated conditions, the Network Based Statistic (NBS) method was used (Zal, 2010). This method identifies significant network components that are related to the experimental effect and is based on a permutation approach. In the first step, paired t-tests are performed for each connection between the conditions and connections exceeding the chosen threshold of $p < 0.001$ are selected. The algorithm then identifies networks within the set of selected connections, after which permutation-based univariate statistical testing is performed to identify significant networks based on size. This approach offers a gain in statistical power compared to analyzing

each connection individually. For more details about the NBS approach, we refer the reader to Zal (2010).

To quantify and describe the obtained significant network components, we subdivided the 34 ROIs of each hemisphere into five groups: Frontal, Temporal, Parietal, Occipital and Cingulate (cf. appendix A.1). The number of connections between and within the different groups in the significant network component was then calculated. To account for the differences in the number of ROIs per group, the number of connections was divided by the number of possible connections between and within the groups, allowing us to identify the relative importance of each group to the differences in functional networks between the conditions.

4.3 Results

4.3.1 Behavioral Results

In the P300 task, mean behavioral accuracy was high for the entire participant group, with 91.67% for standard and 94.08% for deviant trials. In the semantic priming task, participants were more accurate in identifying related (95.8%) compared to unrelated (97.2%) word pairs, demonstrating a facilitation effect in processing meaningful associations. Notably, all participants maintained accuracy above 75% for both tasks, confirming overall reliable task performance.

4.3.2 ERP Results

MMN

A repeated-measures ANOVA (rmANOVA) revealed the presence of a MMN effect in the 100–300 ms time window in the overall participant sample (main condition effect: $F(1,57) = 155.494$; $p<0.001$), as well as each separate age group (condition by age group interaction effect: $F(2,57)=7.307$; $p=0.001$). Across the entire participant group, MMN amplitude in response to deviant trials was on average 0.451 μV (95% CI=0.379–0.524) more negative compared to standard trials. Post-hoc pairwise comparison (Bonferroni) revealed the same pattern for each separate age subgroup. The MMN effect observed in the current participant sample is visualized at frontocentral sites in Figure 4.1

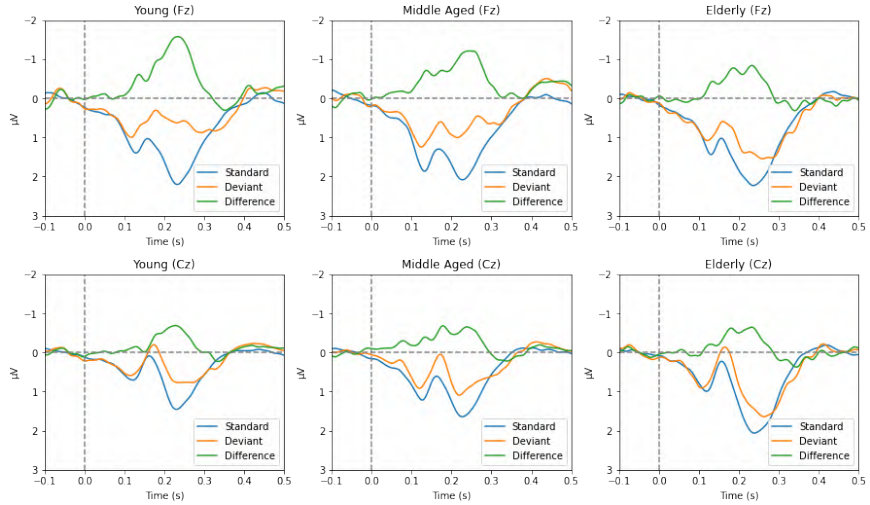

Figure 4.1. MMN in response to standard and deviant sound, as well as the difference, at electrodes Fz and Cz for participants recruited in a young (20-39 years), middle-aged (40-59 years) and elderly(60+ years) age range

P300

Based on an rmANOVA, the presence of a P300 effect was confirmed in the 300–800 ms time window in the overall participant sample (main condition effect: $F(1,57)=145.188$; $p<0.001$), as well as the young, middle-aged and elderly group participants were recruited in based on their age (condition by age group interaction effect: $F(2,57)=2.806$; $p=0.069$). In the overall group, the amplitude in response to standard sounds was on average 1.811 μV (95% CI=1.510–2.112) smaller compared to deviant sounds. Post-hoc pairwise comparison of the marginally significant age group by condition interaction effect revealed that the same pattern was observed in each of the three subgroups based on the age range participants were recruited in ($p<0.001$ in all). Figure 4.2 provides a visualization of the P300 effect at parietal electrode sites.

N400

The presence of the N400 effect at the central electrode sites in the 400-800 ms window in both young, middle-aged and elderly participants was indicated by a rmANOVA, showing a main effect of condition ($F(1,57) = 47.166$; $p < 0.001$) but no main age group effect ($F(2,57) = 0.488$; $p = 0.616$) or condition by age group interaction effect ($F(2,57) = 0.194$; $p = 0.824$). N400 amplitude was

Figure 4.2. P300 in response to standard and deviant sound, as well as the difference, at electrode Pz for participants recruited in a young (20-39 years), middle=aged (40-59 years) and elderly(60+ years) age range

on average 0.996 µV more negative for unrelated compared to related trials. Likewise, a univariate ANOVA, showing no main effect of age group ($F(2,57) = 0.973$; $p = 0.384$) on the onset latency of the N400 difference wave, indicated a comparable onset for the N400 effect across age groups. The time series of the N400 (effect) as recorded at the central scalp electrodes, are shown in Figure 4.3.

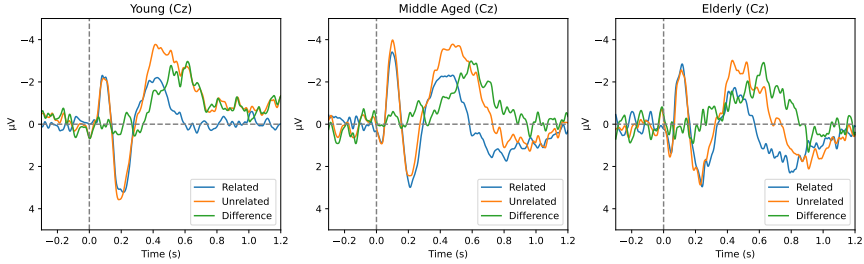

Figure 4.3. N400 in response to standard and deviant sound, as well as the difference, at electrode Cz for participants recruited in a young (20-39 years), middle=aged (40-59 years) and elderly(60+ years) age range

4.3.3 Source Reconstruction

MMN

Results of eLORETA source reconstruction of the time series in the broad time window (100-300 ms) in response to the standard and deviant condition, as well as the difference (deviant minus standard), are visualized in Figure 4.4. For each subject, the source reconstruction explained between 32.5% and 83.7% of the variance (mean 68.8%, std 9.5%). In both the early (140-190

ms), middle (190-240 ms) and late (240-290 ms) time windows, dipole clusters contributing to MMN generation were identified based on spatial clustering (Figure 4.7). In the early time window, both the cluster-based permutation test and the paired t-tests followed by fdr-correction revealed a significant difference between the standard and deviant conditions. This difference was most pronounced in the left insula and in the right frontal lobe. Significant differences between both conditions were also identified in the middle time window, mainly in the left parietal cortex, the left temporal cortex and the right frontal cortex. Finally, in the late time window, differences were identified in the left insular cortex and in the right frontal, insular and temporal cortex. Similar results were found using dipole-level statistical comparisons followed by fdr-correction (Figure A.1).

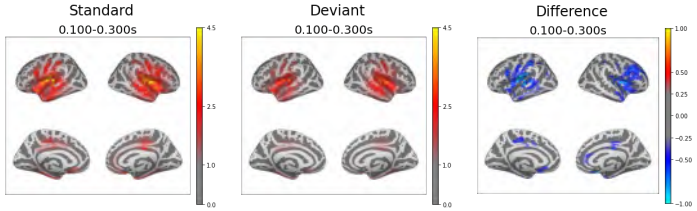

Figure 4.4. eLORETA source reconstruction results of the MMN in response to the standard condition and deviant condition, and the difference between both in the 100-300 ms time window.

P300

The results of source reconstruction of the P300 time series in response to the standard condition, deviant condition and difference between both in the 300-800 ms broad time window using eLORETA are shown in Figure 4.5. In this case, the source reconstruction explained between 32.1% and 81.5% of the variance (mean 68.4%, std 7.3%) in each subject. Spatial clustering and paired t-tests followed by fdr-correction in the early (370-420 ms), middle (460-510 ms) and late (590-640 ms) time windows revealed significant differences to underlie P300 generation (Figure 4.8 and A.2). In the early window, these differences were most pronounced in the left cingulate cortex, in the left frontal cortex, in the right cingulate cortex and in the right parietal cortex. In the middle time window significant differences were localized to the left cingulate, right cingulate, right parietal and right occipital cortex. Lastly, the left and

right cingulate and right parietal cortex were identified to contain significant differences between both conditions in the late window.

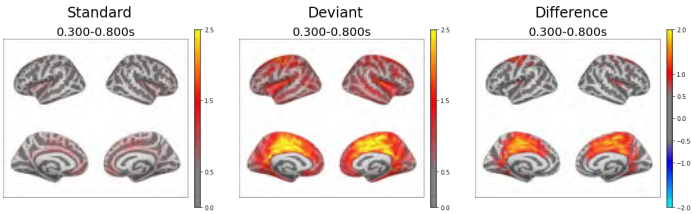

Figure 4.5. eLORETA source reconstruction results of the P300 in response to the standard condition and deviant condition, and the difference between both in the 300-800 ms time window.

N400

Results of eLORETA source reconstruction for related trials, unrelated trials and the difference, in the broad time window (400-800 ms) are visualized in Figure 4.6. Spatial clustering in early (460-510 ms), middle (520-570 ms) and late (630-680 ms) component-specific time windows revealed five significant dipole clusters underlying the generation of the N400 effect (Figure 4.9). In the early time window, a combination of cluster-based permutation testing and fdr-corrected paired t-tests (Figure A.3) revealed a difference between the related and unrelated condition, mainly located in the left lateral orbitofrontal cortex, the left pars opercularis and left pars triangularis of the inferior frontal gyrus, and the left precentral gyrus. In the middle time window, significant activation differences between related and unrelated trials were predominantly identified in the left posterior cingulate cortex. In the late time window, no condition effect could be observed.

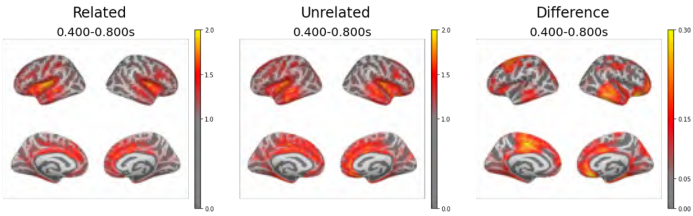

Figure 4.6. eLORETA source reconstruction results of the N400 in response to the standard condition and deviant condition, and the difference between both in the 400-800 ms time window.

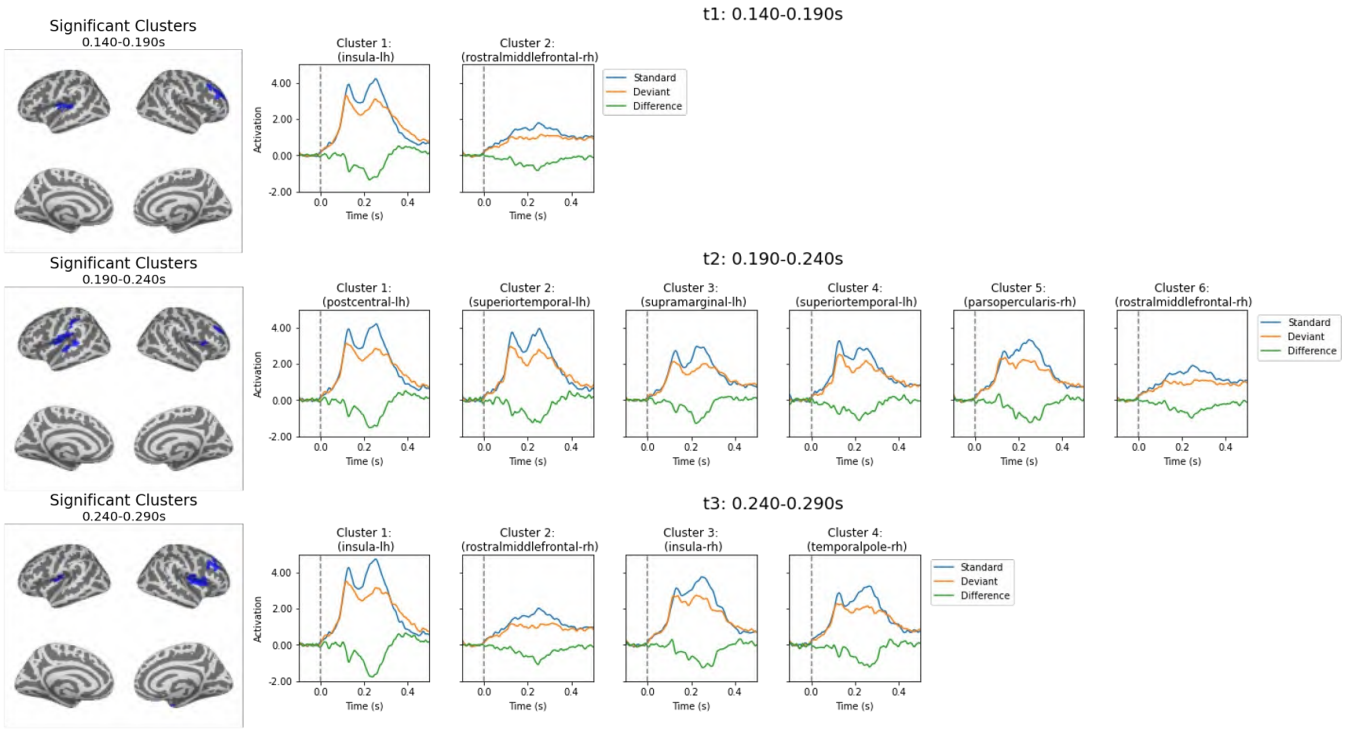

Figure 4.7. Results of clustering analysis on the eLORETA source reconstruction of the MMN difference in the early (140-190 ms), middle (190-240 ms) and late (240-290 ms) time window. The time series of each significant cluster, as averaged over all dipoles of the cluster, is shown.

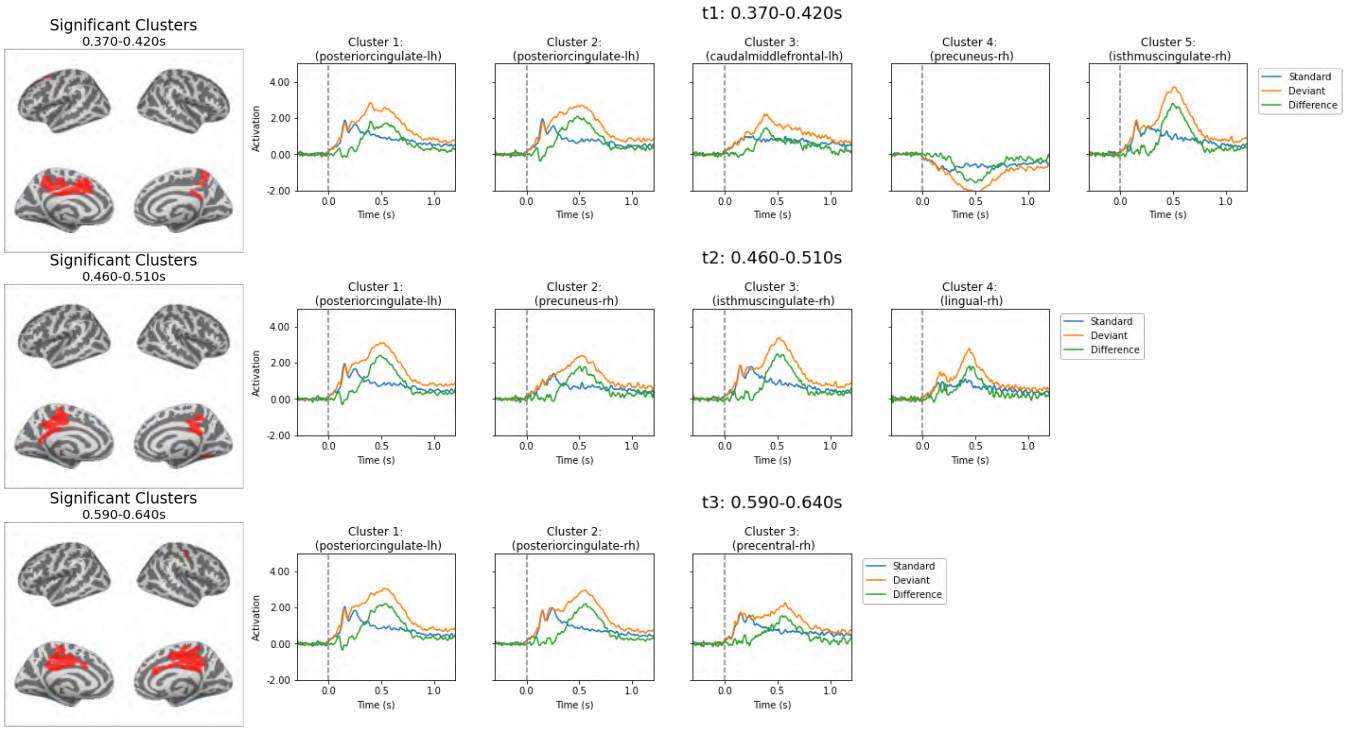

Figure 4.8. Results of clustering analysis on the eLORETA source reconstruction of the P300 difference in the early (370-420 ms), middle (460-510 ms) and late (590-640 ms) time window. Also the time series of each significant cluster, as averaged over all dipoles of the cluster, is shown.

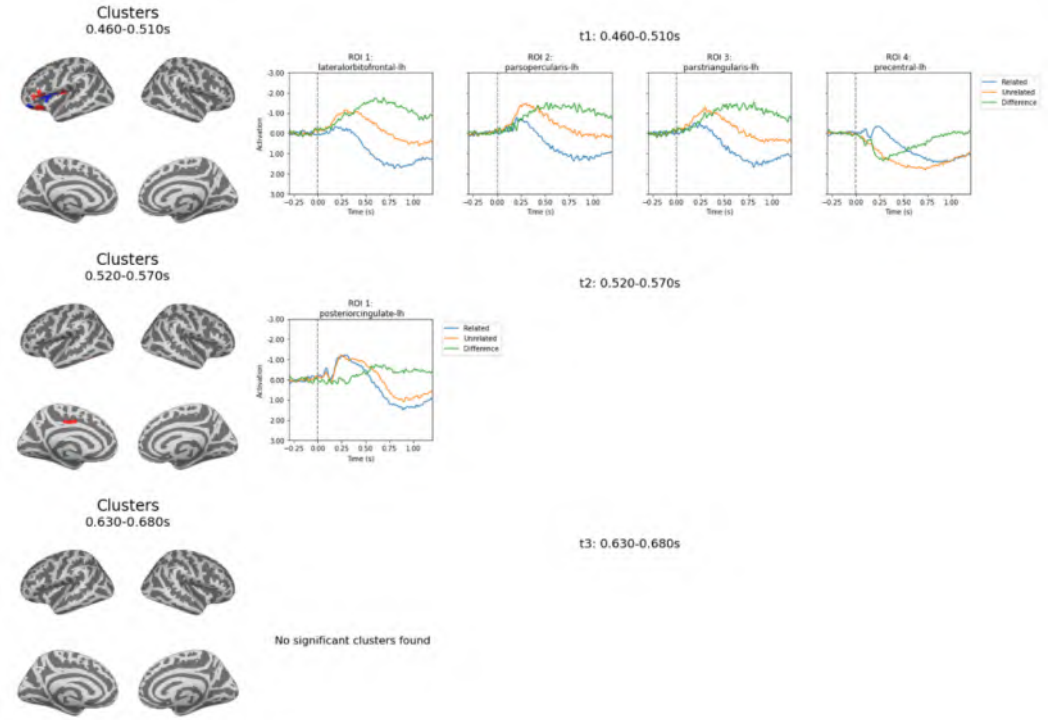

Figure 4.9. Results of clustering analysis on the eLORETA source reconstruction of the N400 difference in the early (460-510 ms), middle (520-570 ms) and late (630-680 ms) time window. Also the time series of each significant cluster, as averaged over all dipoles of the cluster, is shown.

4.3.4 Functional Connectivity

MMN

A network encompassing 10 nodes, connected by 12 edges ($p = 0.013$), was identified to significantly differ between deviant versus standard phoneme processing (Figure 4.10). This network comprised short intrahemispheric connections within the right temporal and right parietal region, as well as long intrahemispheric connections between the right temporal and parietal, and right parietal and occipital nodes. Interhemispheric connections were established between the left frontal nodes on the one hand, and the right temporal and parietal regions on the other hand. The right bank superior temporal sulcus showed the highest number of connections during deviant processing ($n = 6$). No edges were identified showing stronger functional connectivity in the standard compared to the deviant condition.

P300

A network showing significantly stronger functional connectivity for deviant compared to standard phoneme processing was identified, comprising 54 edges that connect 31 nodes ($p < 0.001$) (Figure 4.11). The network predominantly involved intra- and interhemispheric connections between temporal, parietal, cingulate and occipital nodes. More specifically, intrahemispheric connections were mainly located between cingulate and parietal, cingulate and temporal and temporal and occipital regions in both the left and right hemisphere, with additional links between parietal and occipital nodes in only the left hemisphere. The network featured interhemispheric connections between right parietal regions on the one hand and left temporal, occipital, frontal and cingulate nodes on the other hand. Links were also found between the right cingulate and left parietal and occipital cortex, as well as between the left cingulate and right frontal and temporal nodes. Lastly, interhemispheric connections were established between the left temporal and right occipital, right temporal and left occipital, and left and right occipital cortex. The left fusiform gyrus was the most connected node in the network underlying deviant processing ($n = 12$). Contrasting the standard compared to the deviant condition, a network containing 19 nodes and 22 edges was identified ($p = 0.002$) (Figure 4.11). This network mainly consisted of intrahemispheric connections, with short

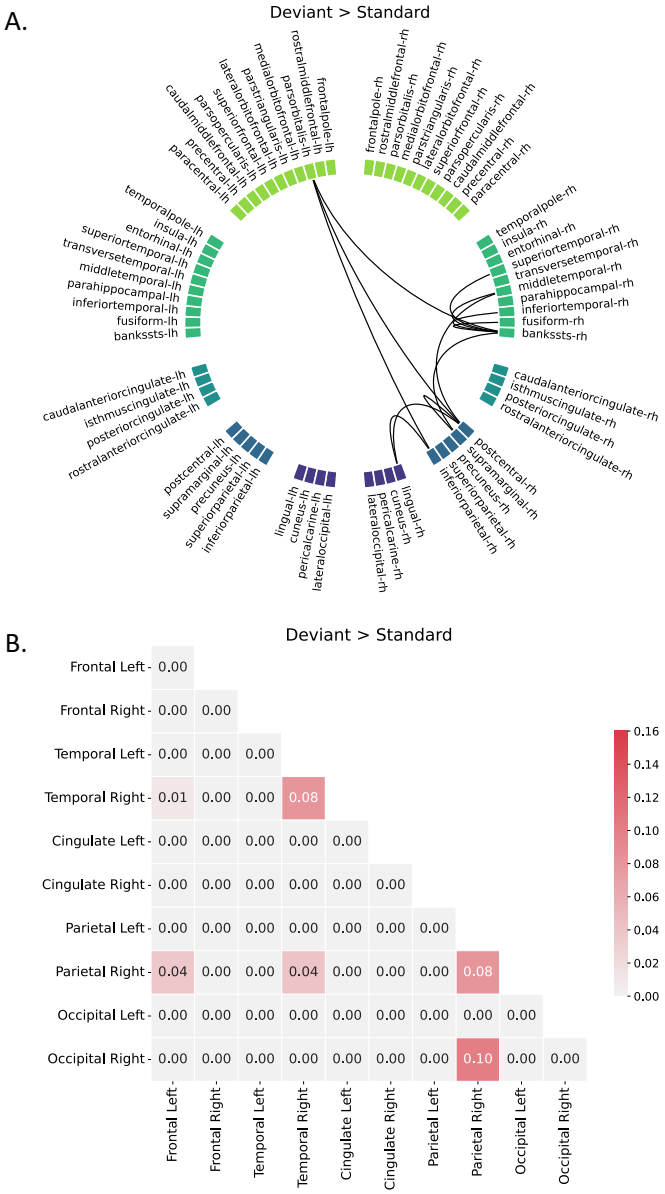

(a) Functional MMN networks showing a significant effect of condition ($p < 0.001$). (A) Graph representation of significant network edges between 68 ROIs for deviant > standard processing. (B) Normalized connectivity matrix of significant network edges between frontal, temporal, parietal, cingulate and occipital ROIs for deviant > standard and processing

Figure 4.10.

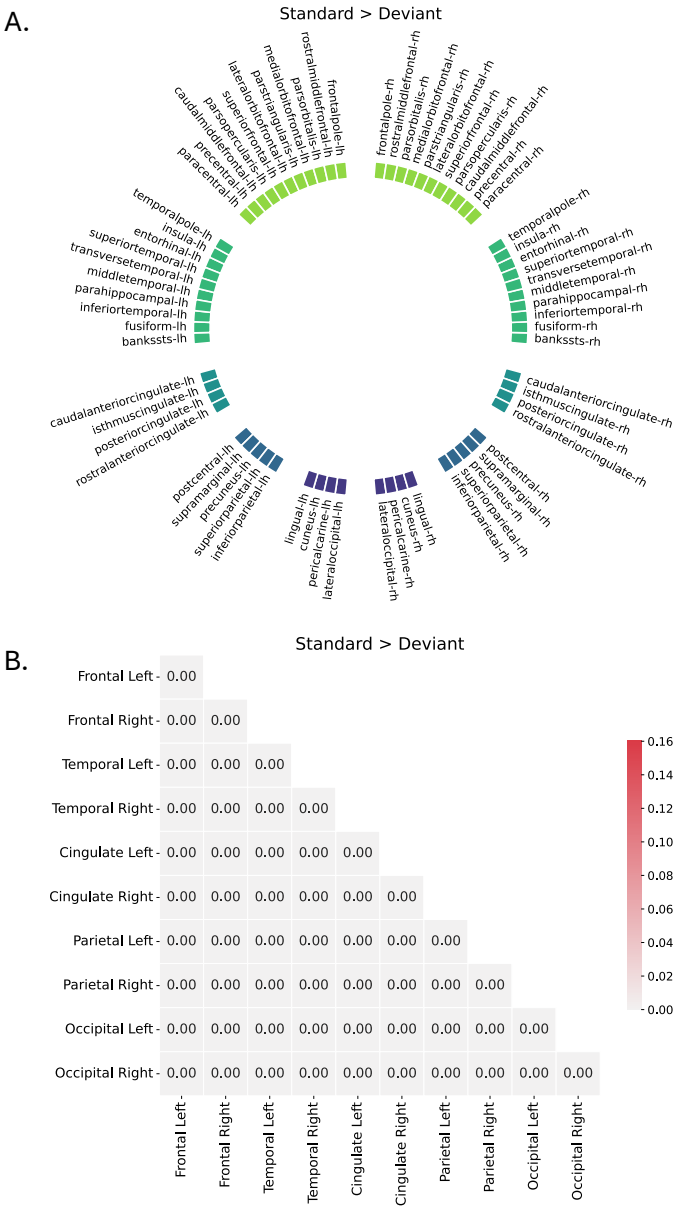

(b) Functional MMN networks showing a significant effect of condition ($p < 0.001$). (A) Graph representation of significant network edges between 68 ROIs for standard > deviant processing. (B) Normalized connectivity matrix of significant network edges between frontal, temporal, parietal, cingulate and occipital ROIs for standard > deviant processing

Figure 4.10.

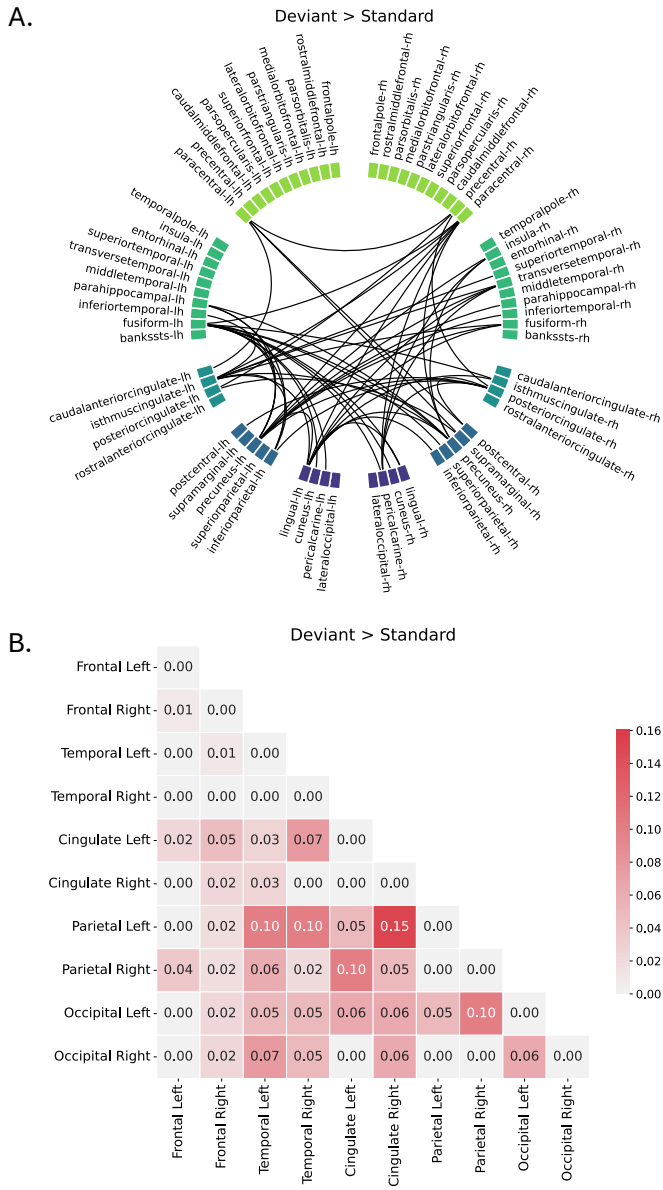

(a) Functional P300 networks showing a significant effect of condition ($p < 0.001$). (A) Graph representation of significant network edges between 68 ROIs for deviant > standard processing. (B) Normalized connectivity matrix of significant network edges between frontal, temporal, parietal, cingulate and occipital ROIs for deviant > standard and processing

Figure 4.11.

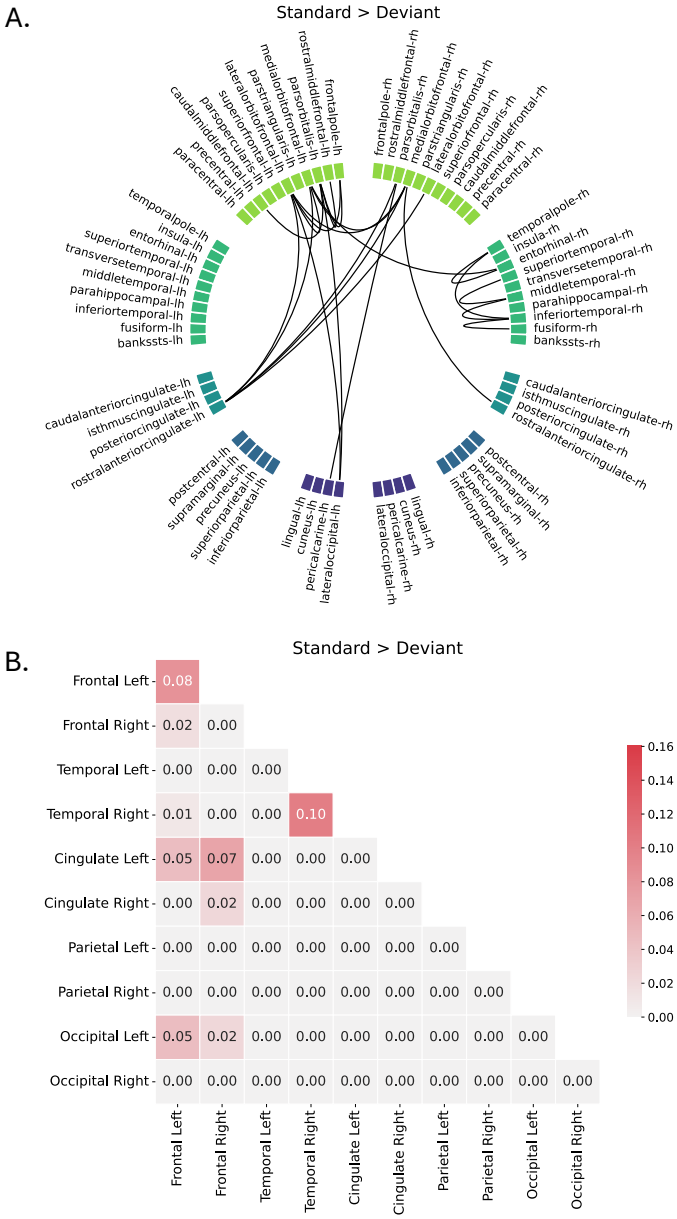

(b) Functional P300 networks showing a significant effect of condition ($p < 0.001$). (A) Graph representation of significant network edges between 68 ROIs for standard > deviant processing. (B) Normalized connectivity matrix of significant network edges between frontal, temporal, parietal, cingulate and occipital ROIs for standard > deviant processing

Figure 4.11.

connections within the left frontal and left temporal lobe, as well long connections between left frontal nodes on the one hand and left cingulate and occipital nodes on the other hand. Interhemispheric links were established between the left cingulate and right frontal cortex. The left lateral orbitofrontal gyrus and left rostral anterior cingulate cortex showed the highest number of connections during standard processing ($n = 5$).

N400

Network Based Statistics identified a significant network for related (related > unrelated) but not unrelated (unrelated > related) target processing, at a threshold of $p < 0.01$ (Figure 4.12). The significant network for related processing encompassed 15 nodes, connected by 12 edges ($p = 0.014$). The network mainly comprised short connections within the left frontal lobe, connecting the frontal pole, pars orbitalis, pars triangularis, pars opercularis and lateral orbitofrontal cortex. Additional short-range connections linked left temporal areas, specifically the entorhinal and inferior temporal region. Long-range connections essentially linked the left frontal cortex (especially the pars orbitalis of the IFG) with right frontal (interhemispheric; the frontal pole and medial orbitofrontal cortex), left parietal (intrahemispheric; the precuneus) and left occipital (intrahemispheric; the cuneus) cortices.

4.4 Discussion

The present study investigated the neural mechanisms underlying auditory deviance processing and speech sound discrimination, focusing on the mismatch negativity (MMN), P300, and N400 components. Our findings highlight a more extensive and interconnected neural network than traditionally proposed, extending beyond temporo-frontal interactions to include significant parietal and cingulate contributions. In the following sections, we discuss the implications of these findings for predictive coding theories, attentional modulation, and the role of parietal and cingulate regions in speech perception and semantic processing.

4.4.1 Mismatch Negativity

Our combined source reconstruction and connectivity findings suggest that speech sound discrimination is supported by a temporo-parieto-frontal

network, rather than the traditionally proposed temporo-frontal circuitry. While temporo-frontal interactions are well-established as the core network for passive auditory deviance processing (Doeller et al., 2003; Kim et al., 2017; Li et al., 2019b; MacLean and Ward, 2016), the present data highlight parietal involvement, particularly in the left supramarginal and postcentral gyrus. The possibility of parietal activation being an artifact from temporal sources cannot be entirely excluded (Fulham et al., 2014), but several factors argue against this explanation. First, increasing evidence supports parietal contributions to passive auditory deviance processing (Marco-Pallarés et al., 2005; Zhang et al., 2018). Second, parietal engagement was corroborated not only by source localization but also by functional connectivity analyses, which revealed robust synchronization between parietal, temporal, and frontal cortices. Given that absolute time lag corrections were applied, potential spreading effects were minimized. Third, structural connections between the parietal and other cortical regions (Schmahmann et al., 2008) likely support functional interactions observed here and in prior research (Hsiao et al., 2010).

The temporal sources were primarily located in and around the auditory cortex, including the superior temporal sulcus, the insula, and the banks of the superior temporal sulcus, the latter showing the strongest connectivity during deviant processing. Frontal activation was identified in the rostral middle frontal gyrus (MFG) and pars opercularis of the inferior frontal gyrus (IFGop). While the MFG has frequently been linked to frontal MMN generation (Deouell, 2007; Takahashi et al., 2013), fewer studies have localized MMN-related activity to the IFGop (Molholm et al., 2005; Doeller et al., 2003). Given the IFGop's well-documented role in motor and phonetic processing (Amunts et al., 2004; Heim and Alter, 2006; Heim et al., 2010), its involvement in MMN generation may reflect phoneme-specific computations.

Our findings align with the predictive coding framework of auditory discrimination (Garrido et al., 2009), which posits that bottom-up sensory processing in the temporal cortex interacts with frontal regions to update predictive models of auditory stimuli. The observed functional connectivity between temporal and frontal cortices supports this mechanism (Choi et al., 2013; MacLean and Ward, 2014). However, unlike previous studies that reported a temporal-to-frontal directional pattern in MMN activation (Fulham et al., 2014; Kim et al., 2017; Opitz et al., 2002), we observed persistent frontal activity across all time

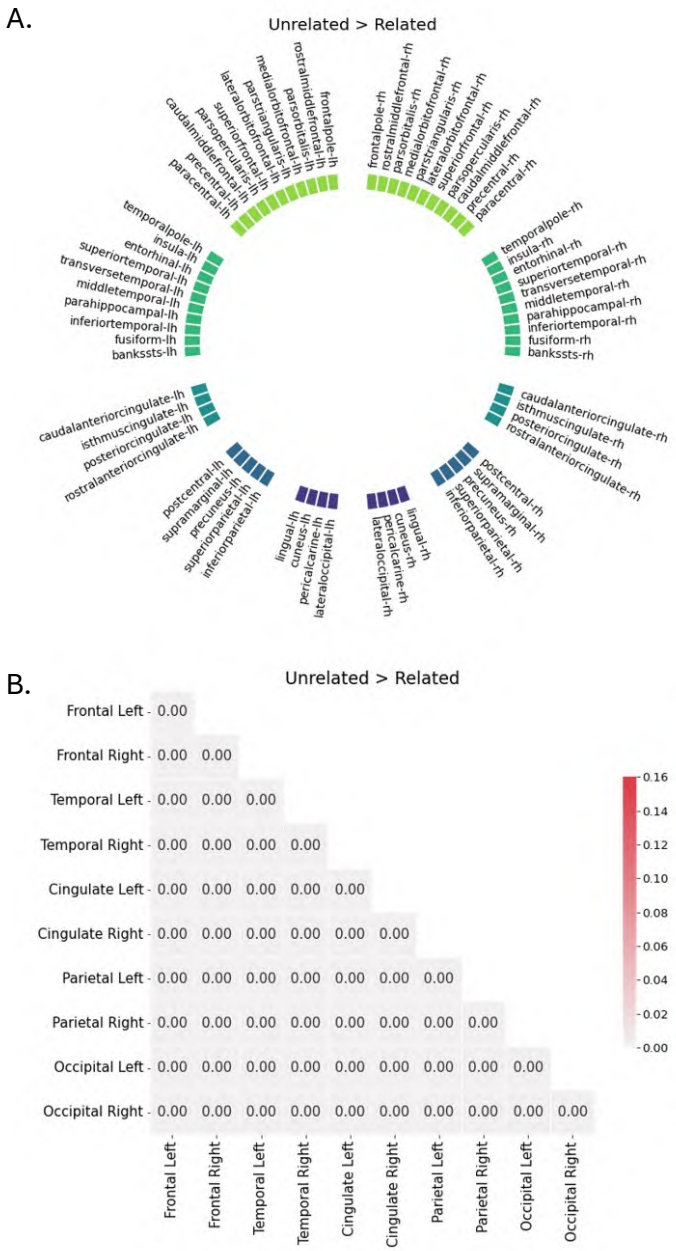

(a) Functional N400 networks showing a significant effect of condition ($p < 0.001$). (A) Graph representation of significant network edges between 68 ROIs for related > unrelated processing. (B) Normalized connectivity matrix of significant network edges between frontal, temporal, parietal, cingulate and occipital ROIs for related > unrelated and processing

Figure 4.12.

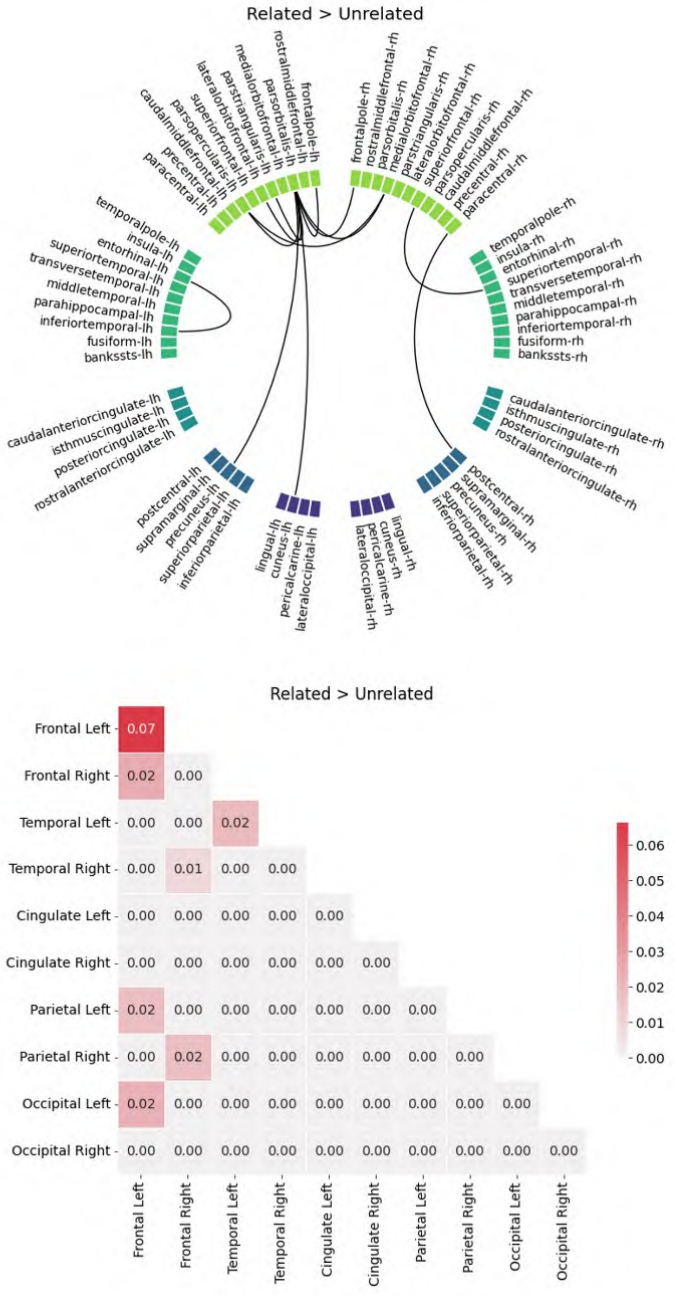

(b) Functional N400 networks showing a significant effect of condition ($p < 0.001$). (A) Graph representation of significant network edges between 68 ROIs for unrelated > related processing. (B) Normalized connectivity matrix of significant network edges between frontal, temporal, parietal, cingulate and occipital ROIs for unrelated > related processing

Figure 4.12.

windows. This suggests an early frontal role in processing stimulus predictions, consistent with findings by Xiao et al. (2018), where frontal activation preceded sensory input processing. Methodological differences in determining peak latencies versus analyzing time-segmented activation may explain these discrepancies.

The role of parietal sources within the predictive coding framework remains less clear. Some authors have linked parietal MMN activation to the P3a response, associated with attentional reallocation (Molholm et al., 2005), but this explanation does not fit our data, as parietal activation was observed in the middle (190–240 ms) rather than the late (240–290 ms) MMN time window. Another possibility is that parietal cortices contribute to multisensory integration during deviance processing (Fulham et al., 2014), aiding in the extraction of supplementary information from other sensory modalities. Given the strong temporo-parietal connectivity in our dataset, our results support this hypothesis. Additionally, the supramarginal gyrus is implicated in phonological working memory (Deschamps et al., 2014), which could explain its engagement in the linguistic oddball task. Thus, parietal involvement may reflect either multisensory integration, phonological working memory, or both, facilitating bottom-up processing in the temporal cortex and predictive modeling via temporo-parietal-frontal connections.

The hemispheric lateralization of phoneme processing was also examined. Our results indicate a bilateral network, with left-lateralized activation in temporal and parietal areas, but high interhemispheric connectivity in the right temporo-parietal cortex. Frontal activation clusters were right-lateralized, yet functional connectivity patterns confirmed engagement of both hemispheres. This finding contrasts with the conventional view that MMN responses to linguistic stimuli originate from a predominantly left-lateralized network (Pulvermüller, 2001; Näätänen et al., 1997; Sorokin et al., 2010). As suggested by Criel et al. (2023), the inclusion of a non-native phoneme (deviant [gə] vs. standard [bə]) may have influenced lateralization patterns. The deviant phoneme, lacking a well-established memory trace in Dutch speakers, might have been processed similarly to a tonal frequency contrast, engaging a more bilateral network.

In summary, our findings support a widespread, interconnected network for speech sound discrimination, including temporal, frontal, and parietal regions. The engagement of the supramarginal gyrus suggests a role for multisensory integration and phonological working memory, while bilateral connectivity chal-

lenges traditional views on lateralization in phoneme processing. Further research should explore whether parietal involvement is specific to linguistic stimuli or generalizes to non-speech contrasts.

4.4.2 P300

Broad bilateral activation was observed in the cingulate cortex, particularly the posterior part and isthmus, the parietal lobule (with maximal activation in the precuneus), and the frontal cortex (notably the left caudal middle frontal and right precentral areas) during P300 generation in response to speech sounds. These findings align with previous accounts of a broad fronto-parietal network, with cingulate activation contributing to deviant detection (Bocquillon et al., 2011; Linden, 2005). Similar brain structures are involved in both tonal contrast and phoneme processing, suggesting attentional and working memory-related functions (Bledowski et al., 2004; Leech and Sharp, 2014; Sabeti et al., 2016).

Justen and Herbert (2018) examined cortical activity related to pure-tone deviant processing within the dorsal and ventral fronto-parietal attention networks (DAN and VAN) (Corbetta and Shulman, 2002). The DAN, which includes the superior parietal lobe/precuneus and inferior frontal junction, governs top-down perceptual attention, while the VAN, involving the temporoparietal junction, inferior frontal gyrus, and anterior cingulate cortex, supports bottom-up attention reallocation. The present findings confirm DAN involvement in deviant categorization, with activation in the caudal middle frontal gyrus and precuneus, linked to selective attention and voluntary attention switching (Le et al., 1998; Rossi et al., 2009). No major VAN source clusters were found, but connectivity analysis identified VAN components (e.g., right supramarginal gyrus, bilateral inferior parietal cortex, right insula, and right superior temporal gyrus) as part of the speech sound detection network. The VAN's early activation, preceding the P300, might explain its absence in eLORETA results (Justen and Herbert, 2018). Additionally, increased connectivity in the superior temporal cortex and insula may reflect modality-specific processing.

Beyond fronto-parieto-cingulate activation, occipital lobe involvement was evident, particularly through its connectivity with parietal and cingulate cortices, as well as the lingual gyrus. Occipital contributions to P300 generation have been noted in prior studies (Justen and Herbert, 2018; Peng et al., 2012). Given its role in visual processing, this connectivity might be inhibitory or re-

late to attentional modulation, with effective connectivity from occipital alpha desynchronization sources to posterior cingulate P300 sources supporting auditory and visual target detection.

Studies on P300 activation timing have reported varying patterns, from early fronto-cingulate engagement preceding parietal activation (Volpe et al., 2007) to the reverse sequence (Li et al., 2019a; Tao et al., 2022). Our findings suggest an early activation of DAN structures (precuneus and caudal middle frontal gyrus), followed by later engagement of the posterior cingulate cortex, which exhibited increasing current source density (CSD) in later time windows. This supports the hypothesis that top-down attentional mechanisms modulate target categorization (Bledowski et al., 2004; Donchin and Coles, 1988; Kok, 2001; Li et al., 2016).

The functional role of the posterior cingulate in P300 remains complex. Increased activation in the late P300 phase may reflect attention reallocation following deviant detection or working memory updating (Sabeti et al., 2016). Our hemispheric analysis revealed a largely bilateral network, mirroring MMN results. Despite left hemispheric dominance in the posterior cingulate (possibly due to phonemic stimuli), active speech categorization did not rely on a strongly lateralized system. This aligns with the view that P300 reflects domain-general cognitive functions rather than modality-specific processes (Linden et al., 1999; Peng et al., 2012; Sabeti et al., 2016).

The oddball task design, requiring a button press for deviants, likely influenced observed activation. Precentral cortex activation in the late P300 window suggests motor-related processing. Additionally, inhibition of a behavioral response to standard stimuli may have contributed to observed frontal connectivity patterns. Future studies should compare tasks requiring responses to both standard and deviant stimuli to clarify methodological effects.

4.4.3 N400

Significant N400 source clusters were identified in the left frontal and left posterior cingulate cortices, supporting a left-dominant network for semantic processing (Binder et al., 2009) and N400 elicitation during semantic priming (Geukes et al., 2013; Ghosh Hajra et al., 2018). Frontal and temporal areas govern semantic priming at long SOAs (Kircher et al., 2009; O'Hare et al., 2008), with the inferior frontal gyrus (IFG) emerging as a major N400 generator. The IFG consists of the pars opercularis (BA 44), pars triangularis (BA 45), and pars orbitalis (BA 47) (Petrides and Pandya, 2004), which are involved

in semantic retrieval and selection (Moss et al., 2005; Noppeney et al., 2004). As part of the semantic control network (Diveica et al., 2021; Jackson, 2021), the IFG mediates top-down retrieval and selection, with reduced activation for primed targets due to facilitated processing (Lau et al., 2008). Increased posterior IFG activation for unrelated targets suggests heightened semantic control demands. However, given the inherent localization errors in EEG source estimation (Asadzadeh et al., 2020), caution is warranted in interpreting these results.

The absence of a priming-related N400 generator in the temporal cortex, particularly in the posterior middle temporal gyrus (pMTG), contrasts with previous findings (Ghosh Hajra et al., 2018; Holderbaum, 2019). However, some fMRI studies on long SOA priming also identified only frontal generators (Kircher et al., 2009). A more liberal analysis revealed bilateral pMTG activation in later time windows, suggesting that while temporal contributions exist, semantic control processes may dominate long SOA priming effects. No activation was observed in the anterior temporal lobe, contradicting its proposed role in taxonomic semantic processing (Lau et al., 2013; Mirman et al., 2017).

Another cluster was identified in the left posterior cingulate cortex (PCC), with delayed activation relative to the IFG. The PCC is generally linked to the default mode network (Buckner et al., 2008) and domain-general attention (Corbetta and Shulman, 2002), with functional segregation into ventral and dorsal subregions (Vogt et al., 2006). The ventral PCC interfaces semantic retrieval and episodic memory encoding (Binder et al., 2009), potentially explaining its reduced activation for primed targets due to facilitated encoding. The dorsal PCC, implicated in response control, has been suggested to categorize stimuli (O'Hare et al., 2008). Increased PCC activation for unrelated targets may reflect response selection demands, though the lack of an oddball task design challenges this interpretation. Alternatively, activation in the late 630–680 ms window may relate to extended semantic integration demands (Yacovone et al., 2021) or working memory and cognitive control processes (Coulson and Kutas, 2021; Lee and Federmeier, 2009).

Enhanced functional connectivity was observed among left intrahemispheric and interhemispheric frontal areas for related targets, aligning with findings by Kujala et al. (2012). Increased connectivity between distinct neuronal assemblies in primed conditions reduces local processing demands, supporting the hypothesis that semantic priming relies on efficient information transfer rather than localized activation (Matsumoto and Kakigi, 2014). The strongest connec-

tivity was in the left IFG, consistent with its role in top-down retrieval (Moss et al., 2005).

Additionally, enhanced connectivity was observed between the left pars orbitalis and left parieto-occipital areas (precuneus, cuneus). This aligns with the hub-and-spoke model (Patterson and Lambon Ralph, 2016), where parietal and occipital cortices encode modality-specific representations, particularly visual object features (Dilkina and Lambon Ralph, 2012). The auditory nature of the priming task suggests this connectivity reflects facilitated retrieval of visual representations rather than direct stimulus processing. Alternatively, frontoparietal synchronization may indicate engagement of domain-general control processes (Bulut, 2023), as the IFG participates in both domain-specific language processing and broader cognitive control functions (Belyk et al., 2017).

4.4.4 Limitations and directions for future research

This study provides insight into the cortical sources and functional networks underlying speech sound perception and semantic priming. However, several limitations must be acknowledged, along with directions for future research.

Methodological Considerations

The study design did not allow for a full investigation of stimulus modality effects. For instance, different subareas in the auditory cortex respond to specific deviant types (Frodl-Bauch et al., 1997), but the present findings do not clarify whether the activation of certain regions (e.g., the supramarginal gyrus) is specific to linguistic stimuli. Additionally, the question of whether the P300 is modality-specific (Crottaz-Herbette and Menon, 2006; Peng et al., 2012; Sabeti et al., 2016) remains unresolved, highlighting the need for comparative studies on tonal versus phonemic contrasts. Furthermore, our paradigms, while controlled, do not fully replicate natural speech perception (Hickok and Poeppel, 2007), raising concerns about generalizability beyond the phoneme level.

Furthermore, we employed the Desikan-Killiany atlas (Desikan et al., 2006) for cortical parcellation, balancing spatial resolution with EEG localization error constraints (Pascual-Marqui et al., 2018). However, this atlas does not differentiate between anterior and posterior portions of the lateral temporal lobe, which is significant for semantic processing research. Although our analysis did not reveal significant activation clusters in the temporal cortex, future studies should consider alternative atlases, such as the Destrieux (Destrieux et al.,

2010) or Brainnetome (Fan et al., 2016) atlases, for finer parcellation of semantic networks.

Influence of Age and Biological Factors

Our participant pool spanned a wide age range (20-80 years), allowing for generalizable findings. However, aging-related neural changes may have influenced our results. Structural (Fjell and Walhovd, 2010) and functional (Cabeza, 2002; Davis et al., 2008) network alterations, such as the Posterior-to-Anterior Shift in Aging (PASA; Davis et al. (2008)) and Hemispheric Asymmetry Reduction in Older Adults (HAROLD; Cabeza (2002)), could impact phoneme and semantic processing. Notably, Hoffman and Morcom (2018) observed reduced activation in key semantic areas (e.g., the left inferior prefrontal and posterior temporal cortex) in older adults. While our scalp-level results do not suggest age-related N400 differences, the absence of a temporal N400 source cluster could reflect reduced engagement of this area in elderly participants. This warrants further investigation into age-related semantic processing changes.

Previous studies (Criel et al., 2023; Geal-Dor et al., 2006; Tsolaki et al., 2015) have also documented age-related shifts in P300 amplitude, latency, and source localization. Tsolaki et al. (2015) found that aging alters P300 generators in tonal contrast tasks but not MMN sources. While our study did not focus on biological influences, future research could explore how age and sex modulate the neural architecture of speech perception and semantic priming.

Functional Connectivity and Directionality

The functional connectivity approach used in this study provided valuable insights but also had limitations. While our connectivity analysis considered all 68 ROIs, an alternative approach could involve targeted assessments of interactions between key N400 generator sites, such as the inferior frontal gyrus and the posterior temporal cortex, as well as their connections with the posterior cingulate area. Exploring directional connectivity (e.g., using Granger Causality or transfer entropy) could clarify the dynamic interactions within semantic networks.

Additionally, our methodology did not capture high-frequency synchronization, as trial averaging eliminates high-frequency activity. Since synchronization in specific frequency bands may play a role in MMN and P300 generation,

future studies should apply alternative connectivity measures that retain high-frequency information. Moreover, while maximal cross-correlation was used to assess connectivity, this measure is not well-suited for networks with bidirectional interactions (Bastos and Schoffelen, 2015), limiting its reliability in the context of higher-order cognitive processing.

4.5 Conclusion

Our results support a broader conceptualization of speech sound discrimination and auditory deviance detection, emphasizing the contributions of parietal, frontal, and cingulate cortices alongside traditional temporo-frontal pathways. The identification of temporo-parietal-frontal interactions in MMN generation suggests an expanded role for the parietal cortex in predictive coding and phonological working memory. Similarly, P300-related activation patterns reinforce the involvement of attentional networks in deviant categorization, while N400 findings underscore the IFG's role in semantic priming and retrieval. The observed bilateral connectivity patterns challenge classical lateralization models, suggesting a more distributed and adaptable neural framework for auditory processing. Future research should investigate whether these findings generalize across different linguistic contexts and non-speech auditory stimuli, further refining our understanding of the neural architecture underlying speech perception.

Part III

How simulations can help us understand the working mechanisms of the brain

5 | Single-trial ERP quantification using neural networks

Abstract

Traditional approaches to quantify components in Event-Related Potentials (ERPs) are based on averaging EEG responses. This, however, ignores the trial-to-trial variability in the component's latency, leading to a smeared version of the component's shape and underestimations of its amplitude. Therefore, different techniques to quantify ERP components in single trials have been described in literature. In this study, two approaches based on neural networks are proposed. We compared the neural networks' performance with other techniques using both simulated data and two experimental datasets. The results on simulated data showed that both neural networks outperformed other techniques for most signal-to-noise ratios. Furthermore, the single-trial latency quantification methods resulted in better estimates of the topography and shape of the ERP component compared to those obtained using averaging-based methods. In the first experimental dataset, the highest correlation values between the estimated latencies and the reaction times were found using the neural networks, while in the second dataset, the networks allowed us to better investigate the changes in amplitude of the component with age. Here, we were able to show significant differences in amplitude between the age groups, that were not found using the traditional averaging approaches. Our results illustrate the applicability and the added value of neural network-based approaches for the quantification of ERP components in single trials. A limitation, however, is that simulated data is needed to train the networks, which can be difficult when the ERP components to be found are not known a-priori. Nevertheless, we have illustrated that single-trial latency estimation methods offer more information on the variability of the timing of the component and result in better estimates of their shape and topography.

This chapter is based on the following article:

Depuydt, E., Criel, Y., De Letter, M., & van Mierlo, P. (2023). Single-trial ERP quantification using neural networks *Brain Topography 36.6*: 767-790. doi: 10.1007/s10548-023-00991-8

5.1 Introduction

Event-related potentials (ERPs) are responses in the brain that directly result from a specific sensory, cognitive, or motor event and consist of multiple peaks and troughs that are referred to as the ERP components (Luck, 2014). These responses can be measured using electroencephalography (EEG), a technique in which electrical brain activity is recorded by electrodes placed on the scalp. Because of the high temporal resolution of EEG, ERPs are extensively used in neuroscience to study the timing of neural responses.

When recording ERPs during tasks, EEG signals not only capture the activity associated with the stimuli, but also the ongoing spontaneous brain activity and noise. Unfortunately, the amplitude of the ERP components is often small in comparison to the background EEG, which makes it challenging to extract reliable and meaningful information. In order to characterize ERPs accurately, signal processing techniques that improve the signal-to-noise ratio (SNR) are required. One of the most commonly used approaches is to average the EEG signals across multiple trials. This technique is based on the assumptions that event-induced responses are consistent across different trials, and that spontaneous brain activity unrelated to the event is random and thus can be attenuated by averaging. After averaging, the ERP component of interest is typically quantified by measuring the amplitude and latency of this component in the averaged ERP. For this quantification, different measures can be used, such as the amplitude and the latency of the peak voltage, or the mean amplitude and fractional area latency (Luck, 2014; Hansen and Hillyard, 1980; Kiesel et al., 2008). Also other analysis techniques, such as ERP topographic analyses of variance and microstate analyses (Murray et al., 2008), have been proven to be effective, but still rely on single trial averaging in most cases.

In practice, the assumption that the ERP component is identical across trials often proves invalid, as it is known that both the latency and the amplitude of different ERP components show significant variability across single trials (Handy, 2005; Brazier, 1964). This is especially the case for later components, such as the P300, N400 and P600 components, that express more complex cognitive processing in the brain (Polich, 2012). The variability has multiple implications on the averaging approach (D'Avanzo et al., 2011). First, in order to obtain robust estimations of the latency and the amplitude of the ERP component, a large number of trials needs to be included (Clayson et al., 2013). This

however increases the recording time, which may be challenging for certain patient groups.

Another limitation of the averaging technique is that it is unable to provide detailed information on the mechanisms underlying differences in ERP components between subject groups. For instance, in schizophrenic patients, P3 amplitudes are often smaller compared to healthy controls (Jeon and Polich, 2003). However, as schizophrenic patients also typically show a higher variability in reaction times (Ford et al., 1994; Roth et al., 2007), the amplitude variation in the averaged ERP waveform could also in part be caused by the variability in latency jitter (Ouyang et al., 2016). This variability in latency jitter has also been observed in other populations, such as aging populations (MacDonald et al., 2008) or in individuals suffering from brain damage (Fjell et al., 2011). Also here, variations in the amplitude of an average ERP component may be due to changes in the amplitudes of individual trials, variability in latency, or a combination of both factors (Walhovd et al., 2008). Correcting for this latency variability may help to better understand the neural mechanisms underlying different tasks. For example, in a recent study Murray et al. (2019) have shown the parietal retrieval success effect to be both variable and thresholded in older adults by compensating for the trial-to-trial latency jitter.

Many different single-trial estimation algorithms have been proposed in literature. One of the currently most widely used techniques to quantify the single-trial latency consists of an iterative approach based on template matching and was proposed by Woody et al. (1967). The component's latency is estimated using the cross-correlation between a template and the single trial, after which all single trials are realigned to the estimated latencies and averaged, resulting in a new template. The assumption behind this method is that while the latency of the ERP component varies in different trials, its shape does not. This iterative scheme results in a subject-specific estimation of the shape of the ERP component, which has, however, proven to be sensitive to noise. Errors made in the latency estimation can deform the shape of the template, enlarging the error made in subsequent iterations (Möucks et al., 1988). Another important drawback of this method is that it relies on the analysis of the EEG data in a single channel. Given that in most recording set-ups multiple electrodes are used and that different electrodes instantaneously capture the evoked response, only a fraction of the available information is thus used. Therefore, techniques that also consider the topographic information in the EEG data have been extensively explored. For example, the cross-correlation curves calculated

in Woody's method can be obtained for multiple electrodes and averaged, after which the peak lag is extracted from the averaged curve (Ouyang et al., 2017). A similar template matching technique that has been proposed is dynamic time warping (DTW) (Zoumpoulaki et al., 2015). This alignment algorithm matches the different components of the template to the single trial through local compressions and extensions of the signal, allowing to estimate the time-points in the single trial that best resemble the ERP component. The algorithm can be extended to include topographic information by using a multi-dimensional generalization of the algorithm as proposed in (Shokoohi-Yekta et al., 2017). Different spatiotemporal filters have also been proposed, including multi-channel Wiener filters (Maki et al., 2015) and spatiotemporal LCMV beamformers (van Vliet et al., 2016). Another group of techniques exploiting the spatiotemporal information in the EEG data are decomposition techniques, such as principal component analysis (PCA) (Dien, 2010) and independent component analysis (ICA) (De Lucia et al., 2010). While PCA decomposes the signal in orthogonal components that capture the maximum amount of variance in the data, ICA decomposition is based on the idea that the recorded signal in the different electrodes is a mixture of the signals generated by several independent sources in the brain and that one or a combination of multiple of these sources corresponds to the ERP component (Bugli and Lambert, 2007).

It is interesting to note that many of the methods for the quantification of ERP components in single trials have also been used in research focusing on Brain-Computer Interfaces (BCIs). Here, for each trial, a decision has to be made whether a certain ERP component is present in the data or not. Most recent advances in this field, however, have been made using deep learning techniques, such as convolutional NNs (CNN) (Lawhern et al., 2018; Vařeka, 2020), recurrent CNNs (Maddula et al., 2017) and convolutional Long Short-Term Memory (convLSTM) NNs (Joshi et al., 2018). This research has shown that neural networks are able to learn the pattern of the ERP component from the data. Therefore, deep learning approaches might also be able to improve the quantification of ERP components in single trials.

The aim of this work is to investigate the applicability of neural networks to the quantification of ERP components in single trials. Therefore, we will adapt two existing neural networks described in literature for BCIs, namely the compact convolutional neural network, EEGNet, introduced by Lawhern et al. (2018) and the convolutional LSTM neural network proposed by Joshi et al. (2018). We will compare these neural networks to other single-trial latency

estimation techniques described in literature, such as (iterative) template matching using cross-correlation and DTW, an (iterative) spatiotemporal LCMV beamformer and a decomposition based approach using ICA. Furthermore, the different single-trial latency estimation techniques will be compared to the traditional averaging approach to assess the added value of single-trial ERP quantification by evaluating the topography and morphology of the obtained ERP components, using both simulated and experimental data. While we will focus on the P300 and N400 components in the remainder of the study, we believe that the proposed methods could easily be adapted for other ERP components.

5.2 Materials and Methods

5.2.1 Experimental data

In our study, we have used two different datasets. In the first dataset, an attentive oddball task was used in which two types of phonemes were presented to the subjects, while in the second dataset, a semantic sentence congruity task was used. The collection of both datasets and the analysis of the data in this study were carried out in accordance with the Declaration of Helsinki and were approved by the Ethical Committee of the University Hospital Ghent (BC-11771). All participants signed an informed consent.

Dataset 1: Oddball task eliciting a P300 component

Different methods to quantify the P300 component were compared and evaluated on both simulated and experimental data. The normative dataset collected by Aerts et al. (2013) for phonological input, consisting of 71 healthy subjects, was used in this work both as the experimental dataset and to generate the simulated trials. In the experiment, an attentive oddball paradigm for auditory phoneme discrimination was used. The participants had to discriminate the deviant phoneme [gə] from the standard phoneme [bə]. In total, 150 stimuli of 250 ms were presented to the participants with an interstimulus interval of 2000 ms and a deviant/standard ratio of 1/4. Participants were asked to press a button each time a deviant stimulus was presented, allowing us to measure the reaction times to the stimuli. The data was recorded using 20 electrodes: Fp1, Fpz, Fp2, F7, F3, Fz, F4, F8, T3, C3, Cz, C4, T4, T5, P3, Pz, P4, T6, O1 and

Oz, at a sampling rate of 500 Hz. More details about the recording procedure can be found in (Aerts et al., 2013).

Dataset 2: Semantic sentence congruity task eliciting an N400 component

For the second experimental dataset involving an N400 component, we used the dataset recorded by Cocquyt et al. (2023) who used a semantic sentence congruity task (SSCT). Briefly, 120 sentences, half of which were semantically correct while the other half contained a semantic violation at the end, were presented to 110 individuals. After the final word of each sentence, the Dutch word 'Druk' ('press') appeared on the screen, asking participants to press the green (correct sentences) or red (incorrect sentences) button. In this experiment, the response was thus delayed to avoid influence of the button press to the ERPs of experimental interest. More details about the complete experiment can be found in Cocquyt et al. (2023).

Data preprocessing

The offline preprocessing of the data was done using the MNE-Python library (Gramfort et al., 2013). Bad electrode channels were automatically detected and removed. The data was then band-pass filtered between 0.3 Hz and 30 Hz (half-amplitude cut-off, 12 dB/octave roll-off), as well as notch-filtered at 50 Hz. Independent component analysis was performed to remove both eye blinks and horizontal eye movements. The data was re-referenced to an average common reference, after which the data was segmented. For the oddball paradigm, the data was segmented into 1100 ms long epochs, starting from 100 ms before the stimulus onset to 1000 ms post-onset, while for the SSCT dataset, the data was segmented into epochs of 300 ms pre- and 1200 ms post-presentation of the critical nouns. Baseline correction was performed using the pre-stimulus window for both paradigms. Finally, automatic artefact rejection was applied, rejecting epochs where the signal exceeded ±100 μV, where the peak-to-peak signal amplitude exceeded 150 μV or where the peak-to-peak signal amplitude was less than 0.5 μV. Figure 5.1 depicts the averages across all trials and all subjects of both conditions, and the difference between these conditions, are shown for both datasets.

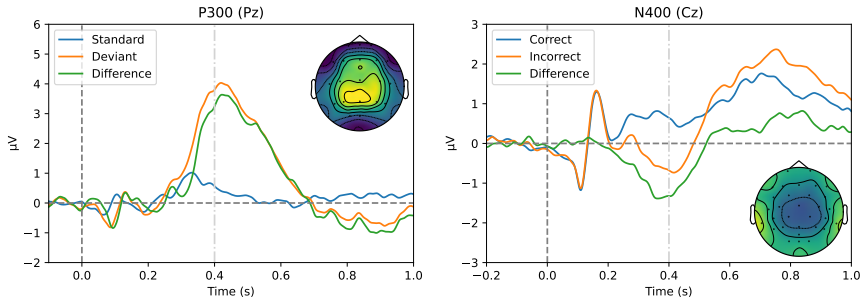

Figure 5.1. The averaged waveforms across all trials and subjects for both conditions, and the difference between these conditions for both experimental datasets used in this work. For both datasets, also the topography at 0.400 s after the stimulus onset is shown.

5.2.2 Methods for ERP component quantification

The methods used for the quantification of the ERP components can be split up in two different groups. The first group of methods follows the traditional approach where the individual trials for each subject are averaged before quantifying the latency, the topography and the shape of the ERP component using the average waveform. The second group are methods that first estimate the latency of the ERP component in single trials. Based on these estimations, the different trials are realigned for each subject before averaging, after which the obtained waveform is used to quantify the topography and the shape of the ERP component.

Averaged trial ERP component quantification

Two different techniques were used to quantify the ERP component's latency after averaging, namely the peak latency and the 50%-area latency.

M1: Peak latency: The most commonly used technique for measuring the latency of ERP components is by defining a time window and finding the latency of the maximal value in this time window at a specific electrode. For the P300 component, we used the time window between 250 ms and 650 ms post-stimulus at the Pz electrode, while for the N400 component, we focussed on the Cz electrode using the 200 ms-600 ms time window. This measurement window was chosen based on visual inspection of the data averaged across patients (Luck, 2014), while the Pz and Cz electrodes were chosen as the P300

and N400 components typically reach maximum values over the parietal and central electrodes, respectively (Polich, 2012).

M2: 50%-Area latency: An alternative method for calculating the component latency on the averaged waveform is by calculating the area under the ERP waveform over a specified time-window and then finding the time point where a fraction of this area is reached (Luck, 2014). In this work, the 50%-area was used. As for the calculation of the peak latency, a time window from 250 ms to 650 ms post-stimulus was used and the ERP waveform was considered at the Pz and Cz electrodes for the P300 and N400 components, respectively.

Single trial ERP component quantification based on template matching

Seven different approaches were selected for the single-trial latency estimation: non-iterative and iterative template matching using cross-correlation, non-iterative and iterative template matching using DTW, a non-iterative and an iterative spatiotemporal LCMV beamformer and template matching after decomposition using ICA.

M3: Template matching using the cross-correlation curve: In this method, the resemblance between the template and the single trials was measured by calculating the correlation between both at each time lag. This corresponds to calculating the cross-correlation curve between the template and the signal. To take the spatial information present in the data into account, the approach proposed by Ouyang et al. (2017) was used. Here, cross-correlation curves were calculated for all electrodes, after which they were averaged. The optimal latency was then determined as the latency corresponding to the peak in this averaged cross-correlation curve.

M4: Template matching using subsequence Dynamic Time Warping (DTW): A second template matching approach that was used is based on DTW. Different variants of the DTW algorithm exist that differ in the posed constraints. In the original version, one of these constraints is the boundary condition. This states that in the alignment, the first and the last indices of the first sequence must be matched with the first and last indices of the second time series (Müller, 2007). However, the goal in this work is to find a subsequence, i.e. a template, within a longer sequence, namely the EEG signal. Therefore, the subsequence DTW variant, in which this constraint is

dropped, was used as implemented in the tslearn library (Tavenard et al., 2020) in Python. The optimal alignment between the template and the single trial is expressed as a mapping between the time indices of the two signals. The latency of the ERP component is then estimated as the time-point to which the peak latency of the template is matched in the optimal alignment path.

M5: Spatiotemporal LCMV Beamformer: The spatiotemporal linearly constrained minimum variance (LCMV) beamformer is a flexible spatiotemporal filter developed by van Vliet et al. (2016) to estimate the amplitude of ERP components. We have extended their method to allow estimation of the latency of the ERP component by shifting the template in time. For each time-shift, the amplitude of the ERP component is estimated after which the time-shift with the highest amplitude is selected as the latency of the ERP component in the single trial.

M6, M7 and M8: Iterative approaches: Each of the single-trial latency estimation algorithms M3, M4 and M5 can be extended by iteratively applying the methods. This approach was first described for the cross-correlation by Woody in 1967 (Woody, 1967) and allows the estimation of a subject-specific template. In each iteration, the different trials were realigned based on the estimated latencies to obtain a subject-specific estimate of the ERP component. However, incorrectly estimated latencies can have a large influence and distort the shape of the obtained component estimate. Therefore, a weighted average of the old template (80%) and the subject-specific component estimate (20%) was used as the new template in the following iteration.

M9: Template matching after Independent Component Analysis: Multiple ICA decomposition approaches can be used for the latency quantification of the ERP component in single trials. The first choice that can be made is the specific ICA algorithm that is used for the decomposition. Algorithms that are typically used for EEG data include FastICA (Hyvarinen, 1999), extended Infomax (Lee et al., 1999), picard (Ablin et al., 2018) and adaptive mixture ICA (AMICA) (Palmer et al., 2012; Delorme et al., 2012). Secondly, we can consider the ERP component either a single peak within the ICA decomposition, or as a combination of several components, each with an independent topography, which are mixed at the scalp level due to volume conduction (Onton et al., 2006). In the first case, we can determine the

latency of the ERP component by determining the ICA component which has the highest cross-correlation with the template. The latency is then estimated as the time lag for which this correlation value was obtained. In the second case, several components from the ICA decomposition were combined before calculating the cross-correlation with the template to determine the latency of the ERP component. To determine which components to take into account, i.e. which subspace of the ICA components form the ERP component, two different criteria were used: the correlation between the IC topography after backprojection to the scalp and the template should be positive, and the p-value should be less than 0.01 (Ouyang et al., 2017). The different ICA algorithms and the two latency quantification approaches were evaluated in this work using the simulated data. These results can be found in appendix. Based on these results, we decided to focus in this article on the extended Infomax ICA algorithm.

Single trial ERP component quantification using neural networks

Finally, two deep learning approaches, namely the EEGNet network and a convLSTM neural network, were used for the quantification of the ERP components in single trials.

M10: EEGNet, a convolutional neural network: EEGnet is a compact convolutional neural network that was developed by Lawhern et al. (2018) for EEG-based BCIs. The network combines depthwise and separable convolutions, allowing the model to combine spatial and temporal information present in the data. It consists of two convolutional blocks, followed by a Softmax classification layer. In the first convolutional block, two convolutional steps are performed in sequence. First, a number of 2D convolutional filters are fitted to the data to capture the frequency information present in the data. A depthwise convolution is then used to learn a spatial filter. This combination of convolutional layers allows the model to learn frequency-specific spatial filters for each feature map. In the next layer, batch normalization is used, before applying the exponential linear unit non-linearity and reducing the dimensionality using Average Pooling. Finally, to reduce overfitting of the model, the dropout technique is applied with a probability of 0.5. The second convolutional block consists of a separable convolution, both decoupling the relationship between feature maps and reducing the number of parameters. This convolutional layer is again followed by batch normalization, ELU activation, average pooling and dropout, af-

ter which the features are passed to the classification block (Alvarado-Gonzalez et al., 2021).

In this work, the two convolutional blocks will be kept as in the original model, but the classification block is adapted to allow the estimation of the P300 latency by flattening the data and using a dense layer with linear activation instead of the Softmax classification layer. To reduce the number of parameters in the model, the EEG data is downsampled to 250 Hz. The model was fitted using the Adam optimizer, with the default parameters available in the Keras API, to minimize the mean squared error loss function. An overview of the final architecture of the model and the chosen parameters is shown in table 5.1.

M11: Convolutional LSTM neural network (ConvLSTM): ConvLSTM is a specific type of recurrent neural network that is used for spatiotemporal predictions and was first introduced in precipitation nowcasting (Shi et al., 2015). The model can learn both spatial and temporal features at the same time. Furthermore, as convolution operations share parameters, the number of parameters in a convLSTM is greatly reduced compared to the traditional LSTM approach. As mentioned in the introduction, the model was recently used by Joshi et al. (2018) in the area of BCIs to determine the presence of the P300 component in single trials. In this work, the proposed architecture was adapted to allow estimation of the latency of the ERP components.

As convLSTM networks perform better on shorter sequences, the trials were again downsampled to 250 Hz. To preserve the spatial information present in the data, the electrodes were mapped to a 5x5 2D map as shown in figure 5.2. This was done for each time sample, converting each trial to a (number of time samples x 5 x 5) 3D matrix that can be used as input for the neural network. The first layer of the network was a convLSTM layer in which the sequence of 2D input maps was passed through the recurrent convolutions of 6 filters with size 2x2. Here, the tanh-function was used as the activation function. In order to reduce overfitting, a dropout of 0.2 was used together with a recurrent dropout of 0.1. In the second layer, the data was batch normalized with the batch size set to 128 samples. The convLSTM and the batch normalization layers were repeated in the third and fourth layers of this network. For each time index, the maximum value obtained across the different filters is selected, after which the data is flattened into a 1D array of size (number of time samples). The final layer of the model was a dense layer that outputs the estimate of the P300

Table 5.1. Full details of the EEGNet architecture. The network starts in the first block with a temporal convolution (Conv2D) to learn the frequency filters, after which the depthwise convolutions (DepthwiseConv2D) are used to learn frequency-specific spatial filters. The second block initially learns a temporal summary for each feature map individually (SeperableConv2D), and finally learns to mix the feature maps together. More details about the network architecture can be found in the work of Lawhern et al. (2018).

Block	Layer	No. filters	Size	No. params	Output	Activation function	Options
1	Input		1 x 20 x 101				
	Conv2D	8	1 x 64	512	(8, 20, 101)	Linear	padding = same, use_bias = False
	BatchNorm			32	(8, 20, 101)		
	DepthwiseConv2D		20 x 1	320	(16, 1, 101)	Linear	use_bias = False, number of depth wise convolution output channels = 2, max norm constraint function = 1
	BatchNorm			64	(16, 1, 101)		
	Activation				(16, 1, 101)	ELU	
	AveragePool2D		1 x 4		(16, 1, 25)		
	Dropout				(16, 1, 25)		p = 0.5
2	SeperableConv2D	16	1 x 16	512	(16, 1, 25)	Linear	padding = same, use_bias = False
	BatchNorm			64	(16, 1, 25)		
	Activation				(16, 1, 25)	ELU	
	AveragePool2D		1 x 8		(16, 1, 3)		
	Dropout				(16, 1, 3)		p = 0.5
	Flatten				(48)		
Latency estimation	Dense	1		49	(1)	Linear	

latency. The model was again fitted using the Adam optimizer, with the default parameters available in the Keras API, to minimize the mean squared error loss function. A summary of the network architecture is given in table 5.2 and shown in figure 5.2.

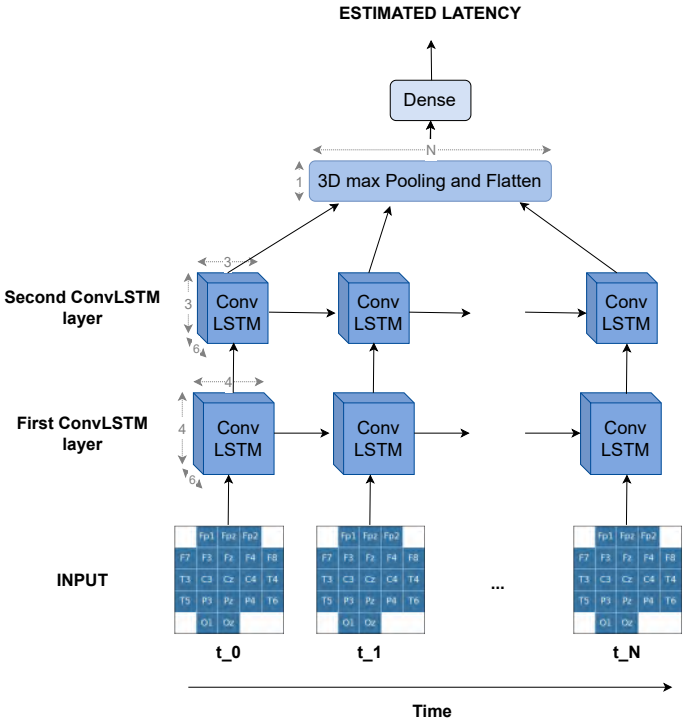

Figure 5.2. Overall visualization of the ConvLSTM network. Full details of the architecture can be found in table 5.2. The network consists of two consecutive ConvLSTM layers followed by a pooling layer and a linear dense layer to estimate the latency of the ERP component. In this type of recurrent neural network, the model can hold and use information obtained from previous time points it has seen to make decisions.

5.2.3 Experimental pipeline

Data simulation

In this work, simulated data is needed 1) to train the neural networks and 2) to quantify the performance of the different methods. The general approach that is used here is to add an ERP waveform at a known latency to background EEG data. A visual overview of the process described here is shown in figure

Table 5.2. Full details of the ConvLSTM architecture. The network consists of two consecutive convolutional LSTM layers followed by a pooling layer and a linear dense layer to estimate the latency of the ERP component.

Layer	No. filters	Size	No. params	Output	Activation function	Options
Input				101 x 1 x 5 x 5		
ConvLSTM2D	6	2 x 2	696	(101, 6, 4, 4)	hyperbolic tangent	dropout = 0.2, recurrent_dropout = 0.1
BatchNorm			16	(101, 6, 4, 4)		
ConvLSTM2D	6	2 x 2	1176	(101, 6, 3, 3)	hyperbolic tangent	dropout = 0.2, recurrent_dropout = 0.1
BatchNorm			12	(101, 6, 3, 3)		
MaxPooling3D		6 x 3 x 3		(101, 1, 1, 1)		
Flatten				(101)		
Dense	1		102	(1)	Linear	

5.3. To create the simulated ERP waveform, we start by calculating the average response over trials and participants for both conditions separately, i.e. for the standard and deviant stimuli in the oddball paradigm (P300 dataset) and the correct and incorrect stimuli in the SSCT (N400 dataset). We then calculate the difference between both conditions to obtain the topography of the ERP waveform that will be used. The shape of the ERP component is simulated as a half-cycle sinusoidal wave. As the goal is to generate a dataset that resembles the experimental data, we decided to use the epochs recorded while presenting the standard phoneme (P300 dataset) and the correct sentences (N400 dataset) as background EEG data.

Simulated epochs were then generated using the EEG data of all participants in the experimental dataset. For each simulated subject, the EEG data of only one participant was used as background EEG data. To introduce inter-subject variability, the frequency of the sinusoidal waves used for the ERP component was uniformly drawn to obtain a signal length between 100 ms and 300 ms. Furthermore, different uniform latency distributions were simulated for each participant by sampling a mean latency between 350 ms and 550 ms and a standard deviation between 40 ms and 80 ms. For the mean latency, the shape of the grand-average of the experimental data within this time window was used as the sampling distribution, while a uniform distribution was used for the standard deviation. After randomly selecting half of the standard/correct trials, the ERP component was added to the data using latencies sampled from the previously created distribution. In order to keep the latency of the ERP component within the expected range for healthy controls, trials for which the generated latency was outside the time window of 300 ms to 600 ms were excluded from the dataset (Aerts et al., 2015). Finally, to increase the amount of generated data, this process was repeated 30 times.

Pipeline for the performance evaluation on simulated data

We evaluated the performance of each of the different ERP quantification methods on a simulated dataset using different SNRs. For the simulated data, the P300 dataset was used as the basis. The proposed approach for data simulation easily allows generating data with different SNRs by scaling the amplitude of the ERP component that is added to the data. Here, the SNR of the original dataset was determined as the ratio of the power at the peak of the grand-average deviant waveform and the power of the standard trials. Five different SNRs were simulated, namely -6dB, -3dB, +0dB, +3dB and +6dB. For each

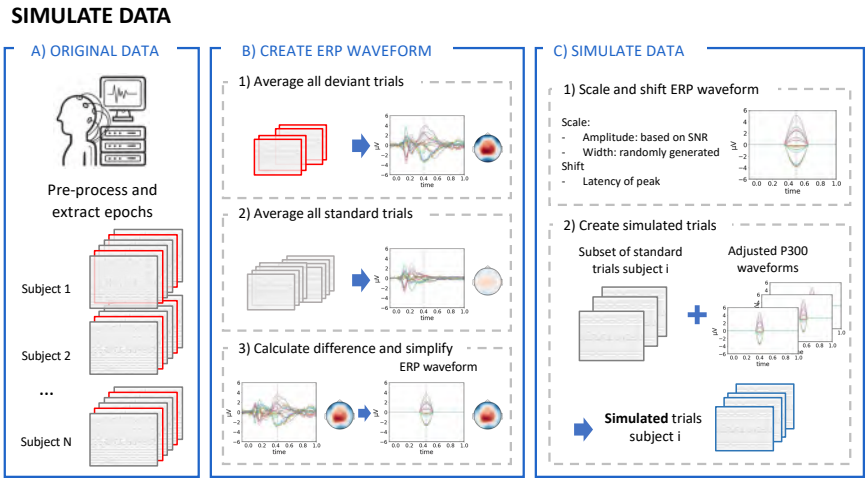

Figure 5.3. Visual overview of the approach used to generate simulated data. The images used in this overview figure are generated using the P300 dataset, however, the same approach can be used to simulate data based on other datasets and other ERP components. The general approach that is used here is to add an ERP waveform at a known latency to background EEG data. (A) To do this, we start by pre-processing the original data and extracting the epochs for both conditions. (B) We then generate the topography of the ERP waveform by calculating the average response over trials and participants for both conditions separately, after which the difference between both conditions is calculated. The topography at the time of the peak in this difference waveform is then used for the ERP waveform. (C) Finally, the simulated trials are generated by first scaling the amplitude of the ERP waveform according to the SNR and the width. The ERP waveform is then shifted to the correct latency, after which it is added to the data of a standard trial, serving as background EEG data, to construct the deviant trials.

SNR, the topography of the added ERP component was scaled so that the ratio of the power at the peak of a waveform obtained after averaging the same amount of trials as in the original dataset, and the power of the standard trials was respectively -6dB smaller, -3dB smaller, equal, +3dB larger, or +6dB larger compared to the SNR of the original dataset.

As each of the proposed latency estimation techniques needs a form of training or learning from the data (i.e. defining the template or learning the model parameters), the performance of the different ERP quantification techniques was evaluated using a seven-fold cross-validation approach. The simulated data was split into seven different groups, so that all data generated using the original data from a particular subject was included within the same split. This

was done to guarantee independence between the train and test sets. For each fold, the (initial) template used by the template matching methods was created using only the data in the training set. This was done by calculating the difference wave between the grand averages of the deviant and standard trials between 300 ms and 600 ms, after which a 5 Hz low-pass filtered was applied. The obtained template was then used to estimate the latency of the ERP component in the trials of the test set. Similarly, both the EEGNet network and the convLSTM network were trained using the data in the training set after which the model was used to estimate the ERP latencies in the test set.

Different evaluation criteria were used to evaluate the performance of the methods on the simulated trials. First, to assess the latency estimation in the single trials, the mean absolute error between the true and the estimated latencies were calculated for the different SNRs. This was done by calculating the absolute error for each trial separately and then averaging the errors over all trials and all subjects. The different methods were also evaluated at the level of individual subjects. After estimating the latencies in the single trials, the mean latency was calculated per subject. This approach allows us to compare the latencies obtained using the averaging-based methods with the single-trial estimation methods. To do this, the mean absolute error between the true mean latency and the estimated mean latency was calculated for each subject and each SNR. Also the topography and the shape of the ERP component obtained with the different methods were evaluated. First the correct topography and shape of the ERP component were calculated by realigning all trials of a specific subject according to the correct latencies. For the averaging-based methods, no realignment was done, and the average waveform was used to quantify the topography and shape of the ERP component. For the single-trial estimation methods, on the other hand, the different trials were realigned according to the estimated latencies before averaging and quantifying the topography and shape of the component. The topographies obtained with the different methods were then compared with the true topography using the mean absolute error. The obtained P300 shapes were compared over the specified time window by calculating the mean absolute error between the true realignment and the realignment based on the estimated latencies. As the SNR of the dataset influences the obtained metrics, the measures were normalized by the absolute amplitude and the area of the true P300 component, respectively, resulting in the relative mean absolute error (RMAE). This approach allows comparing the methods over the different datasets in the simulated data. A visual overview of

this pipeline is shown in figure 5.4. The process was repeated for each of the different train-test splits, allowing us to also evaluate if the results are biased by the specific selection of samples within each fold.

Finally, the (realigned) average waveforms of all subjects were realigned to the estimated mean latencies before averaging to obtain the realigned grand-average waveform for each method. Then, the relative absolute error between the true and the estimated grand-average for each of the different methods was calculated to evaluate the obtained shape of the P300 component.

Pipeline for the performance evaluation on experimental data

The different proposed methods were also applied to both experimental datasets. In these datasets, the true latency of the P300 component in the individual trials is unknown, making it impossible to use this data to train the parameters in the convLSTM network and to use error-based metrics to evaluate the performance of the different methods. A visual overview of the pipeline used in this scenario is shown in figure 5.5. For the template matching-based methods, the (original) template is created by calculating the difference between averages of the deviant and standard trials across all subjects, after which a 5 Hz low-pass filtered is applied to smooth the template. For the neural network based approaches, simulated data is created to train the parameters in the networks using the approach described before. The latencies of the ERP component in the experimental trials are then calculated using the trained networks.

Dataset 1: Oddball paradigm eliciting a P300 component: To evaluate the performance of the methods on the P300 dataset, the approach proposed by Ouyang et al. (2017) was used. Here, the correlation between the estimated latency and the reaction time of the subject was calculated and used to evaluate each of the different methods. This approach is based on the knowledge that, under particular conditions, the neurocognitive processing stream that underlies the stimulus evaluation affects the response time of subjects (Da Pelo et al., 2018). Furthermore, to evaluate the ability of the different methods to estimate the shape of the P300 component on the experimental dataset, all trials were realigned according to the estimated latencies and averaged across all subject, after which the obtained waveforms were visually compared.

Since the first description of the P300 component in 1965 (Sutton et al., 1965), an abundant amount of research has been done to study the component.

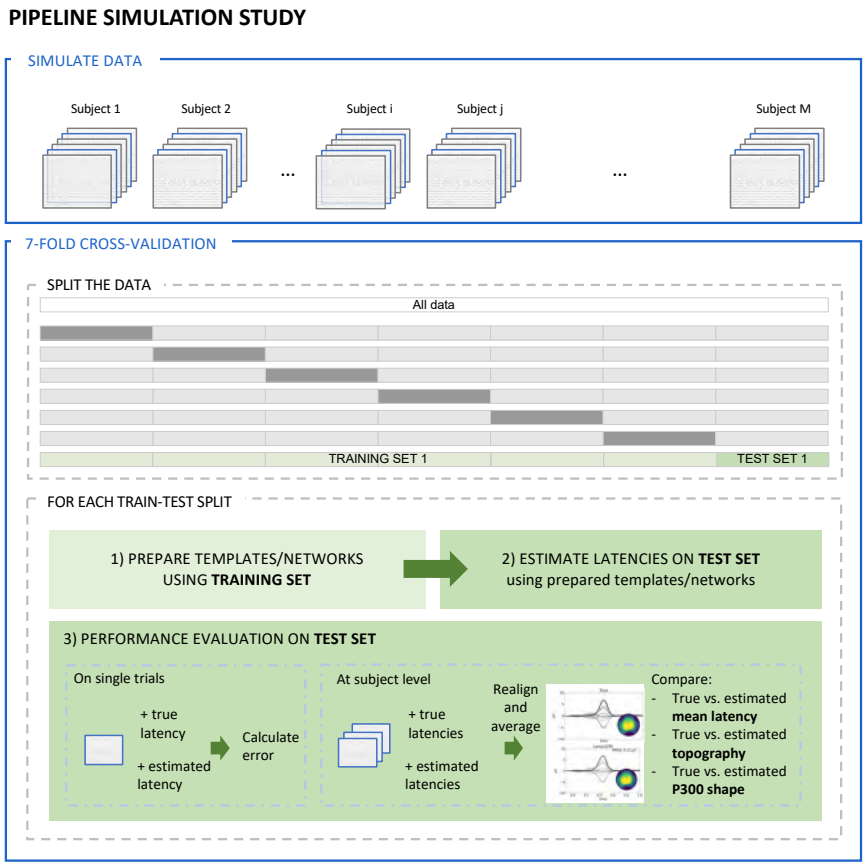

Figure 5.4. Visual overview of the approach used to evaluate the performance of the different single-trial latency estimation methods using simulated data. In the first step, the simulated data is split into seven different folds. To guarantee the independence between the train and test sets, this was done in a way so that all data generated using the original data from a particular subject was included within the same split. For each fold, the (initial) template are created and the neural networks are trained using only the data in the training set. In the next step, these templates and networks are then used to estimate the latencies of the individual trials in the test set. Finally, the performance of each of the different latency estimation techniques is evaluated. By repeating this process for each of the different folds, we can assess the variance across folds.

An important finding is that the P300 latency is sensitive to neural changes in both development and aging. Different studies have shown that while the P300 latency decreases with age during childhood and adolescence (Polich et al., 1990; Sangal et al., 1998; van Dinteren et al., 2014), it starts increasing again in early adulthood (Rossini et al., 2007; Walhovd et al., 2008; van

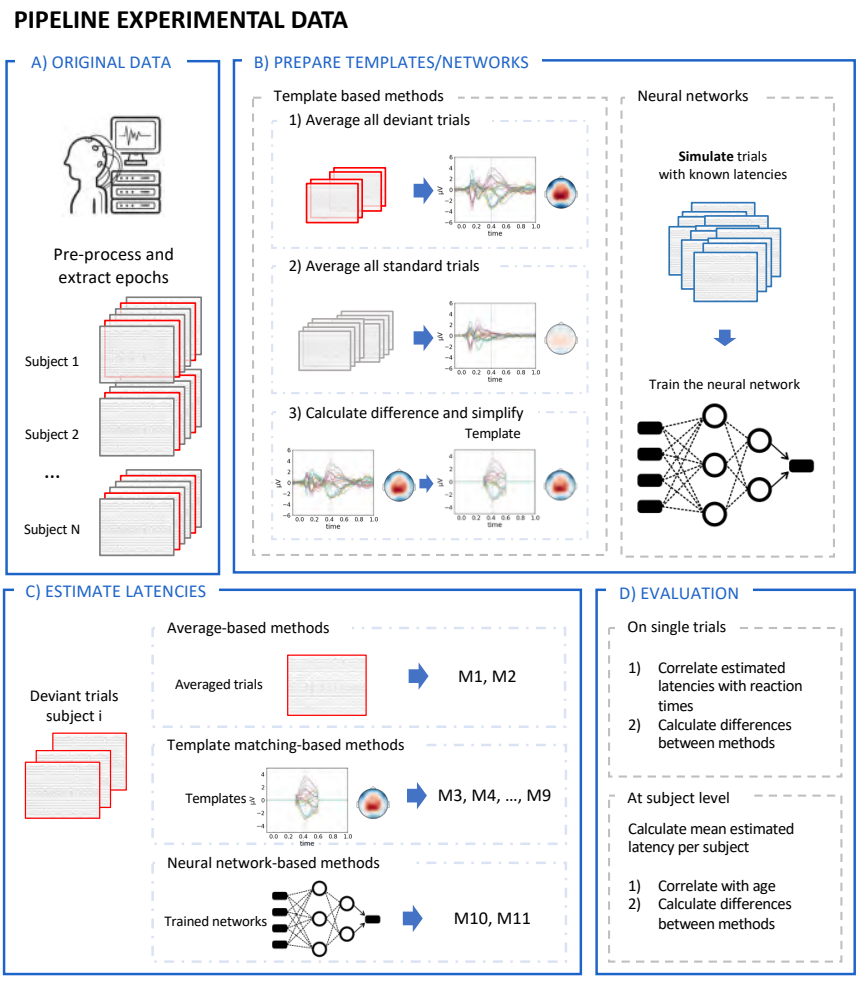

Figure 5.5. Visual overview of the approach used to estimate the latencies of the individual trials on experimental data. Starting from the pre-processed data, the templates used by the template matching methods are created by calculating the average response over trials and participants for both conditions separately, after which the difference between both conditions is calculated. This difference waveform is then filtered to remove noise and cropped to the time window of interest. For the neural networks, first simulated trials are created following the approach described before, after which the networks are trained using this simulated dataset with known latencies. The obtained templates and trained networks are then used to estimate the latencies of the deviant trials, after which the performance of the different methods is evaluated using different methods depending on the dataset that is used.

Dinteren et al., 2014; Brown et al., 1983; Hirayasu et al., 2000). We will use the mean latencies estimated on the experimental data by each of the different methods to model the effect of age on the latency of the P300 component and to see which method results in the best fit of the model. For each method, a linear regression line is fitted to the data and the slope of the curve is observed to evaluate whether an increase of latency with age is found. The goodness of fit of the regression lines is then evaluated using the root mean squared error (RMSE).

Dataset 2: SSCT paradigm eliciting an N400 component: As the button press response was delayed in the SSCT task, it is not possible in this case to use the reaction times as a measure to evaluate the single trial latency estimation methods. Instead, in this dataset we will investigate the effect of age on the N400 component using the different single trial latency estimation methods.

In the paper of Cocquyt et al. (2023), the authors found that the amplitude of the N400 effect, i.e. the difference between the incorrect and correct evoked responses between 0.3 s and 0.5 s after stimulus onset, was significant smaller in the older subjects (ages 60-79) compared to the young subjects (ages 20-39). Furthermore, also the latency of the N400 effect was significantly delayed in elderly compared to both the young and the middle-aged subjects (ages 40-59). In this study, we will try to replicate these findings and investigate if the changes in amplitude across age are caused by changes in the amplitudes of individual trials, by variability in latency, or by a combination of both factors. To do this, we will estimate the latency of the N400 effect using both the averaging based methods and the single-trial latency estimation methods. As in this case the N400 effect is investigated, we will subtract the averaged response to the correct trials from the incorrect trials for each subject before estimating the latency of the N400 effect. The amplitude of the N400 effect will be calculated as the mean amplitude of the difference in evoked responses between the incorrect and correct conditions within the 0.3 s-0.5 s time window at the Cz electrode for the averaging-based method. For the single-trial latency estimation techniques, the averaged response to the correct trials will be subtracted from the incorrect trials before realignment. The amplitude of the N400 effect is then again calculated as the mean amplitude of this realigned waveform within the 0.3 s-0.5 s time window at the Cz electrode. For each method, the effect of aging on both the latency and the amplitude of the N400 effect will be investigated using a univariate analysis of variance (ANOVA) approach with

age group as independent variable. Significant main effects will be investigated by post hoc multiple comparisons with a Bonferroni correction.

5.3 Results

5.3.1 Simulated data

Performance at single trial level

In figure 5.6, the mean absolute error between the true and the estimated latencies are shown for each single-trial latency estimation method in function of the SNR level of the trials averaged of the different folds. Also the standard deviation of the mean absolute errors over the different folds is shown. The figure indicates that for the lower SNRs, both neural network-based approaches and single component ICA outperform all other methods. For higher SNRs, similar performance is also achieved by the cross-correlation based techniques. As expected, in general the estimated latencies improved for higher SNRs. However, only limited improvement is obtained using single component ICA and even a small decrease in performance is found using DTW-based template matching. For the single component ICA approach, this effect might be caused by the nature of the simulated data, as these simulations were created by adding an independent P300 component with varying amplitude to background noise. The results suggest that the decomposition algorithm might be able to extract this P300 component from the data even for very low SNRs. For the multiple component ICA approach, the performance does improve with increasing SNR, but large differences in performance are found compared to the single component ICA approach. It is probable that by selecting multiple components to create the P300 ICA subspace, also non-P300 related activity and noise are included, disrupting the time-series that are subsequently used to correlate with the template.

The DTW-based approach leads to large errors in the latency estimation for all SNRs, with the method performing only slightly better or even worse than randomly estimating the single trial latency. This is probably caused by the difference in amplitude of the template and the P300 component in single trials. The template is created by calculating the difference wave between the grand-averages of the deviant and standard trials within a time window and therefore represents a smeared version of the P300 component. As the DTW algorithm calculates the Euclidean distance between the template and the time

series to obtain the optimal warping path, this difference in amplitude strongly influences the latency estimates obtained.

Finally, comparing the template-matching techniques with their iterative variants, the results indicate that the performance of the DTW technique is improved by iteratively updating the template, especially for larger SNRs. Likely, the amplitude difference between the template and the single-trial P300 component becomes smaller, as fewer trials are taken into account when updating the template per subject, improving the performance of the DTW algorithm in the estimation of the P300 latency. The performance of the beamformer, on the other hand, decreases when the template is updated for each subject, while the performance of the correlation method and that of its iterative variant are similar.

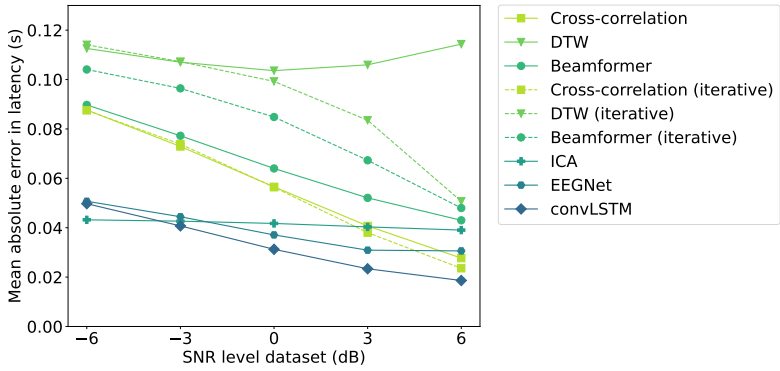

Figure 5.6. Comparison of the different methods regarding the mean absolute error between the estimated latencies and the true latencies in single trials for each each SNR in the simulated data.

Performance at subject level

The different latency estimation approaches were also compared at the level of individual subjects. In figures 5.7A, B and C respectively, the mean absolute error in mean latency, the relative absolute error in the topography and the relative absolute error between the shapes of the estimated and correct realignments are shown for the different SNR levels of the trials. Looking at the error in the mean latency, the figure shows that the EEGNet network, the convLSTM network and the single component ICA-based approach all outperform both averaging-based methods. The results also indicate that using the peak method, larger errors in the estimated mean latency are made and more

variability across the different cross-validation folds are found compared to all other methods, especially for small SNRs.

Figures 5.7B and C indicate that both the topography and the shape of the estimated P300 component after realignment improve with increasing SNR for all methods except the DTW-based approach. As for the latency estimations, best results regarding the estimation of topography and shape of the component are obtained using the neural network approaches and the single component ICA-based method. Furthermore, figure 5.7C indicates that the shape of the P300 component is better approximated using these methods compared to the averaging approach, even for low SNRs. Estimating the latency of the P300 component at the level of single trials thus not only offers more information on the variability of the timing of the P300 component within a subject, but also results in a better estimate of the shape of the component.

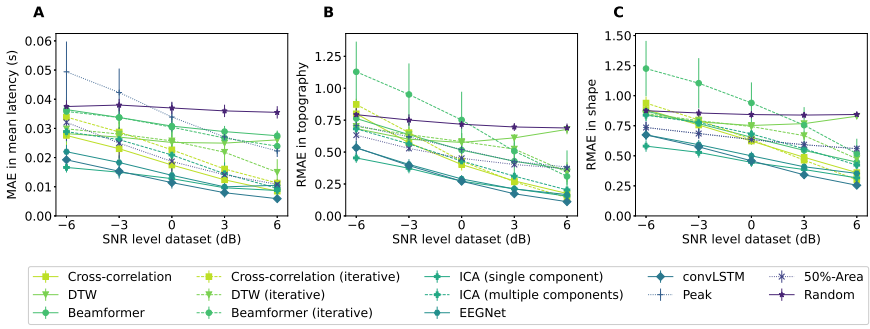

Figure 5.7. Comparision of the P300 quantification results of the different methods on the simulated datasets on subject level. **(A)** Mean absolute error between the estimated mean latencies and the true mean latencies for each method and each dataset. **(B)** Relative absolute error in topography between the estimated topography and the true topography for each method and each dataset. **(C)** Relative absolute error in shape between the estimated shape of the P300 component and the true shape of the P300 component for each method and each dataset.

Finally, in figure 5.8 the realignment of the single trials averaged across all subjects with SNR +0dB is shown for each of the different methods, along with the topography at the time of the peak. Also the non-realigned grand-average and a random realignment are plotted as a reference. The realigned grand-averages are compared with the correct realignment to check how well the shape of the P300 component is estimated by each of the different methods by calculating the mean relative absolute error (MRAE). The figures show that the realignment based on the convLSTM network gives the best results. While

the topographies at the peak are very similar across all methods, apart from a scaling factor due to smearing, the shape of the obtained P300 component clearly varies. In the iterative cross-correlation, the (iterative) beamformer and the multiple component ICA based approaches, artefacts are being introduced into the shape of the component due to errors in latency estimations. The figures for the other SNRs are added in appendix B.

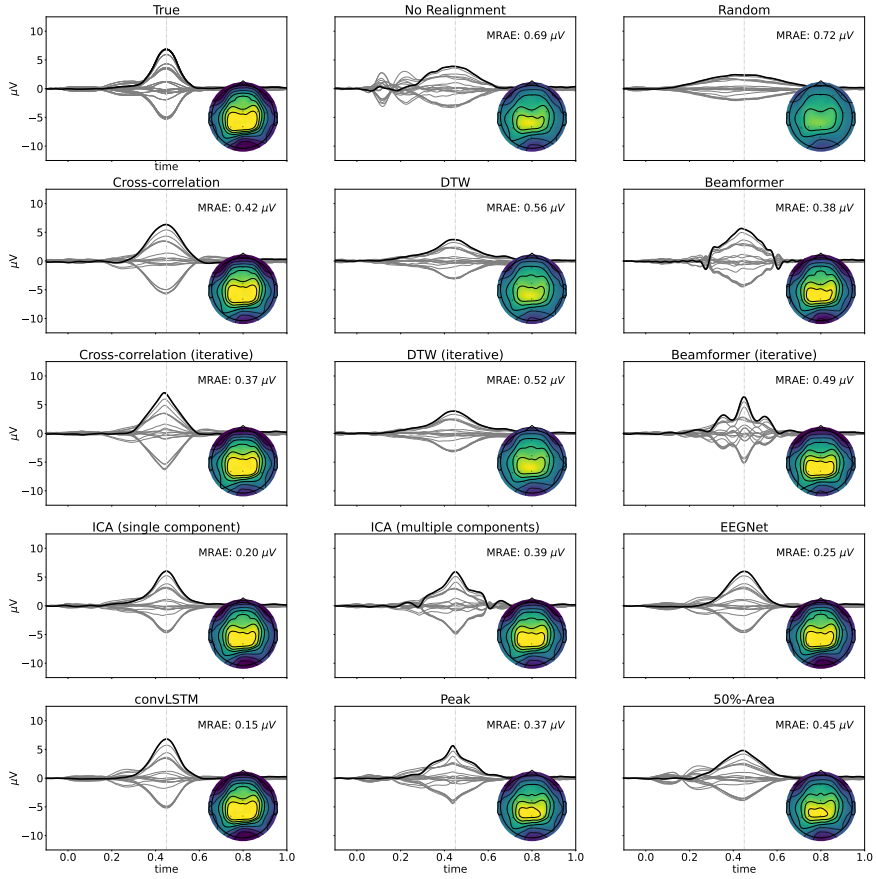

Figure 5.8. Realignment of the single trials averaged across all subjects with SNR +0dB for each of the different methods. Grey lines represent the different channels, with Pz being marked in black. Also the topography of the realignment at 0.420 s after the stimulus onset is shown. The realigned waveforms are compared to the correct realignment to evaluate how well the shape of the simulated P300 component is estimated. For each method, the mean relative absolute error between the true and the estimated realigned waveforms across all subjects is reported.

5.3.2 Experimental data

Dataset 1: Oddball task eliciting a P300 component

The performance of each of the different methods on the experimental data was first evaluated by looking at the correlation of single-trial latencies with the corresponding reaction times (table 5.3). The highest correlations were found for the neural network approaches, followed by the iterative cross-correlation method and the beamformer technique. Comparing the template matching techniques with their iterative variants, we see that iteratively updating the template improves the correlation value for the cross-correlation method and DTW, which is in line with the results obtained using the simulated data. While the performance of the neural networks and that of the single component ICA-based approach was similar on the simulated data, the correlation between the latencies estimated by single component ICA and the reaction times is very low in the experimental dataset. Furthermore, while the performance of single component ICA was better than the multiple component approach on the simulated data, the opposite is found on the experimental data. This confirms our theory of the excellent performance of single component ICA on the simulated dataset being due to the nature of the simulations.

Next, figure 5.9 shows the realigned averaged waveforms across all subjects, using the estimates of the different methods. By visually inspecting the figures, we see that most single-trial methods result in a more narrow P300 component with similar topography to that obtained without realignment of the trials. While the realigned waveforms using the peak and area method are slightly more narrow than the waveform without realignment, the effect is clearer for the single-trial methods. This indicates that there is indeed within-subject variability of the P300 latency. The figures also show that the realignments using the DTW- and single component ICA-based approaches result in a more smeared out version of the P300 component, resembling the waveform obtained using random latencies in the simulated dataset. This suggests that the latencies obtained using these methods might be incorrect. On the other hand, realigning the epochs using the iterative cross-correlation, the iterative beamformer or the peak methods results in peaks in the realignment, which are similar to the shapes obtained with these methods on the simulated data, indicating that this might be an artefact induced due to errors in the latency estimation.

Finally, the relationship between the mean estimated P300 latency and age of the subjects for each of the different methods is shown in figure 5.10. For each

Table 5.3. The correlation between the reaction time and the latencies estimated by the different methods for each single trial in the P300 experimental dataset

Method	Correlation with RT
Cross-correlation	0.20
DTW	0.08
Beamformer	0.25
Cross-correlation (iterative)	0.26
DTW (iterative)	0.14
Beamformer (iterative)	0.23
ICA (single component)	0.10
ICA (multiple components)	0.17
EEGNet	**0.29**
convLSTM	**0.30**

method, a linear regression line was fitted to the data. The goodness-of-fit of the regression is evaluated using the RMSE, and the slope of the curve is used to evaluate the relationship between the mean estimated P300 latency and the age of the subject. As expected based on literature (van Dinteren et al., 2014), most methods show an increase in estimated P300 latency with age. However, this is not the case for single component ICA and iterative DTW, where even a small decrease is found. The effect is also very limited for the multiple component ICA approach. These results further illustrate that these approaches to estimate the latency in single trials may lead to incorrect results. The strongest increases in latency with age are found for the averaging-based methods and for the cross-correlation techniques. Comparing the results of the peak method and the 50%-area latency estimation method, a better fit is found for the 50%-area method, as the RMSE is smaller, illustrating that the 50%-area latency estimation technique should be preferred over the peak method when using averaging-based approaches. While these methods result in the largest slope, the best fits to the regression line are found using the neural networks and the ICA-based approaches.

Dataset 2: Semantic sentence congruity task eliciting an N400 component

Also for the second experimental dataset, the realigned averaged waveforms across all subjects were visually compared, using the estimates of the different methods. This result is shown in figure 5.11. We again notice more narrow ERP components when realigning according to the single trial latency estimates for the neural network based approaches, as well as for the (iterative) cross-

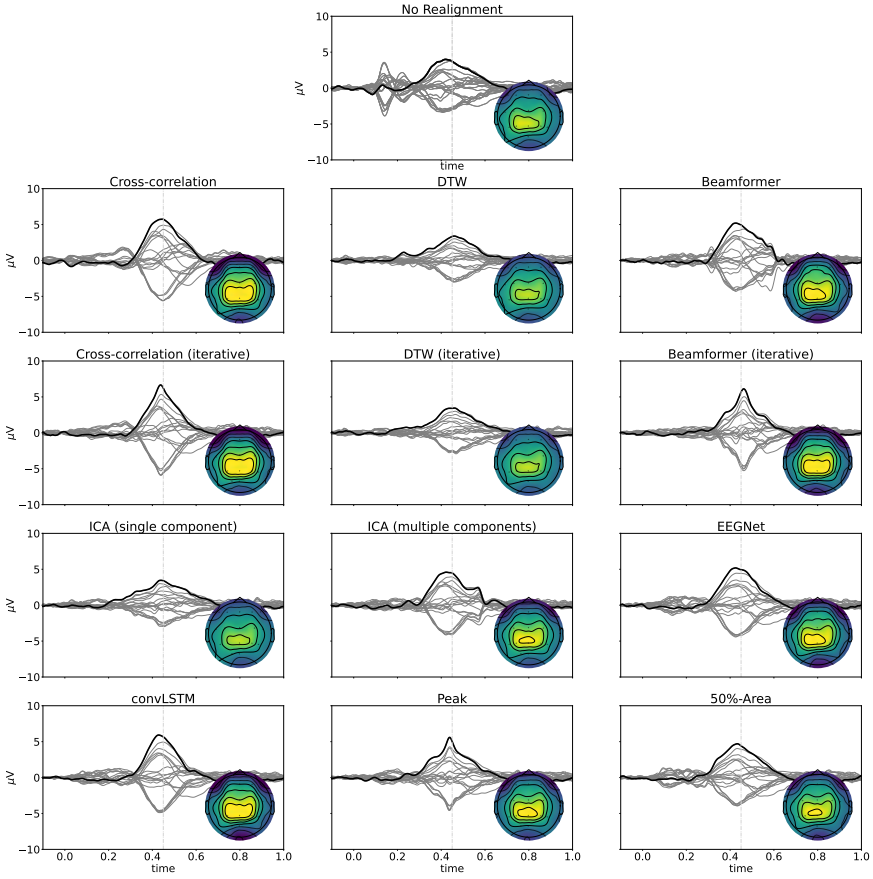

Figure 5.9. Realignment of the single trials averaged across all subjects in the P300 experimental dataset, obtained with the different methods. Grey lines represent the different channels, with Pz being marked in black. Also the topography of the realignment at 0.420 s after the stimulus onset is shown.

correlation and (iterative) DTW based template matching methods. The figure also indicates that realignments using the ICA based techniques result in smeared out versions of the N400 effect, again resembling the waveform obtained using random latencies in the simulated dataset.

Furthermore, we investigated the effect of using single-trial latency estimation techniques compared to the classical averaging approach on the statistical analysis of the effect of age on the latency and the amplitude of the N400 effect. To do this, we estimated for each subject the mean and the standard deviation of the estimated latency, and compared the obtained results over three different age categories: young (ages 20-39), middle-aged (ages 40-59) and elderly

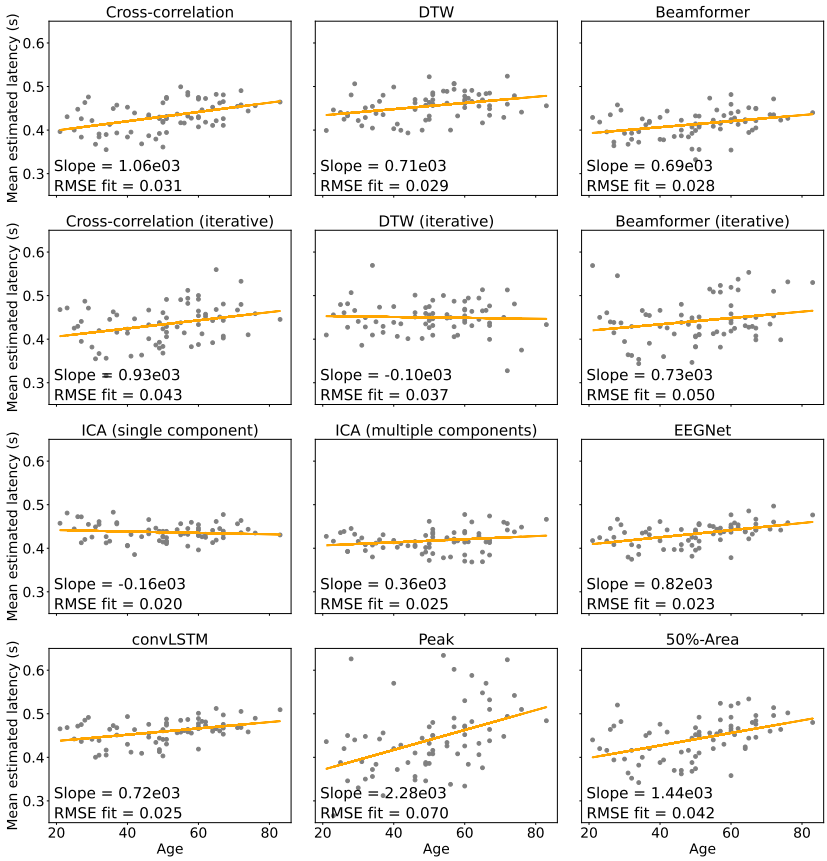

Figure 5.10. Scatterplot and regression lines of the relationship between the mean estimated latency of the P300 component and the age of the subject for each of the different methods.

(60-79). The results are shown in table 5.4. The original paper by Cocquyt et al. 2023 reported a significant effect of age group on the latency of the N400 effect, with post hoc pairwise comparisons using bonferroni correction revealing a significant delay in elderly compared to both the young and middle-aged subjects. We reproduced these results using the 50%-area approach, as was done in the original paper, and were able to find similar results using the EEGNet and the convLSTM networks. While significant effects of age were also found using the DTW and iterative beamformer approaches, post-hoc analyses in these cases only reported significant delays between the elderly and the young subjects. Looking at the standard deviation per subject over the estimated latencies, significant effects of age are found using the cross-correlation,

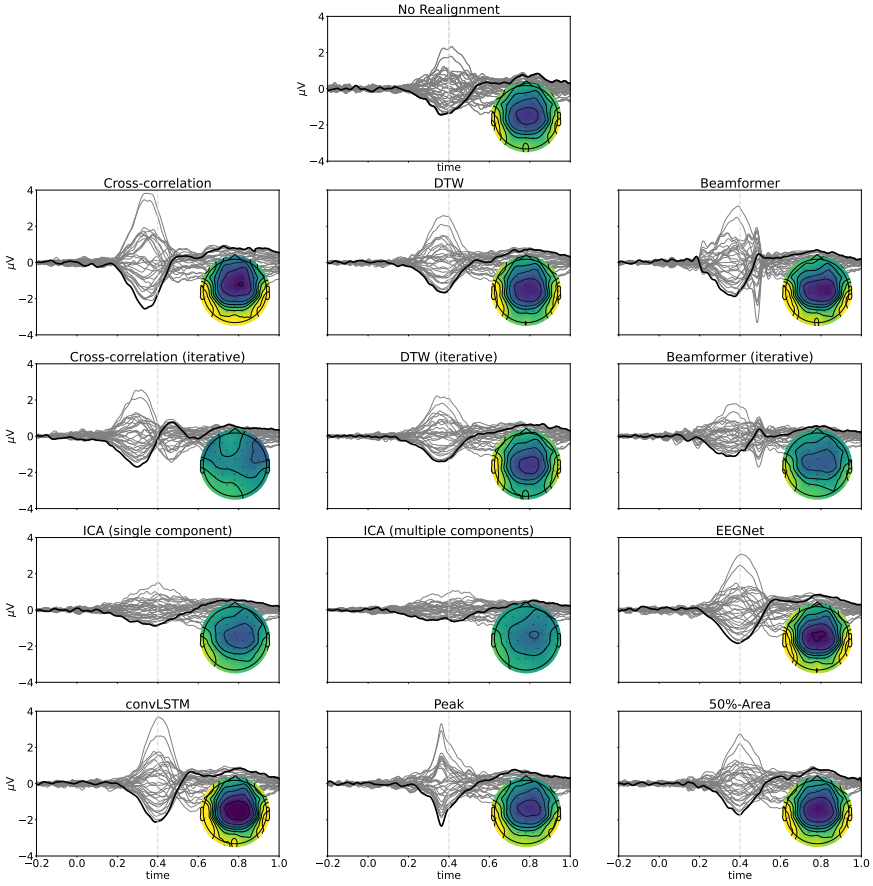

Figure 5.11. Realignment of the single trials averaged across all subjects in the N400 experimental dataset obtained with the different methods. Grey lines represent the different channels, with Cz being marked in black. Also the topography of the realignment at 0.400 s after the stimulus onset is shown. The realigned waveforms are compared to the correct realignment to check how well the shape of the N400 component is estimated.

beamformer and multiple component ICA approaches, as well as for the neural networks. Post-hoc analyses reveal increased variations in latency in the young subjects compared to the middle-aged (EEGNet and convLSTM) as well as compared to the elderly subjects (cross-correlation, multiple component ICA, EEGNet and convLSTM).

Finally, we compared the effect of age on the amplitude of the N400 effect using both the classical averaging approach and using the estimated latencies to realign the single trials before calculating the amplitude. Here, we found a

significant effect of age for the classical averaging approach, as well as after realignment using the (iterative) cross-correlation techniques, the iterative DTW and both neural networks. As in the original paper, post-hoc analyses showed that the young subjects had a significant larger N400 effect compared to the elderly subjects (all methods with significant effect of age). However, using the (iterative) cross-correlation methods and the neural networks, also significant differences were found between the young and the middle-aged subjects, with the young subjects having a larger N400 effect.

Table 5.4. Overview of the statistical results on the mean and standard deviations of the estimated latencies, and on the amplitudes of the N400 effect, elicited during the semantic sentence congruity task.

	Mean latency		Standard deviation latency		Amplitude	
	F-values	p-values	F-values	p-values	F-values	p-values
Cross-correlation	0.355	ns	7.154	***	4.277	*
DTW	3.828	*	0.167	ns	0.257	ns
Beamformer	2.227	ns	3.284	*	2.528	ns
Cross-correlation (iterative)	1.386	ns	2.024	ns	4.295	*
DTW (iterative)	0.564	ns	1.052	ns	3.831	*
Beamformer (iterative)	3.759	*	1.733	ns	2.060	ns
ICA (single component)	0.872	ns	2.321	ns	1.892	ns
ICA (multiple components)	2.636	ns	4.566	*	1.992	ns
EEGNet	9.355	***	4.581	*	6.585	**
convLSTM	7.308	***	12.360	***	7.230	***
Peak	1.149	ns	NA	NA	5.501	**
50%-area	6.095	**	NA	NA	5.501	**

5.4 Discussion

Different methods for the quantification of the ERP component were evaluated both on simulated data and on experimental data. We have shown that deep learning-based methods, namely the EEGNet approach and the convLSTM network, perform very well on all, proving the applicability of these neural networks to quantify ERP components in single trials. For low SNRs in the simulated dataset, the single component ICA approach worked slightly better than the neural networks. However, only limited differences were found between the estimated latencies, the topographies and the shapes of the ERP components obtained using these approaches. Interesting to notice is that while single component ICA gave excellent results on the simulated dataset for all SNRs, the performance of this method is much lower on the experimental data. This discrepancy between the results could be explained by the nature of the simulated dataset. As this dataset was created by adding an independent ERP compo-

nent to background EEG data, the ICA algorithm was probably able to clearly separate this component. Therefore, it is likely that a good fit between this component and the template was found. In the experimental dataset, however, the data is more complex. There is likely more variability in the topography of the ERP component, resulting in a mismatch between the template and the selected ICA component containing the ERP. This is further confirmed by the differences in performance between the single and multiple component ICA approaches, as the multiple component ICA approach performed better than the single component approach on the experimental data.

The performance of the single-trial latency estimation techniques was also compared to that of averaging-based approaches in terms of the estimated latencies, and the topography and shape of the obtained ERP component after realignment. The results on both the experimental datasets and the simulated data showed that the neural network based approaches typically performed better than the averaging approaches. The results also clearly indicate that when using averaging-based approaches, the 50%-area based approach should be preferred over the peak-based method. The drawback of this averaging approach, however, is still that it is unable to correctly capture the shape of the ERP component and that it does not provide information on the variability of the latency of the ERP component.

The added value and the usability of single trial latency estimation using the neural networks was proven on the SSCT dataset, where we were able to show a larger N400 effect in the young subjects compared to both the middle-aged and elderly subject, while only significant differences between the young and elderly subjects were found using the averaging approach in both the original paper and this work. This amplitude reduction of the N400 effect with age from middle age on, was already shown by Gunter et al. (1992), and Cocquyt et al. (2023) attributed the discrepancy in the result to differences in the age range under investigation. However, our results using the neural networks showed that the effect of age on the amplitude of the N400 effect is indeed present in the data from the middle age on. Furthermore, by including the information from the standard deviation of the estimated latencies in the single trials, which was found to be larger in younger subjects compared to both the middle-aged and elderly subject, we are able to confirm that the significant changes in the amplitude of the N400 effect are indeed due to changes in amplitude and are not caused by latency jitter of the N400 effect. This is also in line with the findings of Hoffman & Morcom (2018), who reported reduced activity in some regions

of the typical left-hemisphere semantic network which have been reported as potential generators of the N400 effect, namely the inferior prefrontal, posterior temporal and inferior parietal cortex, in older subjects compared to the younger. These findings show the added value of including single trial latency estimations in the analysis of the data.

In this paper, we adapted different neural networks to quantify the ERP component in single trials and compared it to other methods commonly used in literature using both simulated and experimental data. Even though we attempted to create the simulated dataset as realistic as possible, certain assumptions, such as the topography and simplified shape of the ERP component, influence the obtained dataset and the performance of the different methods. Furthermore, these assumptions also affect the results obtained on the experimental dataset. As no information on the component latency is present in the experimental data, the parameters of the neural networks can only be learned based on simulated data. This is an important limitation of deep learning approaches for single-trial ERP component quantification. If the assumptions about the shape or the topography of the ERP component in the simulated data are incorrect, the network will not be able to perform well on the experimental data. The need for the simulated data also limits the applicability of the networks on datasets where the ERP components of interest are not known a-priori. In this case, data-driven approaches, such as topographic analyses of variance and microstate analyses, have a clear advantage, as they allow to estimate the ERPs without being limited to one peak selected beforehand. Another remark that can be made is that the same ERP component may have different characteristics in different populations. In this case, however, it would be possible to train different networks for the different populations, or to include characteristics of both populations under investigation in the simulated data, thereby making the network more robust. Also more advanced methods to generate the simulated data could be used, for example using ICA to extract one or more subcomponents of the ERP component from the original data and using them as ERP waveform that is added to the background EEG data that is used to train the network.

A final limitation of the neural networks approaches is that they work as a so-called black box, returning an estimation of the latency of the ERP component without giving insight into what the network's decision is based upon. This makes the deep learning approaches less interpretable compared to other methods such as the (iterative) cross-correlation method. Lastly, it is important

to note that each method always returns an estimate of the component latency even when no ERP component is present in the data. Therefore, it could be useful in future work to combine the ERP component classifiers used in BCIs with these latency estimation techniques.

5.5 Conclusion

Two deep learning approaches were proposed for single-trial latency estimation in ERP data. Application of these methods on both simulated and experimental data has shown that the neural networks outperform other single-trial latency estimation methods and thus that deep learning techniques can be used as a new approach to estimate the latency of ERP components in single trials. More specifically, we were able to show that the proposed approaches to quantify the ERP components resulted in better estimates of the topography and the shape of the components. On the P300 experimental data, higher correlations were found between the P300 single trial latencies and the reaction times of the subject. Furthermore, using the N400 dataset, we were able to show a larger N400 effect in the young subjects compared to both the middle-aged and elderly subjects, while only significant differences between the young and elderly subjects were found using the averaging approach. By including the information from the standard deviation of the estimated latencies in the single trials, we were also able to confirm that the significant changes in the amplitude of the N400 effect are indeed due to changes in amplitude and are not caused by latency jitter of the N400 effect, showing the added value of the neural networks for single-trial latency estimation compared to the averaging-based approaches. While the EEGNet network and the convLSTM network are more complex than other techniques proposed in literature, it allows researchers to better study the trial-to-trial latency variability of the ERP component, even in data with a low SNR. A drawback, however, is that simulated data needs to be created upfront to train the network, limiting the applicability of the proposed network to study ERP components about which limited information is known. In future work, the proposed neural network approach could be applied to both other ERP components, as well as to other populations where the ERP components may have different characteristics, to further study its validity.

6 | Disentangling ERP and Oscillatory Sources with eLORETA and DICS: A Comparative Study with Simulations and Empirical Data

Abstract

Event-related potentials (ERPs) and oscillations are often-used tools for investigating neural processing. The relationship between these two phenomena, however, remains debated: while some argue they reflect the same underlying neural processes, others suggest they arise from distinct mechanisms. In this work, we show that combining different EEG source imaging methods, namely eLORETA and DICS, can help us address this open question. We use simulations to illustrate the strengths and limitations of both methods, and real data to show how the complementarity of eLORETA and DICS can help us identify if the ERP and the oscillations originate from common or distinct neural sources. The source localization results for the P300 ERP component using eLORETA and DICS in the delta range converge. In this case, while the time-course of the alpha desynchronization aligns closely with that of the P300, the obtained localizations do not overlap. For the auditory N1, bilateral activation is found using eLORETA. While similar activity is found when localizing theta power in the corresponding time window using DICS, the accuracy in this case seems to be better when using eLORETA. Finally, the eLORETA and DICS localization results converge on a view of the N400 as a product of oscillatory dynamics within a distributed semantic network. The DICS localizations of the delta power increase, and the alpha and beta power decreases, all overlap with the obtained sources found using eLORETA. These findings point towards amplitude asymmetry mechanisms responsive to task demands. In sum, this study provides empirical and conceptual evidence for the complementary use of eLORETA and DICS in ERP research. By harnessing the strengths of both methods, we gain a richer, more mechanistic understanding of the temporal and spectral processes that give rise to stimulus-locked brain responses.

6.1 Introduction

Event-related potentials (ERPs) are a powerful tool for investigating the temporal dynamics of neural processing, offering millisecond-level resolution of brain activity. ERPs are time-locked responses to specific events, which can interact with oscillatory activity—both evoked and induced—and can be quantified using time-frequency analysis (TFA). The relationship between ERPs and oscillations remains debated: some researchers argue they reflect the same underlying neural processes (Hagoort et al., 2004; Roehm et al., 2007; Schneider et al., 2016), while others suggest they arise from distinct mechanisms (Bastiaansen and Hagoort, 2015; Wang et al., 2012).

Three prominent theoretical accounts have emerged to explain this relationship (Cohen, 2014). The additive model proposes that ERPs are generated by neural activity that is elicited by a stimulus and simply added to ongoing background oscillations, which are then attenuated through averaging. In contrast, the phase-resetting model suggests that ERPs arise when the phase of ongoing oscillations is reset by a stimulus, leading to a consistent phase alignment across trials without requiring an increase in overall power (Makeig et al., 2002). A third perspective highlights the role of amplitude asymmetry and baseline shifts. Although neural currents are theoretically balanced in polarity, outward-directed currents may be less detectable at the scalp surface (Mazaheri and Jensen, 2008). This detection bias can introduce asymmetries in the recorded oscillatory waveform, such that peaks and troughs are unequally represented. Such asymmetries, or subtle shifts in the oscillatory baseline, could generate ERP-like signals even in the absence of stimulus-locked activity (Nikulin et al., 2010). Fluctuations in oscillatory power, when averaged across trials, might therefore mimic slow ERP components through mechanisms unrelated to traditional evoked responses (van Dijk et al., 2010; Mazaheri and Jensen, 2010). Despite these differing accounts, conclusive evidence supporting one over the others remains limited, and the neural underpinnings of ERP generation are still not fully understood.

A major obstacle in resolving this debate lies in the ambiguity of scalp-level EEG data. Due to volume conduction and spatial smearing, it is often unclear which neural sources contribute to observed signals. Electrophysiological source imaging (ESI) has therefore become a crucial tool in disentangling these processes. By reconstructing the cortical origins of EEG activity, ESI can help

identify whether the same or different sources give rise to ERPs and oscillatory dynamics.

Various source localization methods have been developed to address the inverse problem of estimating cortical sources from scalp-recorded potentials. Minimum-norm-based approaches like sLORETA, dSPM, and eLORETA estimate distributed source activity by minimizing the overall power of the source solution, typically under a smoothness constraint (Hämäläinen and Ilmoniemi, 1994; Dale et al., 2000; Pascual-Marqui et al., 2011). eLORETA (exact Low Resolution Electromagnetic Tomography), in particular, improves on earlier variants by providing zero localization error for single sources under ideal conditions and reducing depth bias, making it well-suited for time-domain analyses of event-related potentials (ERPs). It computes current density estimates assuming that neighboring neuronal populations exhibit highly correlated activity. This allows for a spatially smooth yet temporally precise reconstruction of source activity across time. In contrast, spatial filtering techniques such as LCMV (Linearly Constrained Minimum Variance) and DICS (Dynamic Imaging of Coherent Sources) take a beamforming approach (Van Veen et al., 1997; Gross et al., 2001). DICS operates in the frequency domain and constructs adaptive spatial filters based on the cross-spectral density (CSD) matrix of the EEG data to localize oscillatory sources at specific frequencies. Unlike distributed methods like eLORETA that tend to produce spatially extended solutions, DICS provides more focal source estimates by maximizing the signal-to-noise ratio for narrowband oscillatory activity. This makes it particularly suitable for analyzing sustained or transient oscillations and inter-regional coherence, allowing for detailed mapping of frequency-specific neural dynamics.

While several studies have compared these methods in terms of spatial accuracy, precision and resolution (e.g. Halder et al. (2019); Pellegrini et al. (2023); Babajani-Feremi et al. (2023)), fewer have explored how their complementary strengths can be leveraged to clarify the relationship between ERPs and oscillations. Notably, minimum-norm-based inverse solutions have been used to localize ERP components such as the P300 (Criel et al., 2024; Bocquillon et al., 2011; Ehlers et al., 2015; van Dinteren et al., 2018) and N400 (Criel et al., 2025; Khateb et al., 2010; Geukes et al., 2013), while DICS has been applied to identify task-related alpha and beta oscillations in attention and language paradigms (Wang et al., 2012; Mazaheri et al., 2014). However, relatively few studies have used both methods in tandem to disentangle whether time-domain and frequency-domain activity stem from shared or distinct cortical generators.

Interesting though is that other works have tried to link the oscillatory dynamics and event-related responses in other ways. Schneider and Maguire (2018), for example, identified a significant relationship between the N400 and P600 ERPs and theta and beta oscillatory dynamics during respectively semantic and syntactic processing using Pearson's r correlation analyses. Based on these findings, they suggested that ERPs and neural oscillations measure similar neural processes. Similarly, Torrence et al. (2021) investigated the link between theta oscillations and N170 amplitudes in a dot-probe task, and found that greater N170 amplitudes were associated with greater theta oscillations, indicating that both are related to each other. Studenova et al. (2023) stated that the P300 evoked response and alpha oscillations (8–12 Hz) can be linked through the amplitude asymmetry model. They showed that the temporal evolution of the P300 and alpha amplitude is similar, and that their spatial localisations overlap. Additionally, they showed that the oscillations exhibit a non-zero mean, and both the P300 and alpha amplitude correlate with cognitive scores in a similar manner, further supporting the view that these two phenomena may share a common underlying neural mechanism.

While these studies offer valuable insights into the potential relationship between ERPs and oscillatory activity, they often infer this link indirectly -through correlations between ERP components and power in specific frequency bands- rather than explicitly examining whether these signals originate from common or distinct neural generators. As such, these associations do not clarify the mechanistic or spatial overlap between ERP and oscillatory sources. Without source-level analyses, it remains unclear whether these signals reflect shared cortical origins or merely co-occur due to parallel processes. Thus, a more integrated methodological approach is needed to directly test the extent of overlap between ERP and oscillatory sources.

We argue that combining different ESI methods offers a promising approach to address the open question of how ERPs and neural oscillations are related. In this study, we use both simulations to illustrate the strengths and limitations of eLORETA and DICS, and demonstrate how these tools can be applied to localize the sources of the P300 and N400 ERP components in real data. Through this, we aim to provide new insights into the interplay between phase-locked and non-phase-locked activity, and to assess whether distinct neural mechanisms contribute to each.

6.2 Methods

6.2.1 Simulations

To illustrate how ESI can help us understand the relationship between ERPs and neural oscillations, we simulated the three prominent theoretical accounts. In short, our simulation approach consists of generating neural activity in distinct brain regions, adding realistic noise, and projecting the resulting signals to the scalp using a template head model.

This head model was based on Freesurfer's standard template brain, fsaverage (Fischl, 2012). A three-layer boundary element model (BEM) was constructed, using the inner skull, outer skull, and scalp surfaces to define the compartments. Standard conductivity values were assigned to each layer: 0.3 S/m for both the brain and scalp, and 0.006 S/m for the skull. Dipoles were placed across the cortical surface with approximately 3 mm spacing, resulting in roughly 10,000 dipoles per hemisphere. Each dipole was constrained to be oriented normal to the cortical surface. The EEG leadfield matrix was then computed using the BEM approach.

Two different scenarios were simulated. In each scenario, we simulated a network involving two active brain regions: the left occipital pole and the left inferior temporal sulcus for the first scenario, and the right inferior frontal cortex (pars opercularis) and the left supramarginal gyrus in the second scenario. These regions were defined using the Destrieux cortical atlas (Destrieux et al., 2010), and for each region of interest (ROI), dipoles within a 10 mm radius of the parcellation center were selected. Additionally, we modeled a change in the amplitude of an ongoing oscillation. In Scenario 1, we included an increase in the amplitude of a 9 Hz oscillation in the frontal lobe between 400–800 ms, and in Scenario 2, a decrease in amplitude of a 22 Hz oscillation was modeled in the precentral gyrus, again between 400–800 ms.

In each simulation scenario, 80 epochs of 1600 ms were simulated, half of which contained the ERP as well as pink noise and ongoing oscillatory activity, while only the noise and ongoing oscillations were included in the other half. In each epoch, a pre-stimulus window of 300 ms was considered. By including epochs which only contain noise, and thus simulating two different conditions, it is possible to investigate the difference between the localizations obtained for both conditions. The noise amplitude was adjusted to achieve a signal-to-noise ratio (SNR) of -5 dB. The SNR was defined as the ratio of the peak ampli-

tude of the ERP component to the peak-to-peak amplitude measured within the pre-stimulus window. This approach helps in reducing systematic biases in the source reconstruction process. If certain types of noise or non-specific activity consistently affect the EEG data, this might lead to similar localization errors across both conditions. By subtracting one condition from another, these systematic errors can be reduced, leading to a more accurate estimate of the neural sources.

The additive model:

The additive model assumes that ERPs arise from stimulus-evoked neural activity that is linearly added to ongoing background oscillations, which are attenuated through trial averaging (Cohen, 2014). In this simulation, ERP waveforms were modeled using half-cycle sinusoidal signals.

As stated before, two different scenarios were simulated. In Scenario 1, we simulated a network involving the left occipital pole and the left inferior temporal sulcus. ERP activity was generated as a 4 Hz half-cycle sinusoidal waveform lasting 125 ms. To mimic a simple propagation pattern, a temporal delay was introduced: the ERP began in the first ROI at 200 ms post-stimulus and in the second ROI 10 ms later. Additionally, we modeled an increase in the amplitude of a 9 Hz ongoing oscillation in the frontal lobe between 400–800 ms.

In Scenario 2, a different network was simulated involving the right inferior frontal cortex (pars opercularis) and the left supramarginal gyrus. ERP activity here was modeled using a 6 Hz half-cycle sinusoid, and an amplitude decrease was applied to an ongoing 22 Hz oscillation in the precentral gyrus, again between 400–800 ms.

The phase-resetting model:

The phase-resetting model, on the other hand, suggests that ERPs arise when the phase of ongoing oscillations is reset by a stimulus, leading to a consistent phase alignment across trials without requiring an increase in overall power (Makeig et al., 2002).

In this case, again two different scenarios were simulated. An ongoing oscillation of respectively 4 Hz (Scenario 1) and 6 Hz (Scenario 2) was simulated in the same ROIs as before, i.e. the left occipital pole and the left inferior temporal sulcus for Scenario 1 and the right inferior frontal cortex pars opercularis and the left supramarginal gyrus for Scenario 2. The phases of the oscillations

were in both scenarios reset at 200 ms post stimulus onset, eliciting an ERP. As in the additive model scenarios, also here an increase in the amplitude of a 9 Hz ongoing oscillation at the frontal lobe was added between 400 ms and 800 ms in the first scenario, while a decrease in the amplitude of an ongoing oscillation in the precentral gyrus at 22 Hz was added in the second scenario.

The amplitude asymmetry model:

The amplitude asymmetry model posits that ERPs can emerge from a stimulus-induced bias in the amplitude distribution of ongoing oscillations, without necessarily involving additive activity or phase resetting. In this account, even a symmetric oscillation can produce ERP-like components if it exhibits a non-zero mean, such that post-stimulus amplitude increases result in a consistent shift in the trial-averaged signal (Mazaheri and Jensen, 2008).

For these simulations, we used the same two ROIs as in the previous models. In both scenarios, we simulated ongoing oscillatory activity at either 4 Hz (Scenario 1) or 6 Hz (Scenario 2), using sinusoidal waveforms with a small positive baseline shift. This offset caused the oscillations to have a slightly positive mean, thereby introducing an asymmetry in the waveform. No explicit ERP waveform was added, and no phase resetting was applied.

A transient increase in the amplitude of the ongoing oscillation was introduced starting at 200 ms post-stimulus and lasting for 250 ms. Due to the baseline shift, this amplitude modulation led to a consistent deflection in the averaged signal, mimicking an ERP component while remaining purely oscillatory in origin.

In parallel with the other models, both scenarios included modulation of ongoing oscillations: an increase in amplitude of a 9 Hz oscillation in the frontal lobe between 400 ms and 800 ms in Scenario 1, and a decrease in amplitude of a 22 Hz oscillation in the precentral gyrus in the same time window in Scenario 2. This allowed consistent control over non-specific oscillatory activity across all simulation models.

6.2.2 Real data

Participants and data

To assess the complementarity of eLORETA and DICS, as well as if this approach allows us to get a better understanding of the link between the ERPs

and the oscillations in real data, we incorporated datasets from our previous research exploring the cortical generators and functional connectivity associated with the P300 and N400 ERP components (Criel et al., 2024, 2025). The dataset includes 60 Dutch-speaking adults (30 men and 30 women), with an equal number of male and female participants represented in each of the following age brackets: 20–39 years, 40–59 years, and 60+. Participants ranged in age from 23 to 80 years, with a mean age of 49.3 years (SD = 16.84). This balanced sample, stratified by age and sex, was designed to ensure the generalizability of the findings to the broader population. All participants were right-handed, as confirmed by a score of ≥ 8 on the Dutch Handedness Inventory (DHI; (Van Strien, 1992)). Cognitive status was screened using the Montreal Cognitive Assessment (MoCA; (Nasreddine et al., 2005)), with a minimum score of 26 required for inclusion (Thissen et al., 2010). General language functioning was evaluated using the Dutch version of the Comprehensive Aphasia Test (CAT-NL; (Swinburn et al., 2014)). Participants scoring below the cut-off on any test item were excluded. Additionally, participants self-reported no hearing impairments, normal or corrected-to-normal vision, and no history of neurological, psychiatric, or developmental disorders. The study was approved by the Ethics Committee of Ghent University Hospital (ONZ-2022-0127), and all participants provided written informed consent.

For each participant, high-density EEG was recorded from 128 electrodes using an EasyCap system (Brain Products, Germany). The ground electrode was placed at AFz, and the online reference at FCz. Impedances were maintained below 20 kΩ using an abrasive electrolyte gel (Abralyt 2000, EasyCap). EEG signals were acquired with a BrainVision BrainAmp amplifier (Brain Products, Germany) and digitized at a sampling rate of 500 Hz. Data collection was performed using the BrainVision Recorder software.

Participants completed two experimental tasks: an attentive auditory oddball paradigm designed to elicit a P300 response, and an auditory categorical priming task targeting the N400 component. In the oddball task, the standard stimulus [bə] was presented with a probability of 80%, while the deviant stimulus [gə] appeared in 20% of the trials. Both types stimuli lasted 250 ms. The main experiment consisted of 160 standard and 40 deviant trials, presented with a 2000 ms interstimulus interval (ISI), resulting in a total duration of 8 minutes. A brief practice block (16 standard and 4 deviant trials) preceded the main task. Participants were instructed to press a button on a Chronos response

box (Psychology Software Tools, Pittsburgh, PA, USA) whenever they detected a deviant stimulus, allowing assessment of stimulus categorization.

The auditory categorical priming task was adapted from Hagoort et al. (1996) by Cocquyt et al. (2022). It consisted of 120 Dutch word pairs, each comprising a prime and a target word. Half of the pairs were semantically related (e.g., cat – horse), while the other half were unrelated (e.g., pink – coffee), with no pairs exhibiting thematic associations. Psycholinguistic properties of the target words were carefully matched across conditions for word frequency, phonological length, number of phonological neighbors, concreteness, imageability, age of acquisition, valence, arousal, dominance, and duration. For more details on stimulus selection, see Cocquyt et al. (2022). Word pairs were presented with a stimulus onset asynchrony (SOA) of 1800 ms. The interstimulus interval (ISI) between the prime and target words varied from 830 to 1520 ms to account for differences in word length. After the target word, participants were asked to judge the semantic relatedness of the word pair via button press. A delayed response design was employed to minimize movement artifacts and avoid contamination of the ERP by motor-related activity (Van Vliet et al., 2014). Responses were again collected using the Chronos response box, with participants pressing a green button for related word pairs and a red button for unrelated pairs.

ERP Preprocessing

The high-density EEG data recorded during an auditory oddball task (P300) and an auditory categorical priming task (N400) were processed using the MNE-python library (Gramfort et al., 2013). Bad electrode channels were automatically detected using the different noisy channel detection methods in the PREP pipeline (Bigdely-Shamlo et al., 2015). The electrodes indicated as bad were excluded from further analysis. The data was band-pass filtered using a zero phase shift Butterworth filter with half-amplitude cut-off frequencies of 0.3 Hz and 100 Hz and a 12 dB/octave slope. The power line noise was then removed using a 50 Hz notch filter. Independent component analysis was applied for eye blink and horizontal eye movement artefact removal. In case bad electrode channels were identified and excluded in the first step, these channels were interpolated at this stage. Subsequently, data were re-referenced to an average common reference. In the next step, the data was segmented into epochs going from 200 ms before the stimulus onset to 1000 ms after. Finally, epochs containing artefacts were rejected using the following criteria: 75 μV maximum

gradient criterion; 100 μV minimal/maximal amplitude criterion; 150 μV maximum difference criterion; 0.5 μV low activity criterion during 100 ms.

6.2.3 Time-Frequency Analysis

To examine the spectral dynamics associated with both the simulated data and the experimental data, time-frequency analysis was performed using Morlet wavelet convolution. The analysis was applied to the epoched EEG data from the simulations as well as from all participants, separately for the different conditions. For each epoch, time-frequency representations (TFRs) of oscillatory power were computed using the MNE-Python package. A total of 75 logarithmically spaced frequencies were analyzed, ranging from 3 to 80 Hz. To balance temporal and spectral resolution across frequencies, the number of cycles per frequency increased linearly from 1.5 cycles at the lowest frequency to 15 cycles at the highest frequency. Wavelet transforms were computed using the fast Fourier transform (FFT) with downsampling (decimation factor = 3) to reduce computational load. The resulting TFRs were then cropped to a time window from -0.1 to 1.0 seconds relative to stimulus onset to remove edge artifacts.

The obtained TFRs were then averaged, over all trials and channels in the case of the simulations and over trials, channels and subjects for the experimental data, after which the data was baseline-corrected using a log-ratio transformation. To identify the time-frequency windows of interest, we applied a data-driven clustering approach to the grand-average TFR. Specifically, we selected the top 5% of absolute power values based on a percentile threshold. A binary mask was then created, marking these high-power values. Using connected component labeling, contiguous clusters of high activity were identified in the time-frequency plane. For each resulting cluster, we extracted the corresponding time and frequency boundaries. This allowed us to objectively define windows of interest that captured the most prominent task-related modulations in spectral power.

6.2.4 Source Reconstruction

Since individual MRI scans were not available for the real dataset, the same BEM head model used in the simulation setup—based on Freesurfer's standard template subject fsaverage—was also applied for source localization in the real data (Fischl, 2012).

Two complementary inverse methods were applied for source reconstruction of both the real and the simulated EEG datasets: exact Low-Resolution Electromagnetic Tomography (eLORETA) and Dynamic Imaging of Coherent Sources (DICS). These methods target different aspects of the neural signal, with eLORETA focusing on time-locked evoked potentials and DICS estimating oscillatory power in specific frequency bands.

eLORETA:

Source reconstruction was performed separately for each subject and condition (ERP vs. noise, standard vs. deviant, or related vs. unrelated) using the eLORETA algorithm (Pascual-Marqui et al., 2011). Given that the signal-to-noise ratio (SNR) is influenced by the number of epochs, an equal number of trials was used for both conditions before averaging and applying the inverse model.

Subsequent analyses focused on the absolute magnitude of the reconstructed dipoles—i.e., current source density (CSD)—ignoring dipole orientation. As highlighted by Fulham et al. (2014), CSD reflects both signal and noise components. To account for inter-subject differences in noise levels, CSD values were normalized using z-scores. This normalization was based on a noise estimate generated per subject: 50% of trials from each condition were randomly selected, and half of those were polarity-inverted to cancel out the ERP signal, yielding a noise-only signal with similar statistical characteristics. This synthetic noise signal was source-reconstructed, and the procedure was repeated 100 times to compute a mean and standard deviation for noise at each dipole location. The original CSD values were then z-transformed using these subject-specific noise estimates.

DICS:

To investigate oscillatory activity in source space, Dynamic Imaging of Coherent Sources (DICS; Gross et al. (2001)) was applied. This method was used to reconstruct frequency-specific power differences between conditions—ERP vs noise for the simulations, standard vs. deviant for the P300 oddball paradigm, and related vs. unrelated for the N400 paradigm.

Cross-spectral density (CSD) matrices were computed using Morlet wavelet convolution, with the number of cycles and frequency ranges tailored to the frequencies of interest identified in the prior time–frequency analysis.

For each subject, CSDs were estimated separately for each condition and for a pre-stimulus baseline period, providing both condition-specific and noise-related CSDs. Spatial filters were then computed using the forward model, the average CSD across all epochs, and the baseline CSD as the noise estimate. These filters were subsequently applied to the condition-specific CSDs to obtain source-level power estimates. To enable group-level comparisons and normalize for individual variability, the power difference between conditions (e.g., ERP minus noise, deviant minus standard, or unrelated minus related) was divided by the baseline power at each source location. The resulting normalized power changes were averaged across subjects to obtain a group-level source estimate for time-frequency window of interest.

6.3 Results

6.3.1 Simulations

Figure 6.1 displays the average ERP waveforms obtained from each of the three simulation models—additive, phase-resetting, and amplitude asymmetry—across both scenarios. As expected, all models produced clear ERP-like components, with peak amplitudes occurring around 265 ms in Scenario 1 and approximately 240 ms in Scenario 2. Each model exhibited distinct temporal profiles, consistent with their underlying generative mechanisms. In the phase-resetting model, oscillatory activity with similar frequency and spatial distribution persisted throughout the entire epoch, reflecting the continuous presence of the underlying rhythm. Due to the relatively small number of simulated epochs ($n = 40$), the non-phase-aligned oscillations were not fully averaged out, though a noticeable reduction in amplitude was observed outside the reset window. In the amplitude asymmetry model, the ERP component arose from transient amplitude modulations of an ongoing oscillation with a slight baseline shift. As a result, the evoked waveforms also exhibited lower-amplitude deflections at other time points, mirroring the same topographical distribution as the main component. Finally, subtle effects of the additional frontal oscillation modulations were visible in the waveforms for Scenario 1, where an amplitude increase was introduced. This was less evident in Scenario 2, where a decrease in oscillatory amplitude was simulated.

The corresponding time-frequency representations are displayed in Figure 6.2. In both the additive and amplitude asymmetry models, prominent tran-

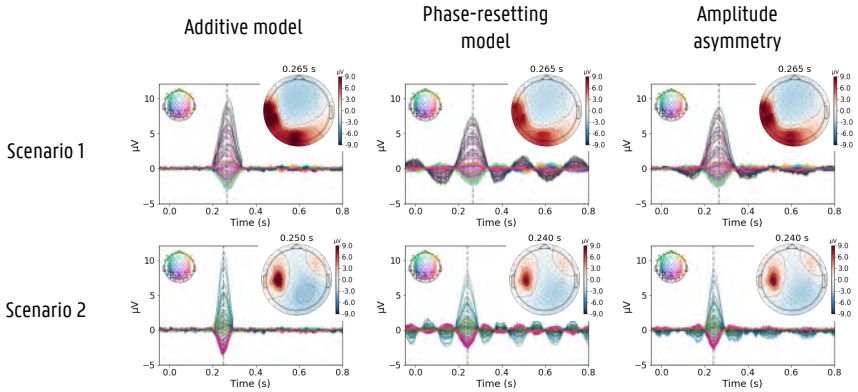

Figure 6.1. The average ERP waveforms for each simulation model and scenario, showing distinct temporal patterns linked to their underlying mechanisms.

sient increases in low-frequency power were observed around the time of the ERP component. Notably, these increases extended beyond the specifically simulated frequency band, affecting adjacent frequencies as well. This spread can be attributed to the inherent time-frequency trade-off associated with the spectral decomposition method, as well as the use of a finite time window that introduces spectral leakage. In contrast, the phase-resetting model did not exhibit a marked increase in power around the ERP component. This aligns with its theoretical basis, where ERP-like features emerge primarily through phase alignment across trials rather than changes in amplitude. As expected, across all simulation models, modulations were also detected in the ongoing oscillatory activity during the post-stimulus window (e.g., 400–800 ms), with peaks centered at 9 Hz and 22 Hz, depending on the scenario. These changes reflect the background oscillatory dynamics that were explicitly embedded into the simulated data.

To identify time-frequency windows of interest, we applied a percentile-based clustering procedure to the average time-frequency representations (TFRs). This revealed consistent clusters within the expected frequency bands and time windows for each model. In the additive model, the ERP-related cluster in Scenario 1 spanned 3–8.7 Hz and 146–392 ms, while in the amplitude asymmetry model it appeared between 3–7 Hz and 122–404 ms. In Scenario 2, the corresponding clusters were found between 3–15.5 Hz and 108–394 ms for the additive model, and 3–10 Hz and 150–344 ms for the amplitude asymmetry model. As expected, no ERP-related clusters were identified in the phase-

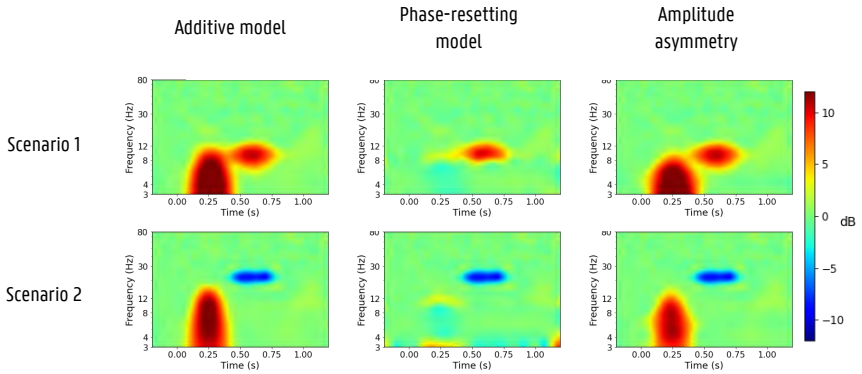

Figure 6.2. The time-frequency plots corresponding to the simulated data, showing transient power increases in the additive and amplitude asymmetry models, with the phase-resetting model reflecting phase-based alignment.

resetting model for either scenario. For ongoing oscillations, power-related clusters were detected in Scenario 1 at 550–640 ms / 8.7–10.0 Hz (additive), 252–808 ms / 7.3–13.6 Hz (phase-resetting), and 526–664 ms / 8.3–10.4 Hz (amplitude asymmetry). In Scenario 2, the clusters were located at 456–746 ms / 19.3–25.2 Hz (additive), 474–732 ms / 20.2–24.1 Hz (phase-resetting), and 496–718 ms / 21.1–23.1 Hz (amplitude asymmetry).

Based on these results, we selected 130–400 ms as the time window for ERP source localization in Scenario 1, using eLORETA, and 130–400 ms / 3–8 Hz for DICS. For Scenario 2, we used 100–450 ms for eLORETA and 100–450 ms / 3–12 Hz for DICS. For localizing ongoing oscillations with power changes, we used 450–800 ms / 8–10 Hz in Scenario 1 and 480–750 ms / 21–23 Hz in Scenario 2 for DICS and used the same time windows for eLORETA.

Figure 6.3 presents the source localization results for the ERP time window using both eLORETA and DICS. For all three simulation models, eLORETA successfully localized source activity to the two simulated ROIs—the left occipital pole and left inferior temporal sulcus in Scenario 1, and the right inferior frontal cortex (pars opercularis) and left supramarginal gyrus in Scenario 2—closely matching the ground truth. In contrast, DICS yielded more variable results. In Scenario 1, both the additive and amplitude asymmetry models showed source activity in the simulated ROIs, but also exhibited spurious activations outside these regions. For the phase-resetting model, no clear or consistent source localization was observed. A similar pattern emerged in Scenario 2: while DICS captured activity near the simulated sources for the additive and amplitude

asymmetry models, localization was less accurate and more spatially diffuse compared to eLORETA. Again, no meaningful localization was achieved for the phase-resetting model.

Figure 6.4 shows the source localization results for the ongoing oscillations using both eLORETA and DICS. In this case, DICS successfully identified the simulated ROIs, accurately localizing the amplitude changes in the ongoing oscillations across all models. In contrast, eLORETA did not yield clear localization results for the additive model. Interestingly, for the phase-resetting and amplitude asymmetry models, eLORETA localized some of the same regions involved in the ERP simulation. This is not entirely unexpected, as in these models, the oscillations underlying the ERP are not confined to the ERP time window but persist throughout the trial.

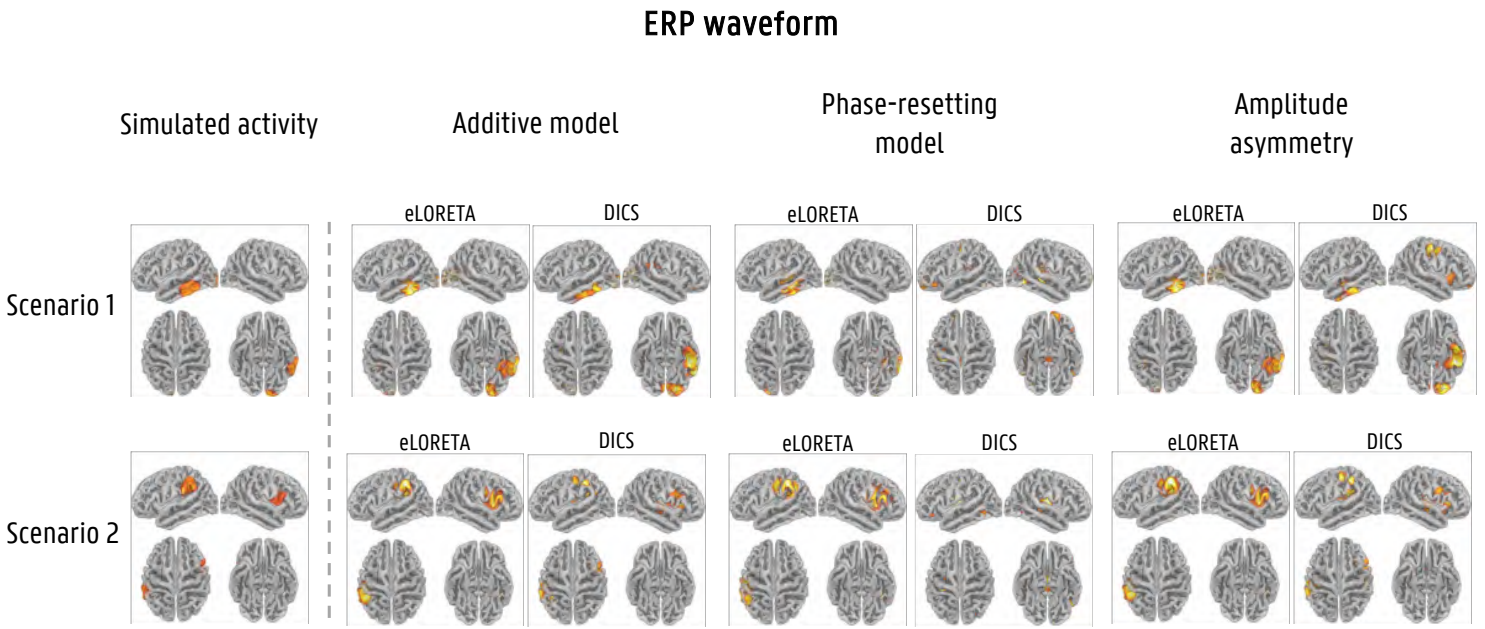

Figure 6.3. The source localization results for the simulated ERP components using both eLORETA and DICS. In the first column, the ground truth of the simulated sources is shown. In Scenario 1, a 130–400 ms / 3–8 Hz time-frequency window was used for the localization using DICS, and a 100–450 ms / 3–12 Hz time-frequency window in Scenario 2. The same time windows were also used for the localizations using eLORETA.

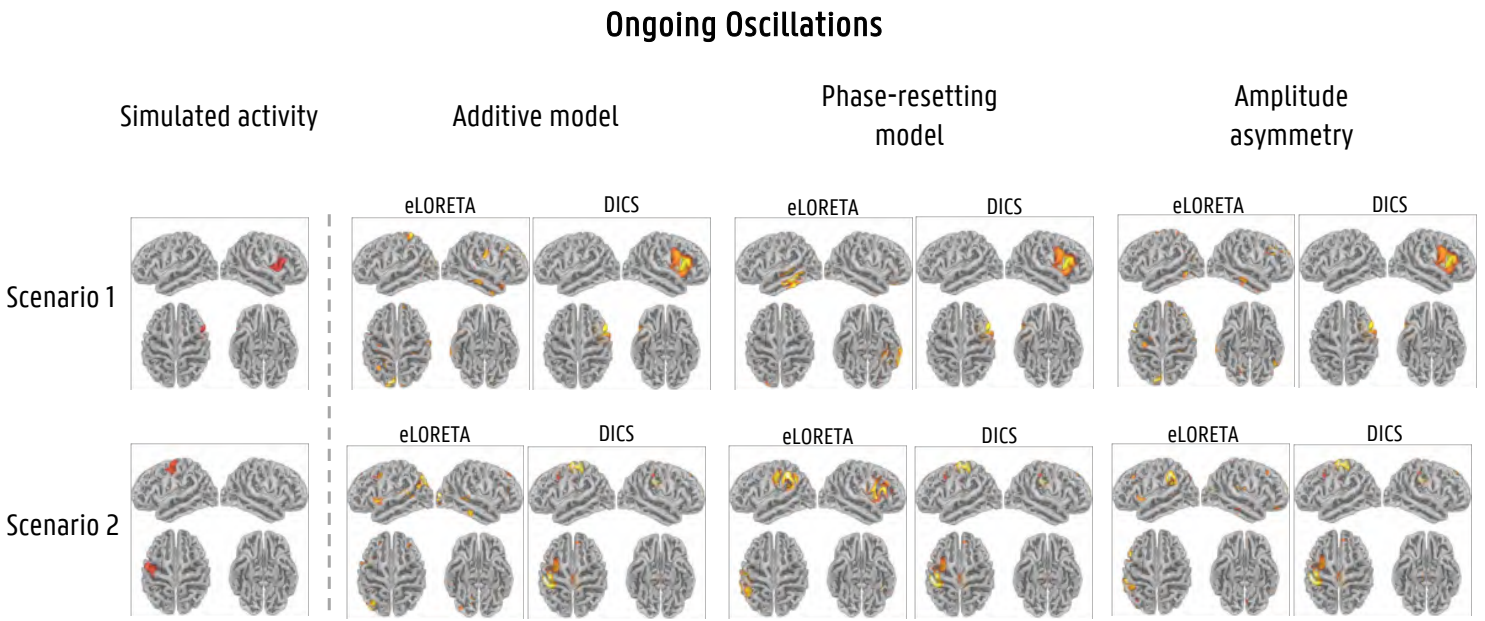

Figure 6.4. The source localization results for the simulated ongoing oscillations using both eLORETA and DICS. In the first column, the ground truth of the simulated sources is shown. In Scenario 1, a 450–800 ms / 8–10 Hz time-frequency window was used for the localization using DICS, and a 480–750 ms / 21–23 Hz time-frequency window in Scenario 2. The same time windows were also used for the localizations using eLORETA.

6.3.2 Real Data

Grand-average ERP waveforms for the oddball (P300) and semantic priming (N400) tasks are shown in Figure 6.5. As expected, the P300 was characterized by a positive deflection between approximately 300-800 ms post-stimulus at parietal electrodes, while the N400 showed a negative deflection between 400-800 ms at central-posterior sites.

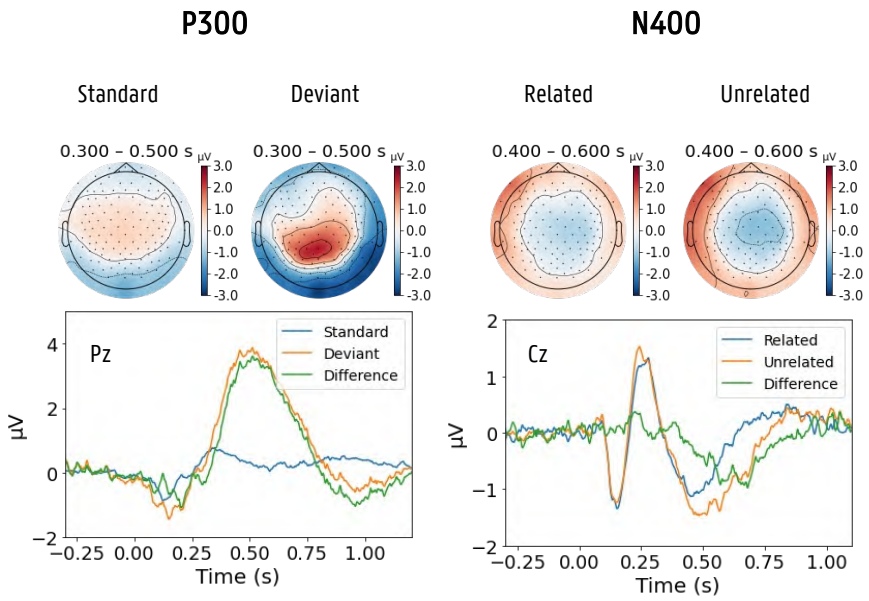

Figure 6.5. Grand-average evoked potentials for the P300 and N400 paradigms, showing characteristic stimulus-locked components.

Figure 6.6 displays the average time-frequency representations (TFRs) across participants for both the standard and deviant trials in the P300 paradigm, as well as the related and unrelated trials in the N400 paradigm. In both tasks, stimulus-related spectral modulations were evident. The P300 task revealed post-stimulus increases in low-frequency power (3–8 Hz), along with modulations in the alpha (8–12 Hz) and beta (15–30 Hz) bands. In the N400 task, broader frequency changes were observed, extending across delta, theta, alpha, and beta ranges.

Cluster analysis of the TFRs revealed distinct time-frequency windows of interest for each condition. For the P300, a prominent cluster was identified in standard trials between 3 and 6.3 Hz and 96–900 ms. In the deviant trials, three clusters were found: a low-frequency cluster between 3 and 5.8 Hz from

228 to 552 ms, an alpha-band cluster between 7.6 and 11.4 Hz from 408 to 948 ms, and a beta-band cluster between 17.7 and 25.2 Hz from 354 to 594 ms. In the N400 paradigm, both the related and unrelated trials showed an early theta cluster between 3 and 5.8 Hz from 132 to 336 ms, as well as a broader cluster from 6.1 to 19.3 Hz between 330 and 1002 ms. Also a smaller cluster from 3 to 3.9 Hz between 600 and 756 ms was found in both conditions.

These cluster results were used to guide the selection of time-frequency windows for source localization using DICS. For the P300 task, we localized delta/theta power (3–7 Hz) between 200 and 400 ms across both conditions. We also examined alpha desynchronization (6–13 Hz) between 300 and 1000 ms and beta desynchronization (20–22 Hz) between 400 and 500 ms, both derived from the deviant-minus-standard contrast. In parallel, we applied eLORETA to localize temporally defined ERP components, i.e. the P300 was localized between 300 and 800 ms. This dual approach allowed us to separately capture the spatial patterns of both evoked and induced activity.

For the N400 dataset, we adopted a similar approach. DICS windows were again based on the cluster findings, while eLORETA was informed by the timing of components in the grand-average evoked potentials. DICS was used to localize delta power between 600 and 1000 ms (3-4 Hz), theta power between 100 and 300 ms (4–6 Hz), alpha desynchronization between 300 and 1000 ms (6–12 Hz), and beta desynchronization between 300 and 1000 ms (15–20 Hz). The N1 and N400 were localized using eLORETA within the 120–180 ms and 400–800 ms windows, respectively.

The results of the source localization analyses for both the P300 and N400 paradigms are summarized in Figures 6.7 and 6.8. In the P300 paradigm, eLORETA localized the P300 component to the left and right cingulate cortex, with additional activity observed in the left superior premotor cortex. The DICS results revealed condition-specific power changes across frequency bands. Delta/Theta-band activity (3–7 Hz) between 200 and 400 ms was localized to the left superior premotor and frontal cortex. Alpha desynchronization (6–13 Hz) between 300 and 1000 ms was observed in the left superior parietal lobe, while beta desynchronization (20–22 Hz) between 400 and 500 ms was primarily localized to the left motor cortex.

In the N400 paradigm, eLORETA localized the N1 component to the bilateral auditory cortices. The N400 component was primarily found in the left frontal cortex, with additional activation in the right frontal and right middle temporal regions, and weaker involvement of the left temporal cortex. DICS

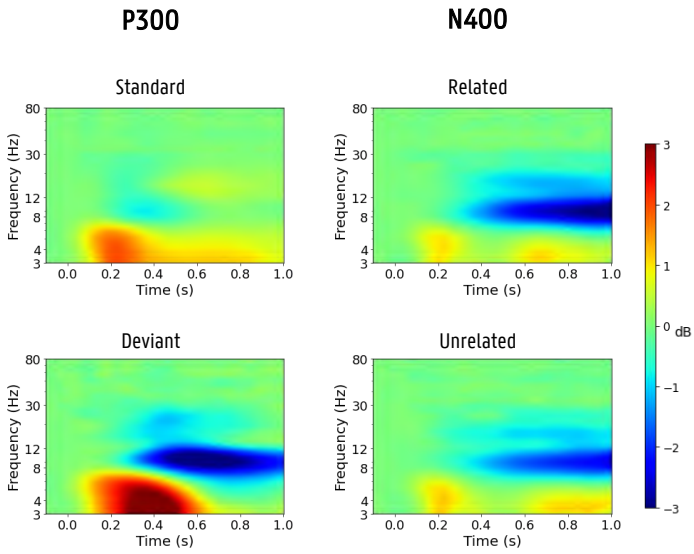

Figure 6.6. Time-frequency representations for the P300 and N400 tasks, revealing distinct patterns of low- and high-frequency modulations following stimulus onset.

analysis revealed theta-band power changes (4–6 Hz, 100–300 ms) in the left and right auditory cortices, extending toward the supramarginal gyrus. These early components—the N1 and theta activity—were analyzed by combining both conditions and comparing them to baseline, based on the expectation that they reflect shared auditory processing mechanisms present in both conditions. In contrast, delta synchronization (3-4 Hz, 600-1000 ms) and alpha desynchronization (6–12 Hz, 300–1000 ms), primarily observed in the left frontal cortex with some extension to the left middle temporal gyrus, and beta desynchronization (15–20 Hz, 300– 1000 ms), localized bilaterally to the posterior temporal poles, were analyzed by comparing the two conditions directly. This approach was taken to capture condition-specific neural dynamics associated with the N400 time window.

6.4 Discussion

In this work, we combined simulation-based and empirical approaches to explore how different neurophysiological mechanisms underlying event-related potentials can be disentangled using two complementary source localization methods: eLORETA and DICS. By systematically simulating ERPs based on

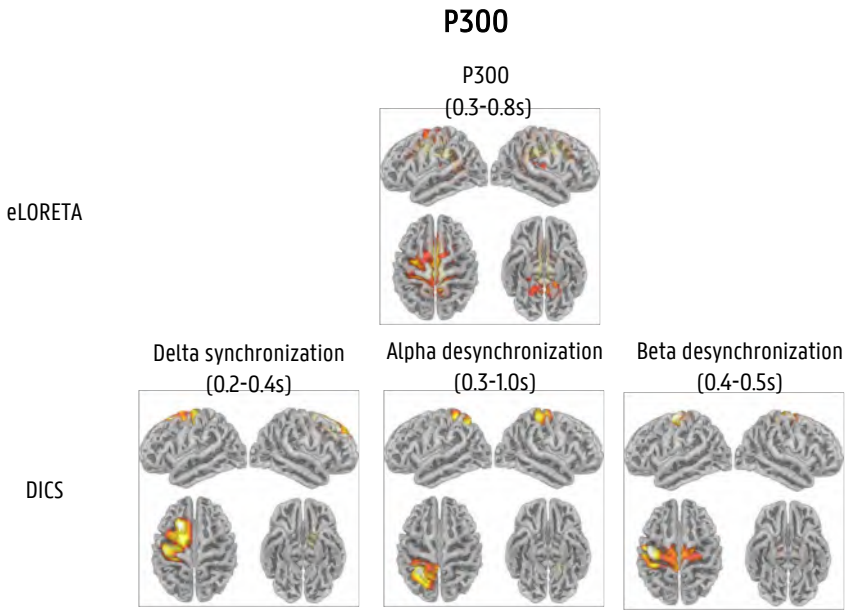

Figure 6.7. Source localization results for the P300 paradigm using eLORETA and DICS, showing distinct regions involved in evoked responses and frequency-specific activity. All results were obtained by comparing the localizations obtained for both conditions.

three models, namely the additive, phase-resetting, and amplitude asymmetry models, and applying these source reconstruction methods to both simulated and real EEG data, we gained novel insights into how each method captures different facets of brain activity, and how they can be jointly used to better infer the origins of observed ERPs.

6.4.1 Complementarity of eLORETA and DICS in ERP Localization

Our simulations demonstrated a clear dissociation in the localization performance of eLORETA and DICS depending on the underlying mechanism. eLORETA, which localizes activity based on evoked signals, reliably recovered the known sources of ERP components across all three models, regardless of whether the ERP was generated through additive, phase-resetting, or amplitude asymmetry mechanisms. In contrast, DICS—which localizes sources based on oscillatory power changes in the frequency domain—was particularly sensitive to amplitude-related changes, showing accurate localization only

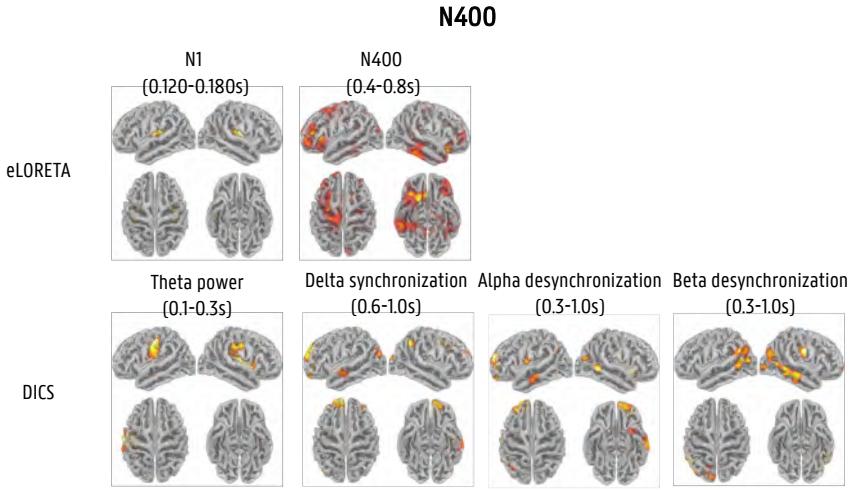

Figure 6.8. Source localization results for the N400 paradigm using eLORETA and DICS, highlighting frontal and temporal contributions to semantic processing. Note that the early components—the N1 and theta activity—were analyzed by combining both conditions and comparing them to baseline, based on the expectation that they reflect shared auditory processing mechanisms present in both conditions. In contrast, the N400 effect, delta synchronization, alpha desynchronization and beta desynchronization were analyzed by comparing the two conditions directly.

in the additive and amplitude asymmetry models. Notably, DICS failed to recover meaningful sources in the phase-resetting model, aligning with the theoretical understanding that phase-resetting does not necessarily produce power changes detectable by spectral methods. These results are consistent with, and expected from, the patterns observed in our time-frequency analysis, which likewise showed no power changes in the phase-resetting condition, underscoring this limitation of DICS.

This divergence underscores the methodological complementarity of eLORETA and DICS. Whereas eLORETA is well-suited to identify sources of time-locked ERP components, DICS is more sensitive to stimulus-induced modulations in oscillatory power, even when they are not strictly phase-locked. Therefore, interpreting ERP components solely through one method may lead to incomplete conclusions about their neural generators. When used together, these methods provide a more nuanced picture—eLORETA highlights the evoked, time-locked responses, while DICS reveals the induced, frequency-specific dynamics that may underlie or accompany ERP generation.

6.4.2 ERP Mechanisms in Light of Source Localization

The different localization patterns observed across simulation models also inform the longstanding debate on what generates ERPs. While simulations cannot confirm any single model of ERP generation, they offer a controlled framework for probing how different mechanisms, such as additive activity or amplitude asymmetry, interact with different source localization techniques. The additive model, which assumes that ERPs result from the addition of transient activity to ongoing background oscillations, led both eLORETA and DICS to localize activity to the simulated sources within the ERP time window and during ongoing oscillation. Similarly, in the amplitude asymmetry model—which assumes transient amplitude increases in ongoing oscillations—both methods again identified meaningful source patterns, with DICS accurately capturing power changes and eLORETA detecting the consistent topography of the evoked component.

In contrast, the phase-resetting model—where ERPs emerge through trial-wise realignment of ongoing oscillatory phase—showed a clear dissociation: only eLORETA captured the simulated sources, while DICS yielded no consistent results. This reflects a fundamental limitation of DICS, which relies on changes in spectral power and is insensitive to phase-based dynamics. Since phase-resetting does not necessarily produce measurable power changes, DICS is unable to detect such activity. Interestingly, eLORETA also identified some of the ERP-related sources in the later (post-ERP) time windows, particularly in the phase-resetting and amplitude asymmetry models, suggesting that these mechanisms involve more sustained spatially-specific dynamics, even beyond the ERP time window.

Taken together, these findings suggest that the additive and amplitude asymmetry models are more readily detectable using both evoked and induced measures, while the phase-resetting model cannot be adequately assessed using frequency-based source localization methods like DICS, due to their insensitivity to phase dynamics. Therefore, multimethod source reconstruction provides critical leverage for adjudicating between competing mechanistic accounts of ERP generation.

6.4.3 Insights from Real Data: The P300

In the P300 oddball paradigm, we observed partial convergence between the source localization results obtained with eLORETA and DICS, particularly in the

delta/theta band. While the peak time windows of these effects were not identical, they nonetheless point to potentially overlapping neural sources. This discrepancy in timing is likely due to the intrinsic trade-off in frequency-based methods—lower frequency components such as delta inherently suffer from reduced temporal resolution due to time–frequency smearing. Despite this, the spatial overlap between eLORETA's evoked activity and DICS's delta-band power increase suggests that both methods may be tapping into the same underlying neural process that supports the generation of the P300.

Moreover, time-frequency analysis and DICS revealed additional frequency-specific changes: an alpha-band desynchronization localized to the superior parietal cortex, and a beta-band desynchronization localized to the left motor cortex. These findings align with the cognitive and motor demands of the task. Alpha desynchronization in the parietal cortex has been robustly associated with attentional allocation (van Winsun et al., 1984; Capotosto et al., 2016; Woodman et al., 2022), which is expected to be enhanced in response to deviant stimuli in an oddball paradigm. The beta desynchronization observed in the motor cortex during deviant trials also fits this model: beta suppression is classically linked to motor preparation and execution (Stancák Jr and Pfurtscheller, 1996; Gross et al., 2005; Engel and Fries, 2010; Heinrichs-Graham and Wilson, 2016). Given that participants were required to press a button only in response to deviant tones, the beta decrease in these trials likely reflects the engagement of motor systems, again through transient amplitude modulations of ongoing oscillations.

These real data observations provide evidence for both additive and amplitude asymmetry mechanisms in the generation of the P300. The convergence of eLORETA and DICS in the delta range supports the additive model, where evoked components are superimposed on ongoing oscillations and lead to both increased ERP amplitude and low-frequency power. More surprising though is that while the time-course of the alpha desynchronization aligns closely with that of the P300, the obtained localizations do not overlap. It is however not possible to rule out the amplitude asymmetry model in this case, as it is possible that both models are involved in the P300 component generation and that the obtained amplitude shift gets lost in the combination with the additive model.

6.4.4 Insights from Real Data: The N400

In the N400 paradigm, eLORETA localized the early N1 component to the bilateral auditory cortices, in line with its well-established role in early auditory

processing (Bertrand et al., 1991; Giard et al., 1994). The N400 component was primarily found in the left frontal cortex, with additional activation in the right frontal and right middle temporal regions, and weaker involvement of the left temporal cortex. This spatial pattern is consistent with prior studies implicating a predominantly left-lateralized frontotemporal network in semantic processing and integration (Kutas and Federmeier, 2011; Lau et al., 2008).

DICS analysis revealed theta-band power changes (4–6 Hz, 100–300 ms) localized to the left and right auditory cortices, extending toward the supramarginal gyrus. These results closely align with the N1 findings from eLORETA, and were similarly analyzed by collapsing across conditions and comparing them to baseline. This approach was based on the expectation that these early components reflect shared auditory and early context-processing mechanisms that are not specific to semantic deviation (Bastiaansen et al., 2005).

In contrast, delta synchronization (3-4 Hz, 600-1000 ms), alpha desynchronization (6–12 Hz, 300–1000 ms) and beta desynchronization (15–20 Hz, 300–1000 ms) were evaluated by directly contrasting the deviant and standard conditions, aiming to isolate neural dynamics specific to the semantic deviation captured by the N400. Alpha desynchronization was predominantly observed in the left frontal cortex, with some spread to the left middle temporal gyrus—regions associated with semantic control and attentional engagement (Klimesch, 2012). This suggests that increased semantic or cognitive demands in unrelated trials may drive greater alpha suppression, consistent with theories linking alpha decreases to active information processing. Interestingly is that the same cortical generators were found for the delta synchronization (3-4 Hz, 600-1000 ms).

The convergence of neural sources for both delta and alpha activity strongly supports the amplitude asymmetry model. In this framework, fluctuations in alpha amplitude can modulate the phase or amplitude of delta oscillations in the same regions, reflecting a cross-frequency coupling mechanism. This interdependence suggests that high-frequency alpha and low-frequency delta oscillations interact nonlinearly, providing a shared neural mechanism for cognitive processes. These findings align with existing literature, such as the work of Varga and Manns (2021) on delta-modulated alpha oscillations in memory integration, where delta-phase modulation of alpha amplitude contributes to the synchronization of distributed cortical networks. A similar interaction may also apply to the N400 component during semantic processing.

Beta desynchronization was found bilaterally in the posterior temporal poles, a region increasingly implicated in conceptual integration and context updating during language comprehension (Lewis and Bastiaansen, 2015; Lam et al., 2016). The observed beta suppression may reflect a mismatch between predicted and incoming semantic content or the need to reconfigure the current context, both of which are heightened during unrelated trials.

Together, the eLORETA and DICS results converge on a view of the N400 as a product of both evoked potentials and induced oscillatory dynamics within a distributed semantic network. The N1 evoked component seems to correspond to additive neural activity, as we find an increase in theta power in the corresponding window, while the alpha and beta desynchronizations in the N400 time window point toward amplitude asymmetry mechanisms responsive to task demands.

6.4.5 Implications and Future Directions

This study highlights the value of multimodal source localization for disentangling the neural basis of ERPs. While eLORETA provides reliable localization of phase-locked responses, DICS offers complementary insights into frequency-specific, non-phase-locked processes. The divergence in performance across different simulation models further illustrates that observed ERP components could arise from distinct and overlapping mechanisms, each with unique implications for how brain dynamics are temporally organized.

Moreover, the interaction between different frequency bands—such as cross-frequency coupling—emerges as a critical factor in understanding ERP components. Specifically, the interplay between higher-frequency oscillations (e.g., alpha desynchronization) and lower-frequency rhythms (e.g., delta synchronization) may help explain the dynamic coordination of brain networks engaged in cognitive processing. This cross-frequency coupling provides insight into the neural mechanisms underlying complex ERP components like the N400, highlighting the importance of studying both spectral and temporal dynamics in tandem.

Moving forward, this dual-method approach can be used to characterize ERPs in clinical or cognitive populations, helping to identify whether atypical ERP responses arise from altered evoked activity, disrupted oscillatory dynamics, or both. Moreover, combining these tools with techniques like dynamic causal modeling or intracranial recordings may further deepen our understanding of the causal architecture underlying ERP phenomena.

In sum, this study provides empirical and conceptual evidence for the complementary use of eLORETA and DICS in ERP research. By harnessing the strengths of both methods, we gain a richer, more mechanistic understanding of the temporal and spectral processes that give rise to stimulus-locked brain responses.

7 | Investigating the effect of template head models on Event-Related Potential source localization: A simulation and real-data study

Abstract

Event-Related Potentials (ERPs) are valuable for studying brain activity with millisecond-level temporal resolution. While the temporal resolution of this technique is excellent, the spatial resolution is limited. Source localization aims to identify the brain regions generating the EEG data, thus increasing the spatial resolution, but its accuracy depends heavily on the head model used. This study compares the performance of subject-specific and template-based head models in both simulated and real-world ERP localization tasks. Simulated data mimicking realistic ERPs was created to evaluate the impact of head model choice systematically. The results indicate that the template models capture the simulated activity less accurately, producing more spurious sources and identifying less true sources correctly. Furthermore, the results show that while creating more accurate and detailed head models, such as finite element method (FEM) models instead of boundary element method (BEM) models, improves the localization accuracy for subject-specific head models, this advantage is less pronounced when using template head models. The different modelling approaches were also applied to a face recognition dataset. The main N170 source was correctly localized to the fusiform gyrus, a known face processing area, using the subject-specific models. Apart from the fusiform gyrus, the template models also reconstructed several other sources, illustrating the localization inaccuracies. While template models allow researchers to investigate the neural generators of ERP components when no subject-specific MRIs are available, it could lead to misinterpretations. Therefore, it is important to consider a priori knowledge and hypotheses when interpreting results obtained with template head models, acknowledging potential localization errors.

This chapter is based on the following article:

Depuydt, E., Criel, Y., De Letter, M., & van Mierlo, P. (2024). Investigating the effect of template head models on Event-Related Potential source localization: A simulation and real-data study *Frontiers in Neuroscience 18*(2024): 1443752. doi:10.3389/fnins.2024.1443752

7.1 Introduction

Electroencephalography (EEG) is an essential tool for analyzing brain activity, which allows researchers to study the neuronal mechanisms at work when executing specific tasks at a millisecond scale (Luck, 2014). While this technique offers excellent temporal resolution, its spatial resolution is limited, as the signals are measured at the scalp using a limited number of electrodes. Moreover, due to volume conduction, the activity recorded by each electrode does not represent a single underlying brain source, but rather a composite of activities from various brain regions, again limiting the spatial accuracy of EEG. EEG source imaging was introduced to overcome this limitation as a computational technique to estimate the electrical neuronal activity in the brain. This technique identifies the underlying generators of the electrophysiological activity recorded at the scalp by combining the EEG signals with structural MR images. During recent decades, EEG Source Imaging (ESI) has been an important area of research. However, while it has introduced significant advances in multiple research domains such as epilepsy (Mégevand and Seeck, 2020) and sleep (Del Felice et al., 2014; Fernandez Guerrero and Achermann, 2019), the precise localization of the neuronal activity is still a challenge, and the spatial resolution remains unclear.

Source analysis of EEG data consists of two different processes, namely a forward model and an inverse model. The forward or head model describes how a known source of electrical activity within the brain contributes to the signal observed at each EEG electrode on the scalp. The inverse model then estimates the location and the strength of the electrical activity within the brain based on the EEG signals recorded at the scalp, and relies on the forward model to obtain an accurate solution. As this is a non-unique problem, regularization techniques or constraints are needed to find plausible solutions. Many different techniques have been proposed for solving the inverse problem, such as single dipole models, multiple dipole models, including multiple emitter location and signal parameter estimation (MUSIC) (Schmidt, 1986), and distributed source estimation methods, including the minimum norm estimate (MNE), dynamic statistical parametric mapping (dSPM), standardized low-resolution brain electromagnetic tomography (sLORETA) and exact low-resolution brain electromagnetic tomography (eLORETA) (Hämäläinen and Ilmoniemi, 1994; Dale et al., 2000; Pascual-Marqui, 2002; Pascual-Marqui et al.,

2011). However, the accuracy of the EEG reconstruction obtained with each of these techniques still depends on the accuracy of the forward model.

The construction of the forward model is thus a critical step in the source reconstruction. The model takes into account the anatomical structure of the head, as well as the electrical conductivity of the different tissue types. Many different studies have investigated the effect of the head model on the obtained localization errors. Vorwerk et al. (2012) and Birot et al. (2014), for example, have investigated the effect of using different methods for the creation of the head model, such as boundary element models (BEMs), finite difference models (FDMs) or finite element models (FEMs). In other studies, the influence of including more head tissue compartments in the model was investigated (Vorwerk et al., 2014; Neugebauer et al., 2017). Recently, Nielsen et al. (2023) specifically investigated the influence of anatomical accuracy and electrode positions on the accuracy of the forward solutions. Other work by (Montes-Restrepo et al., 2014) and (Montes-Restrepo et al., 2016), for example, studied the influence of different skull modelling approaches on EEG source localization, while Stenroos and Hauk (2013) looked into the robustness of source estimation in the case of skull conductivity errors. Also the influence of head tissue conductivity uncertainties on dipole reconstructions has been investigated (Vorwerk et al., 2019), as McCann et al. (2019) have shown that the electrical conductivity values assumed for each compartment likely vary between individuals. It is clear that the ideal head model for the most accurate reconstruction of the neural activity is a realistic head model created using the subject's individual MRI and accurate electrical properties of the different tissue types (Akalin Acar and Makeig, 2013; Vorwerk et al., 2018; Conte and Richards, 2021).

Unfortunately, in many EEG studies the additional acquisition of MRI data proves difficult. The acquisition of MRI data for each subject would require more time, research funds, and the availability of an MRI scanner. Therefore, many studies using ESI to source localize ERP data use an approximate, average or template-based head model (Sabeti et al., 2016; Dorme et al., 2023; Criel et al., 2024). The effect of this simplification has been studied extensively before. Valdés-Hernández et al. (2009), for example, investigated the performance of approximate models of the head in ESI using simulations and showed that the average of many individual MRI-based models outperforms a randomly selected individual model. Liu et al. (2023) quantified source localization discrepancies introduced by using template head models, inexact electrode locations, and inaccurate skull conductivity for both younger and older

adults using real EEG data. They found that using template MRIs led to localization discrepancies of up to 2 cm compared to the anatomically accurate subject-specific head models for both younger and older adults.

However, most studies investigating EEG source localization accuracy have focused on the localization of a single source and quantified the localization error associated with each source modelled within the brain (Vorwerk et al., 2014; Hauk et al., 2022). This approach is motivated by applications in which the activity is dominated by a single source, e.g. in the localization of epileptiform interictal discharges. However, it is known that in multiple applications of ESI, such as Event-Related Potential (ERP) research, typically more than one source is involved in the observed waveform, as more than one brain region is involved in processing the stimuli. It is therefore important to investigate the effect of the head model that is used particularly when multiple sources of activity are present. In a study by Cho et al. (2015), the influence of imperfect head models on EEG source connectivity analyses has been studied with multi-source scenarios, where they found that neglecting the distinction between gray and white matter or neglecting CSF causes large connectivity errors. However, they only used a single subject in this study, and they did not yet investigate the effect of using a template head model.

The objective of this study is therefore to investigate the effect of using a template head model instead of subject-specific head models, particularly in the context of Event-Related Potentials (ERPs) involving multiple brain regions, and to quantify the localization error associated with this simplification. By using both simulated and real task data, the aim is to quantify the localization errors introduced by this simplification and assess the interpretability of the reconstructed neural activity.

7.2 Materials and Methods

7.2.1 Participants and data

In this work, the open-source multimodal neuroimaging dataset VEPCON (OpenNeuro Dataset ds003505) was used (Pascucci et al., 2022), in which visual evoked potentials were recorded while the subjects discriminated faces from scrambled faces. This dataset has previously been used in different studies, for example, to improve and validate EEG source imaging methods and time-varying functional connectivity methods (Rubega et al., 2019; Pascucci

et al., 2020). The dataset includes raw data, derivatives of high-density EEG, structural MRI and diffusion-weighted images (DWI), and single-trial behaviour.

The dataset includes the data of twenty participants (3 males, mean age = 23±3.5) who were recruited from the student population at the University of Fribourg, Switzerland. In this work, only the raw high-density EEG, recorded during a face detection task, and the derivatives of the T1-weighted structural MRI data, obtained using the Freesurfer software, were used. Subjects for whom (part of) this data was missing were excluded, resulting in a total of eighteen participants. The EEG data were recorded at a sampling rate of 2048 Hz with a 128-channel Biosemi Active Two EEG system (Biosemi, Amsterdam, The Netherlands) in a dimly lit and electrically shielded room. More information regarding the dataset and recording procedures can be found in the data descriptor provided by Pascucci et al. (2022).

7.2.2 MRI Processing and Head Model Reconstruction

Preprocessed structural MRI data was included in the open-source dataset. For each subject, Pascucci et al. (2022) resampled the T1w images using the Connectome Mapper v3.0.0-beta-RC1 pipeline (Tourbier et al., 2022), and segmented gray and white matter using Freesurfer 6.0.1 (Fischl, 2012). The structures were then parcellated into 83 cortical and subcortical areas according to the Desikan-atlas. Also other parcellations were included in the dataset, such as the parcellation following the Destrieux atlas.

Multiple approaches were used for the construction of the forward model, namely the finite element method (FEM) and the boundary element method (BEM). The FEM method uses a realistic volume mesh of the head, which is generated from the MRI segmentation, and results in anatomically accurate models. The BEM model, on the other hand, relies on the creation of three BEM surfaces (inner skull, outer skull, and skin) and thus includes less detailed segmentations in the model.

FEM

A finite element method (FEM) head model was constructed for each subject in Brainstorm (Tadel et al., 2011), which is documented and freely available for download online under the GNU general public license. In the first step, the tetrahedral FEM meshes were generated using the SimNIBS-charm pipeline

(Puonti et al., 2020). The MRI data was segmented into nine different tissue types: white matter, gray matter, CSF, compact bone, spongy bone, scalp, eyes, blood and muscle, after which the meshes representing the geometry of the head were created. Equivalent current dipoles were then distributed within the grey matter. The dipoles were spaced approximately 3 mm apart, resulting in a dense and uniform grid of dipoles throughout the cortical surface. The forward model was subsequently generated from the obtained mesh using the DUNEuro-FEM computation within Brainstorm (Medani et al., 2023).

Two different forward models were created based on the FEM meshes. In the first model, the conductivity values for the different tissue types were based on the weighted average means from the meta-analysis by McCann et al. (2019): 0.22 S/m for white matter, 0.47 S/m for grey matter, 1.71 S/m for the CSF, 0.006 S/m for the compact bone and 0.048 S/m for the spongiform bone, 0.41 S/m for the scalp, 0.33 S/m for the eyes, 0.57 S/m for blood and finally 0.32 S/m for the muscle layer. In the second model, the default conductivity values as proposed by Brainstorm were used: 0.14 S/m for white matter, 0.33 S/m for grey matter, 1.79 S/m for the CSF, 0.008 S/m for the compact bone and 0.025 S/m for the spongiform bone, 0.43 S/m for the scalp, 0.33 S/m for the eyes, 0.33 S/m for blood and 0.33 S/m for the muscle layer (Vorwerk et al., 2014). By including two models with different conductivity values, it is possible to investigate the effect of using slightly deviant conductivities on the reconstructions.

In addition to individual head models, the same approach was applied to the average MRI, fsaverage, available in Freesurfer. This template brain is based on a combination of 40 MRI scans of real brains. More information on the creation of the fsaverage template and details about the subjects used in this template can be found in the official Freesurfer documentation (Fischl, 2012).

BEM

For each individual, a three-layered head model was created using Freesurfer 6.0.1 and MNE-python (Fischl, 2012; Gramfort et al., 2013). The inner skull, outer skull and outer skin surfaces were obtained from the dataset and then used as boundaries for the different compartments, assigning default electrical conductivity values to the scalp (0.33 S/m), skull (0.006 S/m) and brain (0.33 S/m) compartments of the head model. The same equivalent current dipole locations as used in the FEM models were used here, i.e. the dipoles were distributed in the grey matter with a spacing of 3 mm. Finally, the boundary

element method (BEM) was used to obtain the EEG leadfield matrix. As before, this approach was also applied to the average MRI, fsaverage, to obtain the leadfield matrix for the average head model.

7.2.3 ERP Preprocessing

The high-density EEG data recorded during the face recognition task was processed using the MNE-python library (Gramfort et al., 2013). The data were first downsampled to 250 Hz and bad electrode channels were automatically detected using the different noisy channel detection methods in the PREP pipeline (Bigdely-Shamlo et al., 2015). The electrodes indicated as bad were excluded from further analysis. The data was band-pass filtered using a zero phase shift Butterworth filter with half-amplitude cut-off frequencies of 0.3 Hz and 30 Hz and a 12 dB/octave slope. The power line noise was then removed using a 50 Hz notch filter. Independent component analysis was applied for eye blink and horizontal eye movement artefact rejection. In case bad electrode channels were identified and excluded in the first step, these channels were interpolated at this stage. Subsequently, data were re-referenced to an average common reference. In the next step, the data was segmented into epochs going from 100 ms before the stimulus onset to 500 ms after. Finally, epochs containing artefacts were rejected using the following criteria: 75 μV maximum gradient criterion; 100 μV minimal/maximal amplitude criterion; 150 μV maximum difference criterion; 0.5 μV low activity criterion during 100 ms.

7.2.4 Simulation

Simple ERP waveforms were simulated using half-cycle sinusoidal waveforms to allow the objective quantification of the localization error associated with the subject-specific and average head models. This was done by simulating activity in different regions of the brain, including noise, and projecting this activity to the scalp surface using the individual head models. For each subject, 80 epochs of 1000 ms were simulated, half of which contained the ERP waveform as well as pink noise, while only the noise was included in the other half. In each epoch, a pre-stimulus window of 200 ms was considered. By including epochs which only contain noise, and thus simulating two different conditions, it is possible to investigate the difference between the localizations obtained for both conditions. This approach helps in reducing systematic biases in the

source reconstruction process. If certain types of noise or non-specific activity consistently affect the EEG data, this might lead to similar localization errors across both conditions. By subtracting one condition from another, these systematic errors can be reduced, leading to a more accurate estimate of the neural sources.

Different networks responsible for generating ERP activity were simulated, each involving four symmetrically active brain regions, with two regions in each hemisphere. These regions were identified using the Destrieux cortical atlas parcellations. For each region of interest (ROI), the center of the parcellation was determined, and dipoles within a 10 mm radius around this center were selected. The ERP activity in these selected dipoles was simulated as a 5 Hz half-cycle sinusoidal waveform lasting 100 ms. A small delay was introduced across the ROIs: the ERP waveform began in the first ROI at 100 ms post-stimulus, followed by the second ROI 10 ms later, and then in the third and fourth ROIs at 120 ms. Additionally, the signal amplitude in the third and fourth ROIs was reduced to 80% of the amplitude in the first two ROIs. Table 1 provides an overview of the different ROIs selected for each network. The obtained ERP waveforms and the simulated ROIs can be found in respectively Figure 7.2 and the first column of Figure 7.3. These networks were designed to investigate localization errors across different ROIs, as previous studies have shown that localization errors are typically larger for temporal sources (Cuffin et al., 2001; Kobayashi et al., 2003). To simulate realistic conditions, pink noise was added to all epochs. The noise amplitude was adjusted to achieve different signal-to-noise ratios (SNRs) ranging from -20 dB to +0 dB. The SNR was defined as the ratio of the peak amplitude of the ERP component to the peak-to-peak amplitude measured within the pre-stimulus window. This SNR-range was chosen based on the VEPCON dataset, where an SNR of about -10 dB was observed for the N170 component.

After creating the simulated activity in source space, the source time series were projected to the scalp by applying the subject-specific FEM forward model created using the individual MRI for each subject and using the conductivity values based on the meta-analysis by McCann et al. (2019). This step results in individual epochs in sensor space, or thus the simulated EEG data.

7.2.5 Brain Activity Reconstruction

For the reconstruction of the brain activity, the MNE-python implementation of the exact Low-Resolution Tomography (eLORETA) inverse method was used

Table 7.1. Overview of the different ROIs used for the simulation of the networks. lh: left hemisphere, rh: right hemisphere

Network	ROI 1	ROI 2	ROI 3	ROI 4
Temporo-Occipital network	Occipital Pole (lh)	Occipital Pole (rh)	Inferior Temporal Sulcus (lh)	Inferior Temporal Sulcus (rh)
Fronto-Parietal network	Inferior Frontal Gyrus, pars opercularis (rh)	Inferior Frontal Gyrus, pars opercularis (lh)	Supramarginal gyrus (lh)	Supramarginal gyrus (rh)
Fronto-Occipital network	Occipital Pole (lh)	Occipital Pole (rh)	Inferior Frontal Gyrus, pars opercularis (rh)	Inferior Frontal Gyrus, pars opercularis (lh)
Temporo-Parietal network	Inferior Temporal Sulcus (lh)	Inferior Temporal Sulcus (rh)	Supramarginal gyrus (lh)	Supramarginal gyrus (rh)

(Pascual-Marqui et al., 2011). The source reconstruction was done for each epoch separately, using both the subject-specific head models and the average head models that were previously constructed using the three different modelling pipelines. Noise pre-whitening of the leadfield matrix was applied using the noise covariance matrix before calculating the inverse solution. Next, the absolute magnitude of the dipoles or the current source density (CSD) was calculated, disregarding the orientation information of the dipoles in subsequent analyses. In a final step, for each subject, each condition and for each head model, the average response was calculated. In the case of the simulated data, an evoked response was obtained for the ERP and the noise condition for each subject and both the subject-specific and the average head models, while for the experimental data, an evoked response in source space to the faces and to the scrambled images was obtained, again for each subject and for both the subject-specific and the average head models.

7.2.6 Evaluation of the Source Reconstruction

Simulated Data

Different aspects are taken into account in the evaluation of the source reconstruction: the correspondence between the obtained sources and the simulated sources, the localization error and the spatial dispersion of these reconstructed sources, and the correlation between the originally simulated activity and the reconstructed activity.

For each subject, the difference in source space activity between the ERP and the noise condition is calculated, after which the data is averaged over the time window of interest, in this case from 100 ms to 220 ms post-stimulus. The data is then thresholded so that only the 5% strongest differences between the

ERP and noise conditions remain, after which the remaining active dipoles are grouped into potential clusters based on the spatial adjacency. Two dipoles are considered to be adjacent if the distance between both dipoles is smaller than 5 mm. Finally, only clusters containing at least five dipoles are retained.

For each of the obtained dipole clusters, the distance between the centre of the cluster and the centre of the simulated ROIs is calculated. Each ROI for which at least one reconstructed cluster is found within a 3 cm distance is considered a true positive (TP), while ROIs without a cluster within this distance are considered false negatives (FN). Similarly, clusters that are not within a 3 cm distance of a simulated ROI are annotated as false positives (FP). Based on this classification of the clusters, the sensitivity and the precision of the localization are then calculated as respectively the ratio of the number of TPs over the sum of the TPs and the FNs and the ratio of the number of TPs over the sum of the TPs and FPs. These measures are used to quantify the correctness of the reconstructed activity. To clarify these metrics further, a figure illustrating the calculation of sensitivity and precision is provided (Figure 7.1). As the maximal distance is an important parameter, also the effect of this parameter was investigated by including the results of using a maximal distance of 1 cm and 5 cm in the appendix.

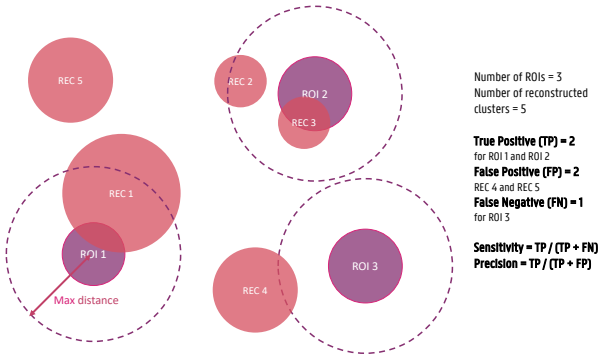

Figure 7.1. Illustration of the calculation of sensitivity and precision of the source reconstructions for the simulated data. True positives (TPs) are defined as reconstructed clusters within a 3 cm distance from the center of the simulated ROIs, while false negatives (FNs) are ROIs without a nearby cluster, and false positives (FPs) are clusters not within 3 cm of any ROI. Sensitivity is calculated as the ratio of TPs to the sum of TPs and FNs, and precision is calculated as the ratio of TPs to the sum of TPs and FPs.

For the calculation of the localization error and the spatial dispersion, only the true positive ROIs are taken into account. The localization error is calcu-

lated as the Euclidean distance between the centre of the simulated ROI and the reconstructed cluster. When more than one cluster is within the 3 cm distance of the ROI, the average of the localization errors is taken into account. The spatial dispersion, on the other hand, is calculated as the difference between the total volume of all reconstructed clusters within the 3 cm distance of the ROI and the total volume of the ROI. This measure is then normalized by dividing by the total volume of the simulated ROI to take into account differences in the dispersion of the original activity.

VEPCON data

As no ground truth data exists for the sources underlying the signals measured during the face task, the evaluation of the reconstructed activity can only be evaluated descriptively. One of the ERP components elicited by the faces task that is used in the VEPCON dataset is the N170. This component is larger when the eliciting stimulus is a face compared to when the stimulus is a non-face object, such as a scrambled face or a car (Rossion and Jacques, 2012). Many researchers have investigated the sources underlying this component. Using a dipolar fit method, Taylor et al. (2001) have located the N170 in the middle part of the fusiform gyrus. This localization corresponds to the fusiform face area that was identified in fMRI studies (Haxby et al., 2000), as well as in intracranial EEG studies (Engell and McCarthy, 2014). Similarly, Henson et al. (2007) found differences between the localization of faces and scrambled faces in the anterior fusiform gyrus, with a strong dominance towards the right hemisphere .

In this work, each of the individual epochs will be source-localized using both the subject-specific head models and the average head models. The obtained localization will then be averaged for each condition dataset and, in the case the subject-specific head model was used, the obtained results will be morphed to the average head model after which averaging can be applied over all subjects. The 5% dipoles with the strongest difference in activation between the two conditions within a time window of 150 ms to 170 ms post-stimulus will then be visualized and compared to the regions identified in the literature.

7.3 Results

7.3.1 Simulated data

The simulated EEG data of the different networks was source localized for each subject using both the subject-specific and the template head models, using both of the FEM models and a BEM model for the reconstruction. Figure 7.2 shows the simulated data at the sensor level. In the figure, the symmetric nature of the simulated data is visible. While in most networks the activity of the different ROIs of a single hemisphere is blended at the surface, for the fronto-occipital network a clear distinction is visible between the frontal and the occipital subcomponents of the simulated ERP waveform, both when looking at the topography of the obtained signal and when inspecting the waveform. This effect might facilitate the source localization compared to the other networks, where the activity from the different sources is less separated spatially at the scalp level.

In Figure 7.3, both the originally simulated data in source space and the reconstructed activity averaged over all subjects for the different networks for an SNR level of -10dB are shown. To reduce systematic biases in the source reconstruction, the difference between the reconstructed activity for the ERP and noise conditions is shown. As averaging over subject-specific anatomies is not possible, the source activity of both the original simulated data and the subject-specific reconstruction was morphed into the anatomy of the average head model before averaging. The figure illustrates the differences between the obtained reconstruction when using the different models. The results obtained with the two FEM models, constructed using different conductivity values, are very similar for most of the networks. While differences in the intensity of the activity can be observed, the location of the activity averaged over all subjects is very similar when using the FEM models with different conductivities. Looking at the different networks, the figures show that the location of the ROI influences on the accuracy of the localization. For the temporo-parietal network, for example, the activity in the temporal lobes is not reconstructed using the subject-specific FEM-based models, while it is clearly present for the temporo-occipital network. The differences between the subject-specific reconstructions and the template reconstructions illustrate that for both FEM approaches better results are obtained using the subject-specific reconstructions. It is clear that while most simulated are reconstructed, i.e. taking into account some

mislocalizations, also many false positive clusters are reconstructed. Finally, the figure shows that the results obtained using the BEM models perform quite poorly. Limited differences are found between the subject-specific reconstructions and the template reconstructions in this case in terms of the location of the reconstructed activity. Upward mislocalizations seem to be present for all of the different networks when using BEM models. The occipital sources are localized more towards the superior parietal lobe, for example, while no clear reconstruction can be found for the temporal ROIs. Finally, the figure also shows that only for the fronto-occipital network two distinct ROIs are localized per hemisphere, while only a single spread-out ROIs is reconstructed per hemisphere for the other networks.

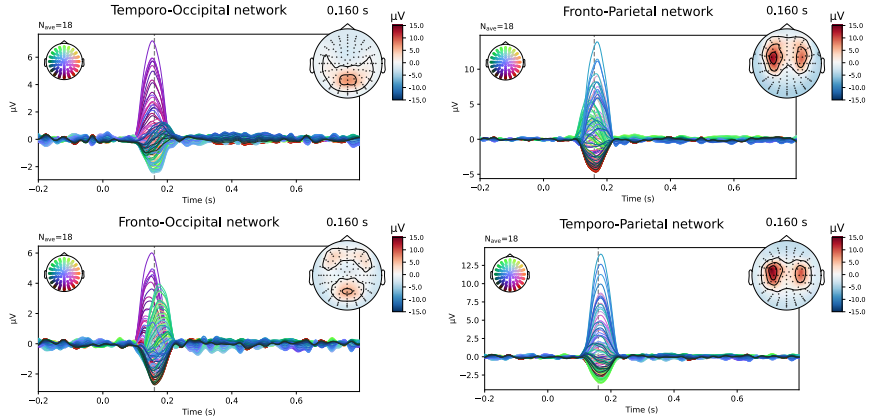

Figure 7.2. Overview of the simulated data at sensor level averaged over all subjects. The simulated epochs in the ERP condition at SNR = -10dB are averaged.

The quantification results of the localization errors associated with the localizations for the individual subjects are shown in Figure 7.4. In this evaluation of the source reconstructions, different aspects were taken into account: the sensitivity and the precision of the obtained sources, the localization error and the spatial dispersion of these reconstructed sources. For each of these measures, the difference between using the subject-specific and the average head models was investigated, as well as the differences between the different modelling approaches. Clusters of activity were considered correctly localized when the difference between the centre of the reconstructed cluster was within 3 cm of the centre of the simulated ROIs. As this maximal distance is an important parameter, the results when using a maximal distance of both 1 cm and 5 cm were

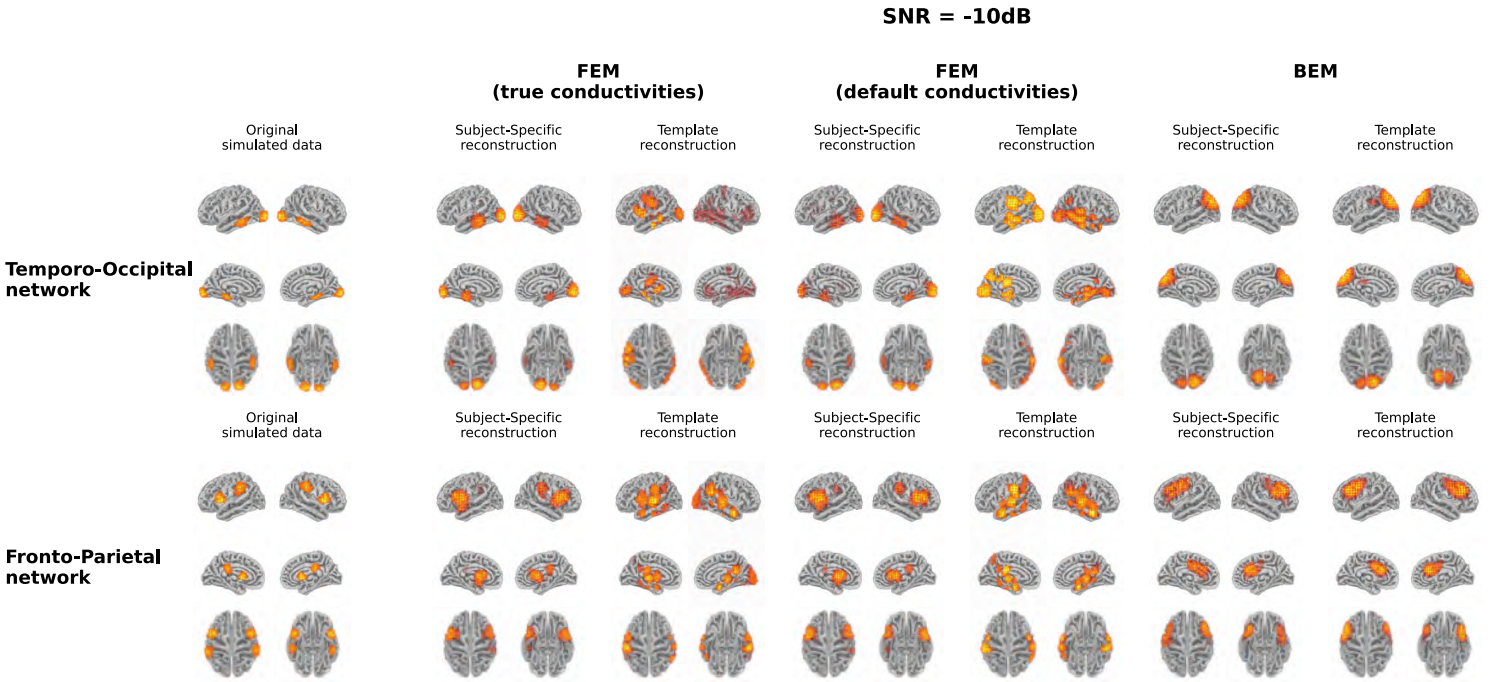

Figure 7.3. Overview of the original simulated data and the reconstructed activity averaged over all subjects for the different networks at SNR = -10dB. For the reconstructed activity, the difference between the ERP- and the noise-conditions is shown. In the case of the simulations and the subject-specific reconstructions, the source activity was morphed to the anatomy of the average head model before averaging.

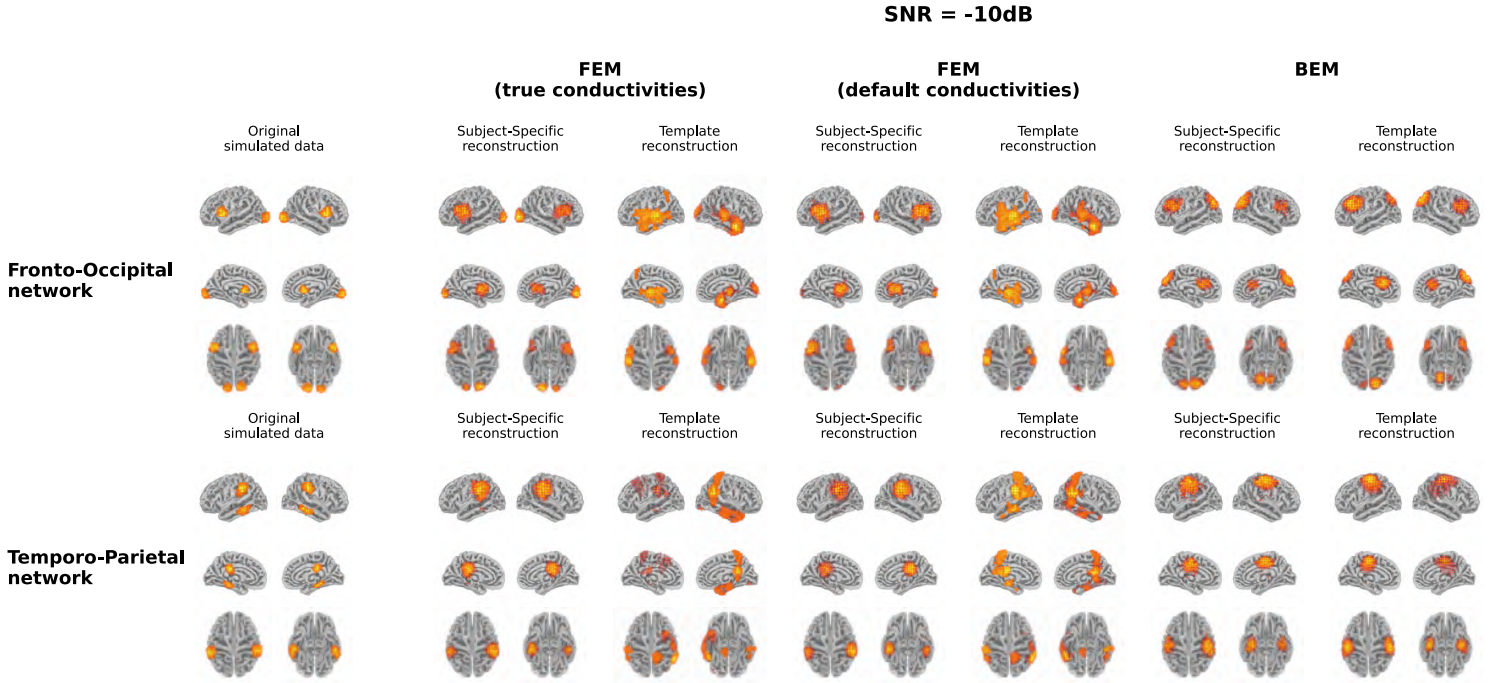

Figure 7.3. (Continued) Overview of the original simulated data and the reconstructed activity averaged over all subjects for the different networks at SNR = -10dB. For the reconstructed activity, the difference between the ERP- and the noise-conditions is shown. In the case of the simulations and the subject-specific reconstructions, the source activity was morphed to the anatomy of the average head model before averaging.

included in the appendix. Looking at the different FEM models, higher sensitivity and precision, as well as smaller localization errors were found when using the subject-specific head models compared to the template head model. These trends were found for the different simulated networks, however, some individual differences were observed. For most subject-specific reconstructions, a sensitivity value of about 0.75 is achieved, meaning that one out of the four simulated ROIs was not reconstructed for most subjects. The mean sensitivity obtained using the template-based head models is lower, around 0.5, illustrating that only two ROIs are correctly reconstructed. The sensitivity of the template-based reconstructions however increases for all models when increasing the maximal distance to consider reconstructed activity to 50 mm, indicating that the ROIs are reconstructed with a large localization error. The precision of the localizations is quite high for all of the subject-specific reconstructions, for all networks, indicating that only a limited number of false positive reconstructed sources were found. Very low precision values are found however when using the template head models. This result again illustrates that while the different ROIs are reconstructed, the localization error associated with them is too large to consider them as true positives.

Only considering the clusters located closely to the simulated ROIs, the localization error and the spatial dispersion were investigated. These results are shown in respectively the third and the fourth row of Figure 7.4. It is clear that for both FEM-based head modelling approaches, the localization error is smaller for subject-specific reconstructions compared to the template reconstructions. Surprisingly, higher spatial dispersion is found when using subject-specific headmodels compared to using the template head models, meaning that larger volumes of reconstructed activity are found compared to the simulated data.

Looking at the BEM models, higher sensitivity values are found when using the template head models compared to the subject-specific head models, while the opposite effect is found for the precision. A large range of precision values is found when using the subject-specific head models, indicating that in this case, the number of false positive reconstructed clusters is very dependent on the individual subject. As expected based on the results shown in Figure 7.3, similar localization errors are found for the subject-specific and the template-based BEM models. Interesting to note is that the quantitative results for all template-based head models in terms of sensitivity, precision, localization error and spatial dispersion are similar for the two FEM models and the BEM model,

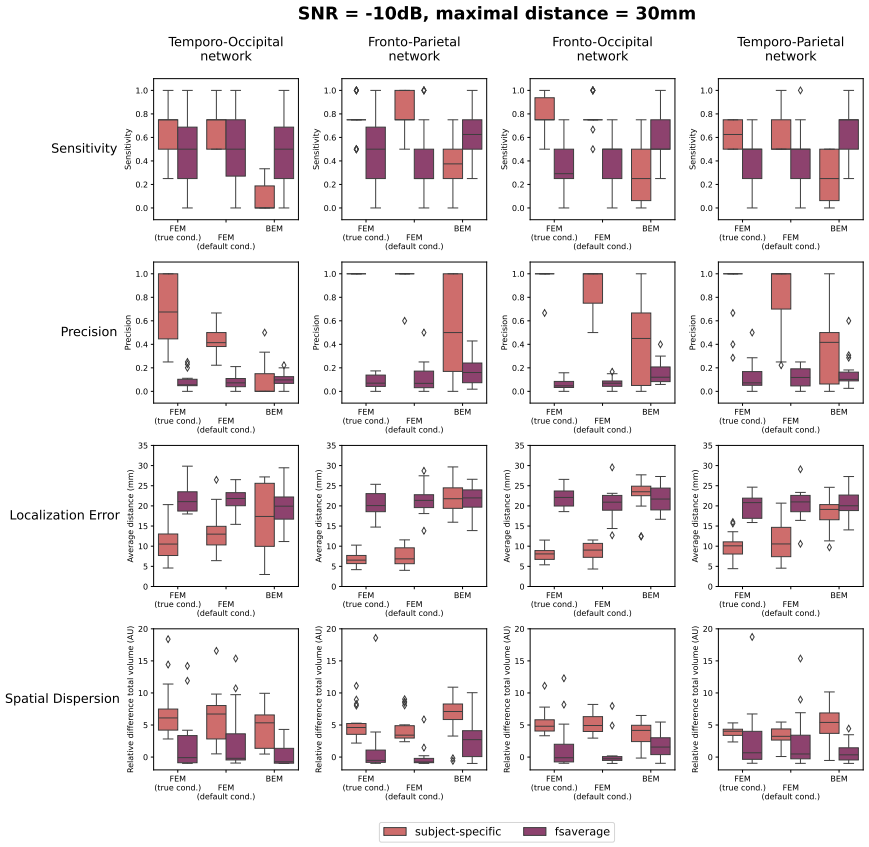

Figure 7.4. Results of the quantification of the localization errors for the SNR = -10dB. In this evaluation the sensitivity and the precision of the obtained sources, the localization error and the spatial dispersion of these reconstructed sources were taken into account. For each of these measures, the difference between using the subject-specific and average head models is shown for each of the different modelling approaches. Clusters of activity were considered to be correctly localized when the difference between the center of the reconstructed cluster was within 3 cm of the center of the simulated ROIs.

while different errors are made in terms of the location of the reconstructed sources (cf. Figure 7.3).

Finally, also the effect of the SNR of the simulated data on the reconstructions is quantified in Figure 7.5. In this figure, the results obtained for the different networks are aggregated. As before, the results when using a maximal distance of both 1 cm and 5 cm are included in the supplementary materials. The figures indicate only a limited effect of the SNR for most measures. A slight increase in sensitivity with increasing SNR can be found for the subject-specific FEM

models, as the boxplots indicate that there are fewer subjects for whom only one or two of the simulated ROIs are reconstructed. Also, an increasing trend with increasing SNR was found when looking at the precision. Finally, a limited improvement can be found in the localization error when increasing the SNR from -20 dB to -10 dB. Further increase of the SNR has almost no effect. The most prominent conclusions that can be drawn from this figure, however, are again that for both FEM-based modelling approaches, the subject-specific head models perform better than the template-based methods in terms of sensitivity, precision and localization errors, while the BEM-based modelling approaches perform worse in the case of subject-specific models but perform similarly when using template-based models compared to the FEM-models.

7.3.2 Real task data

The evoked potentials averaged over all subjects are shown in Figure 7.6 both for the faces and the scrambled faces. A clear difference between both conditions was found between 150 ms and 170 ms after the stimulus onset. The N170 component is thus clearly present in the data when faces were presented to the subjects, while it is not for the scrambled faces. Figure 7.7 shows the difference of the obtained reconstructions between both conditions averaged over all subjects using both the subject-specific head models and the template head model. In the first column of the figure the expected reconstructed area, i.e. the fusiform area, is shown. The figures show that in the case of the subject-specific FEM head models, most activity is found in the left and right fusiform area while using the subject-specific BEM model, most activity is found more occipitally. When using the template head model, on the other hand, the reconstructed activity is more spread out compared to the subject-specific reconstructions. In the case of the FEM-models, activity is found not only in the fusiform area, but also at the frontal and temporal poles as well as in occipital lobe. In case of the template BEM models, the largest differences in activity between both conditions are again found occipitally.

7.4 Discussion

The goal of this work was to investigate the effect of using template head models instead of subject-specific head models when localizing ERPs and to quantify the localization error associated with this simplification. To this end, both simulated data and real task data were used. Different activity networks were

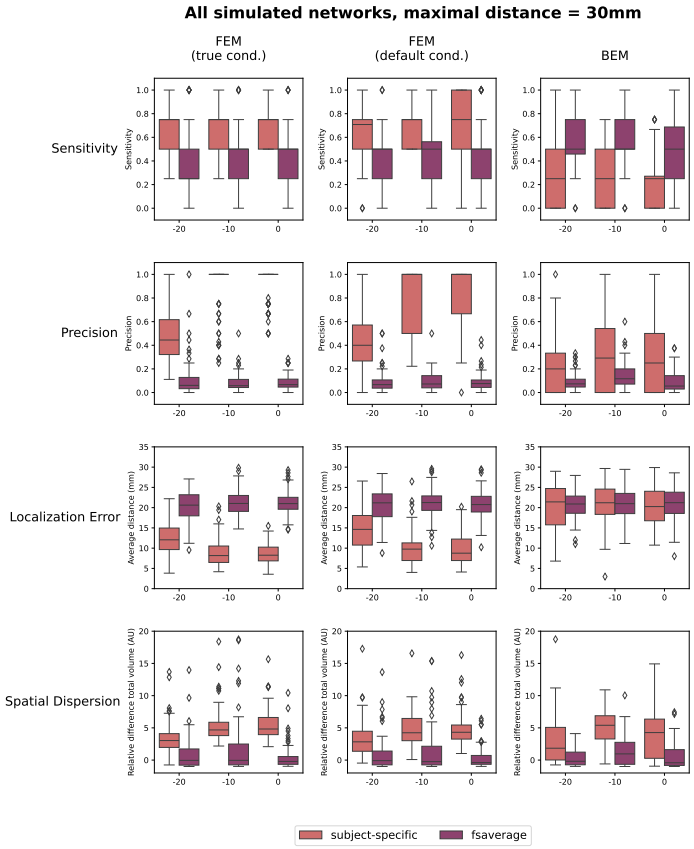

Figure 7.5. Results of the quantification of the localization errors. In this evaluation the sensitivity and the precision of the obtained sources, the localization error and the spatial dispersion of these reconstructed sources were taken into account. For each of these measures, the effect of both the SNR of the simulated data and the difference between using the subject-specific and average head models is shown for each of the different modelling approaches. Clusters of activity were considered to be correctly localized when the difference between the center of the reconstructed cluster was within 3 cm of the center of the simulated ROIs.

simulated, each with four ROIs and specific SNRs using subject-specific head models created using FEM. We found that subject-specific head models perform significantly better than template head models, and that the modelling approach (FEM or BEM) only has a limited influence on the accuracy of the results when using template head models.

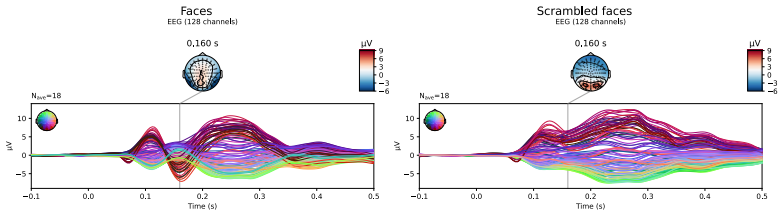

Figure 7.6. Visualization of the evoked potentials averaged over all subjects for both the faces and scrambled faces conditions of the face-detection task in the VEPCON dataset. Also the topography at 160 ms post-stimulus is indicated, as this is considered the peak of the N170 component in the faces condition.

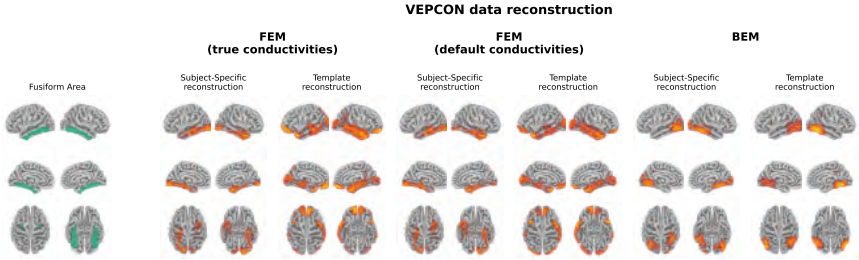

Figure 7.7. Illustration of the fusiform area and the difference in the reconstructed activity between both conditions for the N170 component averaged over all subjects.

7.4.1 Simulated data

Effect of template head model vs. subject-specific models

Looking at the simulations, the results indicate there is a significant decrease in both the sensitivity and precision when using template head models instead of subject-specific head models when using FEM-based head models. Interestingly, when using BEM models the sensitivity is better when using the template head model. Also, clear differences in the localization error were found between the subject-specific and the template FEM models, as values between ±5-20 mm are found using the subject-specific headmodels compared to localization errors between ±15-30 mm are found for the template-based models. These results correspond with our hypothesis and with results found in literature, as many researchers report that the ideal head model for the most accurate reconstruction of the neural activity is a realistic head model created using the subject's individual MRI (Akalin Acar and Makeig, 2013; Conte and Richards, 2021). However, it is also important to note that, as subject-specific models

were used in the simulations, this is also the case for which the best results were expected.

Looking at the results at the group level (Figure 7.3), it is clear that not all simulated ROIs are present, especially when using template-based models, and that a localization error is associated with other reconstructed ROIs. As in most ERP research, the MRI data of individual subjects is not available, it is important to take these limitations into account in the interpretation of obtained results. In cases where no subject-specific data is available, it might be helpful to use a hypothesis-driven approach to investigate the cortical generators of a certain ERP component. This approach can help in identifying FPs and possible FNs in the reconstructed sources.

Effect of using different conductivity values

As mentioned in the introduction, studies have shown that accurate electrical conductivity values for the different tissue types included in the head model are important for accurate source localization of the EEG signals (Vorwerk et al., 2019). Furthermore, McCann et al. (2019) have shown that the electrical conductivities assumed for each compartment likely vary between individuals. As the measurement of the electrical conductivities of the different tissue types in individuals is not feasible, the conductivity values used in the created head models will thus always be (slightly) off. To investigate the effect of this error on the localization accuracy, two different FEM models with different conductivity values assigned to the tissues were used in this work. Differences were found in all of the measures used in the quantification of the results with the models using the 'true' conductivities giving better results. These found differences are however small, both when the subject-specific and the template-based head models are used.

Furthermore, it should be noted that the subject-specific FEM model using the 'true' conductivities was also used in the simulation of the data. This model was thus also expected to yield the best outcome, as an identical transformation was applied to reconstruct the data. Differences between the simulated data and the reconstructed activity in this case can thus be attributed to the assumptions made by the inverse solutions, as this is a non-unique problem. These results thus indicate that, while it is important to use the most accurate conductivity values possible, the effect of deviations in these values is much smaller than the effect of using subject-specific vs. template-based head models.

Effect of FEM vs. BEM models

In this work, different head modelling approaches were used for the reconstruction of the simulated data, namely two FEM models with different conductivity values and a BEM model. As discussed in the previous section, the effect of using different conductivity values for the different tissue types in the FEM models is more limited than the use of subject-specific head models. However, much larger differences are found between the results obtained using the FEM-based head models and the results using the BEM-based models. Looking at the subject-specific reconstruction, the FEM-based models perform better than the BEM-based models across all measures. This result was expected, as BEM models are much less accurate than the FEM-based models that were used because they are unable to take into account cerebrospinal fluid (CSF). Also the influence of including more head tissue compartments in the model has been studied extensively before (Vorwerk et al., 2014; Neugebauer et al., 2017). However, again it is also important to note that, as FEM models were used in the simulations, this is also the case for which the best results were expected.

It is however interesting to note that the quantitative results obtained using the template-based head models are similar across the different modelling approaches. For some networks, the template-based BEM models even perform slightly better than the template-based FEM models in terms of sensitivity. These quantitative results were not what was expected based on the results that were plotted at the group level (Figure 7.3), where the localization errors seem larger for the template-based BEM models compared to the FEM-models. Combining these results indicates that the localization errors made using the template-BEM model are less systematic than those made using the template-FEM models, i.e. the localizations and the associated errors that are obtained at the individual level are more random than in the case of the FEM models. This will cause some of the reconstructed ROIs to cancel out at the group level, seemingly indicating that these ROIs were not reconstructed using these models.

Effect of the Signal-to-Noise Ratio

While the effect of the SNR is limited in this simulated dataset, some differences are still observed between the lowest simulated SNR, -20 dB, and the other SNR levels. For the subject-specific FEM models, for example, lower precision, higher localization errors and less spatial dispersion are found for the

lowest SNR level compared to the others, indicating that more FPs are found for the lower SNRs. It is important to take these results into account when interpreting findings obtained from real data. In the case of low SNRs, multiple sources may be reconstructed which are not related to the true underlying activity of the ERP, even after averaging over all subjects (cf. Figures C3 to C6 in appendix). Another possibility is that due to the larger localization errors and smaller reconstructed volumes, the obtained sources are not pertained after averaging over all subjects, giving the impression that this source is not present in the data. The differences between the averaged results and the quantifications illustrate the importance of also looking at the results of the reconstruction at the level of the individual subject. Furthermore, these results again illustrate that using a hypothesis-driven approach for interpreting the findings can help. Other methods to increase the SNR of the data might be useful, such as using averaged data instead of individual trials when possible.

However, more and more interest is found in functional connectivity analysis in source space to investigate the networks underlying brain activity. As many functional connectivity measures focus on spectral features of the data, in this case, a priori averaging of the epochs is not possible, as high-frequency information would be averaged out in the data, as well as time- but not phase-locked activity (Simoes et al., 2003). While researchers have already investigated the influence of the head model in terms of neglecting white/grey matter distinction or CSF on EEG source connectivity analyses (Cho et al., 2015), this work shows that also the SNR of the data should be taken into account.

Effect of different networks

Finally, the results show some differences in localization performance for the different networks that were simulated. Looking at the averaged reconstructions, it is clear that not all ROIs were reconstructed for the different networks. When using the template-based FEM models for the reconstruction of the fronto-parietal and the fronto-occipital networks, no frontal ROIS were found in the right hemisphere in the averaged reconstructions. However, the quantitative results found for these networks indicate mean sensitivity values of 0.75. One possible explanation for the absence of the frontal sources could be the reduced amplitude of the simulated signals in these ROIs compared to the signals in the respectively parietal and occipital sources.

Looking at the results obtained using the BEM-based head models, large localization errors were found across the different networks. For all networks

except the fronto-occipital network, the different ROIs appear to have been localized as single clusters per hemisphere, indicating that the BEM-based models have more difficulty separating sources of activity. This seems probable, as in the simulated ERP-data at the sensor level, also the fronto-occipital network is the only network in which a clear separation of the underlying sources could be seen in the topography and the waveform of the obtained ERP. Furthermore, for the networks including occipital sources, an upward displacement of these sources could be seen when using the BEM-based head models. Similar mislocalization results were also found by Huang et al. (2016) and Akalin Acar and Makeig (2013), who both identified larger localization errors for occipital sources when using less accurate head models. Multiple explanations can be found in literature for these errors in the localization of occipital sources. The occipital lobes are complex structures with many folds and curves with significant inter-subject variability. Using less accurate head models in this case can thus increase the mislocalization of the sources. In addition to this, also the occipital bone is in general thicker with again significant inter-subject variability. Modelling this using a non-accurate head model will again lead to larger errors in the head model, reducing the localization precision (Michel and Brunet, 2019).

A limitation of this study was that only a limited number of ROIs were investigated. As it was shown that the underlying sources influence the accuracy of the reconstruction, in future work, a more generalized approach should be developed to investigate the effect of different networks more systematically. While such approaches have already been proposed for focal sources (Samuelsson et al., 2021), this problem is much more challenging when considering simultaneous activations and remains, to the best of our knowledge, currently unsolved.

7.4.2 Real task data

Localization of the high-density EEG data in the VEPCON dataset, recorded while presenting faces and scrambled faces to subjects, resulted in different sources using the subject-specific head models and the average head model. Using the subject-specific FEM head models, the N170 component was mainly localized to the left and right fusiform areas. These results correspond to the sources found in other studies (Rossion and Jacques, 2012), both using EEG/MEG data (Henson et al., 2007) and fMRI (Haxby et al., 2000). While the fusiform area is considered the core generator of the N170, there is evidence

suggesting that also the prefrontal cortex plays a role in the processing of faces and that this region contributes to the top-down modulation of face processing (Kornblith and Tsao, 2017; Gazzaniga et al., 2009). There was however no activation found in this region in this work.

Looking at the results obtained using the template FEM models, again the left and right fusiform areas were found as generating sources of the N170. However in this case, also multiple other sources were found, such as the frontal and temporal pole and the occipital lobe. Finally, using both the subject-specific and the template-based BEM models, the N170 component was localized more in the occipital lobe with the activity extending towards the posterior inferior temporal lobe, rather than in the fusiform area. As the results obtained using the subject-specific FEM head models correspond well to results reported in the literature, these results indicate that while the template-based head model can be used for the localization of ERP sources, interpretations should be done with care, as mislocalizations of the sources and localization errors can be present.

7.5 Conclusion

In this study, the effect of using template head models instead of subject-specific head models was investigated in localizing event-related potentials (ERPs) and in quantifying the associated localization error using both simulated and real data. As expected, the results indicated that subject-specific head models outperform template head models in terms of localization accuracy. Using template head models also increases both false positives and false negatives in source reconstructions. Also the effect of using more accurate FEM models compared to simple BEM models was investigated. As found in previous studies, more anatomically accurate head models result in better localization performance. When template-based head models are used however, similar quantitative results in terms of sensitivity, precision, localization error and spatial dispersion were found for the FEM- and BEM-based head models, even though the patterns of mislocalizations are different. Furthermore, the role of the SNR on the localization performance was investigated, with the results showing that low SNRs may lead to larger errors. Finally, the influence of the simulated network also has a significant effect on the accuracy of the source localization, with the results indicating that some regions, such as the temporal and occipital lobes are more prone to mislocalization when using template head models.

While template head models offer a practical alternative for ERP source localization when no subject-specific MRI data is available, their limitations should be considered, and the results should be interpreted with caution. A priori knowledge and hypothesis-driven approaches are crucial for interpreting results obtained with average head models. Interestingly, however, is that while creating more accurate and detailed head models is beneficial for the localization accuracy when using subject-specific head models, this is not the case for template head models. As many studies investigating the effect of modelling approaches for ESI focus on focal sources, it would be beneficial if systematic approaches to assess the influence of multiple sources on localization accuracy would become more prominent.

8 | The impact of brain tumors and craniotomy lesions on scalp ERPs

Abstract

Electroencephalography (EEG) is widely used in both research and clinical settings, yet its accuracy can be significantly impacted by subject-specific anatomical anomalies such as brain lesions and skull defects. This study investigates the effects of glioma-related brain lesions and craniotomy-induced bone discontinuities on scalp-recorded EEG signals. To do this, single- and multi-source simulations were created using individualized forward models with and without these structural anomalies. We assessed changes in signal amplitude and topography, and identified the most affected electrodes. Real EEG recordings were also analyzed to evaluate how these anomalies influence the topography and source localization of early auditory evoked responses (P1 and N1 ERP components). Both single- and multi-source simulations showed that the distortions in the EEG signals depend on the location of the neural source and the location of the lesion. Electrode-level analyses showed that these distortions were most pronounced at the electrodes near the bone flap, and thus near the lesions. Real ERP data supported these findings: a subject with lesions near the auditory cortex showed notable topographic deviations over time for the P1 and N1 ERP components, while a subject with a frontal lesion showed minimal changes in the scalp EEG. These results highlight the need to include detailed brain and skull anatomy in EEG models, especially in studies that track changes over time in clinical populations.

8.1 Introduction

Event-Related Potentials (ERPs) are a valuable tool for investigating brain activity. Recorded using electroencephalography (EEG), they enable researchers to study neuronal processes underlying cognitive functions with millisecond precision (Luck, 2014). Due to its excellent temporal resolution and direct link to neural activity, EEG has played a critical role in advancing our understanding of cognitive processing. Beyond cognitive neuroscience, EEG is increasingly used in clinical and translational research for studying neuroplasticity in individuals with brain damage caused by a stroke or brain tumor.

Neuroplasticity refers to the brain's ability to reorganize itself in response to injury, involving structural and functional adaptations that help maintain or restore brain functions, such as cognitive and motor functions. In the context of gliomas, Cirillo et al. (2019) defined neuroplasticity as "the biological dynamic ability of the central nervous system to reorganize itself in response to injuries." Understanding neuroplasticity is essential for optimizing treatment strategies, including neurosurgical interventions, and for tracking recovery and functional reorganization over time. Given its excellent temporal resolution and sensitivity to dynamic changes in neural activity, EEG is well-suited for studying neuroplasticity. Unlike fMRI, which primarily reflects slow hemodynamic responses, EEG captures rapid changes in brain function and can provide insights into functional reorganization. Moreover, EEG's non-invasive nature makes it particularly useful for longitudinal studies that monitor neuroplasticity over extended periods.

For patients with gliomas located in eloquent brain areas, i.e. regions responsible for critical functions such as language, motor control, and sensory processing, neurosurgical approaches aim to maximize tumour resection while preserving critical functions, such as language processing. Awake craniotomy with intraoperative direct electrical stimulation (DES) has become the gold standard for glioma resection in these cases. This technique allows functional mapping of the brain to identify and spare essential cortical and subcortical structures, thereby reducing the risk of postoperative neurological deficits (Rahimpour et al., 2019; Surbeck et al., 2015). Compared to resections performed under general anaesthesia, awake craniotomy has been shown to improve both the extent of tumour resection and functional outcomes (De Witt Hamer et al., 2012).

While these surgical advancements have improved patient outcomes, they also introduce challenges for EEG research. A craniotomy—the surgical removal of part of the skull—creates structural changes that can significantly affect EEG recordings. The (temporary) removal of a portion of the skull alters the conductivity profile of the head. Previous research has demonstrated the importance of accurate head modelling in EEG source reconstruction, particularly with respect to skull conductivity (Dannhauer et al., 2011; Vorwerk et al., 2014; Montes-Restrepo et al., 2014). Additionally, studies have shown that skull defects, such as those resulting from craniotomy or traumatic injury, can distort the measured EEG signals (Flemming et al., 2005). In stroke patients, Piai et al. (2024) highlighted the impact of cerebrospinal fluid (CSF)-filled lesions on EEG amplitude and topography, further emphasizing the role of structural abnormalities in shaping electrophysiological recordings.

Despite growing awareness of these structural influences, the extent to which lesions caused by gliomas and craniotomies distort EEG/ERP signals remains insufficiently understood. Given that EEG is frequently used to assess neuroplasticity in glioma patients before and after surgery, it is crucial to determine how these anatomical alterations influence EEG measurements. The present study aims to quantify the impact of glioma-related lesions and craniotomy-induced skull defects on EEG, particularly in terms of amplitude (magnitude difference, MAG%) and topographic distortions (relative difference measure, RDM%). By simulating EEG signals using different head models, we assess how lesion-related structural changes influence scalp-level recordings and identify the electrodes most affected by these alterations. We also evaluate if the predictions based on the simulations correspond to the results found using real EEG data recorded in an auditory task in two different subjects, one with a lesion near the left auditory cortex and one with a left frontal lesion. Understanding these effects is essential for improving the accuracy of EEG-based assessments in glioma patients and ensuring reliable interpretations of neuroplasticity-related changes over time.

8.2 Methods

8.2.1 Participants and Data acquisition

For this study, two patients diagnosed with a brain glioma in an eloquent language area were recruited from the department of Neurosurgery at the Ghent

University Hospital in Belgium. The patients were diagnosed by an experienced neurosurgeon and neuroradiologist based on magnetic resonance imaging (MRI) and diffusion tenson imaging (DTI). These images were also used to establish the tumour location and to assess the subcortical glioma infiltration. Based on this information, an awake craniotomy with intraoperative language mapping was selected as part of the course of treatment. Both participants are Dutch native speakers and were between 40 and 60 years of age at the time of surgery. This study was approved by the Ghent University Hospital Ethical Committee (ONZ-2022-0127) and all participants provided informed consent.

Anatomical T1-weighted MRI images were collected for both patients at the Ghent University Hospital with a 1.5T SIEMENS-MAGNETOM Avanto scanner both pre- and postoperatively. The preoperative image was taken 1 day before the surgery, while postoperative images were collected both three and nine months after the surgery. In Figure 8.1, these images are shown for both patients, allowing us to evaluate the changes in the brain anomaly over time. In the pre-op image, the tumor itself is visible, while in the post-op images a lesion filled with oedema and/or cerebrospinal fluid (CSF) can be seen. At each of these evaluation moments, also EEG data was recorded for both patients. An attentive auditory oddball paradigm with phonemic contrasts was used to obtain an electrophysiological language assessment through the recording of the P300 ERP component. The EEG data was recorded at a sampling rate of 500 Hz with a 128-channel EasyCap electrode cap using a BrainVision BrainAmp amplifier in combination with the BrainVision Recorder software (Brain Products, Germany). Impedances were kept below 20 kΩ throughout the recording.

8.2.2 MRI processing and head model construction

For both patients, four individual forward models were computed: one for each of the three time points (T1 – pre-op; T2 – 3 months post; T3 – 9 months post), and one in which the lesion was not considered, creating a “normal”, reference brain. The T1-weighted MRI images at the different evaluation moments were used to create three finite element method (FEM) head models for each patient. In the first step, the SimNIBS-charm pipeline (Saturnino et al., 2019) as implemented in the Brainstorm toolbox (Tadel et al., 2011) was used to segment the MRI images into nine different tissue types: white matter, grey matter, CSF, compact bone, spongy bone, scalp, eyes, blood and muscle. As this tool is unable to segment other tissue types, manual segmentations of the tumour (preop), and oedematous tissue, CSF, titanium fixtures and the bone flap

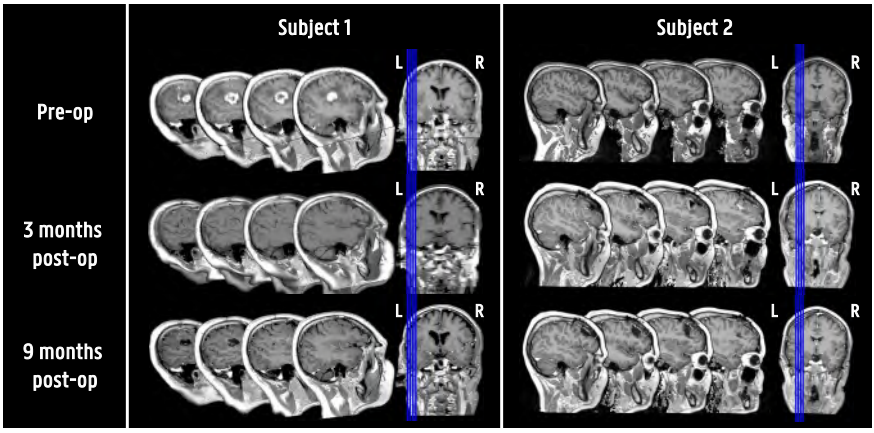

Figure 8.1. Multislice images of the brain tumours and post-surgery lesions on a structural T1 MRI scan of both subjects.

(postop) were created in ITK-snap (Yushkevich et al., 2006) based on the corresponding MRIs. Subsequently, hexahedral volumetric meshes representing the geometry of the head were created with a resolution of 1 mm^3. Conductivity values were specified for each tissue type based on the weighted average means from the meta-analysis by McCann et al. (2019): 0.22 S/m for white matter, 0.47 S/m for grey matter, 1.71 S/m for the CSF, 0.006 S/m for the compact bone, 0.048 S/m for the spongiform bone, 0.41 S/m for the scalp, 0.33 S/m for the eyes, 0.57 S/m for blood and finally 0.32 S/m for the muscle layer. For the gliomas, a conductivity value of 0.50 S/m was used based on values found for low-grade gliomas in the work of Latikka and Eskola (2019), where the resistivity of different types of human brain tumours was investigated in vivo. Conductivity values for titanium (2.38×10^6S/m), oedematous tissue (0.80 S/m), and the bone flap (0.50 S/m) were determined based on literature values and physiological reasoning. The conductivity for titanium is consistent with values reported for commercially pure titanium. A conductivity value of 0.80 S/m was assigned to oedematous tissue, as a physiologically plausible estimate lying between the reported values for vasogenic edema (≈0.71S/m) and interstitial edema (≈2.0S/m) (Lok et al., 2023), under the assumption that the postoperative edema present in our subjects likely exhibits mixed characteristics of these two types. The conductivity value for the bone flap was obtained from averaging the conductivities of dominant bone defect constituents during early bone healing, namely extracellular fluid, hematoma, and cartilage (Verma

et al., 2022). Equivalent current dipoles were distributed within the grey matter to create the source model. The dipoles were spaced 3 mm apart, resulting in a dense and uniform grid of dipoles throughout the cortical surface. The forward model was subsequently calculated using the finite element method based on the SimBio software as implemented in the FieldTrip toolbox (Oostenveld et al., 2011; Vorwerk et al., 2018). All intermediate steps were visually inspected to ensure correct tissue segmentations, mesh generations and proper alignment of the head, source model and electrode positions.

8.2.3 Simulations

Single-source simulations

To examine how individual cortical sources contribute to the scalp EEG signal, we conducted single-source simulations by systematically activating dipoles across the cortical surface. Each dipole was assigned unit-amplitude activity. The forward models, both with (T1, T2, T3) and without (T0) lesions, were used to project these source activations to the scalp, simulating the resulting EEG topographies. The single-source simulations provided a baseline reference for understanding how dipole locations affect EEG scalp distributions. These simulations also allowed us to establish a controlled dataset for later comparisons, particularly in evaluating how lesions influence signal propagation.

Multisource ERP simulations

While single-source simulations provide valuable insight into how anomalies affect the forward model, they do not capture the complexity of cognitive event-related potentials (ERPs), which typically involve multiple simultaneously active brain regions. Given that cognitive ERPs are commonly the primary focus when assessing patients after brain surgery, we developed a set of simulations involving four distinct active cortical regions. The time courses of the different regions-of-interest were derived from an auditory oddball paradigm dataset (Abrahamse et al., 2021) and previously used to generate simulations by Piai et al. (2024) to study CSF-filled lesion effects. Artifact-free EEG data was segmented into epochs from 300 ms before to 1000 ms after the auditory stimulus onset. ICA decomposition was applied to all epochs and used to identify four primary components, assumed to represent cortical source activity from four different sources. The component time courses were then averaged over tri-

als for the two different experimental conditions (362 standard and 57 deviant trials), resulting in four distinct time courses per condition.

Four different dipole configurations were simulated, representing potential neuronal sources of a cognitive ERP. In the first scenario, dipoles were positioned in the left superior temporal lobe, the left inferior frontal lobe, and the left and right supramarginal gyrus (parietal lobe), as indicated in Figure 8.2. The second scenario maintained the same dipole locations but swapped the time courses of the first and second dipoles. In the third scenario, we returned to the first configuration but relocated the left supramarginal gyrus dipole to the right temporal lobe. Finally, in the fourth scenario, the right supramarginal gyrus dipole from the third scenario was moved to the right inferior frontal gyrus, creating a symmetrical dipole distribution. Each dipole was assigned distinct time courses for two experimental conditions. The simulated activity was then projected to the scalp using the different forward models, allowing us to investigate the effects of dipole location and time course variability on the resulting scalp EEG.

8.2.4 Evaluation of the effect of tumour- and craniotomy-induced lesions on simulated data

As we were interested in the effect of the tumour- and craniotomy-induced lesions on the measured EEG signals, we evaluated the differences in magnitude and topography of the signals obtained using the forward models that accurately incorporated these lesions and the reference model (T0), in which no lesions were considered. To quantify these differences, we used the magnitude difference measure (MAG%) and the relative difference measure (RDM%). The magnitude difference measure (MAG%) captures variations in overall signal strength and is defined as

$$MAG\%_i = 100 \cdot \left(\frac{\|V_{T_i}\| - \|V_{T_0}\|}{\|V_{T_0}\|} \right) \tag{8.1}$$

where $\|.\|$ denotes the Euclidean norm and V_{T_i} represents the (Nx1)-vector of the EEG signal, with N the number of electrodes, for the model based on the MRI-scan taken before the operation (T1), three months after the operation (T2) and nine months after the surgery (T3). A high MAG% indicates a substantial difference in signal magnitude due to the presence of lesions.

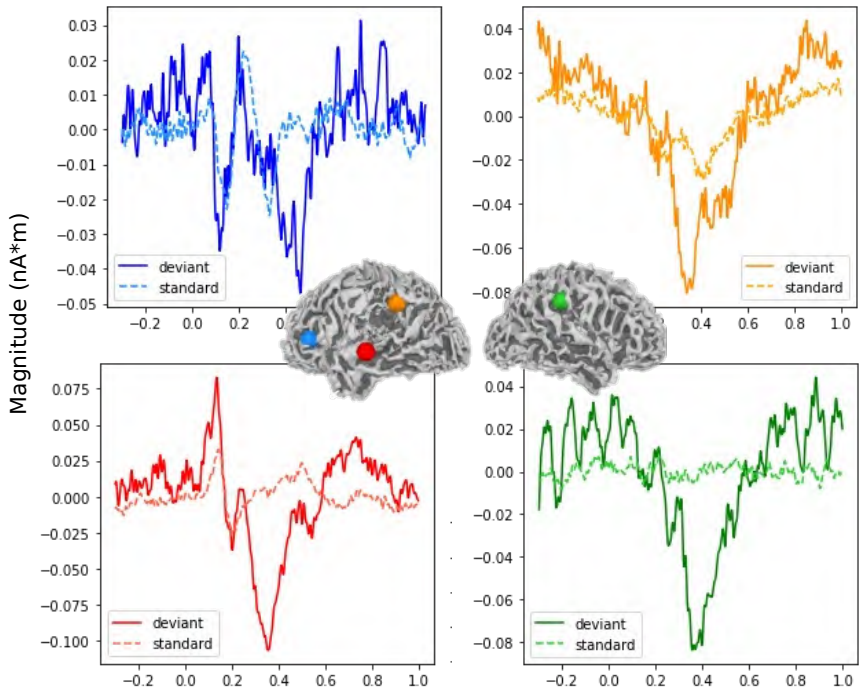

Figure 8.2. Time courses of the activity for four sources in a cognitive paradigm with conditions 1 and 2 (taken from an empirical P300 oddball task). Each set of the standard and deviant dipole activity time courses was assigned to a dipole, as indicated for scenario 1.

To assess differences in EEG topography, we used the relative difference measure (RDM%), which is independent of absolute magnitude and quantifies discrepancies in the spatial distribution of EEG signals. It is defined as

$$RDM\%_i = 50 \cdot \left\| \frac{V_{T_i}}{\|V_{T_i}\|} - \frac{V_{T_0}}{\|V_{T_0}\|} \right\| \tag{8.2}$$

A low RDM% value indicates a similar topographical distribution between the two models, whereas higher values suggest significant alterations due to the lesions.

Single-source evaluation

To evaluate the impact of lesions on the measured EEG, we conducted two analyses: one focusing on how lesion-induced differences in simulated EEG

signals varied depending on dipole location, and another examining how the presence of lesions affected each electrode's sensitivity to brain-wide activity.

In the first analysis, we assessed how lesion-induced differences in simulated EEG signals varied depending on dipole location. As previously described, we simulated unit dipole activity at each cortical source, oriented perpendicular to the cortical surface, and computed the resulting EEG signals for both the lesion (T1, T2, T3) and no-lesion (T0) models. We then calculated MAG% and RDM% values at the scalp level for the simulated data of each individual dipole to quantify changes in signal strength and spatial distribution, respectively. Higher values indicated greater discrepancies between the models, allowing us to identify the sources in the brain on which the presence of the lesions had the most significant impact. In addition, to disentangle the influence of the different types of lesions, we also constructed additional forward models in which either the tumour lesion or the craniotomy-related bone flap lesion was omitted. Specifically, when excluding the tumour lesion, the affected region was modeled as if it consisted of gray matter, based on the tissue segmentations produced by SimNIBS, Similarly, when excluding the bone flap lesion, the corresponding region was modeled as compact and spongiform bone, again following the SimNIBS tissue segmentations. These additional models were generated for T2 and T3, as those are the only time points where both lesion types were present, allowing us to assess their individual contributions to the observed EEG alterations.

While the first evaluation focused on differences per dipole (i.e., across electrodes), the second analysis reversed the perspective to assess lesion-induced changes per electrode, across all dipoles. For each electrode, we extracted the corresponding row of the lead field matrix, representing the spatial pattern of contributions from all dipole sources. By computing MAG% and RDM% across these electrode-specific vectors, we quantified, respectively, changes in the overall sensitivity and in the spatial distribution of contributing sources to each electrode. This allowed us to identify electrodes for which the aggregate cortical input was most altered due to the tumour and craniotomy lesions.

Multisource evaluation

In the evaluation of the multi-source simulations, we first computed the ERP difference wave between condition 1 and condition 2, averaged between 0.340 s and 0.360 s post-stimulus. Then, as in previous analyses, we calculated the

MAG% and RDM% for each scenario by comparing simulations with and without modelled lesions.

8.2.5 Evaluation of the tumour- and craniotomy-induced lesions on real data

To evaluate the effects of the tumour- and craniotomy-induced lesions on the measured EEG activity, we focused on the auditory P1 and N1 components that were obtained from the auditory oddball task with phonemic contrasts. These early components were selected because they have relatively well-defined and focal generators in the left and right auditory cortices, making them easier to localize and interpret compared to later or more distributed ERP components. For each subject and at each evaluation time point, we assessed the P1 and N1 responses in terms of amplitude and scalp topography, and compared these measures to those obtained from a normative dataset of 60 healthy controls.

Additionally, we performed electrical source imaging (ESI) using eLORETA to estimate the neural generators of the components. We compared source reconstructions obtained at each time point using both the model including the lesion (T1, T2, T3) and the one (T0) that did not. To provide a reference for interpreting patient data, we also estimated the generators of the components in the healthy control group. This allowed us to assess the impact of lesion inclusion on source localization accuracy.

The auditory oddball paradigm

In the attentive auditory oddball paradigm designed to elicit the P300 component, the stimuli consisted of phonemes that differed only in place of articulation. The standard stimulus [bə] was presented in 80% of trials, and the deviant stimulus [gə] in 20% of trials. Both auditory stimuli were 250 ms in duration.

The paradigm included 160 standard and 40 deviant stimuli, presented in pseudorandom order with an interstimulus interval (ISI) of 2000 ms, resulting in a total duration of approximately 8 minutes. Prior to the main task, participants completed a practice block consisting of 16 standard and 4 deviant trials to familiarize themselves with the task.

To assess stimulus categorization, participants were instructed to press a button (Chronos response box, Psychology Software Tools, Pittsburgh, PA, USA) whenever they detected a deviant stimulus. All stimuli were delivered binau-

rally at a comfortable listening level via ER1-insert earphones. Stimulus presentation was controlled using E-Prime 3.0 (Psychology Software Tools, Pittsburgh, PA, USA). To minimize eye movement artifacts, participants were instructed to focus on a central white fixation cross displayed on a black background throughout the task.

ERP data processing

The EEG preprocessing was performed in MNE-Python (Gramfort et al., 2013). Initially, noisy electrode channels were automatically detected based on four criteria: extreme amplitude deviations, low correlation with other channels, low predictability from surrounding channels, and the presence of unusually high-frequency noise (Appelhoff et al., 2022; Bigdely-Shamlo et al., 2015). Channels identified as bad were excluded from further analysis and interpolated only after artifact correction had been completed. Continuous EEG data were bandpass filtered using a zero-phase Butterworth filter with cut-off frequencies of 0.3 Hz and 30 Hz and a 12 dB/octave slope. Additionally, a 50 Hz notch filter was applied to remove line noise. To remove ocular and other stereotypical artifacts, independent component analysis (ICA) was performed using the FastICA algorithm (Ablin et al., 2018). The data were then re-referenced to the common average reference. Finally, the EEG recordings were segmented into 1500 ms epochs, from 300 ms before to 1200 ms after stimulus onset. Baseline correction was applied using the 300 ms pre-stimulus interval. Trials were excluded based on the following artifact criteria: a maximum gradient exceeding 75 µV, a peak-to-peak amplitude over 150 µV, amplitudes beyond ±100 µV, or low activity below 0.5 µV sustained for at least 100 ms.

As we are interested in the P1 and N1 components, which are associated with auditory processing and are thus elicited in both of the conditions, we averaged over all trials to obtain the evoked responses (i.e. we did not average separately for both conditions). To quantify and visualize the P1 and N1 component, we evaluated the evoked response in a 40 ms time window around the peak at six frontocentral electrode sites (F3, Fz, F4, C3, Cz, C4). The latency of the peak was calculated between 70 ms to 110 ms after stimulus onset for the P1 and between 120 ms and 180 ms post-stimulus onset for the N1 component.

ERP source reconstruction

Source localization of the evoked responses was performed using the eLORETA inverse solution as implemented in MNE-Python (Pascual-Marqui et al., 2011). For each patient and at each evaluation time point, i.e. pre-op (T1), three months post-op (T2) and nine months post-op (T3), source reconstruction was conducted twice: once using a head model that included the lesion and once using a model that did not. This comparison enabled us to assess the effect of incorporating the lesion into the forward model on the accuracy and spatial distribution of the estimated sources.

Noise pre-whitening was applied using the noise covariance matrix to stabilize the inverse solution. The resulting source estimates were represented as the absolute current source density (CSD), computed as the magnitude of dipole activity, regardless of orientation. This approach ensures that the analyses focused solely on source intensity.

For the normative dataset, no individual anatomical scans were available, so we used the fsaverage template brain provided by FreeSurfer to construct a common forward model. Evoked source activity was averaged across all healthy controls to provide a normative reference for comparison.

8.3 Results

8.3.1 Simulations

Single-source simulations

In Figure 8.3, the MAG% and RDM% values at the scalp level are presented for the simulated data of each individual dipole in Subject 1, while corresponding figures for Subject 2 can be found in the supplementary materials (Figure S1). The first row of Figure 8.3 represents a model incorporating all lesions, including those resulting from tumor resection as well as craniotomy-induced lesions. The second row isolates the effects of tumor-related lesions, while the third row focuses solely on the impact of craniotomy-related lesions.

The results indicate that dipoles located near the lesions exhibit the most pronounced differences in both magnitude and topography. However, these effects are not limited to the immediate vicinity of the lesions but extend across much of the left hemisphere. This widespread influence appears to be predominantly

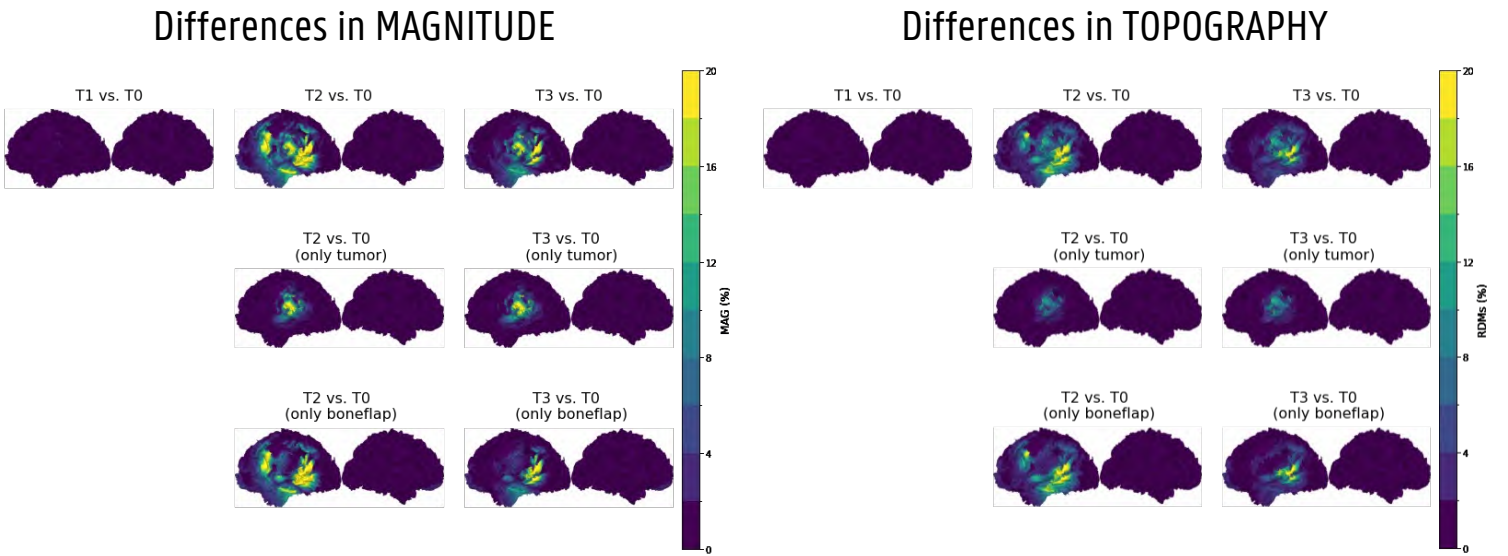

Figure 8.3. The differences in magnitude (left) and topography (right) of the EEG signals generated for each dipole using models with (T1, T2, T3) and without (T0) lesions.

driven by craniotomy-related lesions, while the effects of tumor-related lesions are more localized.

To further investigate how the presence of lesions affected each electrode's sensitivity to brain-wide activity, we quantified changes in the overall sensitivity and in the spatial distribution of contributing sources to each electrode. This was done by calculating MAG%- and RDM%-values for each electrodes across all dipoles. High MAG% values indicate substantial changes in signal magnitude at a given electrode, while elevated RDM% values reflect significant shifts in the distribution of cortical sources influencing that electrode. These results are shown in Figure 8.4. The electrodes exhibiting the highest changes are mainly located near the lesion site and demonstrate significant disruption in sensitivity profiles, with elevated MAG% indicating overall amplitude differences and increased RDM% reflecting shifts in cortical input patterns.

Notably, both the magnitude and spatial pattern of lesion-induced sensitivity changes, as captured by MAG% and RDM% values, varied across the different time point comparisons (T1 vs. T0, T2 vs. T0, and T3 vs. T0). In the preoperative phase (T1 vs. T0), changes were minimal and largely restricted to a small subset of electrodes in close proximity to the tumour site. In contrast, comparisons at later stages—T2 vs. T0 and T3 vs. T0—revealed more extensive and topographically coherent patterns of change. In these conditions, elevated MAG% and RDM% values were concentrated around electrodes along the margins of the craniotomy site.

Multisource simulations

To investigate the influence of dipole location, time-course, and lesion location on magnitude and topography differences, multiple multisource simulations were conducted. Figure 8.5 provides an overview of these simulations, comparing the differences observed between the T0 model (without lesions) and the T1, T2, and T3 models (with lesions). Additionally, it presents the calculated MAG% and RDM% values for each case.

In the first scenario, the largest discrepancies between EEGs obtained using the T0 and T1/T2/T3 models were observed at electrodes positioned near the bone flap. This suggests that lesion-induced effects are predominantly localized. In the second scenario, the time-courses associated with the first two dipoles were swapped. This alteration led to distinct difference patterns compared to scenario 1, indicating that the time series of dipole activity significantly influences the results. In the third scenario, a dipole was moved from the left

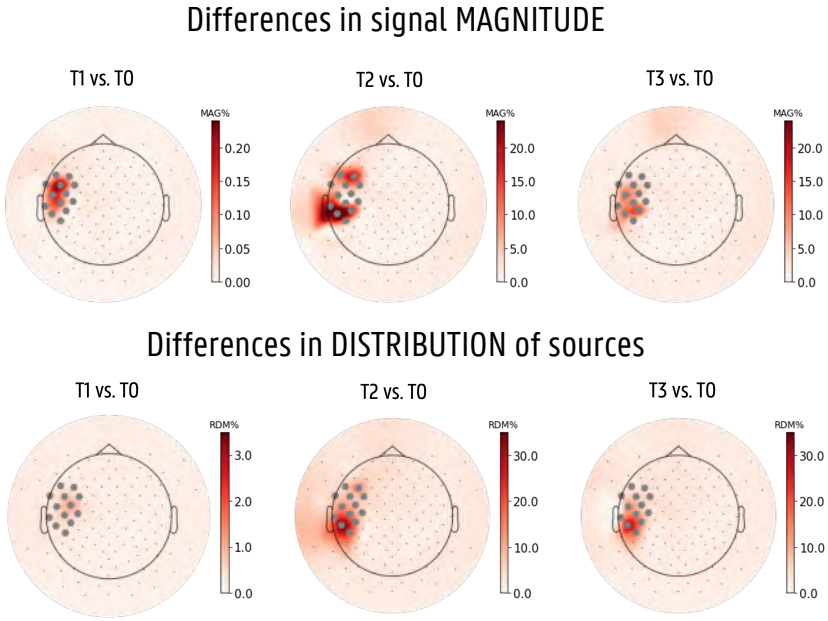

Figure 8.4. Lesion-induced changes in electrode sensitivity to cortical sources. MAG% (top) and RDM% (bottom) values are shown for each electrode, quantifying alterations in signal magnitude and spatial distribution of contributing sources, respectively. The topographic plots visualize the spatial distribution of sensitivity changes across the scalp. The electrodes marked as dark grey hexagons indicate electrodes closer than 2 cm to the boneflap

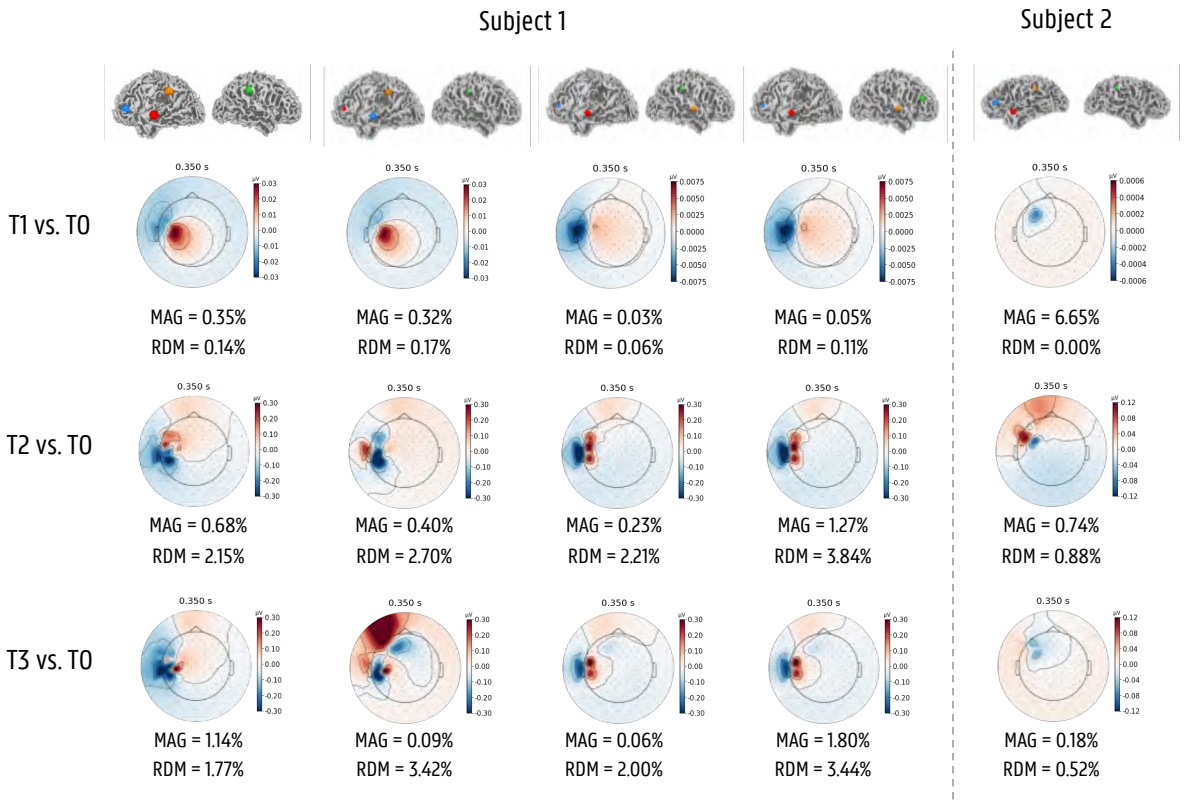

Figure 8.5. Overview of multisource EEG simulations comparing the T0 model (without lesions) to the T1, T2, and T3 models (with lesions). The figure displays the differences in the EEG, along with the calculated MAG% and RDM% values for each scenario.

hemisphere to the right hemisphere. This relocation introduced notable but localized effects on the recorded EEG, again particularly at electrodes near the lesion. In the fourth scenario, the observed effects closely resembled those in scenario 3. When a dipole was shifted within the right hemisphere, the overall impact on EEG measurements was relatively minor, suggesting that dipole movement within the right hemisphere has a limited influence compared to changes within the left hemisphere. Finally, in the fifth scenario, simulations were conducted on a different subject while maintaining the same dipole locations and time courses as in scenario 1. The results revealed similar overall trends, with the most prominent differences localized around the electrodes near the bone flap. However, subject-specific variability influenced the magnitude of these differences.

8.3.2 Real data

For each patient, real EEG data were recorded during an auditory oddball task. We analyzed the early auditory components—specifically the P1 and N1—for both patients and compared them to data from a normative dataset of healthy controls. The results are presented in Figure 8.6.

Regarding the P1 component, the topography for Subject 1 at T1 closely resembles that of the healthy controls. In contrast, at time points T2 and T3, an increase in lateralized activity is evident in the electrodes located near the bone flap. While the healthy controls and recordings at T1 exhibit symmetrical activation, T2 and T3 show a pronounced increase in activity in the left hemisphere, particularly over the electrodes close to the bone flap.

A similar pattern is observed for the N1 component. Across all time points, a disruption in hemispheric symmetry is present, with the most pronounced deviations from the normative data again localized to the electrodes near the tumor site and bone flap lesions. For Subject 2, on the other hand, no clear disruptions can be found. While the overall amplitude of the components shifts slightly over time, the topographies remain similar.

Both ERP components were then also source localized to see which sources are identified (Figure 8.7). For the healthy controls, both the P1 and the N1 were localized to the temporal cortex, as expected from literature (Eggermont and Ponton, 2002). For both patients and at each evaluation point, the source localization of the ERP components was performed twice, i.e. once using the forward models in which the lesions were incorporated and once using the models without the lesions. The results show that the sources obtained at T1 using

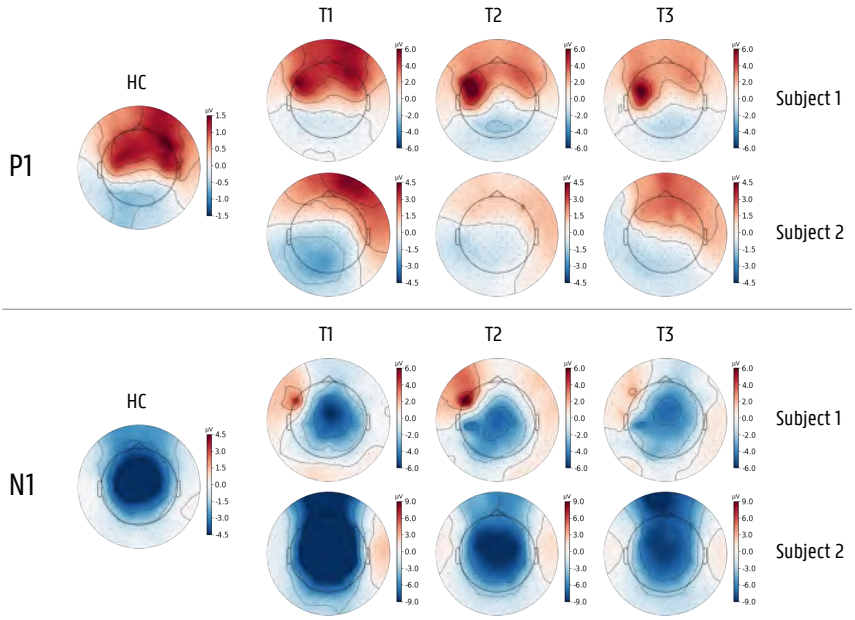

Figure 8.6. The topographies of the P1 and N1 ERP components of the healthy controls, and of both patients at the different evaluation moments.

each of the models are very similar. For T2 and T3 however, clear differences can be found in the obtained localizations, particularly for Subject 1. When not taking into account the lesions in the forward model, only the sources close to the left temporal cortex are found, while no activity in the right temporal cortex was identified. In contrast, when the head model accounted for the lesions, activity was also detected in the contralateral (right) temporal cortex for both the P1 and N1 components, suggesting that lesion-aware modeling enables a more complete and accurate reconstruction of bilateral cortical activity.

8.4 Discussion

This study evaluated the impact of glioma-related lesions and craniotomy-induced skull defects on scalp-recorded EEG signals through individualized forward modeling. By simulating EEG activity using head models both with and without these structural abnormalities, we assessed how lesion-induced changes affect scalp-level recordings and identified the electrodes most influenced by such alterations. Additionally, we examined real EEG data to investigate how the topographies of the P1 and N1 components, as well as

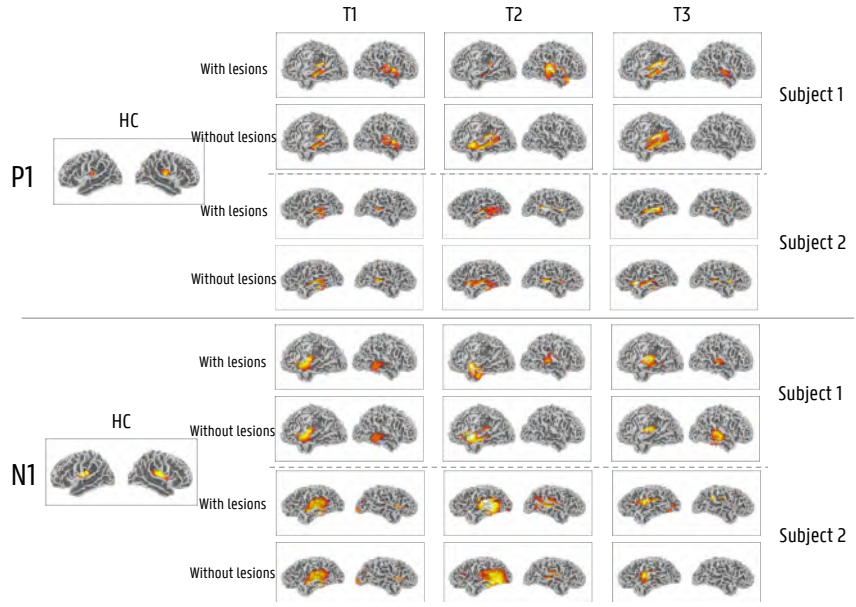

Figure 8.7. The obtained localizations of the P1 and N1 ERP components of the healthy controls, and of both patients at the different evaluation moments. For both patients, source localization was performed using both the accurate models, i.e. including the lesions, and using the forward models in which the lesions were ignored.

their source localizations, are affected by the inclusion or exclusion of lesions in the forward model.

Our single-source simulations demonstrated that both tumor presence and craniotomy-related skull discontinuities can significantly alter the amplitude and spatial distribution of scalp EEG signals. While the effect was quite localized for the tumor-related lesions, i.e. mainly for the dipoles close to the tumor changes in the measured scalp-EEG were observed, the effect of the boneflap was spread out across the left hemisphere. The changes in magnitude and topography were still most strongly present for the dipoles close to the boneflap, but also smaller changes in MAG% and RDM% were found for dipoles located further away.

To investigate how the presence of lesions affected each electrode's sensitivity to brain-wide activity, we quantified changes in the overall sensitivity and in the spatial distribution of contributing sources to each electrode. By quantifying electrode-wise changes in both signal magnitude (MAG%) and spatial source distribution (RDM%), we provide evidence that the presence of a tumour and

subsequent craniotomy can induce both localized and evolving distortions in the leadfield. The minimal changes observed in the pre-operative phase (T1 vs. T0) suggest that the tumour alone exerts only subtle effects on sensitivity, likely constrained to areas immediately adjacent to the lesion. However, the broader and more pronounced alterations observed at later time points (T2 vs. T0 and T3 vs. T0) imply a significant influence of the surgical intervention and post-operative healing processes. These shifts were particularly evident around the bone flap and lesion site. Importantly, such spatially heterogeneous changes in sensitivity may affect the interpretability and accuracy of source localization in lesioned brains, underscoring the need for individualized forward models that account for patient-specific anatomy and post-surgical changes over time.

These observations were further supported by the multisource EEG simulations, which revealed that the effects of omitting lesions in forward models depend on the location of the dipoles, their associated time series, and the anatomical characteristics of the lesions themselves. These simulations illustrated that changes in the timeseries or locations of dipoles close to the lesions have a much stronger influence on the measured scalp-EEG than changes of dipole locations in the right hemisphere. They also showed that the obtained results depend heavily on the specific lesion, highlighting that it is important to evaluate subject data at the individual level. These results are in line with those obtained for the single dipole simulations.

Finally, we evaluated the results obtained using the real data. In the case of Subject 1, the topography of the P1 component at T1 closely resembled that of the healthy controls. At T2 and T3 however, we observed an increase in lateralized activity in the electrodes near the bone flap. A similar pattern was found for the N1 component. For this subject, the results showed the most pronounced deviations from the normative data at the electrodes near the tumor site and bone flap lesions. In contrast, Subject 2 showed no clear disruptions in topography. Although there is a slight shift in the overall amplitude of the components over time, the topographies remained consistent across measurements. These findings align with our predictions based on the simulation study. Specifically, the simulations (Figure 8.3) indicated that dipoles located near the left auditory cortex lead to substantial changes in both magnitude and topography of the scalp-EEG. This is consistent with the observed results for both the P1 and N1 components, where the expected sources lead to topographical distortions at T2 and T3. For Subject 2, the most affected dipoles are located more frontally, and the simulations predict only minor differences in magni-

tude and topography for dipoles in the auditory cortex. This is again supported by the real data, which shows only slight differences in the scalp-EEG over the different time points. Taken together, these results provide further support for the influence of localized dipoles on the scalp-EEG topography, with variations in the extent of the distortion depending on the location of the dipoles.

Together, these findings have important implications for EEG research in clinical settings. They emphasize the need for individualized head models when analyzing EEG in patients with structural brain abnormalities and caution against relying solely on normative datasets or healthy-subject-based models for comparisons in neurosurgical populations. Although our simulations were conducted in simplified scenarios without considering channel noise, they clearly highlight the effects of lesions on EEG signals. Furthermore, the real data collected from patients provides evidence that these observations extend to more realistic situations.

The single-source simulations revealed how the presence of lesions influences both the magnitude and topography of EEG signals. In the case of simple multisource generator configurations, such as the P1 and N1 components, these simulations allowed us to predict the impact of lesions on scalp-level measurements. As seen in Subject 2, no dramatic changes in amplitude or topography occurred for the early auditory evoked responses (P1 and N1) in an individual with a frontal-lobe lesion. In Subject 1, who had a lesion close to the temporal cortex were the neural sources of the P1 and N1 are expected, however, a clear increase in the amplitude measured at electrodes close to the lesion was found. It is important to note that most cognitive processes are driven by complex, often unknown sources. Some of these sources may be located near the lesions, and their distortion will affect the overall EEG signal in nontrivial ways.

The results suggest that the impact of tumors and craniotomy lesions on multisource configurations—commonly used in cognitive neuroscience—cannot be ignored. When making group-level comparisons, the heterogeneity in the location, size, and shape of lesions complicates the interpretation of scalp-level effects. This complexity is even more pronounced in longitudinal studies, where structural changes are expected over time. In such cases, it is crucial to assess anatomical changes between time points before making valid comparisons.

To accurately account for anatomical changes, it is essential to perform source-level analyses, where the effects of lesions can be directly modeled. This approach aligns with findings by Piastra et al. (2022) and Piai et al. (2024) regarding CSF-filled lesions. Piastra et al. (2022) demonstrated the critical

impact of accounting for anatomical abnormalities, such as CSF-filled cavities, in source reconstruction for MEG data. Their study used accurate FEM-based head models in which they modeled the lesions to simulate MEG data from subjects with stroke-related CSF-filled cavities, after which they calculated the reconstructions using models without the cavity. When comparing the obtained reconstructions to the simulated ground truth, they found that excluding the cavity led to significant displacement of the reconstructed dipoles and differences in signal magnitude. Their findings underscore the importance of accurately modeling anatomical features in neuroimaging, as ignoring such abnormalities can distort source localization and signal interpretation. Although their study focused on MEG, the same principles apply to, and are even more important in, EEG. Just as CSF cavities must be considered in EEG/MEG source reconstruction, tumors, lesions, and surgical defects must be accounted for in EEG modeling to ensure reliable results in clinical populations. Our study builds on these insights by highlighting the necessity of individualized modeling approaches to address the specific challenges posed by structural brain abnormalities in EEG analysis.

It is important to note however that performing these analyses at the source level requires having detailed anatomical information, including an anatomical scan as well as the expertise in source reconstruction to create these advanced forward models that include the lesions in the data.

In conclusion, our findings highlight the critical role of individualized modeling for reliable EEG analysis in clinical populations affected by tumors and craniotomy-induced abnormalities. These results support calls for anatomically realistic modeling frameworks and contribute to the growing body of literature emphasizing the need for precision in neuroimaging. Just as previous research has demonstrated the importance of modeling anatomical features like CSF cavities, our study underscores that pathological and surgical changes to the brain significantly alter EEG signals. Therefore, these factors must be accounted for in both research and clinical contexts to ensure accurate interpretations.

Part IV

General Discussion

9 | General discussion

The goal of this dissertation was to investigate the neural mechanisms underlying speech perception and to critically examine the methodological tools used to explore these mechanisms using EEG. Speech perception is a complex, multi-level process that spans from early auditory processing to higher-order semantic integration. By focusing (mainly) on three well-established ERP components—the MMN, P300, and N400—we sought to characterize the cortical generators and their dynamic interactions that support this transformation from sound to meaning. At the same time, the work addressed a series of methodological challenges that influence how accurately we can localize and interpret neural activity. Through a combination of empirical EEG studies and simulation experiments, this dissertation aimed to advance both our neuroscientific understanding of these ERP components, as well as our analytic approaches in this type of EEG research.

In this discussion, I will briefly summarize the findings of the different studies, integrate them within the broader context of cognitive neuroscience and EEG methodology, and reflect on their implications for future research and clinical applications. First, I will revisit the empirical findings presented in Part II, highlighting how the MMN, P300, and N400 components reflect distinct but interconnected stages of speech processing, and how their underlying cortical sources and connectivity patterns contribute to our understanding of the neural architecture of language. Second, I will focus on the methodological insights gained from the simulation studies in Part III. These simulations addressed specific limitations of EEG analysis—namely latency variability, head model accuracy, choise of inverse methods, and anatomical distortions due to

lesions—and demonstrated how such factors can impact the interpretation of ERP data. Special attention will be given to the value of simulations as tools for validating and improving EEG methodologies. Finally, I will reflect on how the integration of empirical and simulated data informs the future of EEG research in both healthy and clinical populations. This includes a discussion of the practical implications for studies involving patients with brain lesions, the importance of personalized modeling, and the broader relevance of this work for non-invasive neuroimaging approaches.

9.1 General overview of the findings

The findings presented in Part II provide important insights into how the brain processes speech at different levels of linguistic complexity. Each of the included ERP components was associated with distinct patterns of cortical activation and connectivity, reflecting their respective functional roles in speech perception.

In **Chapter 4**, the MMN elicited during passive phoneme discrimination, revealed a bilateral network including temporal, frontal, and parietal regions. This suggests that even in the absence of active attention, the brain engages a distributed system to detect auditory deviations, consistent with theories of automatic prediction error signaling. In contrast, the P300, associated with active categorization, engaged a broader fronto-parietal-cingulate network. This aligns with prior work linking the P300 to attentional allocation and task-relevant processing, and highlights how active listening demands greater integration across cognitive control and sensory regions. Finally, the N400 component, elicited during a taxonomic semantic priming task, was predominantly left-lateralized and involved frontal and parietal cortices, including enhanced intra-frontal and fronto-parieto-occipital connectivity. These findings reinforce the view of the N400 as a marker of semantic integration, grounded in a left-lateralized network optimized for linguistic processing.

Together, these results emphasize that speech perception is not localized to a single brain area or stage, but instead unfolds across overlapping, dynamic networks that adapt to task demands and linguistic context. Importantly, they also lay the foundation for investigating how these networks may be disrupted or reorganized in clinical populations, such as patients with language impairments.

A significant part of this dissertation focussed on demonstrating how simulation studies can be used to evaluate, refine, and improve EEG analysis techniques. While empirical EEG provides valuable insight into brain function, interpreting its results accurately depends on the quality and appropriateness of the analytic tools used. The simulations presented in Part III addressed several core issues that directly impact the reliability of ERP-based inferences.

In **Chapter 5**, we investigated single-trial variability and latency estimation using artificial neural networks. Traditional ERP analysis relies on averaging across trials, which ignores trial-to-trial variability and can lead to underestimation of component amplitudes. Chapter 5 addressed this issue by developing artificial neural network-based methods to quantify ERP latencies at the single-trial level. Simulation results showed that these methods outperformed conventional techniques across a range of signal-to-noise ratios, providing more accurate estimates of both component timing and topography. Applied to real data, these single-trial estimates correlated more strongly with behavioral measures (e.g., reaction times) and revealed group differences (e.g., age-related changes) that were not detected using average-based methods. These findings demonstrate how simulations can guide the development of more sensitive and informative ERP quantification approaches, potentially enabling richer interpretations of cognitive and clinical data.

In **Chapter 6**, we explored the possibility of combining multiple source localization techniques to bridge ERPs and oscillations. ERP components and oscillatory brain activity are often studied separately, yet their relationship remains an open question. In this chapter, we studied this relationship using a combination of source localization methods—eLORETA for ERPs and DICS for oscillations—applied to both simulations and real data. The results illustrated both convergence and divergence between ERP and oscillatory sources, depending on the component and frequency band. For instance, while the P300 and delta oscillations showed overlapping sources, alpha desynchronization during the same period was spatially distinct. These findings suggest that ERPs and oscillations can reflect complementary yet partially dissociable neural processes. More broadly, this work demonstrates how simulation-based evaluations of different methods can enhance our mechanistic understanding of EEG data and inform best practices for multi-algorithm analysis.

Chapter 7 focussed on the impact of the head model choice on source localization results. Accurate source localization depends heavily on the head model used to compute the EEG forward solution. While template-based models are

commonly used when subject-specific MRIs are unavailable, Chapter 7 demonstrated—through simulations and real data—that these models introduce systematic localization errors. Simulated data showed that template models failed to accurately reconstruct the underlying sources and produced more diffuse and less specific activations. These limitations were also evident in real EEG data, where template-based localization led to incorrect interpretations of ERP generators. These findings highlight the importance of using subject-specific head models whenever possible, and suggest that researchers using template models should interpret results cautiously, particularly in clinical or patient-specific contexts.

Finally, in **Chapter 8** we looked at the influence of structural anomalies in the brain on the measured ERPs. In clinical populations, EEG interpretation is further complicated by individual anatomical differences such as lesions or craniotomies. Chapter 8 used individualized forward models to simulate the effects of these structural anomalies on EEG signals. The results showed that such disruptions can significantly alter the amplitude and topography of recorded signals, particularly near the lesion site. These distortions were evident in both simulated and real data, underscoring the necessity of accounting for patient-specific anatomy in source localization. The findings support the use of lesion-informed modeling as a critical step toward more accurate and clinically meaningful EEG interpretations, especially in longitudinal or treatment-monitoring studies.

9.2 Integration of Empirical and Methodological Contributions

A key part of this dissertation is the interdependence between empirical neuroscience and methodological innovation. The insights into speech perception presented here could only be achieved through careful attention to the ways in which neural data are recorded, processed, and interpreted. At the same time, methodological challenges encountered during empirical studies motivated the development of targeted simulations, which helped us to refine and contextualize our findings.

Analyzing brain data—especially EEG—is inherently complex. Neural signals are dynamic, noisy, and are the result of activity in distributed networks rather than single, isolated regions. Part of this complexity also arises from the fact that we do not measure directly within the brain, but instead use

electrodes placed on the scalp around the skull. Mathematically, it is impossible to uniquely determine the number and amplitude of the neural sources responsible for the measured signals. As a result, extracting meaningful information from EEG recordings requires complex and advanced analysis techniques. Methods for quantifying and localizing ERP components must be sensitive enough to capture subtle variations, yet robust enough to handle the noise and variability in brain signals. Without careful methodological choices, there is a real risk of misinterpreting the underlying neural processes.

Throughout this work, simulations served as critical tools for evaluating and improving the analytic strategies used. They were not treated as purely technical exercises, but were closely integrated with specific research questions. Whether improving single-trial latency estimates, assessing the impact of head model selection, combining source localization methods for ERPs and oscillations, or modeling the effects of anatomical anomalies, each simulation provided practical insights that enhanced the reliability of the empirical findings.

This integrated approach underscores that methodological refinement is not an optional add-on to empirical research—it is fundamental to it. Advances in the study of brain function depend on the development and validation of analysis methods that are capable of dealing with the complexity of neural data. Furthermore, the work presented here highlights the importance of tailoring methods to the specific demands of the scientific questions and populations under study.

Overall, this dissertation emphasizes that a strong link between empirical investigation and methodological rigor is essential for advancing both our theoretical understanding of speech perception and the broader field of cognitive and clinical neuroscience.

9.3 Clinical Implications and Future Directions

The findings presented in this dissertation have several important implications for the use of EEG in clinical populations. By mapping how speech-related ERP components are organized across distributed cortical networks, this work provides a framework for understanding how these networks may be affected by neurological conditions such as stroke, brain tumors, or degenerative diseases. Identifying disruptions in these well-characterized pathways could in the future aid in diagnosing specific types of language impairment or predicting recovery trajectories.

Beyond the empirical insights, the methodological simulations developed throughout this dissertation—particularly to investigate source localization, single-trial analysis, and lesion-informed modeling—open the door for more personalized and clinically meaningful EEG applications. Accurate localization of neural generators, better handling of variability in ERP data, and individualized head modeling are all critical steps toward making EEG a reliable tool for patient-specific diagnosis, monitoring, and treatment planning.

Looking ahead, several promising directions for future research become clear. One important direction lies in the development of adaptive or hybrid head models that can approximate individual brain anatomy in healthy participants, particularly in situations where acquiring high-resolution MRI scans is not feasible. While this approach could greatly improve the accessibility of personalized EEG analysis for healthy controls, the findings in this dissertation also underscore that truly individualized head models remain essential for clinical populations, especially when structural brain alterations—such as lesions, tumors, or surgical resections—are present. In such cases, deviations from normal anatomy can significantly distort EEG signals, making detailed, patient-specific modeling critical for accurate interpretation. Nonetheless, for large-scale studies or normative research involving healthy individuals, adaptive modeling techniques—leveraging machine learning and initial population-based templates, or simplified anatomical markers—could offer a practical compromise between accuracy and feasibility, thereby broadening the applicability of advanced source localization methods.

In addition, the artificial neural network approaches developed for single-trial latency estimation in this dissertation hold great potential for advancing EEG analysis. These methods could be expanded to handle a wider range of ERP components beyond those studied here, addressing more complex noise conditions and improving the precision of data in clinical populations with irregular or pathological brain activity. Single-trial latency analysis is especially important in these populations, as greater variability in latency across trials can lead to more smeared and reduced ERP components at the group level. These attenuated responses may still reflect activation of the same underlying brain regions and should not necessarily be interpreted as reduced neural activity. By enhancing the capability of neural networks to adapt to diverse ERP patterns, this approach could significantly enhance our ability to measure brain activity in a variety of contexts, from basic cognitive neuroscience research to clinical diagnostics.

Finally, strengthening the test-retest reliability of these advanced EEG measures is an essential area for future exploration. While test-retest reliability has been well established at the group level, where ERP components are averaged over multiple participants, this consistency has yet to be fully demonstrated at the individual level. Given the high noise levels and inherent variability in EEG data, achieving reliable, stable ERP components for individual subjects remains a significant challenge. Moreover, to interpret longitudinal changes effectively in clinical settings, it is crucial to better understand the sources of variability in test-retest results. Only by distinguishing between variability that reflects genuine neurological change and variability that arises from measurement noise or other external factors can we ensure that observed shifts in ERP components are clinically meaningful. This understanding will be critical for using EEG to monitor disease progression or recovery. As clinical applications of EEG expand, particularly in the context of neurodegenerative diseases or post-surgical recovery, ensuring the stability of ERP components across repeated measures in individual patients will be crucial for their usefulness in patient care. Overcoming these challenges in individual reliability and understanding the underlying variability will be a key step toward making advanced EEG measures more useful in clinical diagnostics and treatment monitoring.

Together, these developments—ranging from hybrid head models for healthy participants to expanded neural network approaches and improved test-retest reliability—could significantly enhance the diagnostic, prognostic, and therapeutic potential of EEG in both research and clinical practice. As these innovations unfold, the continued integration of empirical research with methodological advancements will pave the way for more precise, personalized, and effective applications of EEG across diverse settings.

9.4 General conclusion

This dissertation has advanced both our theoretical understanding of speech perception and our methodological approaches for studying neural activity using EEG. By examining how key ERP components—MMN, P300, and N400—reflect distinct stages of speech processing and the neural networks that support them, we have contributed to a more nuanced understanding of how the brain processes auditory information and maps it to meaning. Furthermore, through rigorous simulation studies, we have critically assessed

and refined EEG analysis techniques, providing valuable insights into the challenges and opportunities of interpreting EEG data accurately.

The integration of empirical findings with simulation-based methodology highlights the importance of continually advancing EEG techniques in order to keep pace with the complexity of neural data. The development of more robust methods for single-trial analysis, source localization, and lesion-informed modeling have the potential to revolutionize the clinical use of EEG, making it a more reliable and personalized tool for patient diagnosis, monitoring, and treatment planning. In particular, by addressing key issues such as the impact of head model choice, noise conditions, and test-retest variability, this work lays the groundwork for more precise and clinically applicable EEG measures.

As the field progresses, future research will be crucial in refining these methods, expanding the range of ERP components studied, and improving test-retest reliability at the individual level. The development of adaptive or hybrid head models for healthy controls, as well as the application of advanced machine learning techniques to handle diverse ERP patterns, holds great promise for both basic research and clinical practice. Understanding the variability in test-retest results will also be a key factor in interpreting longitudinal changes, especially in the context of neurodegenerative diseases and post-surgical recovery.

In conclusion, this dissertation underscores the interdependence between empirical research and methodological innovation. By continuing to refine EEG analysis tools, we can unlock deeper insights into the neural processes underlying speech perception, as well as enhance the clinical utility of EEG for diagnosing and monitoring neurological conditions. The future of EEG research—both in healthy individuals and clinical populations—depends on the continued evolution of methods that are both scientifically rigorous and clinically relevant, paving the way for more effective, personalized applications in neuroscience and medicine.

Part V

Appendices for the Interested Reader

A | Cortical Generators and Connections Underlying Phoneme Perception and Semantic Priming: a Mismatch Negativity, P300 and N400 Investigation

Source reconstruction of the MMN, P300 and N400

As described in the main text, significant effects of interest in the results of the source reconstructions were explored in three separate time windows of 50 ms through statistical clustering analysis in source space. The early, middle and late time windows were selected based on the 25%, 50% and 75% fractional area latency of the MMN, P300 and N400 grand average difference wave of all participants in a broad time window of 100-300 ms, 300-800 ms and 400-800 ms, respectively. Two different approaches were used to test for significant differences in source activation between the standard and deviant condition. The first approach consisted of a cluster-based non-parametric permutation test, in which the significance probability was computed under the permutation distribution using the Monte-Carlo method, and was described in the main text. While the cluster-based permutation test controls the multiple comparison problem and at the same time maximizes power, no inference is made over individual dipoles. Consequently, no statements about the spatial location and extend of the significant effect between both conditions based on the cluster locations will be completely accurate. Therefore, a second approach to test for significant differences in source activation between both conditions was used. Here, paired t-tests are performed for each dipole separately, after which the obtained p-value are corrected for multiple comparison with False

Discovery Rate (FDR). The results of these analyses are shown for the MMN, P300 and N400 respectively in Figures A.1, A.2 and A.3

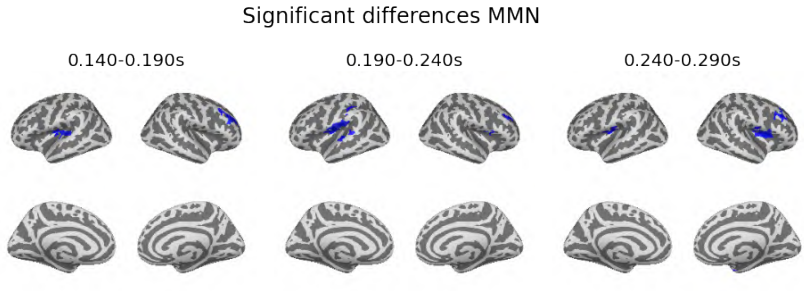

Figure A.1. Results of the paired t-tests analysis on the eLORETA source reconstruction of the MMN to identify significant differences between both conditions in the early (140-190 ms), middle (190-240 ms) and late (240-290 ms) time window.

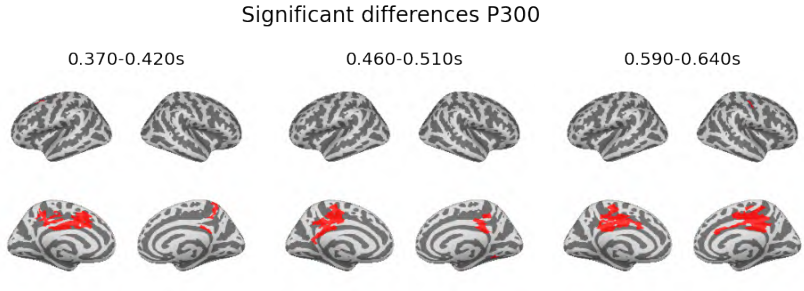

Figure A.2. Results of the paired t-tests analysis on the eLORETA source reconstruction of the P300 to identify significant differences between both conditions in the early (370-420 ms), middle (460-510 ms) and late (590-640 ms) time window.

Functional connectivity analysis of the MMN, P300 and N400

In this study, the functional networks underlying phoneme discrimination (MMN) and categorization (P300), and categorical priming (N400) were mapped based on the 68 ROIs predefined by the Desikan-Killiany atlas (Desikan et al., 2006). To identify significant differences between the networks obtained for the standard and deviant, or related and unrelated conditions,

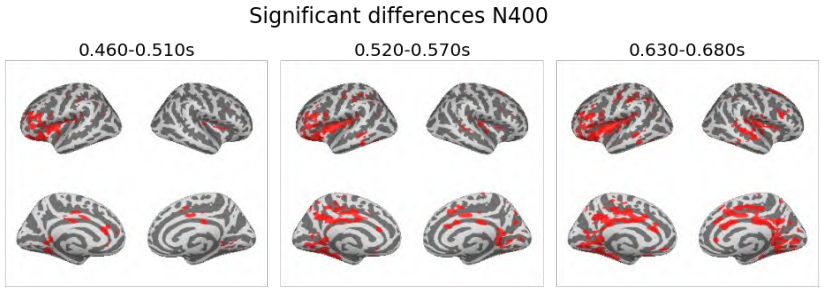

Figure A.3. Results of the paired t-tests analysis on the eLORETA source reconstruction of the N400 to identify significant differences between both conditions in the early (460-510 ms), middle (520-570 ms) and late (630-680 ms) time window.

the Network Based Statistic (NBS) method was used in the main text of the paper (Zal, 2010). To quantify and describe the obtained significant network components, we subdivided the 34 ROIs of each hemisphere into five groups: Frontal, Temporal, Parietal, Occipital and Cingulate. How each ROI was assigned to each group is shown in Table A.1.

Table A.1. Grouping of regions of interest from Desikan-Killiany atlas (34 ROIs in each hemisphere) based on lobe.

frontal	caudal middle frontal gyrus
	frontal pole
	lateral orbitofrontal cortex
	medial orbitofrontal cortex
	paracentral lobule
	pars opercularis
	pars orbitalis
	pars triangularis
	precentral gyrus
	rostral middle frontal gyrus
	superior frontal gyrus
parietal	inferior parietal cortex
	postcentral gyrus
	precuneus cortex
	superior parietal cortex
	supramarginal gyrus
temporal	banks superior temporal sulcus
	entorhinal cortex
	fusiform gyrus
	inferior temporal gyrus
	insula
	middle temporal gyrus
	parahippocampal gyrus
	superior temporal gyrus
	temporal pole
	transverse temporal cortex
cingulate	isthmus-cingulate cortex
	posterior-cingulate cortex
	rostral anterior cingulate cortex
	caudal anterior-cingulate cortex
occipital	cuneus cortex
	lateral occipital cortex
	lingual gyrus
	pericalcarine cortex

B | Single-trial ERP quantification using neural networks

Template matching using ICA: comparison of algorithms and methods

Multiple ICA decomposition approaches for the latency quantification of the ERP component in single trials were compared in this work using the simulated data. The ICA algorithms that were considered in this work included FastICA (Hyvarinen, 1999), extended infomax (Lee et al., 1999), picard (Ablin et al., 2018) and adaptive mixture ICA (AMICA) (Palmer et al., 2012; Delorme et al., 2012). Furthermore, we also compared the effect of using only a single ICA component for the latency estimation or using a combination of multiple components. In figure B.1, the mean absolute error between the true and the estimated latencies are shown in function of the SNR level of the dataset. The figure shows that when we consider only a single ICA component, the SNR level of the dataset has a limited influence on the performance of the latency estimation. This might be caused by the nature of the simulated data, as a single independent P300 component was added to background noise. In this case, the extended Infomax algorithm performs best, and only small differences are found between the fastICA and picard implementations. A clear trend is however found between the performance of the methods and the SNR of the data when considering multiple ICA components. Here, the extended Infomax, fastICA and picard implementations gave almost identical results for all SNRs, with the performance of the AMICA algorithm being slightly worse. This trend is very similar to the one observed for the cross-correlation latency estimation

method (figure 5.6). Therefore, it is probable that by selecting multiple ICA components, not only the ERP component but also noise is included in the combined signal, which leads to larger errors in the single-trial latency estimation for lower SNRs. Based on these results, we decided to use the extended Infomax algorithm for the further comparison of the different latency estimation methods.

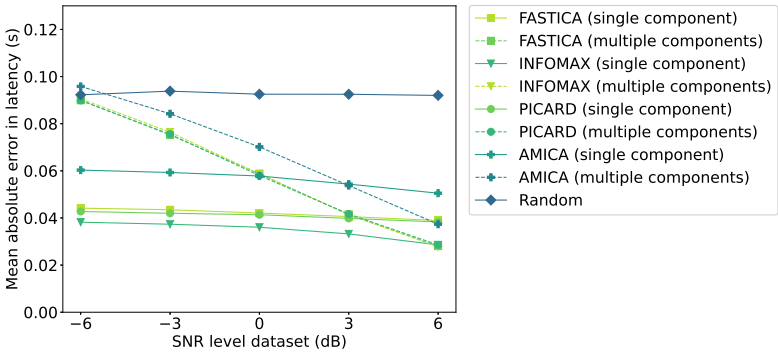

Figure B.1. Comparison of the different ICA decomposition algorithms (extended Infomax, picard, fastica and AMICA) regarding the mean absolute error between the estimated latencies and the true latencies in single trials for each each SNR in the simulated data.

Realigned grand-averages of the simulated data for different SNRs

In figures B.2 and B.3 the realignment of the single trials averaged across all subjects for each of the different SNRs are shown, along with the topography at the time of the peak, comparing the different latency estimation techniques. Also the non-realigned grand-average and a random realignment are plotted as a reference. The realigned grand-averages are compared with the correct realignment to check how well the shape of the P300 component is estimated by each of the different methods by calculating the mean relative absolute error (MRAE). The figures show that the realignment based on the convLSTM network gives the best results. Similar results are found across the different SNRs. While the topographies at the peak are very similar across all methods, apart from a scaling factor due to smearing, the shape of the obtained P300 component clearly varies. In the iterative cross-correlation, the (iterative) beamformer and the multiple component ICA based approaches, artefacts

are being introduced into the shape of the ERP component due to errors in latency estimations.

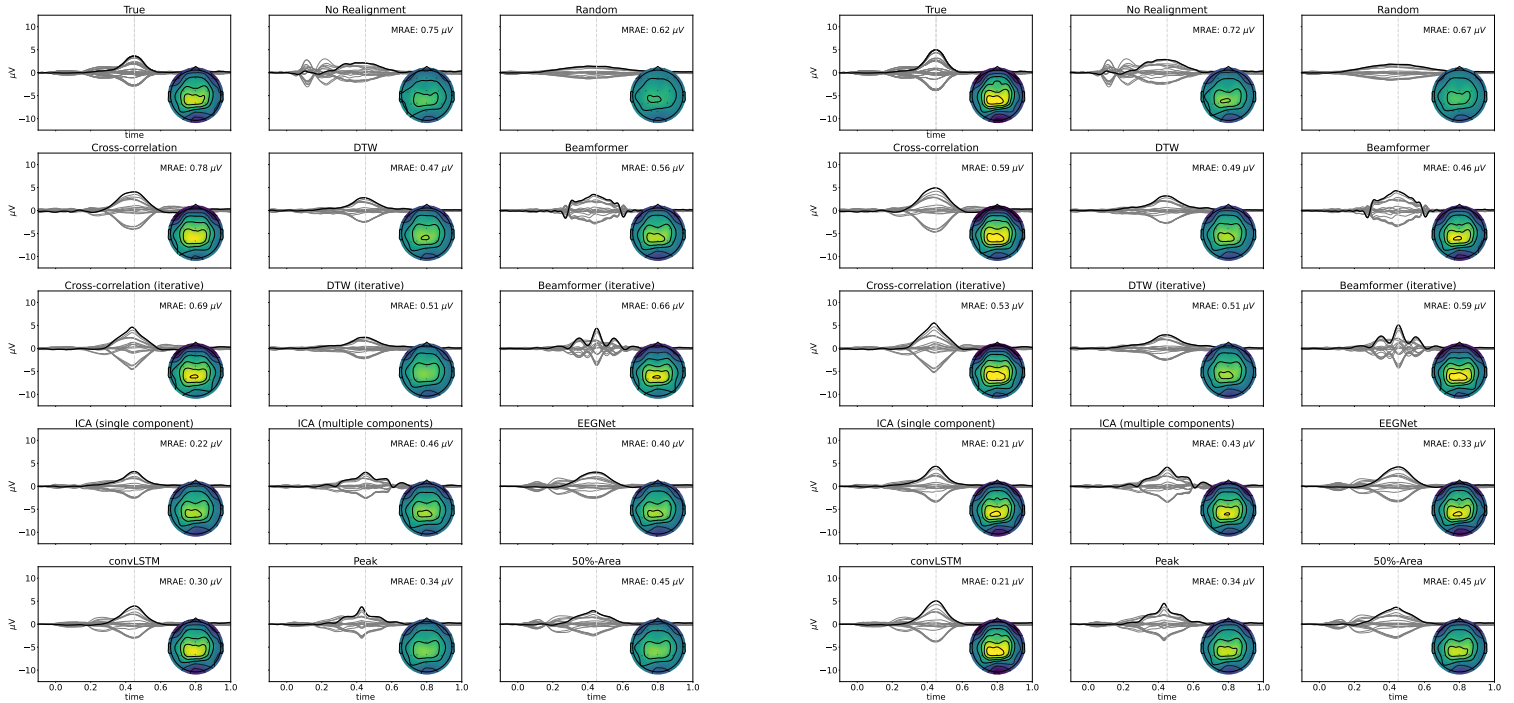

(a) -6dB **(b)** -3dB

Figure B.2. Realignment of the single trials averaged across all subjects with SNR -6dB and -3dB for each of the different methods. Grey lines represent the different channels, with Pz being marked in black. Also, the topography of the realignment at 0.420 s after the stimulus onset is shown. The realigned waveforms are compared to the correct realignment to evaluate how well the shape of the simulated P300 component is estimated. For each method, the mean relative absolute error between the true and the estimated realigned waveforms across all subjects is reported.

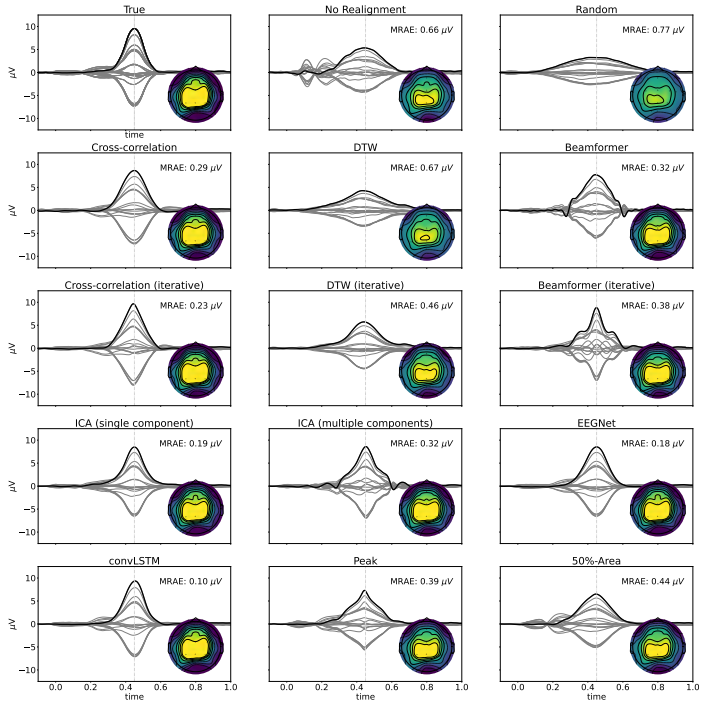

(a) +3dB

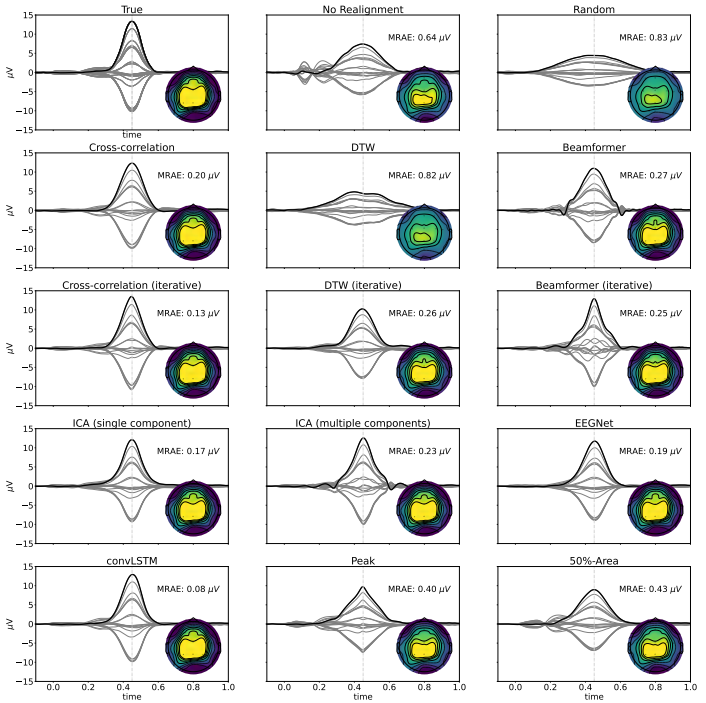

(b) +6dB

Figure B.3. Realignment of the single trials averaged across all subjects with SNR +3dB and +6dB for each of the different methods. Grey lines represent the different channels, with Pz being marked in black. Also the topography of the realignment at 0.420 s after the stimulus onset is shown. The realigned waveforms are compared to the correct realignment to evaluate how well the shape of the simulated P300 component is estimated. For each method, the mean relative absolute error between the true and the estimated realigned waveforms across all subjects is reported.

C | Investigating the effect of template head models on Event-Related Potential source localization: A simulation and real-data study

Simulated epochs for of the different networks for all SNRs

Simple ERP waveforms were simulated using half-cycle sinusoidal waveforms to allow the objective quantification of the localization error associated with the subject-specific and average head models. This was done by simulating activity in different regions of the brain, including noise, and projecting this activity to the scalp surface using the individual head models. Different networks responsible for generating ERP activity were simulated, each involving four symmetrically active brain regions, with two regions in each hemisphere. These regions were identified using the Destrieux cortical atlas parcellations. For each region of interest (ROI), the center of the parcellation was determined, and dipoles within a 10 mm radius around this center were selected. The ERP activity in these selected dipoles was simulated as a 5 Hz half-cycle sinusoidal waveform lasting 100 ms. A small delay was introduced across the ROIs: the ERP waveform began in the first ROI at 100 ms post-stimulus, followed by the second ROI 10 ms later, and then in the third and fourth ROIs at 120 ms. Additionally, the signal amplitude in the third and fourth ROIs was reduced to 80% of the amplitude in the first two ROIs. To simulate realistic conditions, pink noise was added to all epochs. The noise amplitude was adjusted to achieve different signal-to-noise ratios (SNRs) ranging from -20 dB to +0 dB. Figure 7.2 in the main text shows the simulated data at the sensor level for the SNR

equal to -10 dB. Here, the simulated data is visualized for the SNRs equal to -20 dB (Figure C.1) and 0 dB (Figure C.2).

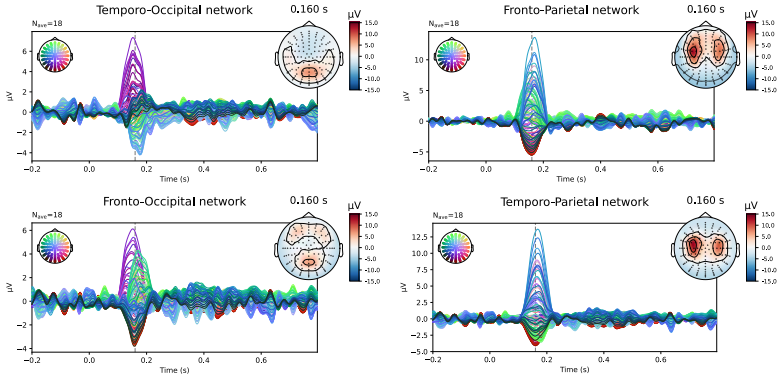

Figure C.1. Overview of the simulated data at sensor level averaged over all subjects. The simulated epochs in the ERP condition at SNR = -20dB are averaged.

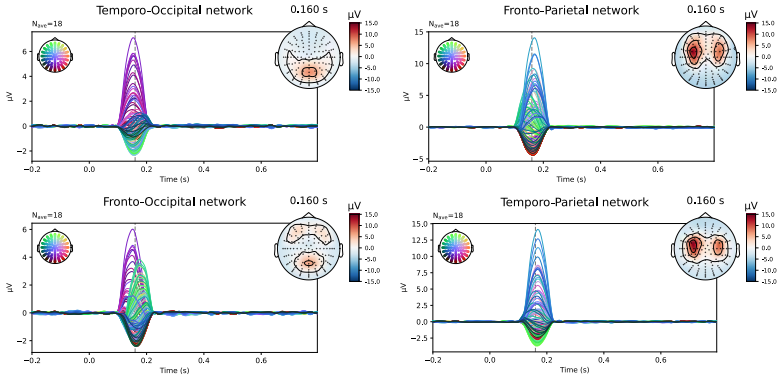

Figure C.2. Overview of the simulated data at sensor level averaged over all subjects. The simulated epochs in the ERP condition at SNR = 0dB are averaged.

Localization results of the different networks for all simulated SNRs

Different aspects are taken into account in the evaluation of the source reconstruction: the correspondence between the obtained sources and the simulated sources, the localization error and the spatial dispersion of these reconstructed sources, and the correlation between the originally simulated activity and the reconstructed activity. For each subject, the difference in source space activity between the ERP and the noise condition was calculated, after which the data is averaged over the time window of interest. The results of the localizations obtained for the simulated dataset with SNR equal to -10 dB were included in the main text. Here, we also include the obtained localizations for the other SNRs, namely -20 dB and 0 dB, for each of the four simulated networks. The results for the temporo-occipital network, the fronto-parietal network, the fronto-occipital network and the temporo-parietal network at each of the different SNRs can be found respectively in Figures C.3, C.4, C.5 and C.6.

The quantification results of the localization errors associated with the localizations for the individual subjects were shown in the main text in Figure 7.4. In this evaluation of the source reconstructions, different aspects were taken into account: the sensitivity and the precision of the obtained sources, the localization error and the spatial dispersion of these reconstructed sources. For each of these measures, the difference between using the subject-specific and the average head models was investigated, as well as the differences between the different modelling approaches. In the main text, clusters of activity were considered correctly localized when the difference between the centre of the reconstructed cluster was within 3 cm of the centre of the simulated ROIs. As this maximal distance is an important parameter, the results when using a maximal distance of both 1 cm and 5 cm are included here in Figures C.7 and C.8. Finally, also the effect of the SNR of the simulated data on the reconstructions was quantified in the main text (Figure 7.5). In this figure, the results obtained for the different networks were aggregated. Again, the results when using a maximal distance of both 1 cm and 5 cm are included here, respectively in Figures C.9 and C.10.

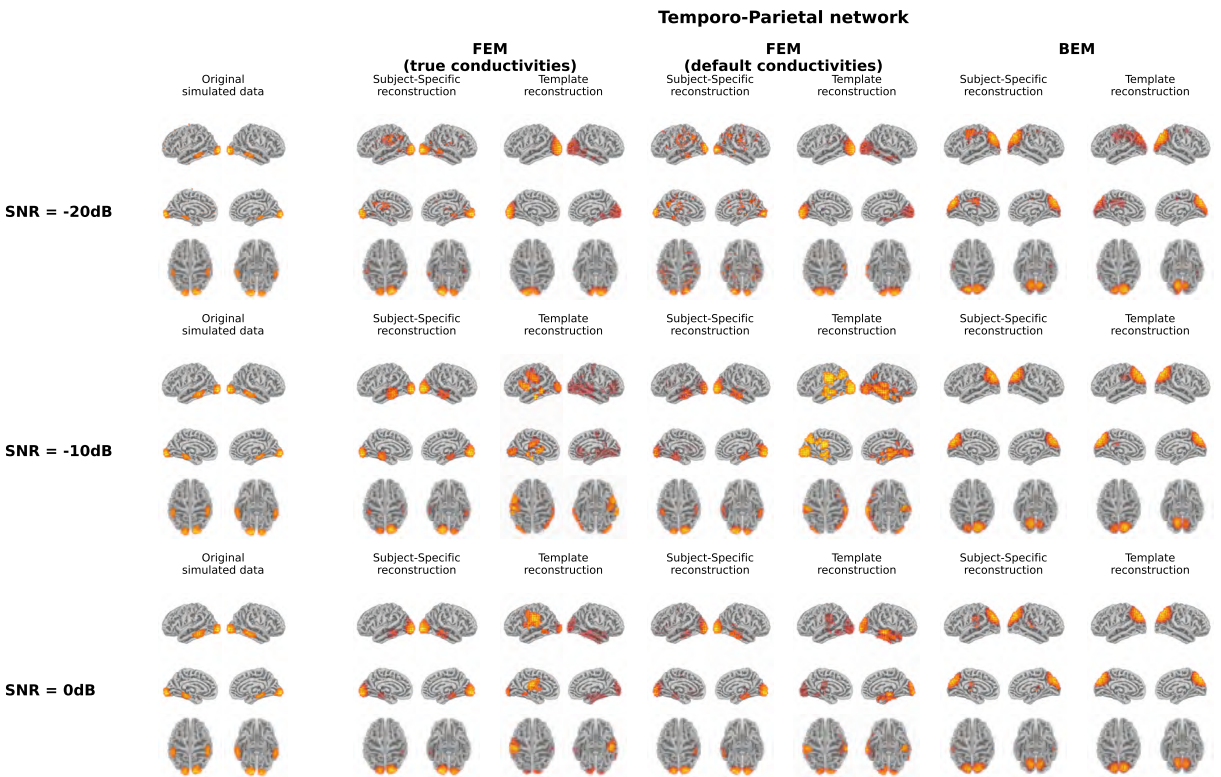

Figure C.3. Overview of the original simulated data and the reconstructed activity averaged over all subjects for the temporo-occipital network at the different SNRs. In the case of the simulations and the subject-specific reconstructions, the source activity was morphed to the average head model before averaging.

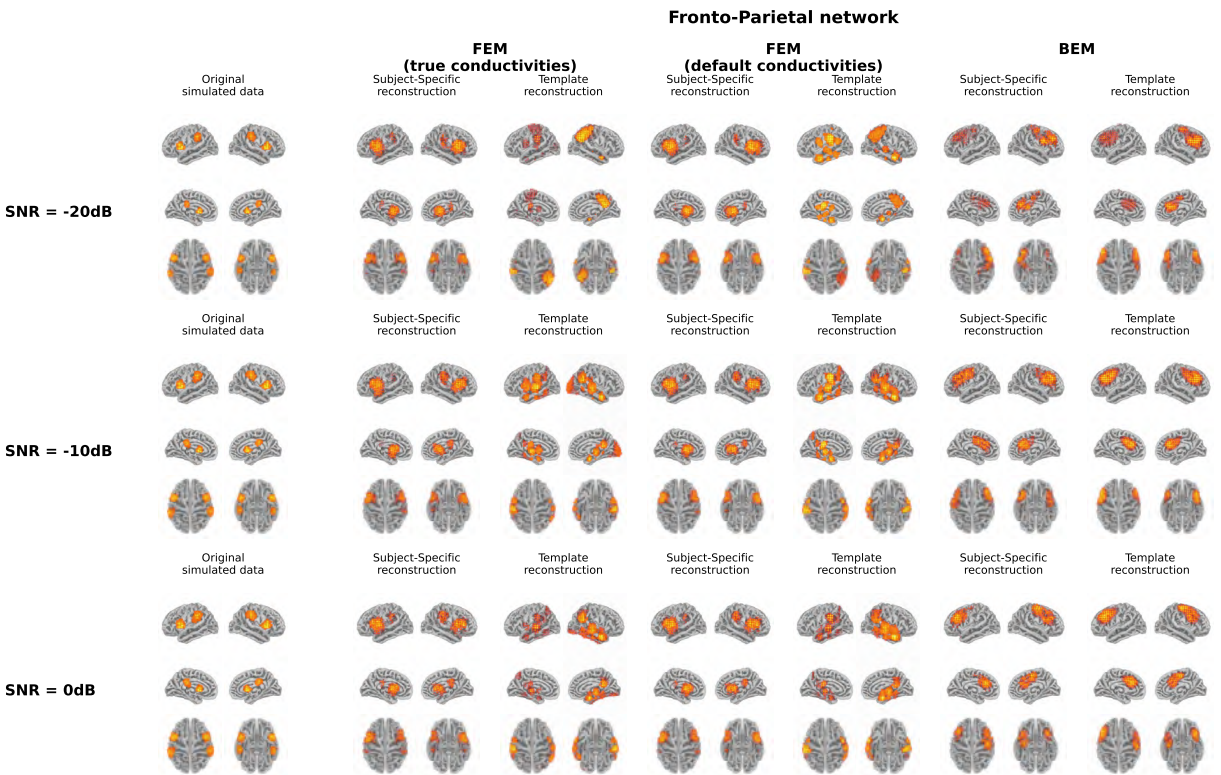

Figure C.4. Overview of the original simulated data and the reconstructed activity averaged over all subjects for the fronto-parietal network at the different SNRs. In the case of the simulations and the subject-specific reconstructions, the source activity was morphed to the average head model before averaging.

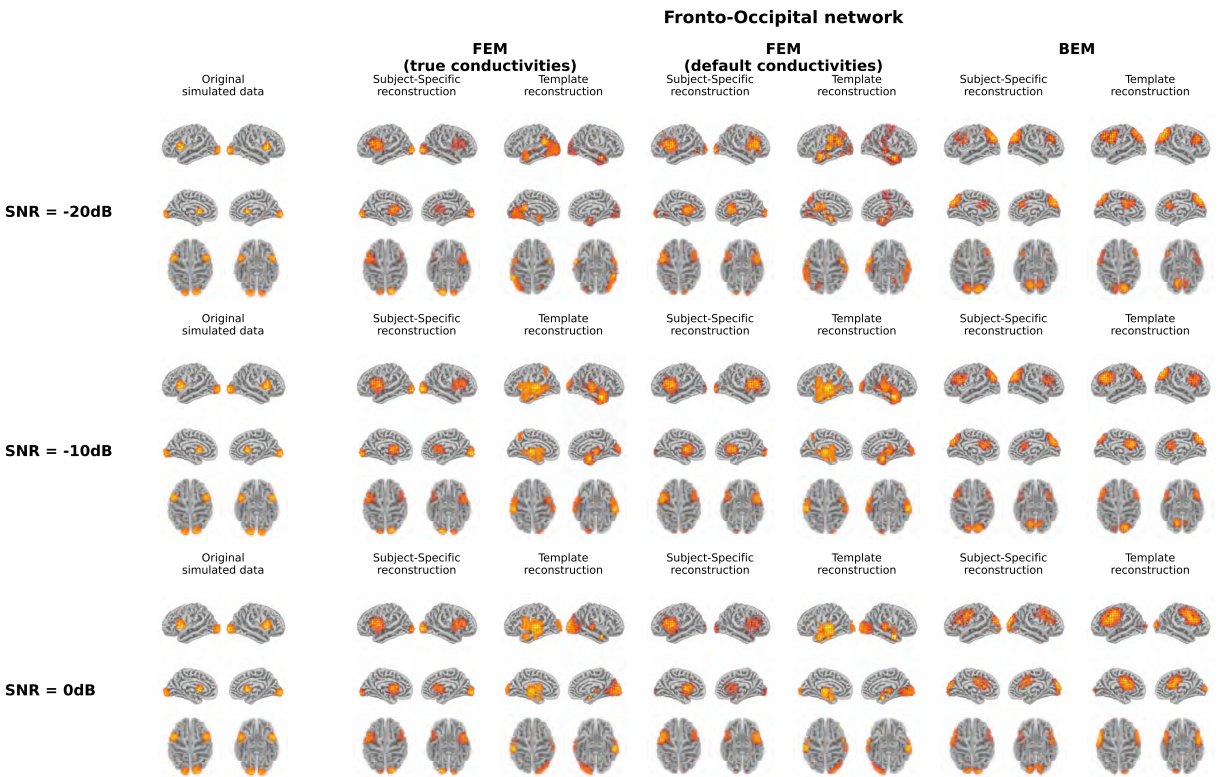

Figure C.5. Overview of the original simulated data and the reconstructed activity averaged over all subjects for the fronto-occipital network at the different SNRs. In the case of the simulations and the subject-specific reconstructions, the source activity was morphed to the average head model before averaging.

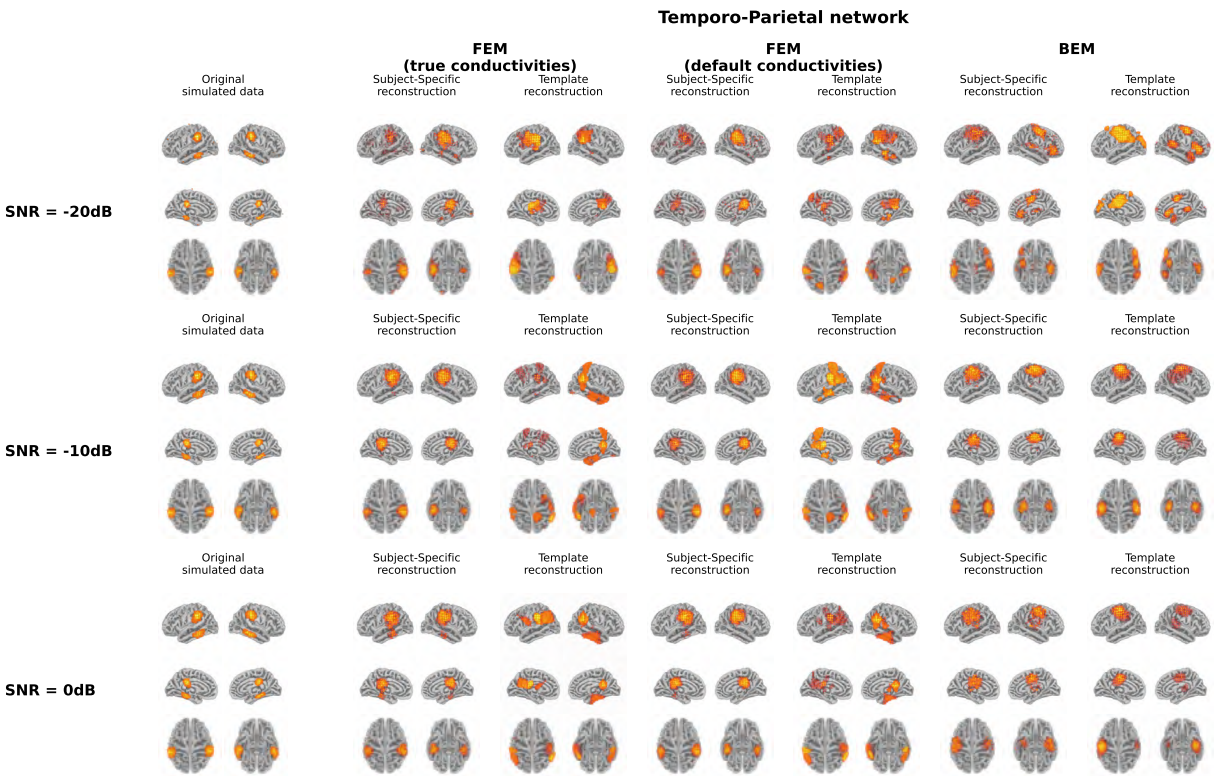

Figure C.6. Overview of the original simulated data and the reconstructed activity averaged over all subjects for the temporo-parietal network at the different SNRs. In the case of the simulations and the subject-specific reconstructions, the source activity was morphed to the average head model before averaging.

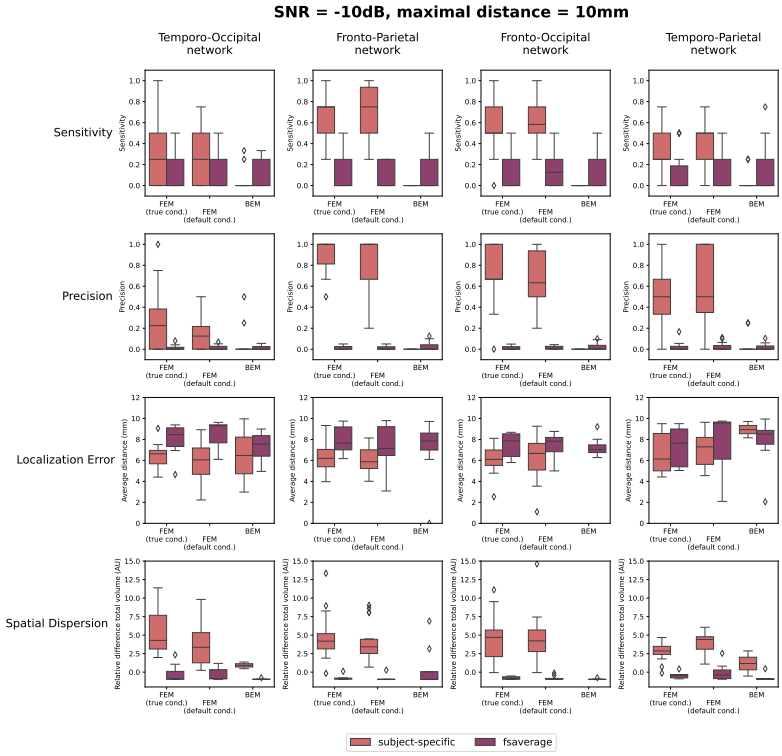

Figure C.7. Results of the quantification of the localization errors. In this evaluation sensitivity and the precision of the obtained sources, the localization error and the spatial dispersion of these reconstructed sources were taken into account. For each of these measures, the difference between using the subject-specific and average head models is shown for each of the simulated networks. Clusters of activity were considered to be correctly localized when the difference between the center of the reconstructed cluster was within 1 cm of the center of the simulated ROIs.

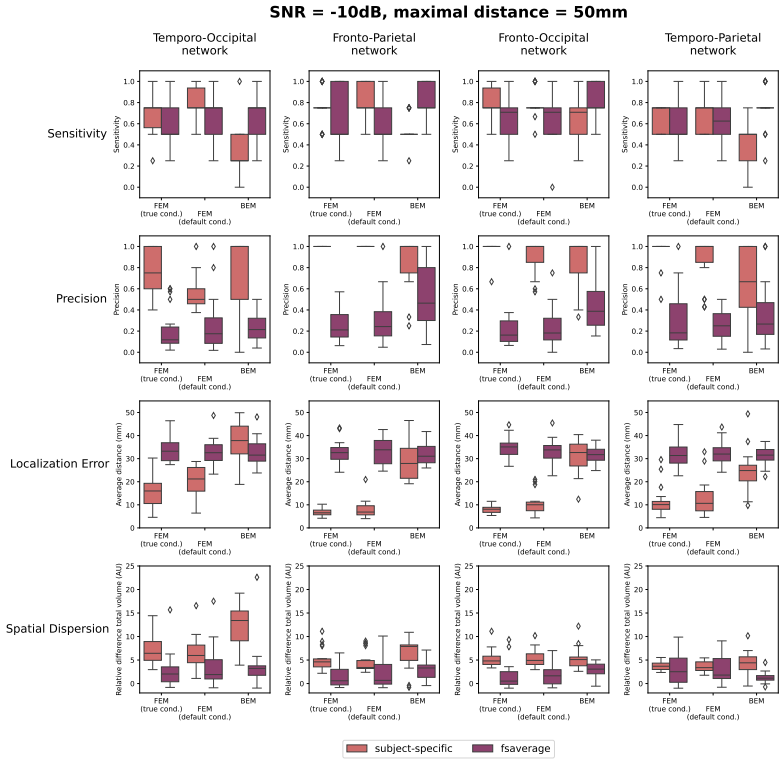

Figure C.8. Results of the quantification of the localization errors. In this evaluation sensitivity and the precision of the obtained sources, the localization error and the spatial dispersion of these reconstructed sources were taken into account. For each of these measures, the difference between using the subject-specific and average head models is shown for each of the simulated networks. Clusters of activity were considered to be correctly localized when the difference between the center of the reconstructed cluster was within 5 cm of the center of the simulated ROIs.

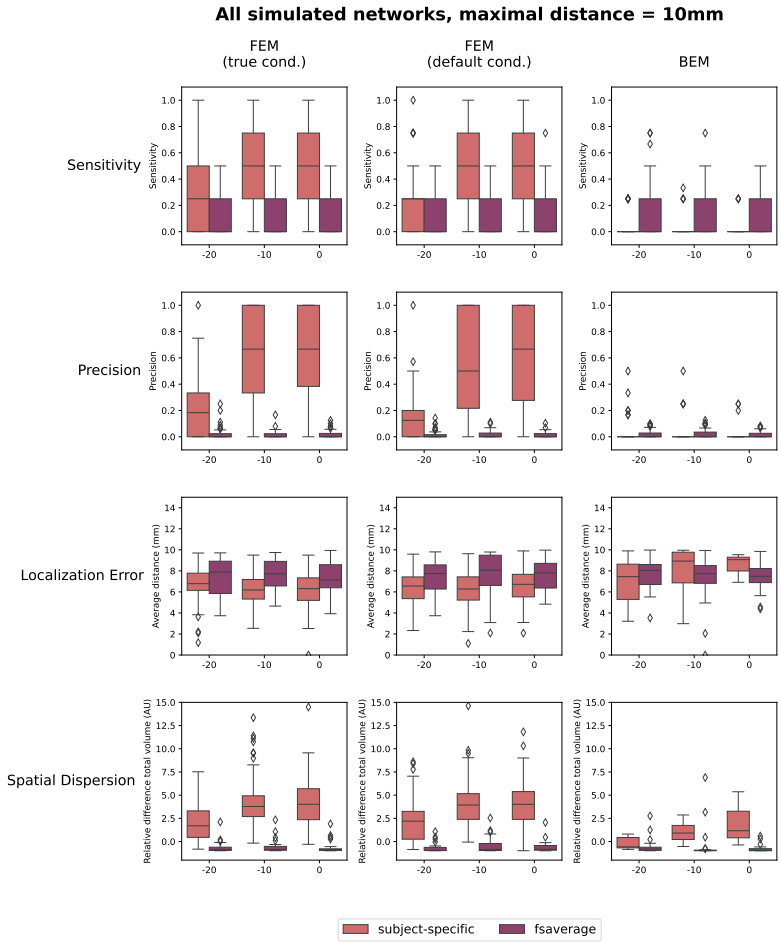

Figure C.9. Results of the quantification of the localization errors. In this evaluation sensitivity and the precision of the obtained sources, the localization error and the spatial dispersion of these reconstructed sources were taken into account. For each of these measures, the effect of both the SNR of the simulated data and the difference between using the subject-specific and average head models is shown. Clusters of activity were considered to be correctly localized when the difference between the center of the reconstructed cluster was within 1 cm of the center of the simulated ROIs.

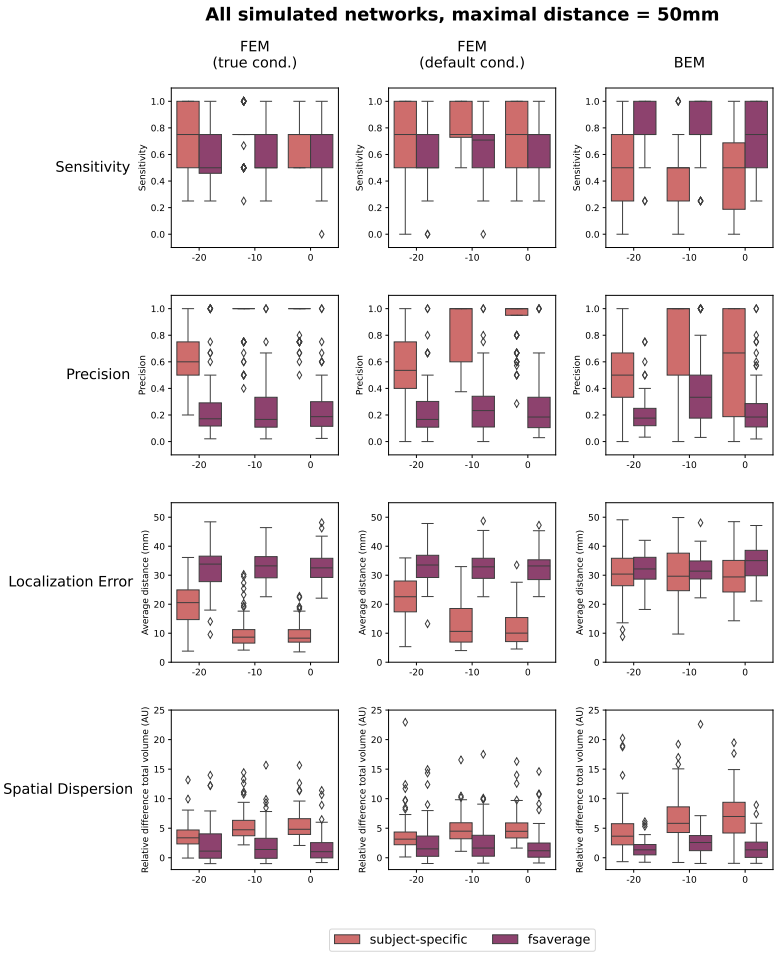

Figure C.10. Results of the quantification of the localization errors. In this evaluation sensitivity and the precision of the obtained sources, the localization error and the spatial dispersion of these reconstructed sources were taken into account. For each of these measures, the effect of both the SNR of the simulated data and the difference between using the subject-specific and average head models is shown. Clusters of activity were considered to be correctly localized when the difference between the center of the reconstructed cluster was within 5 cm of the center of the simulated ROIs.

D | The impact of brain tumors and craniotomy lesions on scalp ERPs

Single-source simulations

In the main text, the MAG% and RDM% values at the scalp level were presented for the simulated data of each individual dipole in Subject 1. Here, we present the corresponding figures for Subject 2. The first row of Figure D.1 represents a model incorporating all lesions, including those resulting from tumor resection as well as craniotomy-induced lesions. The second row isolates the effects of tumor-related lesions, while the third row focuses solely on the impact of craniotomy-related lesions.

These results again indicate that dipoles located near the lesions exhibit the most pronounced differences in both magnitude and topography, and that these effects are not limited to the immediate vicinity of the lesions but extend across much of the left hemisphere. This widespread influence appears to be predominantly driven by craniotomy-related lesions, while the effects of tumor-related lesions are more localized.

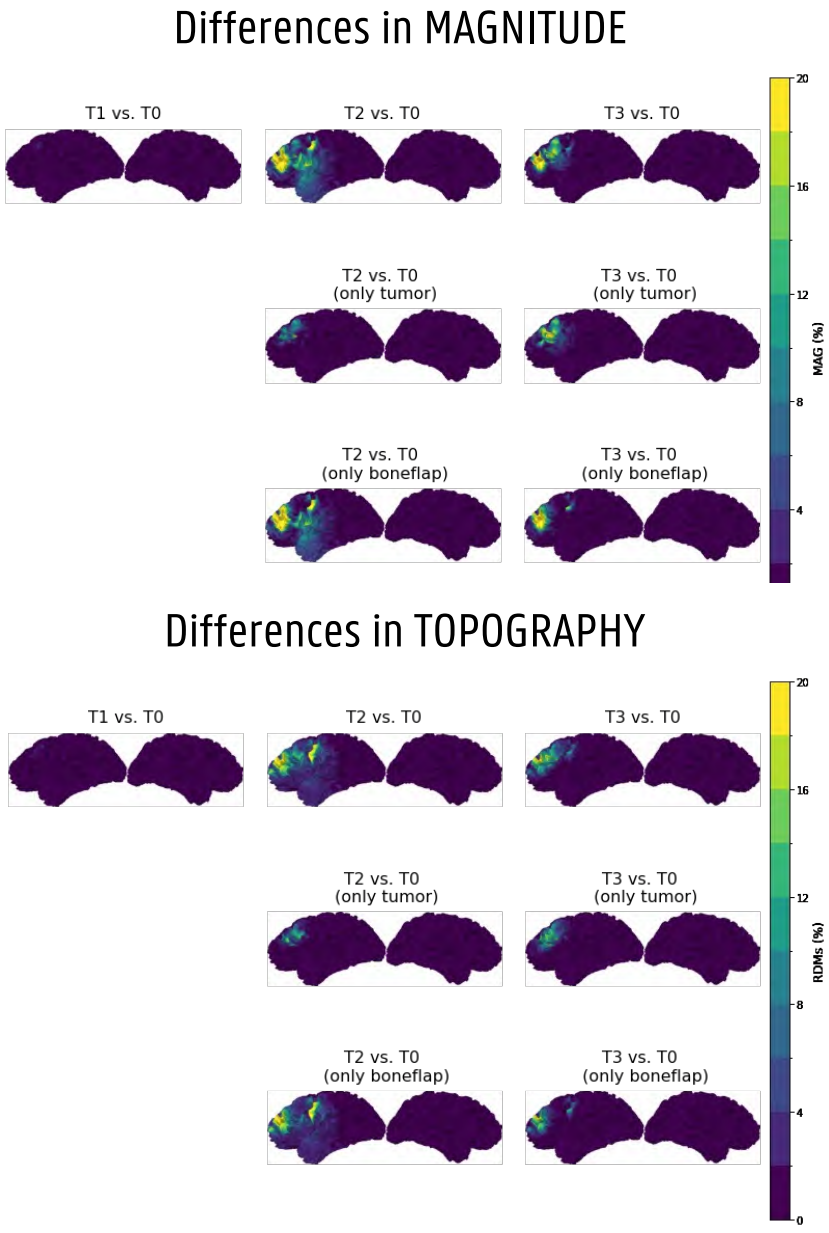

Figure D.1. The differences in magnitude and topography of the EEG signals generated for each dipole using models with and without lesions.

Bibliography

(2010). Network-based statistic: Identifying differences in brain networks. *NeuroImage*, 53(4):1197–1207. https://doi.org/10.1016/j.neuroimage.2010.06.041.

Ablin, P., Cardoso, J.-F., and Gramfort, A. (2018). Faster independent component analysis by preconditioning with hessian approximations. *IEEE Transactions on Signal Processing*, 66(15):4040–4049. https://doi.org/10.1109/TSP.2018.2844203.

Abrahamse, R., Beynon, A., and Piai, V. (2021). Long-term auditory processing outcomes in early implanted young adults with cochlear implants: The mismatch negativity vs. p300 response. *Clinical Neurophysiology*, 132(1):258–268. https://doi.org/10.1016/j.clinph.2020.09.022.

Aerts, A., van Mierlo, P., Hartsuiker, R. J., Hallez, H., Santens, P., and De Letter, M. (2013). Neurophysiological investigation of phonological input: aging effects and development of normative data. *Brain and language*, 125(3):253–263. https://doi.org/10.1016/j.bandl.2013.02.010.

Aerts, A., van Mierlo, P., Hartsuiker, R. J., Santens, P., and De Letter, M. (2015). Sex differences in neurophysiological activation patterns during phonological input processing: an influencing factor for normative data. *Archives of sexual behavior*, 44(8):2207–2218. https://doi.org/10.1007/s10508-015-0560-y.

Akalin Acar, Z. and Makeig, S. (2013). Effects of Forward Model Errors on EEG Source Localization. *Brain Topography*, 26(3):378–396. https://doi.org/10.1007/s10548-012-0274-6.

Alho, K., Woods, D. L., Algazi, A., Knight, R. T., and Näätänen, R. (1994). Lesions of frontal cortex diminish the auditory mismatch nega-

tivity. *Electroencephalography and clinical neurophysiology*, 91(5):353–362. https://doi.org/10.1016/0013-4694(94)00173-1.

Alvarado-Gonzalez, M., Fuentes-Pineda, G., and Cervantes-Ojeda, J. (2021). A few filters are enough: Convolutional neural network for p300 detection. *Neurocomputing*, 425:37–52. https://doi.org/10.1016/j.neucom.2020.10.104.

Amunts, K., Weiss, P. H., Mohlberg, H., Pieperhoff, P., Eickhoff, S., Gurd, J. M., Marshall, J. C., Shah, N. J., Fink, G. R., and Zilles, K. (2004). Analysis of neural mechanisms underlying verbal fluency in cytoarchitectonically defined stereotaxic space—the roles of brodmann areas 44 and 45. *Neuroimage*, 22(1):42–56. https://doi.org/10.1016/j.neuroimage.2003.12.031.

Anwander, A., Wolters, C., Dümpelmann, M., and Knösche, T. (2002). Influence of realistic skull and white matter anisotropy on the inverse problem in eeg/meg-source localization. *Proceedings of The 13th International Conference on Biomagnetism*, pages 679–681.

Appelhoff, S., Hurst, A. J., Lawrence, A., Li, A., Mantilla Ramos, Y. J., O'Reilly, C., Xiang, L., and Dancker, J. (2022). *PyPREP*. Zenodo. https://doi.org/10.5281/zenodo.6363576.

Asadzadeh, S., Yousefi Rezaii, T., Beheshti, S., Delpak, A., and Meshgini, S. (2020). A systematic review of eeg source localization techniques and their applications on diagnosis of brain abnormalities. *Journal of Neuroscience Methods*, 339:108740. https://doi.org/10.1016/j.jneumeth.2020.108740.

Auther, L. L., Wertz, R. T., Miller, T. A., and Kirshner, H. S. (2000). Relationships among the mismatch negativity (mmn) response, auditory comprehension, and site of lesion in ahasic adults. *Aphasiology*, 14(5-6):461–470. https://doi.org/10.1080/026870300401243.

Babajani-Feremi, A., Pourmotabbed, H., Schraegle, W. A., Calley, C. S., Clarke, D. F., and Papanicolaou, A. C. (2023). Meg language mapping using a novel automatic ecd algorithm in comparison with mne, dspm, and dics beamformer. *Frontiers in Neuroscience*, 17:1151885. https://doi.org/10.3389/fnins.2023.1151885.

Bastiaansen, M. and Hagoort, P. (2015). Frequency-based segregation of syntactic and semantic unification during online sentence level language

comprehension. *Journal of cognitive neuroscience*, 27(11):2095–2107. https://doi.org/10.1162/jocn_a_00829.

Bastiaansen, M. C., Van Der Linden, M., Ter Keurs, M., Dijkstra, T., and Hagoort, P. (2005). Theta responses are involved in lexical—semantic retrieval during language processing. *Journal of cognitive neuroscience*, 17(3):530–541. https://doi.org/10.1162/0898929053279469.

Bastos, A. M. and Schoffelen, J. M. (2015). A tutorial review of functional connectivity analysis methods and their interpretational pitfalls. *Frontiers in systems neuroscience*, 9:175. https://doi.org/10.3389/fnsys.2015.00175.

Becker, F. and Reinvang, I. (2007). Mismatch negativity elicited by tones and speech sounds: changed topographical distribution in aphasia. *Brain and language*, 100(1):69–78. https://doi.org/10.1016/j.bandl.2006.09.004.

Belyk, M., Brown, S., Lim, J., and Kotz, S. A. (2017). Convergence of semantics and emotional expression within the ifg pars orbitalis. *Neuroimage*, 156:240–248. https://doi.org/10.1016/j.neuroimage.2017.04.020.

Berger, H. (1929). Über das elektroenkephalogramm des menschen. *Archiv für psychiatrie und nervenkrankheiten*, 87(1):527–570.

Bertrand, O., Perrin, F., and Pernier, J. (1991). Evidence for a tonotopic organization of the auditory cortex observed with auditory evoked potentials. *Acta Oto-Laryngologica*, 111(sup491):116–123. https://doi.org/10.3109/00016489109136788.

Berwick, R. C., Friederici, A. D., Chomsky, N., and Bolhuis, J. J. (2013). Evolution, brain, and the nature of language. *Trends in cognitive sciences*, 17(2):89–98. https://doi.org/10.1016/j.tics.2012.12.002.

Biga, L. M., Bronson, S., Dawson, S., Harwell, A., Hopkins, R., Kaufmann, J., LeMaster, M., Matern, P., Morrison-Graham, K., Oja, K., Quick, D., and Runyeon, J. (2019). *Anatomy & Physiology*. OPENSTAX/OREGON STATE UNIVERSITY.

Bigdely-Shamlo, N., Mullen, T., Kothe, C., Su, K.-M., and Robbins, K. A. (2015). The PREP pipeline: standardized preprocessing for large-scale EEG analysis. *Frontiers in Neuroinformatics*, 9:16. https://doi.org/10.3389/fninf.2015.00016.

Binder, J. R., Desai, R. H., Graves, W. W., and Conant, L. L. (2009). Where is the semantic system? a critical review and meta-analysis of 120 functional neuroimaging studies. *Cerebral Cortex*, 19(12):2767–2796. https://doi.org/10.1093/cercor/bhp055.

Birot, G., Spinelli, L., Vulliémoz, S., Mégevand, P., Brunet, D., Seeck, M., and Michel, C. M. (2014). Head model and electrical source imaging: A study of 38 epileptic patients. *NeuroImage: Clinical*, 5:77–83. https://doi.org/10.1016/j.nicl.2014.06.005.

Bledowski, C., Prvulovic, D., Hoechstetter, K., Scherg, M., Wibral, M., Goebel, R., and Linden, D. E. (2004). Localizing p300 generators in visual target and distractor processing: a combined event-related potential and functional magnetic resonance imaging study. *The Journal of neuroscience : the official journal of the Society for Neuroscience*, 24(42):9353–9360. https://doi.org/10.1523/jneurosci.1897-04.2004.

Bocquillon, P., Bourriez, J. L., Palmero-Soler, E., Betrouni, N., Houdayer, E., Derambure, P., and Dujardin, K. (2011). Use of swloreta to localize the cortical sources of target- and distracter-elicited p300 components. *Clinical neurophysiology : official journal of the International Federation of Clinical Neurophysiology*, 122(10):1991–2002. https://doi.org/10.1016/j.clinph.2011.03.014.

Brazier, M. A. (1964). Evoked responses recorded from the depths of the human brain. *Annals of the New York Academy of Sciences*. https://doi.org/10.1111/j.1749-6632.1964.tb26741.x.

Breier, J. I., Simos, P. G., Zouridakis, G., and Papanicolaou, A. C. (1999). Lateralization of cerebral activation in auditory verbal and non-verbal memory tasks using magnetoencephalography. *Brain topography*, 12(2):89–97. https://doi.org/10.1023/a:1023458110869.

Broca, P. (1861). Perte de la parole, ramollissement chronique et destruction partielle du lobe antérieur gauche du cerveau. *Bull Soc Anthropol*, 2(1):235–238.

Brown, W. S., Marsh, J. T., and LaRue, A. (1983). Exponential electrophysiological aging: P3 latency. *Electroencephalography and clinical Neurophysiology*, 55(3):277–285. https://doi.org/10.1016/0013-4694(83)90205-5.

Buckner, R. L., Andrews-Hanna, J. R., and Schacter, D. L. (2008). The brain's default network: anatomy, function, and relevance to disease. *Annals of the New York Academy of Sciences*, 1124:1–38. https://doi.org/10.1196/annals.1440.011.

Bugli, C. and Lambert, P. (2007). Comparison between principal component analysis and independent component analysis in electroencephalograms modelling. *Biometrical Journal: Journal of Mathematical Methods in Biosciences*, 49(2):312–327. https://doi.org/10.1002/bimj.200510285.

Bulut, T. (2023). Domain-general and domain-specific functional networks of broca's area underlying language processing. *Brain Behav*, 13(7):e3046. https://doi.org/10.1002/brb3.3046.

Cabeza, R. (2002). Hemispheric asymmetry reduction in older adults: the harold model. *Psychology and aging*, 17(1):85–100. https://doi.org/10.1037//0882-7974.17.1.85.

Capotosto, P., Baldassarre, A., Sestieri, C., Spadone, S., Romani, G. L., and Corbetta, M. (2016). Task and regions specific top-down modulation of alpha rhythms in parietal cortex. *Cerebral Cortex*, 27(10):4815–4822. https://doi.org/10.1093/cercor/bhw278.

Caso, F., Cursi, M., Magnani, G., Fanelli, G., Falautano, M., Comi, G., Leocani, L., and Minicucci, F. (2012). Quantitative eeg and loreta: valuable tools in discerning ftd from ad? *Neurobiology of aging*, 33(10):2343–2356. https://doi.org/10.1016/j.neurobiolaging.2011.12.011.

Chen, Q., Ye, C., Liang, X., Cao, B., Lei, Y., and Li, H. (2014). Automatic processing of taxonomic and thematic relations in semantic priming - differentiation by early n400 and late frontal negativity. *Neuropsychologia*, 64:54–62. https://doi.org/10.1016/j.neuropsychologia.2014.09.013.

Chiou, R. and Lambon Ralph, M. A. (2019). Unveiling the dynamic interplay between the hub- and spoke-components of the brain's semantic system and its impact on human behaviour. *Neuroimage*, 199:114–126. https://doi.org/10.1016/j.neuroimage.2019.05.059.

Cho, J.-H., Vorwerk, J., Wolters, C. H., and Knösche, T. R. (2015). Influence of the head model on EEG and MEG source connectivity analyses. *NeuroImage*, 110:60–77. https://doi.org/10.1016/j.neuroimage.2015.01.043.

Choi, J. W., Cha, K. S., Choi, J. D., Jung, K. Y., and Kim, K. H. (2015). Difficulty-related changes in inter-regional neural synchrony are dissociated between target and non-target processing. *Brain research*, 1603:114–123. https://doi.org/10.1016/j.brainres.2015.01.031.

Choi, J. W., Jung, K. Y., Kim, C. H., and Kim, K. H. (2010). Changes in gamma- and theta-band phase synchronization patterns due to the difficulty of auditory oddball task. *Neuroscience letters*, 468(2):156–160. https://doi.org/10.1016/j.neulet.2009.10.088.

Choi, J. W., Lee, J. K., Ko, D., Lee, G. T., Jung, K. Y., and Kim, K. H. (2013). Fronto-temporal interactions in the theta-band during auditory deviant processing. *Neuroscience letters*, 548:120–125. https://doi.org/10.1016/j.neulet.2013.05.079.

Cirillo, S., Caulo, M., Pieri, V., Falini, A., and Castellano, A. (2019). Role of functional imaging techniques to assess motor and language cortical plasticity in glioma patients: a systematic review. *Neural Plasticity*, 2019(1):4056436. https://doi.org/10.1155/2019/4056436.

Clayson, P. E., Baldwin, S. A., and Larson, M. J. (2013). How does noise affect amplitude and latency measurement of event-related potentials (erps)? a methodological critique and simulation study. *Psychophysiology*, 50(2):174–186. https://doi.org/10.1111/psyp.12001.

Cocquyt, E.-M., Depuydt, E., Santens, P., van Mierlo, P., Duyck, W., Szmalec, A., and De Letter, M. (2023). Effects of healthy aging and gender on the electrophysiological correlates of semantic sentence comprehension : the development of dutch normative data. *JOURNAL OF SPEECH LANGUAGE AND HEARING RESEARCH*. https://doi.org/10.1044/2023_JSLHR-22-00545.

Cocquyt, E.-M., Santens, P., van Mierlo, P., Duyck, W., Szmalec, A., and De Letter, M. (2022). Age-and gender-related differences in verbal semantic processing: the development of normative electrophysiological data in the flemish population. *Language, cognition and neuroscience*, 37(2):241–267. https://doi.org/10.1080/23273798.2021.1957137.

Cohen, M. X. (2014). *Analyzing neural time series data: theory and practice*. MIT press.

Conte, S. and Richards, J. E. (2021). The Influence of the Head Model Conductor on the Source Localization of Auditory Evoked Potentials. *Brain Topography*, 34(6):793–812. https://doi.org/10.1007/s10548-021-00871-z.

Corbetta, M. and Shulman, G. L. (2002). Control of goal-directed and stimulus-driven attention in the brain. *Nature reviews. Neuroscience*, 3(3):201–215. https://doi.org/10.1038/nrn755.

Coulson, S. and Kutas, M. (2021). Getting it: human event-related brain responses to jokes in good and poor comprehenders. *Neuroscience Letters*, 316(2):71–74. https://doi.org/10.1016/S0304-3940(01)02387-4.

Criel, Y. (2024). *Functional connectivity of language perception networks in individuals with acquired brain injuries*. PhD thesis, Ghent University.

Criel, Y., Boon, C., Depuydt, E., Stalpaert, J., Huysman, E., Miatton, M., Santens, P., van Mierlo, P., and De Letter, M. (2023). Aging and sex effects on phoneme perception: Evidence from the mismatch negativity and p300. *International Journal of Psychophysiology*. https://doi.org/10.1016/j.ijpsycho.2023.06.002.

Criel, Y., Depuydt, E., Cocquyt, E.-M., Miatton, M., Santens, P., van Mierlo, P., and De Letter, M. (2025). Frontal synchronisation facilitates taxonomic priming: insights from n400 source estimation and functional connectivity. *Language, Cognition and Neuroscience*, pages 1–18. https://doi.org/10.1080/23273798.2025.2501049.

Criel, Y., Depuydt, E., Miatton, M., Santens, P., van Mierlo, P., and De Letter, M. (2024). Cortical generators and connections underlying phoneme perception: A mismatch negativity and p300 investigation. *Brain Topography*, pages 1–29. https://doi.org/10.1007/s10548-024-01065-z.

Crottaz-Herbette, S. and Menon, V. (2006). Where and when the anterior cingulate cortex modulates attentional response: combined fmri and erp evidence. *Journal of cognitive neuroscience*, 18(5):766–780. https://doi.org/10.1162/jocn.2006.18.5.766.

Cuffin, B., Schomer, D. L., Ives, J. R., and Blume, H. (2001). Experimental tests of EEG source localization accuracy in realistically shaped head models. *Clinical Neurophysiology*, 112(12):2288–2292. https://doi.org/10.1016/S1388-2457(01)00669-1.

Da Pelo, P., De Tommaso, M., Monaco, A., Stramaglia, S., Bellotti, R., and Tangaro, S. (2018). Trial latencies estimation of event-related potentials in eeg by means of genetic algorithms. *Journal of neural engineering*, 15(2):026016. https://doi.org/10.1088/1741-2552/aa9b97.

Dale, A. M., Liu, A. K., Fischl, B. R., Buckner, R. L., Belliveau, J. W., Lewine, J. D., and Halgren, E. (2000). Dynamic statistical parametric mapping: combining fmri and meg for high-resolution imaging of cortical activity. *Neuron*, 26(1):55–67. https://doi.org/10.1016/s0896-6273(00)81138-1.

Dannhauer, M., Lanfer, B., Wolters, C. H., and Knösche, T. R. (2011). Modeling of the human skull in eeg source analysis. *Human brain mapping*, 32(9):1383–1399. https://doi.org/10.1002/hbm.21114.

Davis, S. W., Dennis, N. A., Daselaar, S. M., Fleck, M. S., and Cabeza, R. (2008). *Que PASA? The posterior-anterior shift in aging. Cerebral cortex*. , 18(5), 1201-1209, New York, N. Y. 1991.

De Deyne, S., Navarro, D. J., Perfors, A., and Storms, G. (2016). Structure at every scale: A semantic network account of the similarities between unrelated concepts. *Journal of Experimental Psychology: General*, 145(9):1228. https://doi.org/10.1037/xge0000192.

De Lucia, M., Michel, C. M., and Murray, M. M. (2010). Comparing ica-based and single-trial topographic erp analyses. *Brain topography*, 23(2):119–127. https://doi.org/10.1007/s10548-010-0145-y.

De Witt Hamer, P. C., Robles, S. G., Zwinderman, A. H., Duffau, H., and Berger, M. S. (2012). Impact of intraoperative stimulation brain mapping on glioma surgery outcome: a meta-analysis. *Journal of Clinical Oncology*, 30(20):2559–2565. https://doi.org/10.1200/JCO.2011.38.4818.

Del Felice, A., Arcaro, C., Storti, S. F., Fiaschi, A., and Manganotti, P. (2014). Electrical Source Imaging of Sleep Spindles. *Clinical EEG and Neuroscience*, 45(3):184–192. https://doi.org/10.1177/1550059413497716.

Delorme, A., Palmer, J., Onton, J., Oostenveld, R., and Makeig, S. (2012). Independent eeg sources are dipolar. *PloS one*, 7(2):e30135. https://doi.org/10.1371/journal.pone.0030135.

Deouell, L. Y. (2007). The frontal generator of the mismatch negativity revisited. *Journal of Psychophysiology*, 21(3-4):188–203. https://doi.org/10.1027/0269-8803.21.34.188.

Depuydt, E., Criel, Y., De Letter, M., and van Mierlo, P. (2023). Single-trial erp quantification using neural networks. *Brain Topography*, 36(6):767–790. https://doi.org/10.1007/s10548-023-00991-8.

Depuydt, E., Criel, Y., De Letter, M., and Van Mierlo, P. (2024). Investigating the effect of template head models on event-related potential source localization: a simulation and real-data study. *Frontiers in Neuroscience*, 18. Article 1443752.

Deschamps, I., Baum, S. R., and Gracco, V. L. (2014). On the role of the supramarginal gyrus in phonological processing and verbal working memory: evidence from rtms studies. *Neuropsychologia*, 53:39–46. https://doi.org/10.1016/j.neuropsychologia.2013.10.015.

Desikan, R. S., Ségonne, F., Fischl, B., Quinn, B. T., Dickerson, B. C., Blacker, D., Buckner, R. L., Dale, A. M., Maguire, R. P., Hyman, B. T., Albert, M. S., and Killiany, R. J. (2006). An automated labeling system for subdividing the human cerebral cortex on mri scans into gyral based regions of interest. *NeuroImage*, 31(3):968–980. https://doi.org/10.1016/j.neuroimage.2006.01.021.

Destrieux, C., Fischl, B., Dale, A., and Halgren, E. (2010). Automatic parcellation of human cortical gyri and sulci using standard anatomical nomenclature. *Neuroimage*, 53(1):1–15. https://doi.org/10.1016/j.neuroimage.2010.06.010.

Dien, J. (2010). Evaluating two-step pca of erp data with geomin, infomax, oblimin, promax, and varimax rotations. *Psychophysiology*, 47(1):170–183. https://doi.org/10.1111/j.1469-8986.2009.00885.x.

Dilkina, K. and Lambon Ralph, M. A. (2012). Conceptual structure within and between modalities. *Frontiers in Human Neuroscience*, 6:333. https://doi.org/10.3389/fnhum.2012.00333.

Diveica, V., Koldewyn, K., and Binney, R. J. (2021). Establishing a role of the semantic control network in social cognitive processing: A meta-analysis of functional neuroimaging studies. *Neuroimage*, 245:118702. https://doi.org/10.1016/j.neuroimage.2021.118702.

Doeller, C. F., Opitz, B., Mecklinger, A., Krick, C., Reith, W., and Schröger, E. (2003). Prefrontal cortex involvement in preattentive auditory deviance detection: neuroimaging and electrophysiological evidence. *NeuroImage*, 20(2):1270–1282. https://doi.org/10.1016/s1053-8119(03)00389-6.

Dominey, P. F. and Inui, T. (2009). Cortico-striatal function in sentence comprehension: Insights from neurophysiology and modeling. *Cortex*, 45(8):1012–1018. https://doi.org/10.1016/j.cortex.2009.03.007.

Donchin, E. and Coles, M. G. (1988). Is the p300 component a manifestation of context updating? *Behav. Brain Sci.*, 11(3):357–374. https://doi.org/10.1017/S0140525X00058027.

Dorme, A., Van Oudenhove, B., Criel, Y., Depuydt, E., De Groote, E., Stalpaert, J., Huysman, E., van Mierlo, P., and De Letter, M. (2023). Effect of Healthy Aging and Gender on Syntactic Input Processing: A P600 Event-Related Potential Study. *Journal of Speech, Language, and Hearing Research*, 66(8):2701–2732. https://doi.org/10.1044/2023_JSLHR-22-00633.

Duffau, H., Capelle, L., Denvil, D., Sichez, N., Gatignol, P., Taillandier, L., Lopes, M., Mitchell, M.-C., Roche, S., Muller, J.-C., et al. (2003). Usefulness of intraoperative electrical subcortical mapping during surgery for low-grade gliomas located within eloquent brain regions: functional results in a consecutive series of 103 patients. *Journal of neurosurgery*, 98(4):764–778. https://doi.org/10.3171/jns.2003.98.4.0764.

Duncan, C. C., Barry, R. J., Connolly, J. F., Fischer, C., Michie, P. T., Näätänen, R., Polich, J., Reinvang, I., and Van Petten, C. (2009). Event-related potentials in clinical research: guidelines for eliciting, recording, and quantifying mismatch negativity, p300, and n400. *Clinical neurophysiology : official journal of the International Federation of Clinical Neurophysiology*, 120(11):1883–1908. https://doi.org/10.1016/j.clinph.2009.07.045.

D'Avanzo, C., Schiff, S., Amodio, P., and Sparacino, G. (2011). A bayesian method to estimate single-trial event-related potentials with application to the study of the p300 variability. *Journal of neuroscience methods*, 198(1):114–124. https://doi.org/10.1016/j.jneumeth.2011.03.010.

Eddine, S. N., Brothers, T., Wang, L., Spratling, M., and Kuperberg, G. R. (2024). A predictive coding model of the n400. *Cognition*, 246:105755. https://doi.org/10.1016/j.cognition.2024.105755.

Eggermont, J. J. and Ponton, C. W. (2002). The neurophysiology of auditory perception: from single units to evoked potentials. *Audiology and Neurotology*, 7(2):71–99. https://doi.org/10.1159/000057656.

Ehlers, M. R., López Herrero, C., Kastrup, A., and Hildebrandt, H. (2015). The p300 in middle cerebral artery strokes or hemorrhages: Outcome predictions and source localization. *Clinical neurophysiology : official journal of the International Federation of Clinical Neurophysiology*, 126(8):1532–1538. https://doi.org/10.1016/j.clinph.2014.10.151.

Ellis, A. W. and Young, A. W. (1996). *Human cognitive neuropsychology: A textbook with readings*. Psychology Press.

Engel, A. K. and Fries, P. (2010). Beta-band oscillations—signalling the status quo? *Current opinion in neurobiology*, 20(2):156–165. https://doi.org/10.1016/j.conb.2010.02.015.

Engell, A. D. and McCarthy, G. (2014). Face, eye, and body selective responses in fusiform gyrus and adjacent cortex: an intracranial EEG study. *Frontiers in Human Neuroscience*, 8:642. https://doi.org/10.3389/fnhum.2014.00642.

Fan, L., Li, H., Zhuo, J., Zhang, Y., Wang, J., Chen, L., Yang, Z., Chu, C., and Jiang, T. (2016). The human brainnetome atlas: A new brain atlas based on connectional architecture. *Cerebral Cortex*, 26(8):3508–3526. https://doi.org/10.1093/cercor/bhw157.

Fernandez Guerrero, A. and Achermann, P. (2019). Brain dynamics during the sleep onset transition: An EEG source localization study. *Neurobiology of Sleep and Circadian Rhythms*, 6:24–34. https://doi.org/10.1016/j.nbscr.2018.11.001.

Fischer, M. and Löwenbach, H. (1934). Aktionsströme des zentralnervensystems unter der einwirkung von krampfgiften. *Naunyn-Schmiedebergs Archiv für experimentelle Pathologie und Pharmakologie*, 174(5-6):502–516.

Fischl, B. (2012). Freesurfer. *NeuroImage*, 62(2):774–781. https://doi.org/10.1016/j.neuroimage.2012.01.021.

Fjell, A. M. and Walhovd, K. B. (2010). Structural brain changes in aging: courses, causes and cognitive consequences. *Reviews in the neurosciences*, 21(3):187–221. https://doi.org/10.1515/revneuro.2010.21.3.187.

Fjell, A. M., Westlye, L. T., Amlien, I. K., and Walhovd, K. B. (2011). Reduced white matter integrity is related to cognitive instability. *Journal of Neuroscience*, 31(49):18060–18072. https://doi.org/10.1523/JNEUROSCI.4735-11.2011.

Flemming, L., Wang, Y., Caprihan, A., Eiselt, M., Haueisen, J., and Okada, Y. (2005). Evaluation of the distortion of eeg signals caused by a hole in the skull mimicking the fontanel in the skull of human neonates. *Clinical neurophysiology*, 116(5):1141–1152. https://doi.org/10.1016/j.clinph.2005.01.007.

Ford, J. M., White, P., Lim, K. O., and Pfefferbaum, A. (1994). Schizophrenics have fewer and smaller p300s: a single-trial analysis. *Biological psychiatry*, 35(2):96–103. https://doi.org/10.1016/0006-3223(94)91198-3.

Friederici, A. D. (2017). *Language in our brain: The origins of a uniquely human capacity*. MIT Press.

Frodl-Bauch, T., Kathmann, N., Möller, H.-J., and Hegerl, U. (1997). Dipole localization and test-retest reliability of frequency and duration mismatch negativity generator processes. *Brain Topography*, 10:3–8. https://doi.org/10.1023/A:1022214905452.

Fulham, W. R., Michie, P. T., Ward, P. B., Rasser, P. E., Todd, J., Johnston, P. J., Thompson, P. M., and Schall, U. (2014). Mismatch negativity in recent-onset and chronic schizophrenia: a current source density analysis. *PloS one*, 9(6):e100221. https://doi.org/10.1371/journal.pone.0100221.

Garrido, M. I., Kilner, J. M., Stephan, K. E., and Friston, K. J. (2009). The mismatch negativity: a review of underlying mechanisms. *Clinical neurophysiology : official journal of the International Federation of Clinical Neurophysiology*, 120(3):453–463. https://doi.org/10.1016/j.clinph.2008.11.029.

Gazzaniga, M. S., Ivry, R. B., and Mangun, G. R. (2009). Cognitive Neuroscience: The Biology of the Mind.

Geal-Dor, M., Goldstein, A., Kamenir, Y., and Babkoff, H. (2006). The effect of aging on event-related potentials and behavioral responses: comparison of tonal, phonologic and semantic targets. *Clinical neurophysiology : official journal of the International Federation of Clinical Neurophysiology*, 117(9):1974–1989. https://doi.org/10.1016/j.clinph.2006.05.024.

Genovese, C. R., Lazar, N. A., and Nichols, T. (2002). Thresholding of statistical maps in functional neuroimaging using the false discovery rate. *NeuroImage*, 15(4):870–878. https://doi.org/10.1006/nimg.2001.1037.

Geukes, S., Huster, R. J., Wollbrink, A., Junghöfer, M., Zwitserlood, P., and Dobel, C. (2013). A large n400 but no bold effect–comparing source activations of semantic priming in simultaneous eeg-fmri. *PLoS One*, 8(12):e84029. https://doi.org/10.1371/journal.pone.0084029.

Ghosh Hajra, S., Liu, C. C., Song, X., Fickling, S. D., Cheung, T. P. L., and D'Arcy, R. C. N. (2018). Multimodal characterization of the semantic n400 response within a rapid evaluation brain vital sign framework. *Journal of Translational Medicine*, 16(1):151. https://doi.org/10.1186/s12967-018-1527-2.

Giard, M.-H., Perrin, F., Echallier, J. F., Thévenet, M., Froment, J. C., and Pernier, J. (1994). Dissociation of temporal and frontal components in the human auditory n1 wave: a scalp current density and dipole model analysis. *Electroencephalography and Clinical Neurophysiology/Evoked Potentials Section*, 92(3):238–252. https://doi.org/10.1016/0168-5597(94)90067-1.

Goldman, L., Siddiqui, E. M., Khan, A., Jahan, S., Rehman, M. U., Mehan, S., Sharma, R., Budkin, S., Kumar, S. N., Sahu, A., et al. (2022). Understanding acquired brain injury: a review. *Biomedicines*, 10(9):2167. https://doi.org/10.3390/biomedicines10092167.

Gramfort, A., Luessi, M., Larson, E., Engemann, D. A., Strohmeier, D., Brodbeck, C., Goj, R., Jas, M., Brooks, T., Parkkonen, L., et al. (2013). Meg and eeg data analysis with mne-python. *Frontiers in neuroscience*, page 267. https://doi.org/10.3389/fnins.2013.00267.

Gross, J., Kujala, J., Hämäläinen, M., Timmermann, L., Schnitzler, A., and Salmelin, R. (2001). Dynamic imaging of coherent sources: studying neural interactions in the human brain. *Proceedings of the National Academy of Sciences*, 98(2):694–699. https://doi.org/10.1073/pnas.98.2.694.

Gross, J., Pollok, B., Dirks, M., Timmermann, L., Butz, M., and Schnitzler, A. (2005). Task-dependent oscillations during unimanual and bimanual movements in the human primary motor cortex and sma studied with magnetoencephalography. *Neuroimage*, 26(1):91–98. https://doi.org/10.1016/j.neuroimage.2005.01.025.

Gunter, T. C., Jackson, J. L., and Mulder, G. (1992). An electrophysiological study of semantic processing in young and middle-aged academics. *Psychophysiology*, 29(1):38–54. https://doi.org/10.1111/j.1469-8986.1992.tb02009.x.

Hagoort, P. (2008). The fractionation of spoken language understanding by measuring electrical and magnetic brain signals. philosophical transactions of the royal society of london. *Series B, Biological Sciences*, 363(1493):1055–1069. https://doi.org/10.1098/rstb.2007.2159.

Hagoort, P., Brown, C. M., and Swaab, T. Y. (1996). Lexical—semantic event–related potential effects in patients with left hemisphere lesions and aphasia, and patients with right hemisphere lesions without aphasia. *Brain*, 119(2):627–649. https://doi.org/10.1093/brain/119.2.627.

Hagoort, P., Hald, L., Bastiaansen, M., and Petersson, K. M. (2004). Integration of word meaning and world knowledge in language comprehension. *science*, 304(5669):438–441. https://doi.org/10.1126/science.1095455.

Halder, T., Talwar, S., Jaiswal, A. K., and Banerjee, A. (2019). Quantitative evaluation in estimating sources underlying brain oscillations using current source density methods and beamformer approaches. *eneuro*, 6(4). https://doi.org/10.1523/ENEURO.0170-19.2019.

Halgren, E., Marinkovic, K., and Chauvel, P. (1998). Generators of the late cognitive potentials in auditory and visual oddball tasks. *Electroencephalography and clinical neurophysiology*, 106(2):156–164. https://doi.org/10.1016/s0013-4694(97)00119-3.

Hämäläinen, M. S. and Ilmoniemi, R. J. (1994). Interpreting magnetic fields of the brain: minimum norm estimates. *Medical & biological engineering & computing*, 32:35–42. https://doi.org/10.1007/BF02512476.

Hamilton, R. H., Chrysikou, E. G., and Coslett, B. (2011). Mechanisms of aphasia recovery after stroke and the role of noninvasive brain stimulation. *Brain and language*, 118(1-2):40–50. https://doi.org/10.1016/j.bandl.2011.02.005.

Handy, T. C. (2005). *Event-related potentials: A methods handbook*. MIT press.

Hansen, J. C. and Hillyard, S. A. (1980). Endogeneous brain potentials associated with selective auditory attention. *Electroencephalography and clinical neurophysiology*, 49(3-4):277–290. https://doi.org/10.1016/0013-4694(80)90222-9.

Hauk, O., Stenroos, M., and Treder, M. S. (2022). Towards an objective evaluation of EEG/MEG source estimation

methods – The linear approach. *NeuroImage*, 255:119177. https://doi.org/10.1016/j.neuroimage.2022.119177.

Haxby, J. V., Hoffman, E. A., and Gobbini, M. (2000). The distributed human neural system for face perception. *Trends in Cognitive Sciences*, 4(6):223–233. https://doi.org/10.1016/S1364-6613(00)01482-0.

Heim, S. and Alter, K. (2006). Prosodic pitch accents in language comprehension and production: Erp data and acoustic analyses. *Acta neurobiologiae experimentalis*, 66(1):55–68. https://doi.org/10.55782/ane-2006-1587.

Heim, S., van Ermingen, M., Huber, W., and Amunts, K. (2010). Left cytoarchitectonic ba 44 processes syntactic gender violations in determiner phrases. *Human brain mapping*, 31(10):1532–1541. https://doi.org/10.1002/hbm.20957.

Heinrichs-Graham, E. and Wilson, T. W. (2016). Is an absolute level of cortical beta suppression required for proper movement? magnetoencephalographic evidence from healthy aging. *Neuroimage*, 134:514–521. https://doi.org/10.1016/j.neuroimage.2016.04.032.

Henson, R., Mattout, J., Singh, K., Barnes, G., Hillebrand, A., and Friston, K. (2007). Population-level inferences for distributed MEG source localization under multiple constraints: Application to face-evoked fields. *NeuroImage*, 38(3):422–438. https://doi.org/10.1016/j.neuroimage.2007.07.026.

Hickok, G. and Poeppel, D. (2004). Dorsal and ventral streams: a framework for understanding aspects of the functional anatomy of language. *Cognition*, 92(1-2):67–99. https://doi.org/10.1016/j.cognition.2003.10.011.

Hickok, G. and Poeppel, D. (2007). The cortical organization of speech processing. *Nature Reviews Neuroscience*, 8(5):393–402. https://doi.org/10.1038/nrn2113.

Hill, H., Strube, M., Roesch-Ely, D., and Weisbrod, M. (2002). Automatic vs. controlled processes in semantic priming–differentiation by event-related potentials. *International Journal of Psychophysiology*, 44(3):197–218. https://doi.org/10.1016/s0167-8760(01)00202-1.

Hirayasu, Y., Samura, M., Ohta, H., and Ogura, C. (2000). Sex effects on rate of change of p300 latency with age. *Clinical Neurophysiology*, 111(2):187–194. https://doi.org/10.1016/S1388-2457(99)00233-3.

Hodgkin, A. L. and Huxley, A. F. (1952). A quantitative description of membrane current and its application to conduction and excitation in nerve. *The Journal of physiology*, 117(4):500–544. https://doi.org/10.1113/jphysiol.1952.sp004764.

Hoffman, P. and Morcom, A. M. (2018). Age-related changes in the neural networks supporting semantic cognition: A meta-analysis of 47 functional neuroimaging studies. *Neuroscience & Biobehavioral Reviews*, 84:134–150. https://doi.org/10.1016/j.neubiorev.2017.11.010.

Holderbaum, C. S. (2019). A systematic review of brain imaging studies of semantic priming. *Interacao Em Psicologia*, 23(2):197–207. https://doi.org/10.5380/psi.v23i02.58553.

Holmes, C. J., Hoge, R., Collins, L., Woods, R., Toga, A. W., and Evans, A. C. (1998). Enhancement of mr images using registration for signal averaging. *Journal of computer assisted tomography*, 22(2):324–333.

Hsiao, F. J., Cheng, C. H., Liao, K. K., and Lin, Y. Y. (2010). Cortico-cortical phase synchrony in auditory mismatch processing. *Biological psychology*, 84(2):336–345. https://doi.org/10.1016/j.biopsycho.2010.03.019.

Hsu, C. H., Lin, S. K., Hsu, Y. Y., and Lee, C. Y. (2014). The neural generators of the mismatch responses to mandarin lexical tones: an meg study. *Brain research*, 1582:154–166. https://doi.org/10.1016/j.brainres.2014.07.023.

Huang, Y., Parra, L. C., and Haufe, S. (2016). The New York Head—A precise standardized volume conductor model for EEG source localization and tES targeting. *NeuroImage*, 140:150–162. https://doi.org/10.1016/j.neuroimage.2015.12.019.

Hyvarinen, A. (1999). Fast and robust fixed-point algorithms for independent component analysis. *IEEE transactions on Neural Networks*, 10(3):626–634. https://doi.org/10.1109/72.761722.

Jackson, A. F. and Bolger, D. J. (2014). The neurophysiological bases of eeg and eeg measurement: A review for the rest of us. *Psychophysiology*, 51(11):1061–1071. https://doi.org/10.1111/psyp.12283.

Jackson, R. L. (2021). The neural correlates of semantic control revisited. *Neuroimage*, 224:117444. https://doi.org/10.1016/j.neuroimage.2020.117444.

Jatoi, M. A., Kamel, N., Malik, A. S., and Faye, I. (2014). Eeg based brain source localization comparison of sloreta and eloreta. *Australasian physical & engineering sciences in medicine*, 37(4):713–721. https://doi.org/10.1007/s13246-014-0308-3.

Jefferies, E. (2013). The neural basis of semantic cognition: converging evidence from neuropsychology. *neuroimaging and TMS. Cortex*, 49(3):611–625. https://doi.org/10.1016/j.cortex.2012.10.008.

Jemel, B., Achenbach, C., Müller, B. W., Röpcke, B., and Oades, R. D. (2002). Mismatch negativity results from bilateral asymmetric dipole sources in the frontal and temporal lobes. *Brain topography*, 15(1):13–27. https://doi.org/10.1023/a:1019944805499.

Jeon, Y.-W. and Polich, J. (2003). Meta-analysis of p300 and schizophrenia: Patients, paradigms, and practical implications. *Psychophysiology*, 40(5):684–701. https://doi.org/10.1111/1469-8986.00070.

Joshi, R., Goel, P., Sur, M., and Murthy, H. A. (2018). Single trial p300 classification using convolutional lstm and deep learning ensembles method. In *International Conference on Intelligent Human Computer Interaction*, pages 3–15. Springer. https://doi.org/10.1007/978-3-030-04021-5_1.

Justen, C. and Herbert, C. (2018). The spatio-temporal dynamics of deviance and target detection in the passive and active auditory oddball paradigm: a sloreta study. *BMC neuroscience*, 19:1–18. https://doi.org/10.1186/s12868-018-0422-3.

Khachatryan, E., Wittevrongel, B., Fahimi Hnazaee, M., Carrette, E., Dauwe, I., Meurs, A., Boon, P., and Van Hulle, M. (2019). Semantic and perceptual priming activate partially overlapping brain networks as revealed by direct cortical recordings in humans. *Neuroimage*, 203:116204. https://doi.org/10.1016/j.neuroimage.2019.116204.

Khateb, A., Pegna, A. J., Landis, T., Mouthon, M. S., and Annoni, J. M. (2010). On the origin of the n400 effects: an erp waveform and source localization analysis in three matching tasks. *Brain Topography*, 23(3):311–320. https://doi.org/10.1007/s10548-010-0149-7.

Kiesel, A., Miller, J., Jolicœur, P., and Brisson, B. (2008). Measurement of erp latency differences: A comparison of single-participant

and jackknife-based scoring methods. *Psychophysiology*, 45(2):250–274. https://doi.org/10.1111/j.1469-8986.2007.00618.x.

Kim, M., Cho, K. I., Yoon, Y. B., Lee, T. Y., and Kwon, J. S. (2017). Aberrant temporal behavior of mismatch negativity generators in schizophrenia patients and subjects at clinical high risk for psychosis. *Clinical neurophysiology : official journal of the International Federation of Clinical Neurophysiology*, 128(2):331–339. https://doi.org/10.1016/j.clinph.2016.11.027.

Kiran, S. and Thompson, C. K. (2019). Neuroplasticity of language networks in aphasia: Advances, updates, and future challenges. *Frontiers in neurology*, 10:295. https://doi.org/10.3389/fneur.2019.00295.

Kircher, T., Sass, K., Sachs, O., and Krach, S. (2009). Priming words with pictures: neural correlates of semantic associations in a cross-modal priming task using fmri. *Human Brain Mapping*, 30(12):4116–4128. https://doi.org/10.1002/hbm.20833.

Klimesch, W. (2012). Alpha-band oscillations, attention, and controlled access to stored information. *Trends in cognitive sciences*, 16(12):606–617. https://doi.org/10.1016/j.tics.2012.10.007.

Kobayashi, K., Yoshinaga, H., Oka, M., Ohtsuka, Y., and Gotman, J. (2003). A simulation study of the error in dipole source localization for EEG spikes with a realistic head model. *Clinical Neurophysiology*, 114(6):1069–1078. https://doi.org/10.1016/S1388-2457(03)00064-6.

Kok, A. (2001). On the utility of p3 amplitude as a measure of processing capacity. *Psychophysiology*, 38(3):557–577. https://doi.org/10.1017/s0048577201990559.

Kornblith, S. and Tsao, D. Y. (2017). How thoughts arise from sights: inferotemporal and prefrontal contributions to vision. *Current Opinion in Neurobiology*, 46:208–218. https://doi.org/10.1016/j.conb.2017.08.016.

Koshiyama, D., Miyakoshi, M., Joshi, Y. B., Molina, J. L., Tanaka-Koshiyama, K., Sprock, J., Braff, D. L., Swerdlow, N. R., and Light, G. A. (2020). Abnormal effective connectivity underlying auditory mismatch negativity impairments in schizophrenia. biological psychiatry. *Cognitive neuroscience and neuroimaging*, 5(11):1028–1039. https://doi.org/10.1016/j.bpsc.2020.05.011.

Krishna, S., Choudhury, A., Seo, K., Ni, L., Kakaizada, S., Lee, A., Aabedi, A., Cao, C., Sudharshan, R., Egladyous, A., et al. (2021). Glioblastoma remodeling of neural circuits in the human brain decreases survival. *BioRxiv*, pages 2021–02. https://doi.org/10.1038/s41586-023-06036-1.

Kujala, J., Vartiainen, J., Laaksonen, H., and Salmelin, R. (2012). Neural interactions at the core of phonological and semantic priming of written words. *Cerebral Cortex*, 22(10):2305–2312. https://doi.org/10.1093/cercor/bhr307.

Kujala, T., Tervaniemi, M., and Schröger, E. (2007). The mismatch negativity in cognitive and clinical neuroscience: theoretical and methodological considerations. *Biological psychology*, 74(1):1–19. https://doi.org/10.1016/j.biopsycho.2006.06.001.

Kulkarni, N. and Bairagi, V. (2018). *EEG-based diagnosis of alzheimer disease: a review and novel approaches for feature extraction and classification techniques*. Academic Press. https://doi.org/10.1016/C2017-0-00543-8.

Kutas, M. and Federmeier, K. D. (2000). Electrophysiology reveals semantic memory use in language comprehension. *Trends in Cognitive Sciences*, 4(12):463–470. https://doi.org/10.1016/s1364-6613(00)01560-6.

Kutas, M. and Federmeier, K. D. (2011). Thirty years and counting: finding meaning in the n400 component of the event-related brain potential (erp). *Annual Review of Psychology*, 62:621–647. https://doi.org/10.1146/annurev.psych.093008.131123.

Kutas, M. and Van Petten, C. K. (1994). Psycholinguistics electrified. In *Eds. Traxler, M. J., & Gernsbacher, M. A.) Handbook of Psycholinguistics*. Academic Press.

Lam, N. H., Schoffelen, J.-M., Uddén, J., Hultén, A., and Hagoort, P. (2016). Neural activity during sentence processing as reflected in theta, alpha, beta, and gamma oscillations. *NeuroImage*, 142:43–54. https://doi.org/10.1016/j.neuroimage.2016.03.007.

Latikka, J. and Eskola, H. (2019). The resistivity of human brain tumours in vivo. *Annals of biomedical engineering*, 47:706–713. https://doi.org/10.1007/s10439-018-02189-7.

Lau, E. F., Gramfort, A., Hämäläinen, M. S., and Kuperberg, G. R. (2013). Automatic semantic facilitation in anterior temporal cortex revealed through multimodal neuroimaging. *Journal of Neuroscience*, 33(43):17174–17181. https://doi.org/10.1523/jneurosci.1018-13.2013.

Lau, E. F., Phillips, C., and Poeppel, D. (2008). A cortical network for semantics: (de)constructing the n400. *Nature Reviews Neuroscience*, 9(12):920–933. https://doi.org/10.1038/nrn2532.

Lau, E. F., Weber, K., Gramfort, A., Hämäläinen, M. S., and Kuperberg, G. R. (2016). Spatiotemporal signatures of lexical-semantic prediction. *Cerebral Cortex*, 26(4):1377–1387. https://doi.org/10.1093/cercor/bhu219.

Lawhern, V. J., Solon, A. J., Waytowich, N. R., Gordon, S. M., Hung, C. P., and Lance, B. J. (2018). Eegnet: a compact convolutional neural network for eeg-based brain–computer interfaces. *Journal of neural engineering*, 15(5):056013. https://doi.org/10.1088/1741-2552/aace8c.

Le, T. H., Pardo, J. V., and Hu, X. (1998). 4 t-fmri study of nonspatial shifting of selective attention: cerebellar and parietal contributions. *Journal of neurophysiology*, 79(3):1535–1548. https://doi.org/10.1152/jn.1998.79.3.1535.

Lee, C. L. and Federmeier, K. D. (2009). Wave-ering: an erp study of syntactic and semantic context effects on ambiguity resolution for noun/verb homographs. *Journal of Memory and Language*, 61(4):538–555. https://doi.org/10.1016/j.jml.2009.08.003.

Lee, T.-W., Girolami, M., and Sejnowski, T. J. (1999). Independent component analysis using an extended infomax algorithm for mixed subgaussian and supergaussian sources. *Neural computation*, 11(2):417–441. https://doi.org/10.1162/089976699300016719.

Leech, R. and Sharp, D. J. (2014). The role of the posterior cingulate cortex in cognition and disease. *Brain*, 137(1):12–32. https://doi.org/10.1093/brain/awt162.

Levänen, S., Ahonen, A., Hari, R., McEvoy, L., and Sams, M. (1996). *Deviant auditory stimuli activate human left and right auditory cortex differently. Cerebral cortex*. , 6(2), 288-296, New York, N. Y. 1991.

Lewis, A. G. and Bastiaansen, M. (2015). A predictive coding framework for rapid neural dynamics during sentence-level language comprehension. *Cortex*, 68:155–168. https://doi.org/10.1016/j.cortex.2015.02.014.

Li, F., Chen, B., Li, H., Zhang, T., Wang, F., Jiang, Y., Li, P., Ma, T., Zhang, R., Tian, Y., Liu, T., Guo, D., Yao, D., and Xu, P. (2016). The time-varying networks in p300: A task-evoked eeg study. *IEEE transactions on neural systems and rehabilitation engineering : a publication of the IEEE Engineering in Medicine and Biology Society*, 24(7):725–733. https://doi.org/10.1109/tnsre.2016.2523678.

Li, F., Wang, J., Liao, Y., Yi, C., Jiang, Y., Si, Y., Peng, W., Yao, D., Zhang, Y., Dong, W., and Xu, P. (2019a). Differentiation of schizophrenia by combining the spatial eeg brain network patterns of rest and task p300. *IEEE transactions on neural systems and rehabilitation engineering : a publication of the IEEE Engineering in Medicine and Biology Society*, 27(4):594–602. https://doi.org/10.1109/tnsre.2019.2900725.

Li, Q., Liu, G., Yuan, G., Wang, G., Wu, Z., and Zhao, X. (2019b). Single-trial eeg-fmri reveals the generation process of the mismatch negativity. *Frontiers in human neuroscience*, 13:168. https://doi.org/10.3389/fnhum.2019.00168.

Li, R., Mukadam, N., and Kiran, S. (2022). Functional mri evidence for reorganization of language networks after stroke. *Handbook of Clinical Neurology*, 185:131–150. https://doi.org/10.1016/B978-0-12-823384-9.00007-4.

Lin, F.-H., Witzel, T., Ahlfors, S. P., Stufflebeam, S. M., Belliveau, J. W., and Hämäläinen, M. S. (2006). Assessing and improving the spatial accuracy in meg source localization by depth-weighted minimum-norm estimates. *Neuroimage*, 31(1):160–171. https://doi.org/10.1016/j.neuroimage.2005.11.054.

Lindau, M., Jelic, V., Johansson, S.-E., Andersen, C., Wahlund, L.-O., and Almkvist, O. (2003). Quantitative eeg abnormalities and cognitive dysfunctions in frontotemporal dementia and alzheimer's disease. *Dementia and geriatric cognitive disorders*, 15(2):106–114. https://doi.org/10.1159/000067973.

Linden, D. E. (2005). The p300: where in the brain is it produced and what does it tell us? the neuroscientist : a review journal bringing neurobiology. *neurology and psychiatry*, 11(6):563–576. https://doi.org/10.1177/1073858405280524.

Linden, D. E. J., Prvulovic, D., Formisano, E., Völlinger, M., Zanella, F. E., Goebel, R., and Dierks, T. (1999). The functional neuroanatomy of target detection: An fmri study of visual and auditory oddball tasks. *Cerebral Cortex*, 9(8):815–823. https://doi.org/10.1093/cercor/9.8.815.

Liu, C., Downey, R. J., Mu, Y., Richer, N., Hwang, J., Shah, V. A., Sato, S. D., Clark, D. J., Hass, C. J., Manini, T. M., Seidler, R. D., and Ferris, D. P. (2023). Comparison of eeg source localization using simplified and anatomically accurate head models in younger and older adults. *IEEE Transactions on Neural Systems and Rehabilitation Engineering*, 31:2591–2602. https://doi.org/10.1109/TNSRE.2023.3281356.

Lok, E., Clark, M., Liang, O., Malik, T., Koo, S., and Wong, E. T. (2023). Modulation of tumor-treating fields by cerebral edema from brain tumors. *Advances in Radiation Oncology*, 8(1):101046. https://doi.org/10.1016/j.adro.2022.101046.

Luck, S. J. (2014). *An introduction to the event-related potential technique*. MIT press.

MacDonald, S. W., Nyberg, L., Sandblom, J., Fischer, H., and Bäckman, L. (2008). Increased response-time variability is associated with reduced inferior parietal activation during episodic recognition in aging. *Journal of Cognitive Neuroscience*, 20(5):779–786. https://doi.org/10.1162/jocn.2008.20502.

MacLean, S. E. and Ward, L. M. (2014). Temporo-frontal phase synchronization supports hierarchical network for mismatch negativity. *Clinical neurophysiology : official journal of the International Federation of Clinical Neurophysiology*, 125(8):1604–1617. https://doi.org/10.1016/j.clinph.2013.12.109.

MacLean, S. E. and Ward, L. M. (2016). Oscillatory power and functional connectivity in the speech change detection network. *Neuropsychologia*, 89:320–334. https://doi.org/10.1016/j.neuropsychologia.2016.06.039.

Maddula, R., Stivers, J., Mousavi, M., Ravindran, S., and de Sa, V. (2017). Deep recurrent convolutional neural networks for classifying p300 bci signals. *GBCIC*, 201.

Makeig, S., Westerfield, M., Jung, T.-P., Enghoff, S., Townsend, J., Courchesne, E., and Sejnowski, T. J. (2002). Dynamic brain

sources of visual evoked responses. *Science*, 295(5555):690–694. https://doi.org/10.1126/science.106616.

Maki, H., Toda, T., Sakti, S., Neubig, G., and Nakamura, S. (2015). Eeg signal enhancement using multi-channel wiener filter with a spatial correlation prior. In *2015 IEEE International Conference on Acoustics, Speech and Signal Processing (ICASSP)*, pages 2639–2643. IEEE. https://doi.org/10.1109/ICASSP.2015.7178449.

Malmivuo, J. and Plonsey, R. (1995). *Bioelectromagnetism. 13. Electroencephalography*.

Marco-Pallarés, J., Grau, C., and Ruffini, G. (2005). Combined ica-loreta analysis of mismatch negativity. *NeuroImage*, 25(2):471–477. https://doi.org/10.1016/j.neuroimage.2004.11.028.

Marieb, E. N. and Hoehn, K. N. (2015). *Human Anatomy & Physiology*. Pearson, 10th, global edition.

Maris, E. and Oostenveld, R. (2007). Nonparametric statistical testing of eeg- and meg-data. *Journal of neuroscience methods*, 164(1):177–190. https://doi.org/10.1016/j.jneumeth.2007.03.024.

Mark F. Bear, Barry W. Connors, M. A. P. (2006). *Neuroscience: Exploring the Brain*. Lippincott Williams & Wilkins, third edition.

Matsumoto, A. and Kakigi, R. (2014). Subliminal semantic priming changes the dynamic causal influence between the left frontal and temporal cortex. *Journal of Cognitive Neuroscience*, 26(1):165–174. https://doi.org/10.1162/jocn_a_00472.

Mazaheri, A. and Jensen, O. (2008). Asymmetric amplitude modulations of brain oscillations generate slow evoked responses. *Journal of Neuroscience*, 28(31):7781–7787. https://doi.org/10.1523/JNEUROSCI.1631-08.2008.

Mazaheri, A. and Jensen, O. (2010). Rhythmic pulsing: linking ongoing brain activity with evoked responses. *Frontiers in human neuroscience*, 4:177. https://doi.org/10.3389/fnhum.2010.00177.

Mazaheri, A., van Schouwenburg, M. R., Dimitrijevic, A., Denys, D., Cools, R., and Jensen, O. (2014). Region-specific modulations in oscillatory alpha activity serve to facilitate processing in the visual and auditory modalities. *Neuroimage*, 87:356–362. https://doi.org/10.1016/j.neuroimage.2013.10.052.

Mazziotta, J., Toga, A., Evans, A., Fox, P., Lancaster, J., Zilles, K., Woods, R., Paus, T., Simpson, G., Pike, B., et al. (2001). A probabilistic atlas and reference system for the human brain: International consortium for brain mapping (icbm). *Philosophical Transactions of the Royal Society of London. Series B: Biological Sciences*, 356(1412):1293–1322. https://doi.org/10.1098/rstb.2001.0915.

McCann, H., Pisano, G., and Beltrachini, L. (2019). Variation in reported human head tissue electrical conductivity values. *Brain topography*, 32:825–858. https://doi.org/10.1007/s10548-019-00710-2.

McNamara, T. P. (2005). *Semantic priming*. Psychology Press. https://doi.org/10.4324/9780203338001.

Medani, T., Garcia-Prieto, J., Tadel, F., Antonakakis, M., Erdbrügger, T., Höltershinken, M., Mead, W., Schrader, S., Joshi, A., Engwer, C., Wolters, C. H., Mosher, J. C., and Leahy, R. M. (2023). Brainstorm-duneuro: An integrated and user-friendly finite element method for modeling electromagnetic brain activity. *NeuroImage*, 267:119851. https://doi.org/10.1016/j.neuroimage.2022.119851.

Mégevand, P. and Seeck, M. (2020). Electric source imaging for presurgical epilepsy evaluation: current status and future prospects. *Expert Review of Medical Devices*, 17(5):405–412. https://doi.org/10.1080/17434440.2020.1748008.

Michel, C. M. and Brunet, D. (2019). EEG Source Imaging: A Practical Review of the Analysis Steps. *Frontiers in Neurology*, 10:325. https://doi.org/10.3389/fneur.2019.00325.

Mirman, D., Landrigan, J. F., and Britt, A. E. (2017). Taxonomic and thematic semantic systems. *Psychological Bulletin*, 143(5):499–520. https://doi.org/10.1037/bul0000092.

Molholm, S., Martinez, A., Ritter, W., Javitt, D. C., and Foxe, J. J. (2005). *The neural circuitry of pre-attentive auditory change-detection*. , 15(5), 545-551, New York, N. Y. 1991.

Montes-Restrepo, V., Carrette, E., Strobbe, G., Gadeyne, S., Vandenberghe, S., Boon, P., Vonck, K., and van Mierlo, P. (2016). The Role of Skull Modeling in EEG Source Imaging for Patients with Refractory Temporal Lobe Epilepsy.

Brain Topography, 29(4):572–589. https://doi.org/10.1007/s10548-016-0482-6.

Montes-Restrepo, V., van Mierlo, P., Strobbe, G., Staelens, S., Vandenberghe, S., and Hallez, H. (2014). Influence of Skull Modeling Approaches on EEG Source Localization. *Brain Topography*, 27(1):95–111. https://doi.org/10.1007/s10548-013-0313-y.

Moores, K. A., Clark, C. R., Hadfield, J. L., Brown, G. C., Taylor, D. J., Fitzgibbon, S. P., Lewis, A. C., Weber, D. L., and Greenblatt, R. (2003). Investigating the generators of the scalp recorded visuo-verbal p300 using cortically constrained source localization. *Human brain mapping*, 18(1):53–77. https://doi.org/10.1002/hbm.10073.

Mosher, J. and Leahy, R. (1999). Source localization using recursively applied and projected (rap) music. *IEEE Transactions on Signal Processing*, 47(2):332–340. https://doi.org/10.1109/78.740118.

Moss, H. E., Abdallah, S., Fletcher, P., Bright, P., Pilgrim, L., Acres, K., and Tyler, L. K. (2005). Selecting among competing alternatives: selection and retrieval in the left inferior frontal gyrus. *Cerebral Cortex*, 15(11):1723–1735. https://doi.org/10.1093/cercor/bhi049.

Möucks, J., Köuhler, W., Gasser, T., and Pham, D. T. (1988). Novel approaches to the problem of latency jitter. *Psychophysiology*, 25(2):217–226. https://doi.org/10.1111/j.1469-8986.1988.tb00992.x.

Müller, M. (2007). Dynamic time warping. *Information retrieval for music and motion*, pages 69–84. https://doi.org/10.1007/978-3-540-74048-3_4.

Murray, J. G., Ouyang, G., and Donaldson, D. I. (2019). Compensation of trial-to-trial latency jitter reveals the parietal retrieval success effect to be both variable and thresholded in older adults. *Frontiers in Aging Neuroscience*, 11:179. https://doi.org/10.3389/fnagi.2019.00179.

Murray, M. M., Brunet, D., and Michel, C. M. (2008). Topographic erp analyses: a step-by-step tutorial review. *Brain topography*, 20(4):249–264. https://doi.org/10.1007/s10548-008-0054-5.

Näätänen, R., Gaillard, A. W., and Mäntysalo, S. (1978). Early selective-attention effect on evoked potential reinterpreted. *Acta psychologica*, 42(4):313–329. https://doi.org/10.1016/0001-6918(78)90006-9.

Näätänen, R., Kujala, T., Escera, C., Baldeweg, T., Kreegipuu, K., Carlson, S., and Ponton, C. (2012). The mismatch negativity (mmn)-a unique window to disturbed central auditory processing in ageing and different clinical conditions. *Clinical neurophysiology : official journal of the International Federation of Clinical Neurophysiology*, 123(3):424–458. https://doi.org/10.1016/j.clinph.2011.09.020.

Näätänen, R., Lehtokoski, A., Lennes, M., Cheour, M., Huotilainen, M., Iivonen, A., Vainio, M., Alku, P., Ilmoniemi, R. J., Luuk, A., Allik, J., Sinkkonen, J., and Alho, K. (1997). Language-specific phoneme representations revealed by electric and magnetic brain responses. *Nature*, 385(6615):432–434. https://doi.org/10.1038/385432a0.

Nasreddine, Z. S., Phillips, N. A., Bédirian, V., Charbonneau, S., Whitehead, V., Collin, I., Cummings, J. L., and Chertkow, H. (2005). The montreal cognitive assessment, moca: a brief screening tool for mild cognitive impairment. *Journal of the American Geriatrics Society*, 53(4):695–699. https://doi.org/10.1111/j.1532-5415.2005.53221.x.

Neugebauer, F., Möddel, G., Rampp, S., Burger, M., and Wolters, C. H. (2017). The Effect of Head Model Simplification on Beamformer Source Localization. *Frontiers in Neuroscience*, 11:625. https://doi.org/10.3389/fnins.2017.00625.

Nieberlein, L., Rampp, S., Gussew, A., Prell, J., and Hartwigsen, G. (2023). Reorganization and plasticity of the language network in patients with cerebral gliomas. *NeuroImage: Clinical*, 37:103326. https://doi.org/10.1016/j.nicl.2023.103326.

Nielsen, J. D., Puonti, O., Xue, R., Thielscher, A., and Madsen, K. H. (2023). Evaluating the influence of anatomical accuracy and electrode positions on eeg forward solutions. *NeuroImage*, 277:120259. https://doi.org/10.1016/j.neuroimage.2023.120259.

Nikulin, V. V., Linkenkaer-Hansen, K., Nolte, G., and Curio, G. (2010). Non-zero mean and asymmetry of neuronal oscillations have different implications for evoked responses. *Clinical Neurophysiology*, 121(2):186–193. https://doi.org/10.1016/j.clinph.2009.09.028.

Nishida, K., Yoshimura, M., Isotani, T., Yoshida, T., Kitaura, Y., Saito, A., Mii, H., Kato, M., Takekita, Y., Suwa, A., et al. (2011). Differences in

quantitative eeg between frontotemporal dementia and alzheimer's disease as revealed by loreta. *Clinical Neurophysiology*, 122(9):1718–1725. https://doi.org/10.1016/j.clinph.2011.02.011.

Noll, K. R., Sullaway, C., Ziu, M., Weinberg, J. S., and Wefel, J. S. (2015). Relationships between tumor grade and neurocognitive functioning in patients with glioma of the left temporal lobe prior to surgical resection. *Neuro-oncology*, 17(4):580–587. https://doi.org/10.1093/neuonc/nou233.

Noppeney, U., Phillips, J., and Price, C. (2004). The neural areas that control the retrieval and selection of semantics. *Neuropsychologia*, 42(9):1269–1280. https://doi.org/10.1016/j.neuropsychologia.2003.12.014.

O'Hare, A. J., Dien, J., Waterson, L. D., and Savage, C. R. (2008). Activation of the posterior cingulate by semantic priming: a co-registered erp/fmri study. *Brain Research*, 1189:97–114. https://doi.org/10.1016/j.brainres.2007.10.095.

Onton, J., Westerfield, M., Townsend, J., and Makeig, S. (2006). Imaging human eeg dynamics using independent component analysis. *Neuroscience & biobehavioral reviews*, 30(6):808–822. https://doi.org/10.1016/j.neubiorev.2006.06.007.

Oostenveld, R., Fries, P., Maris, E., and Schoffelen, J.-M. (2011). Fieldtrip: open source software for advanced analysis of meg, eeg, and invasive electrophysiological data. *Computational intelligence and neuroscience*, 2011(1):156869. https://doi.org/10.1155/2011/156869.

Opitz, B., Rinne, T., Mecklinger, A., von Cramon, D. Y., and Schröger, E. (2002). Differential contribution of frontal and temporal cortices to auditory change detection: fmri and erp results. *NeuroImage*, 15(1):167–174. https://doi.org/10.1006/nimg.2001.0970.

Ouyang, G., Hildebrandt, A., Sommer, W., and Zhou, C. (2017). Exploiting the intra-subject latency variability from single-trial event-related potentials in the p3 time range: a review and comparative evaluation of methods. *Neuroscience & Biobehavioral Reviews*, 75:1–21. https://doi.org/10.1016/j.neubiorev.2017.01.023.

Ouyang, G., Sommer, W., and Zhou, C. (2016). Reconstructing erp amplitude effects after compensating for trial-to-trial latency jitter: a solution based on a novel application of residue iteration

decomposition. *International Journal of Psychophysiology*, 109:9–20. https://doi.org/10.1016/j.ijpsycho.2016.09.015.

Palmer, J. A., Kreutz-Delgado, K., and Makeig, S. (2012). Amica: An adaptive mixture of independent component analyzers with shared components. *Swartz Center for Computatonal Neursoscience, University of California San Diego, Tech. Rep*.

Partanen, E., Vainio, M., Kujala, T., and Huotilainen, M. (2011). Linguistic multifeature mmn paradigm for extensive recording of auditory discrimination profiles. *Psychophysiology*, 48(10):1372–1380. https://doi.org/10.1111/j.1469-8986.2011.01214.x.

Pascual-Marqui, R., Faber, P., Kinoshita, T., Kochi, K., Miltz, P., Nishida, K., and Yoshimura, M. (2018). Comparing eeg/meg neuroimaging methods based on localization error, false positive activity, and false positive connectivity. https://doi.org/10.1101/269753.

Pascual-Marqui, R. D. (2002). Standardized low-resolution brain electromagnetic tomography (sLORETA): technical details. *Methods and findings in experimental and clinical pharmacology*, 24 Suppl D(Suppl D):5–12.

Pascual-Marqui, R. D., Lehmann, D., Koukkou, M., Kochi, K., Anderer, P., Saletu, B., Tanaka, H., Hirata, K., John, E. R., Prichep, L., Biscay-Lirio, R., and Kinoshita, T. (2011). Assessing interactions in the brain with exact low-resolution electromagnetic tomography. *Philosophical Transactions of the Royal Society A: Mathematical, Physical and Engineering Sciences*, 369(1952):3768–3784. https://doi.org/10.1098/rsta.2011.0081.

Pascual-Marqui, R. D., Michel, C. M., and Lehmann, D. (1994). Low resolution electromagnetic tomography: a new method for localizing electrical activity in the brain. *International Journal of psychophysiology*, 18(1):49–65. https://doi.org/10.1016/0167-8760(84)90014-X.

Pascucci, D., Rubega, M., and Plomp, G. (2020). Modeling time-varying brain networks with a self-tuning optimized Kalman filter. *PLOS Computational Biology*, 16(8):e1007566. https://doi.org/10.1371/journal.pcbi.1007566.

Pascucci, D., Tourbier, S., Rué-Queralt, J., Carboni, M., Hagmann, P., and Plomp, G. (2022). Source imaging of high-density visual evoked potentials with multi-scale brain parcellations and connectomes. *Scientific Data*, 9(1):9. https://doi.org/10.1038/s41597-021-01116-1.

Pasquini, L., Di Napoli, A., Rossi-Espagnet, M. C., Visconti, E., Napolitano, A., Romano, A., Bozzao, A., Peck, K. K., and Holodny, A. I. (2022). Understanding language reorganization with neuroimaging: how language adapts to different focal lesions and insights into clinical applications. *Frontiers in human neuroscience*, 16:747215. https://doi.org/10.3389/fnhum.2022.747215.

Patterson, K. and Lambon Ralph, M. A. (2016). The hub-and-spoke hypothesis of semantic memory. In Hickok, G. and Smalls, S. L., editors, *The neurobiology of language*, pages 765–775. Academic Press. https://doi.org/10.1016/C2011-0-07351-9.

Pawlowski, G. M., Ghosh-Hajra, S., Fickling, S. D., Liu, C. C., Song, X., Robinovitch, S., others, and D'Arcy, R. C. (2019). Brain vital signs: expanding from the auditory to visual modality. *Frontiers in Neuroscience*, 12:968. https://doi.org/10.3389/fnins.2018.00968.

Pellegrini, F., Delorme, A., Nikulin, V., and Haufe, S. (2023). Identifying good practices for detecting inter-regional linear functional connectivity from eeg. *NeuroImage*, 277:120218. https://doi.org/10.1016/j.neuroimage.2023.120218.

Peng, W., Hu, L., Zhang, Z., and Hu, Y. (2012). Causality in the association between p300 and alpha event-related desynchronization. *PloS one*, 7(4):e34163. https://doi.org/10.1371/journal.pone.0034163.

Petrides, M. and Pandya, D. N. (2004). The frontal cortex. In Paxinos, G. and Mai, J. K., editors, *The human nervous system*, pages 950–972. Academic Press, 2 edition. https://doi.org/10.1016/B978-0-12-547626-3.X5000-5.

Pettigrew, C., Murdoch, B. E., Chenery, H. J., and Kei, J. (2004). The relationship between the mismatch negativity (mmn) and psycholinguistic models of spoken word processing. *Aphasiology*, 18(1):3–28. https://doi.org/10.1080/02687030344000463.

Piai, V., Oostenveld, R., Schoffelen, J. M., and Piastra, M. C. (2024). The impact of csf-filled cavities on scalp eeg and its implications. *Psychophysiology*, 61(10):e14624. https://doi.org/10.1111/psyp.14624.

Piastra, M. C., Oostenveld, R., Schoffelen, J. M., and Piai, V. (2022). Estimating the influence of stroke lesions on meg source reconstruction. *NeuroImage*, 260:119422. https://doi.org/10.1016/j.neuroimage.2022.119422.

Polich, J. (2007). Updating p300: an integrative theory of p3a and p3b. *Clinical neurophysiology : official journal of the International Federation of Clinical Neurophysiology*, 118(10):2128–2148. https://doi.org/10.1016/j.clinph.2007.04.019.

Polich, J. (2012). Neuropsychology of p300.

Polich, J., Ladish, C., and Burns, T. (1990). Normal variation of p300 in children: age, memory span, and head size. *International Journal of Psychophysiology*, 9(3):237–248. https://doi.org/10.1016/0167-8760(90)90056-J.

Pulvermüller, F. (2001). Brain reflections of words and their meaning. *Trends in cognitive sciences*, 5(12):517–524. https://doi.org/10.1016/s1364-6613(00)01803-9.

Puonti, O., Van Leemput, K., Saturnino, G. B., Siebner, H. R., Madsen, K. H., and Thielscher, A. (2020). Accurate and robust whole-head segmentation from magnetic resonance images for individualized head modeling. *NeuroImage*, 219:117044. https://doi.org/10.1016/j.neuroimage.2020.117044.

Rahimpour, S., Haglund, M. M., Friedman, A. H., and Duffau, H. (2019). History of awake mapping and speech and language localization: from modules to networks. *Neurosurgical focus*, 47(3):E4. https://doi.org/10.3171/2019.7.FOCUS19347.

Ralph, M. A., Jefferies, E., Patterson, K., and Rogers, T. T. (2017). The neural and computational bases of semantic cognition. *Nature Reviews Neuroscience*, 18(1):42–55. https://doi.org/10.1038/nrn.2016.150.

Rinne, T., Degerman, A., and Alho, K. (2005). Superior temporal and inferior frontal cortices are activated by infrequent sound duration decrements: an fmri study. *NeuroImage*, 26(1):66–72. https://doi.org/10.1016/j.neuroimage.2005.01.017.

Roehm, D., Bornkessel-Schlesewsky, I., and Schlesewsky, M. (2007). *The internal structure of the N400: Frequency characteristics of a language related ERP component*. Nova Science Publishers Inc.

Rossi, A. F., Pessoa, L., Desimone, R., and Ungerleider, L. G. (2009). The prefrontal cortex and the executive control of attention. *Experimental brain research*, 192(3):489–497. https://doi.org/10.1007/s00221-008-1642-z.

Rossini, P. M., Rossi, S., Babiloni, C., and Polich, J. (2007). Clinical neurophysiology of aging brain: from normal aging to neurodegeneration. *Progress in neurobiology*, 83(6):375–400. https://doi.org/10.1016/j.pneurobio.2007.07.010.

Rossion, B. and Jacques, C. (2012). The N170: Understanding the Time Course of Face Perception in the Human Brain. *The Oxford Handbook of Event-Related Potential Components*, pages 115–142. https://doi.org/10.1093/oxfordhb/9780195374148.013.0064.

Roth, A., Roesch-Ely, D., Bender, S., Weisbrod, M., and Kaiser, S. (2007). Increased event-related potential latency and amplitude variability in schizophrenia detected through wavelet-based single trial analysis. *International Journal of Psychophysiology*, 66(3):244–254. https://doi.org/10.1016/j.ijpsycho.2007.08.005.

Rubega, M., Pascucci, D., Queralt, J. R., Van Mierlo, P., Hagmann, P., Plomp, G., and Michel, C. (2019). Time-varying effective EEG source connectivity: the optimization of model parameters. *2019 41st Annual International Conference of the IEEE Engineering in Medicine and Biology Society (EMBC)*, pages 6438–6441. https://doi.org/10.1109/EMBC.2019.8856890.

Sabeti, M., Katebi, S., Rastgar, K., and Azimifar, Z. (2016). A multiresolution approach to localize neural sources of p300 event-related brain potential. *Computer Methods and Programs in Biomedicine*, 133:155–168. https://doi.org/10.1016/j.cmpb.2016.05.013.

Samuelsson, J. G., Peled, N., Mamashli, F., Ahveninen, J., and Hämäläinen, M. S. (2021). Spatial fidelity of MEG/EEG source estimates: A general evaluation approach. *NeuroImage*, 224:117430. https://doi.org/10.1016/j.neuroimage.2020.117430.

Sangal, R. B., Sangal, J. M., and Belisle, C. (1998). P300 latency and age: a quadratic regression explains their relationship from age 5 to 85. *Clinical Electroencephalography*, 29(1):1–6. https://doi.org/10.1177/155005949802900105.

Saturnino, G. B., Puonti, O., Nielsen, J. D., Antonenko, D., Madsen, K. H., and Thielscher, A. (2019). Simnibs 2.1: a comprehensive pipeline for individualized electric field modelling for transcranial brain stimulation. *Brain and human body modeling: computational human modeling at EMBC 2018*, pages 3–25. https://doi.org/10.1007/978-3-030-21293-3_1.

Schall, U., Johnston, P., Todd, J., Ward, P. B., and Michie, P. T. (2003). Functional neuroanatomy of auditory mismatch processing: an event-related fmri study of duration-deviant oddballs. *NeuroImage*, 20(2):729–736. https://doi.org/10.1016/s1053-8119(03)00398-7.

Schmahmann, J. D., Smith, E. E., Eichler, F. S., and Filley, C. M. (2008). Cerebral white matter: neuroanatomy, clinical neurology, and neurobehavioral correlates. *Annals of the New York Academy of Sciences*, 1142:266–309. https://doi.org/10.1196/annals.1444.017.

Schmidt, R. (1986). Multiple emitter location and signal parameter estimation. *IEEE transactions on antennas and propagation*, 34(3):276–280.

Schneck, S. M., Entrup, J. L., Duff, M. C., and Wilson, S. M. (2021). Unexpected absence of aphasia following left temporal hemorrhage: a case study with functional neuroimaging to characterize the nature of atypical language localization. *Neurocase*, 27(1):97–105. https://doi.org/10.1080/13554794.2021.1886309.

Schneider, J. M., Abel, A. D., Ogiela, D. A., Middleton, A. E., and Maguire, M. J. (2016). Developmental differences in beta and theta power during sentence processing. *Developmental cognitive neuroscience*, 19:19–30. https://doi.org/10.1016/j.dcn.2016.01.001.

Schneider, J. M. and Maguire, M. J. (2018). Identifying the relationship between oscillatory dynamics and event-related responses. *International Journal of Psychophysiology*, 133:182–192. https://doi.org/10.1016/j.ijpsycho.2018.07.002.

Shestakova, A., Brattico, E., Huotilainen, M., Galunov, V., Soloviev, A., Sams, M., Ilmoniemi, R. J., and Näätänen, R. (2002). Abstract phoneme representations in the left temporal cortex: magnetic mismatch negativity study. *Neuroreport*, 13(14):1813–1816. https://doi.org/10.1097/00001756-200210070-00025.

Shi, X., Chen, Z., Wang, H., Yeung, D.-Y., Wong, W.-K., and Woo, W.-c. (2015). Convolutional lstm network: A machine learning approach for precipitation nowcasting. *arXiv preprint arXiv:1506.04214*. https://doi.org/10.48550/arXiv.1506.04214.

Shokoohi-Yekta, M., Hu, B., Jin, H., Wang, J., and Keogh, E. (2017). Generalizing dtw to the multi-dimensional case requires an adaptive approach. *Data mining and knowledge discovery*, 31(1):1–31. https://doi.org/10.1007/s10618-016-0455-0.

Shriram, R., Sundhararajan, M., and Daimiwal, N. (2013). Eeg based cognitive workload assessment for maximum efficiency. *Int. Organ. Sci. Res. IOSR*, 7:34–38.

Silva-Pereyra, J., Rivera-Gaxiola, M., Aubert, E., Bosch, J., Galán, L., and Salazar, A. (2003). N400 during lexical decision tasks: a current source localization study. *Clinical Neurophysiology*, 114(12):2469–2486. https://doi.org/10.1016/s1388-2457(03)00248-7.

Simoes, C., Jensen, O., Parkkonen, L., and Hari, R. (2003). Phase locking between human primary and secondary somatosensory cortices. *Proceedings of the National Academy of Sciences*, 100(5):2691–2694. https://doi.org/10.1073/pnas.0437944100.

Sörnmo, L. and Laguna, P. (2005). *Bioelectrical signal processing in cardiac and neurological applications*, volume 8. Academic Press. https://doi.org/10.1016/B978-0-12-437552-9.X5000-4.

Sorokin, A., Alku, P., and Kujala, T. (2010). Change and novelty detection in speech and non-speech sound streams. *Brain research*, 1327:77–90. https://doi.org/10.1016/j.brainres.2010.02.052.

Stancák Jr, A. and Pfurtscheller, G. (1996). Event-related desynchronisation of central beta-rhythms during brisk and slow self-paced finger movements of dominant and nondominant hand. *Cognitive brain research*, 4(3):171–183. https://doi.org/10.1016/S0926-6410(96)00031-6.

Steinhauer, K., Royle, P., Drury, J. E., and Fromont, L. A. (2017). The priming of priming: Evidence that the n400 reflects context-dependent post-retrieval word integration in working memory. *Neuroscience Letters*, 651:192–197. https://doi.org/10.1016/j.neulet.2017.05.007.

Stenroos, M. and Hauk, O. (2013). Minimum-norm cortical source estimation in layered head models is robust against skull conductivity error. *NeuroImage*, 81:265–272. https://doi.org/10.1016/j.neuroimage.2013.04.086.

Studenova, A., Forster, C., Engemann, D. A., Hensch, T., Sanders, C., Mauche, N., Hegerl, U., Loffler, M., Villringer, A., and Nikulin, V. (2023). Event-related modulation of alpha rhythm explains the auditory p300-evoked response in eeg. *eLife*, 12. https://doi.org/10.7554/eLife.88367.

Surbeck, W., Hildebrandt, G., and Duffau, H. (2015). The evolution of brain surgery on awake patients. *Acta neurochirurgica*, 157:77–84. https://doi.org/10.1007/s00701-014-2249-8.

Sutton, S., Braren, M., Zubin, J., and John, E. (1965). Evoked-potential correlates of stimulus uncertainty. *Science*, 150(3700):1187–1188. https://doi.org/10.1126/science.150.3700.1187.

Swinburn, K., Porter, G., and Howard, D. (2014). Comprehensive aphasia test nederlandstalige bewerking (cat-nl), (nederlandstalige bewerking door visch-brink, e., vandenborre, d., smet, de. h.j., & mariën, p.).

Tadel, F., Baillet, S., Mosher, J. C., Pantazis, D., and Leahy, R. M. (2011). Brainstorm: A user-friendly application for meg/eeg analysis. *Computational intelligence and neuroscience*, 2011(1):879716. https://doi.org/10.1155/2011/879716.

Takahashi, H., Rissling, A. J., Pascual-Marqui, R., Kirihara, K., Pela, M., Sprock, J., Braff, D. L., and Light, G. A. (2013). Neural substrates of normal and impaired preattentive sensory discrimination in large cohorts of nonpsychiatric subjects and schizophrenia patients as indexed by mmn and p3a change detection responses. *Neuroimage*, 66:594–603. https://doi.org/10.1016/j.neuroimage.2012.09.074.

Tang, J., Yuan, F., Shen, X., Wang, Z., Rao, M., He, Y., Sun, Y., Li, X., Zhang, W., Li, Y., et al. (2019). Bridging biological and artificial neural networks with emerging neuromorphic devices: fundamentals, progress, and challenges. *Advanced materials*, 31(49):1902761. https://doi.org/10.1002/adma.201902761.

Tao, Q., Jiang, L., Li, F., Qiu, Y., Yi, C., Si, Y., Li, C., Zhang, T., Yao, D., and Xu, P. (2022). Dynamic networks of p300-related process. *Cognitive neurodynamics*, 16(5):975–985. https://doi.org/10.1007/s11571-021-09753-3.

Tavenard, R., Faouzi, J., Vandewiele, G., Divo, F., Androz, G., Holtz, C., Payne, M., Yurchak, R., Rußwurm, M., Kolar, K., and Woods, E. (2020). Tslearn, a

machine learning toolkit for time series data. *Journal of Machine Learning Research*, 21(118):1–6. https://doi.org/10.5555/3455716.3455834.

Taylor, M. J., Itier, R. J., Allison, T., and Edmonds, G. E. (2001). Direction of gaze effects on early face processing: eyes-only versus full faces. *Cognitive Brain Research*, 10(3):333–340. https://doi.org/10.1016/S0926-6410(00)00051-3.

Tervaniemi, M., Kujala, A., Alho, K., Virtanen, J., Ilmoniemi, R. J., and Näätänen, R. (1999). Functional specialization of the human auditory cortex in processing phonetic and musical sounds: A magnetoencephalographic (meg) study. *NeuroImage*, 9(3):330–336. https://doi.org/10.1006/nimg.1999.0405.

Thissen, A., Van Bergen, F., De Jonghe, J., Kessels, R., and Dautzenberg, P. (2010). Bruikbaarheid en validiteit van de nederlandse versie van de montreal cognitive assessment (moca-d) bij het diagnosticeren van mild cognitive impairment. *Tijdschrift voor gerontologie en geriatrie*, 41:231–240. https://doi.org/10.1007/s12439-010-0218-0.

Torrence, R. D., Troup, L. J., Rojas, D. C., and Carlson, J. M. (2021). Enhanced contralateral theta oscillations and n170 amplitudes in occipitotemporal scalp regions underlie attentional bias to fearful faces. *International Journal of Psychophysiology*, 165:84–91. https://doi.org/10.1016/j.ijpsycho.2021.04.002.

Tourbier, S., Rue Queralt, J., Glomb, K., Aleman-Gomez, Y., Mullier, E., Griffa, A., Schöttner, M., Wirsich, J., Tuncel, A., Jancovic, J., Bach Cuadra, M., , and Hagmann, P. (2022). connectomicslab/connectomemapper3: Connectome mapper v3.0.0-rc4. https://doi.org/10.5281/zenodo.7249263.

Traut, T., Sardesh, N., Bulubas, L., Findlay, A., Honma, S. M., Mizuiri, D., Berger, M. S., Hinkley, L. B., Nagarajan, S. S., and Tarapore, P. E. (2019). Meg imaging of recurrent gliomas reveals functional plasticity of hemispheric language specialization. *Human brain mapping*, 40(4):1082–1092. MEG imaging of recurrent gliomas reveals functional plasticity of hemispheric language specialization.

Tsolaki, A., Kosmidou, V., Hadjileontiadis, L., Kompatsiaris, I. Y., and Tsolaki, M. (2015). Brain source localization of MMN, P300 and N400: Aging and gender differences. *Brain Research*, 1603:32–49. https://doi.org/10.1016/j.brainres.2014.10.004.

Valdés-Hernández, P. A., Von Ellenrieder, N., Ojeda-Gonzalez, A., Kochen, S., Alemán-Gómez, Y., Muravchik, C., and Valdés-Sosa, P. A. (2009). Approximate average head models for eeg source imaging. *Journal of neuroscience methods*, 185(1):125–132. https://doi.org/10.1016/j.jneumeth.2009.09.005.

van Dijk, H., van der Werf, J., Mazaheri, A., Medendorp, W. P., and Jensen, O. (2010). Modulations in oscillatory activity with amplitude asymmetry can produce cognitively relevant event-related responses. *Proceedings of the National Academy of Sciences*, 107(2):900–905. https://doi.org/10.1073/pnas.0908821107.

van Dinteren, R., Arns, M., Jongsma, M. L., and Kessels, R. P. (2014). P300 development across the lifespan: a systematic review and meta-analysis. *PloS one*, 9(2):e87347. https://doi.org/10.1371/journal.pone.0087347.

van Dinteren, R., Huster, R. J., Jongsma, M. L. A., Kessels, R. P. C., and Arns, M. (2018). Differences in cortical sources of the event-related p3 potential between young and old participants indicate frontal compensation. *Brain topography*, 31(1):35–46. https://doi.org/10.1007/s10548-016-0542-y.

Van Strien, J. (1992). Classificatie van links-en rechtshandige proefpersonen. *Nederlands Tijdschrift voor de Psychologie en haar Grensgebieden*, 47:88–92.

Van Veen, B. D., Van Drongelen, W., Yuchtman, M., and Suzuki, A. (1997). Localization of brain electrical activity via linearly constrained minimum variance spatial filtering. *IEEE Transactions on biomedical engineering*, 44(9):867–880. https://doi.org/10.1109/10.623056.

van Vliet, M., Chumerin, N., De Deyne, S., Wiersema, J. R., Fias, W., Storms, G., and Van Hulle, M. (2016). Single-trial erp component analysis using a spatiotemporal lcmv. *IEEE Transactions on Biomedical Engineering*, 63(1):55–66. https://doi.org/10.1109/TBME.2015.2468588.

Van Vliet, M., Manyakov, N. V., Storms, G., Fias, W., Wiersema, J. R., and Van Hulle, M. M. (2014). Response-related potentials during semantic priming: the effect of a speeded button response task on erps. *PloS one*, 9(2):e87650. https://doi.org/10.1371/journal.pone.0087650.

van Winsun, W., Sergeant, J., and Geuze, R. (1984). The functional significance of event-related desynchronization of alpha rhythm in attentional

and activating tasks. *Electroencephalography and Clinical Neurophysiology*, 58(6):519–524. https://doi.org/10.1016/0013-4694(84)90042-7.

Vařeka, L. (2020). Evaluation of convolutional neural networks using a large multi-subject p300 dataset. *Biomedical Signal Processing and Control*, 58:101837. https://doi.org/10.1016/j.bspc.2019.101837.

Varga, N. L. and Manns, J. R. (2021). Delta-modulated cortical alpha oscillations support new knowledge generation through memory integration. *NeuroImage*, 244:118600. https://doi.org/10.1016/j.neuroimage.2021.118600.

Verma, N., Le, T., Mudge, J., Nicksic, P. J., Xistris, L., Kasole, M., Shoffstall, A. J., Poore, S. O., Ludwig, K. A., and Dingle, A. M. (2022). Efficacy of bone stimulators in large-animal models and humans may be limited by weak electric fields reaching fracture. *Scientific Reports*, 12(1):21798. https://doi.org/10.1038/s41598-022-26215-w.

Vogt, B. A., Vogt, L., and Laureys, S. (2006). Cytology and functionally correlated circuits of human posterior cingulate areas. *Neuroimage*, 29(2):452–466. https://doi.org/10.1016/j.neuroimage.2005.07.048.

Volpe, U., Mucci, A., Bucci, P., Merlotti, E., Galderisi, S., and Maj, M. (2007). The cortical generators of p3a and p3b: a loreta study. *Brain research bulletin*, 73(4-6):220–230. https://doi.org/10.1016/j.brainresbull.2007.03.003.

Vorwerk, J., Aydin, Ü., Wolters, C. H., and Butson, C. R. (2019). Influence of Head Tissue Conductivity Uncertainties on EEG Dipole Reconstruction. *Frontiers in Neuroscience*, 13:531. https://doi.org/10.3389/fnins.2019.00531.

Vorwerk, J., Cho, J.-H., Rampp, S., Hamer, H., Knösche, T. R., and Wolters, C. H. (2014). A guideline for head volume conductor modeling in EEG and MEG. *NeuroImage*, 100:590–607. https://doi.org/10.1016/j.neuroimage.2014.06.040.

Vorwerk, J., Clerc, M., Burger, M., and Wolters, C. H. (2012). Comparison of Boundary Element and Finite Element Approaches to the EEG Forward Problem. *Biomedical Engineering / Biomedizinische Technik*, 57(SI-1 Track-O):795–798. https://doi.org/10.1515/bmt-2012-4152.

Vorwerk, J., Oostenveld, R., Piastra, M. C., Magyari, L., and Wolters, C. H. (2018). The FieldTrip-SimBio pipeline for EEG forward solutions. *BioMedical*

Engineering OnLine, 17(1):37. https://doi.org/10.1186/s12938-018-0463-y.

Walhovd, K. B., Rosquist, H., and Fjell, A. M. (2008). P300 amplitude age reductions are not caused by latency jitter. *Psychophysiology*, 45(4):545–553. https://doi.org/10.1111/j.1469-8986.2008.00661.x.

Wang, L., Jensen, O., Van den Brink, D., Weder, N., Schoffelen, J.-M., Magyari, L., Hagoort, P., and Bastiaansen, M. (2012). Beta oscillations relate to the n400m during language comprehension. *Human brain mapping*, 33(12):2898–2912. https://doi.org/10.1002/hbm.21410.

Wernicke, C. (1881). *Lehrbuch der Gehirnkrankheiten für Aerzte und Studirende. v. 2-3, 1881-83*, volume 2. Fischer.

Wertz, R. T., Auther, L. L., Burch-sims, G. P., Abou-khalil, R., Kirshner, H. S., and Duncan, G. W. (1998). A comparison of the mismatch negativity (mmn) event-related potential to tone and speech stimuli in normal and aphasic adults. *Aphasiology*, 12(7-8):499–507. https://doi.org/10.1080/02687039808249553.

Woodman, G. F., Wang, S., Sutterer, D. W., Reinhart, R. M., and Fukuda, K. (2022). Alpha suppression indexes a spotlight of visual-spatial attention that can shine on both perceptual and memory representations. *Psychonomic Bulletin & Review*, 29(3):681–698. https://doi.org/10.3758/s13423-021-02034-4.

Woody, C. D. (1967). Characterization of an adaptive filter for the analysis of variable latency neuroelectric signals. *Medical and biological engineering*, 5(6):539–554. https://doi.org/10.1007/BF02474247.

Wronka, E., Kaiser, J., and Coenen, A. M. (2012). Neural generators of the auditory evoked potential components p3a and p3b. *Acta neurobiologiae experimentalis*, 72(1):51–64. https://doi.org/10.55782/ane-2012-1880.

Xiao, X.-Z., Wong, H. K., Wang, Y., Zhao, K., Zeng, G. Q., Yip, L.-Y., Wong, G. C.-S., and Tse, C.-Y. (2018). Detecting violation in abstract pitch patterns with mismatch negativity. *Psychophysiology*, 55(8):e13078. https://doi.org/10.1111/psyp.13078.

Yacovone, A., Moya, E., and Snedeker, J. (2021). Unexpected words or unexpected languages? two erp effects of code-switching in naturalistic discourse. *Cognition*, 215:104814. https://doi.org/10.1016/j.cognition.2021.104814.

Yago, E., Escera, C., Alho, K., and Giard, M. H. (2001). Cerebral mechanisms underlying orienting of attention towards auditory frequency changes. *Neuroreport*, 12(11):2583–2587. https://doi.org/10.1097/00001756-200108080-00058.

Yuan, B., Zhang, N., Gong, F., Wang, X., Yan, J., Lu, J., and Wu, J. (2022). Longitudinal assessment of network reorganizations and language recovery in postoperative patients with glioma. *Brain communications*, 4(2):fcac046. https://doi.org/10.1093/braincomms/fcac046.

Yuan, T., Zuo, Z., Ying, J., Jin, L., Kang, J., Gui, S., Wang, R., and Li, C. (2020). Structural and functional alterations in the contralesional medial temporal lobe in glioma patients. *Frontiers in neuroscience*, 14:10. https://doi.org/10.3389/fnins.2020.00010.

Yushkevich, P. A., Piven, J., Cody Hazlett, H., Gimpel Smith, R., Ho, S., Gee, J. C., and Gerig, G. (2006). User-guided 3D active contour segmentation of anatomical structures: Significantly improved efficiency and reliability. *Neuroimage*, 31(3):1116–1128. https://doi.org/10.1016/j.neuroimage.2006.01.015.

Zhang, Y., Yan, F., Wang, L., Wang, Y., Wang, C., Wang, Q., and Huang, L. (2018). Cortical areas associated with mismatch negativity: A connectivity study using propofol anesthesia. *Frontiers in human neuroscience*, 12:392. https://doi.org/10.3389/fnhum.2018.00392.

Zorzos, I., Kakkos, I., Ventouras, E. M., and Matsopoulos, G. K. (2021). Advances in electrical source imaging: a review of the current approaches, applications and challenges. *Signals*, 2(3):378–391. https://doi.org/10.3390/signals2030024.

Zoumpoulaki, A., Alsufyani, A., Filetti, M., Brammer, M., and Bowman, H. (2015). Latency as a region contrast: Measuring erp latency differences with dynamic time warping. *Psychophysiology*, 52(12):1559–1576. https://doi.org/10.1111/psyp.12521.